2013

High Energy, High Average Power, Picosecond Laser Systems To Drive Few-cycle Opcpa

Andreas Vaupel
University of Central Florida

HIGH ENERGY, HIGH AVERAGE POWER, PICOSECOND LASER SYSTEMS TO DRIVE FEW-CYCLE OPCPA

by

ANDREAS VAUPEL
Diploma-Physicist, Philipps-University Marburg, Germany, 2008
M.S., University of Central Florida, USA, 2009

A dissertation submitted in partial fulfillment of the requirements
for the degree of Doctor of Philosophy
in the College of Optics and Photonics
at the University of Central Florida
Orlando, Florida

Summer Term
2013

Major Professors:
Martin Richardson
Eric Cormier

ABSTRACT

The invention of chirped-pulse amplification (CPA) in 1985 led to a tremendous increase in obtainable laser pulse peak intensities. Since then, several table-top, Ti:sapphire-based CPA systems exceeding the 100 TW-level with more than 10 W average power have been developed and several systems are now commercially available. Over the last decade, the complementary technology of optical parametric chirped-pulse amplification (OPCPA) has improved in its performance to a competitive level. OPCPA allows direct amplification of an almost-octave spanning bandwidth supporting few-cycle pulse durations at center wavelengths ranging from the visible to the mid-IR. The current record in peak power from a table-top OPCPA is 16 TW and the current record average power is 22 W. High energy, few-cycle pulses with stabilized carrier-envelope phase (CEP) are desired for applications such as high-harmonic generation (HHG) enabling attoscience and the generation keV-photon bursts.

This dissertation conceptually, numerically and experimentally describes essential aspects of few-cycle OPCPA, and the associated pump beam generation. The main part of the conducted research was directed towards the few-cycle OPCPA facility developed in the Laser Plasma Laboratory at CREOL (University of Central Florida, USA) termed HERACLES. This facility was designed to generate few-cycle pulses in the visible with mJ-level pulse energy, W-level average power and more than 100 GW peak power. Major parts of the implementation of the HERACLES facility are presented.

The pump generation beam of the HERACLES system has been improved in terms of pulse energy, average power and stability over the last years. It is based on diode-pumped, solid-state amplifiers with picosecond duration and experimental investigations are presented in detail. A

robust system has been implemented producing mJ-level pulse energies with ~100 ps pulse duration at kHz repetition rates. Scaling of this system to high power (>30 W) and high peak power (50-MW-level) as well as ultra-high pulse energy (>160 mJ) is presented. The latter investigation resulted in the design of an ultra-high energy system for OPCPA pumping. Following this, a new OPCPA facility was designed termed PhaSTHEUS, which is anticipated to reach ultra-high intensities.

Another research effort was conducted at CELIA (Univeristé de Bordeaux 1, France) and aimed towards a previously unexplored operational regime of OPCPA with ultra-high repetition rates (10 MHz) and high average power. A supercontinuum seed beam generation has been established with an output ranging from 1.3 to 1.9 μm and few ps duration. The pump beam generation has been implemented based on rod-type fiber amplifiers producing more than 37 W average power and 370 kW peak power. The utility of this system as an OPCPA pump laser is presented along with the OPA design.

The discussed systems operate in radically different regimes in terms of peak power, average power, and repetition rate. The anticipated OPCPA systems with few-cycle duration enable a wide range of novel experimental studies in attoscience, ultrafast materials processing, filamentation, LIBS and coherent control.

To my family

ACKNOWLEDGMENTS

With these words, I would like to thank the many individuals who contributed in some way to this dissertation and towards my completion of the PhD program. Research projects with broader scope would not be possible without the tremendous support of my knowledgeable colleagues.

First and foremost, I would like to thank Dr. Martin Richardson, my advisor at the University of Central Florida, for his guidance, support and inspiration over the years leading to this dissertation. From the beginning, he was open to the idea of a co-tutelle PhD dissertation and provided me the many opportunities which led to the successful realization.

I am very thankful to Dr. Eric Cormier, my advisor at the Université de Bordeaux 1, for his immediate availability for this co-tutelle dissertation and the opportunity to collaborate with his laboratories. The visit in his research laboratories was very pleasant and I enjoyed working with him despite the time difference of six to nine hours between the countries.

I would like to acknowledge the Embassy of France in the United States, which awarded me a Chateaubriand Fellowship supporting my stay in France and this co-tutelle dissertation.

My gratitude goes to Dr. Axel Schülzgen, Dr. Peter Delfyett, and Dr. Bhimsen Shivamoggi, my dissertation committee members, for their active encouragements, useful help and advices during my years as PhD student.

My thanks go to Dr. Lawrence Shah, Benjamin Webb, Nathan Bodnar and Dr. Michaël Hemmer, the current and former members of the ultrafast team in the Laser Plasma Laboratory. Most of the analyses, simulations and experiments would not have been possible without their contribution and solid work. Especially Larry gave me plenty of support with his comprehensive

technical experiences, fruitful discussions and his unchallenged editing/reviewing skills. I also would like to thank Dr. Matthieu Baudelet for supporting me similarly over the years.

I must thank my colleagues at the Université de Bordeaux 1, namely Dr. Sébastien Février, Dr. Jerome Lhermite, Guillaume Machinet, Dr. Sébastien Montant, Dr. Julien Nillon, Dr. Stephane Petit, and Romain Royon, which provided plenty of help during my visit.

Many thanks to all current and former members of LPL for their immediate help in numerous crucial situations over the years. Also, thanks to all other CREOL students and visiting students and to all, who “enjoyed” playing regularly soccer in the humid summer evenings in Florida.

I would like to thank all other CREOL faculty and scientists for sharing their expertise openly and the comprehensive course work. I would like to thank the CREOL staff for their support in many situations.

Finally, I would like to thank Clémence Jollivet and my family, who always supported me during this long journey. Their understanding, trust and patience was very imported for me. Merci.

TABLE OF CONTENTS

LIST OF FIGURES

LIST OF TABLES

LIST OF ACRONYMS/ABBREVIATIONS

AOM	Acousto-optical modulator
AOPDF	Acousto-optical programmable dispersive filter
APD	Avalanche photo diode
AR	Anti-reflection (coating)
ASE	Amplified spontaneous emission
BaF2	Barium fluoride glass
BBO	Beta barium borate
BK7	A type of crown glass
CEP	Carrier-envelope phase
CM	Chirped mirror
CPA	Chirped-pulse amplification
cw	Continuous wave
Dazzler	A special type of AOPDF
DF	Difference frequency
DFG	Difference frequency generation
DM	Dielectric mirror
DPSS	Diode-pumped solid-state (amplifier)
DPSS	Diode-pumped solid-state laser
EUV	Extreme ultra-violet
FEA	Finite element analysis
FOD	Fourth order dispersion
FR	Faraday Rotator
FS	Fused silica
FWHM	Full width half maximum
GD	Group delay
Grism	An optical pulse stretching device
GVD	Group velocity dispersion
GVM	Group velocity mismatch
HCF	Hollow core fiber
HERACLES	High-energy, repetition-rate adjustable, carrier-locked-to-envelope system
HHG	High harmonic generation
HR	High reflectivity (mirror)
HWP	Half-wave plate, also "$\lambda/2$"
IR	Infrared
LBO	Lithium triborate
LCD	Liquid crystal display
LD	Laser diode
LMA	Large mode area (fiber)
LP	Linear polarized transverse mode
M^2	Beam quality parameter
MFD	Mode field diameter

MOPA	Master oscillator power amplifier
NA	Numerical aperture
Nd	Neodymium
NOPA	Noncollinear optical parametric amplification
OC	Output coupler
OPA	Optical parametric amplification or optical parametric amplifier
OPCPA	Optical parametric chirped-pulse amplification
OPG	Optical parametric generation
OPO	Optical parametric oscillator
OPP	Optical parametric phase
OSA	Optical spectrum analyzer
PC	Pockels cell
PCF	Photonic crystal fiber
PhaSTHEUS	PHAse-Stabilized, Terawatt, High-Energy, Ultra-Short system
PM	Polarization maintaining
PPLN	Periodically-poled Lithium Niobate
QR	Quartz rotator
QWP	Quarter-wave plate, also ”$\lambda/4$”
SF	Super fluorescence or sum frequency, depending on context
SF8, SF11, SF57	Highly dispersive types of optical glass
SFG	Sum frequency generation
SH	Second harmonic
SHG	Second harmonic generation
SLM	Spatial light modulator
SMF	Single-mode fiber
SPM	Self-phase modulation
SSFS	Soliton self-frequency shift
ssg	Small signal gain
TBP	Time-bandwidth product
TEM	Transverse electric field mode
TFP	Thin-film polarizer
TH	Third harmonic
THG	Third harmonic generation
Ti	Titanium
TOD	Third order dispersion
UV	Ultraviolet
VBG	Volume Bragg Grating
WDM	Wavelength de-multiplexer
WLG	White light generation
XPM	Cross-phase modulation
YAG	Yttrium aluminum garnet crystal
Yb	Ytterbium
YVO_4	Yttrium orthovanadate crystal, “Vanadate”

1 INTRODUCTION

Since their first demonstration in 1964, ultrafast mode-locked laser oscillators have evolved quickly into extremely popular research tools [1]. The main characteristic of such lasers is that the optical energy output is not continuous, but concentrated in time into ultrashort optical pulses. Typical ultrashort pulse durations are in the regimes of pico- (1 ps = 10^{-12} seconds) and femtoseconds (1 fs = 10^{-15} seconds). Even with the moderate pulse energies available directly from the mode-locked oscillators, the resulting peak intensity is high with strong electric field strength. These extreme driving fields open a wide range of novel applications, such as highly nonlinear experiments [2], ablation [3], waveguide fabrication [4], micro welding [5] or ultra-broadband spectroscopy with sub-10-fs resolution [6]. Another important characteristic of ultrashort mode-locked lasers is the generation of almost octave-spanning optical frequency combs, which are a direct consequence of the mode-locking process itself [7]. The high frequency-stability of these combs and the ability to control and measure their absolute frequency with high accuracy enabled a variety of spectroscopic applications [8]. Some systems have been employed to synthesize electro-magnetic radiation spanning more than 100 THz of bandwidth with fractional uncertainty on the order of 10^{-19} [9].

Some ultrafast mode-locked oscillators already exhibit peak powers beyond the 100-kW-level corresponding to sub-10-fs pulse duration and more than 1 nJ pulse energy. These obtainable peak powers can be even further increased by ultrafast amplifier schemes. For example, if the output of an ultrafast oscillator with 1 nJ optical pulse energy is amplified to 2 mJ with a 8 fs pulse duration, the corresponding peak power is 0.25 TW. When focusing these optical pulses to a 25

µm spot-diameter, the corresponding peak intensity is on the order of $10^{16}\ W/cm^2$. These intense ultrashort pulses have been proven extremely useful in nonlinear optical experiments. An exemplary experimental configuration that greatly benefits from few-cycle pulse durations and higher electric field strengths from the driving laser is high-harmonic generation (HHG) [2]. Attosecond (1 as = 10^{-18} seconds) pulses can be generated through HHG from an intense femtosecond pulse [10] [11]. In this process, each half-cycle of the electrical driving field generates a burst of extreme ultra-violet (XUV) photons. The first pulse with a duration of less than 1 fs was reported in 2001 [12]. These XUV sources have been employed in exciting studies to measure the dynamics in molecules with high photon energies and at ultrahigh time resolution [13] [14]. Advances in the generation of ultra-high energy lasers pulses as a driving laser source with quasi-single cycle duration enabled the production of isolated attosecond pulses via HHG through the temporal gating method. Notable achievements include the generation of isolated optical pulses as short as 80 as duration [15] and photons in the XUV regime with energies up to 1 kiloelectronvolt (keV) [16]. Optical polarization gating techniques, such as double optical gating (DOG) [17], have also been used to produce isolated attosecond pulses as short as 67 as from a high intensity, multi-cycle driving laser [18]. Recent developments in the HHG process as well as new high-intensity laser amplifier systems have enabled the generation of attosecond pulses with moderate pulse energies, establishing a new research field called attoscience [19].

A few exemplary studies employing intense few-cycle pulses are briefly described in the following:

- Time-resolved experiments with XUV attosecond bursts enabled, for the first time, deeper insight in the temporal evolution of inner atomic processes. For example, the electron in the standard hydrogen atom has been studied and shown to have an oscillation period of

about 400 as [20]. In another investigation, intense attosecond pulses were employed to observe the electron tunneling effect in atoms with sub-fs temporal resolution [21].

- An XUV photon burst typically consists of high-harmonics of the driving fundamental electric field. If the fundamental field has a center wavelength of 800 nm, the 50^{th} harmonic corresponds to a wavelength of 16 nm. Since the HHG process can result in a coherent XUV photon burst, these beams can be used in diffraction imaging. In one study, a 219 nm image was resolved utilizing this method [22].
- Intense laser radiation and HHG can be employed as seed source for free-electron lasers [23]. The scheme benefits from the coherent nature of the HHG process with the temporally confined XUV photon burst at the sub-fs time scale.
- Numerical results suggested in 1999 that peak intensities in the relativistic regime would allow the acceleration of protons [24] [25]. Recently, proton beams with energies up to 23 MeV were reported driven by a 130 TW laser system [26]. The effect was also studied with a table-top system with kHz-repetition rate and a few-cycle pulse duration and a dependence of the cut-off energy with driving laser intensity was presented [27].

1.1 Few-Cycle Laser Pulses

To date, few-cycle optical pulses are routinely generated in laboratories around the world by utilizing ultra-broadband Ti:sapphire oscillators [1]. The development was initiated by the successful manipulation of the intra-cavity dispersion of ultrashort Ti:sapphire oscillators with a prism pair [28] and pairs of chirped-mirrors [29]. This enables oscillators with ultrabroad bandwidth, which under certain conditions can even exceed the stimulated emission bandwidth of the Ti:sapphire gain material. The time-bandwidth product describes the relationship between pulse duration and bandwidth given by

$$TBP = \Delta\tau\Delta\nu \geq 0.441 \quad (1)$$

for transform-limited Gaussian pulses [30].

The shortest durations directly obtained from these mode-locked Ti:sapphire oscillators approach the time period of an electric field oscillation, typically 2.66 fs at 800 center wavelength. Figure 1-1 shows an example of a Gaussian pulse with 5 fs full width half maximum (FWHM) duration at 800 nm center wavelength corresponding to 2.1 optical cycles. Ultrashort pulses in this regime are commonly termed few- or quasi-single cycle pulses.

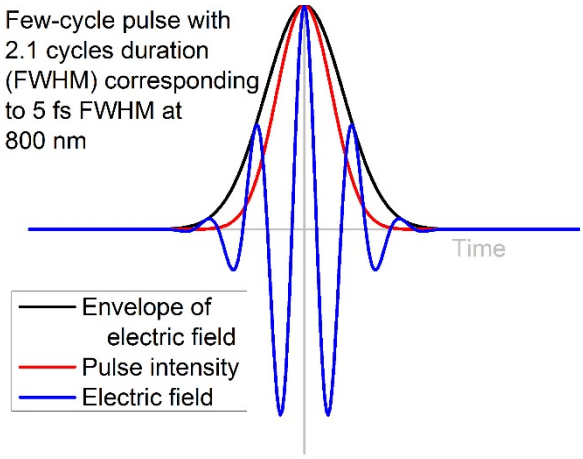

Figure 1-1: Sketch of an electric field (optical pulse) with few-cycle duration. The envelope of the electric field (black), the pulse intensity (red) and the electric field (blue) are shown.

The full electric field in the time domain of an optical pulse is given by the expression

$$E(t) = E_0(t)\exp(i\omega_0 t + \varphi_{CE}) + c.c. , \quad (2)$$

where $E_0(t)$ is typically the Gaussian- or sech^2-shaped envelope of the electric field, ω_0 the fundamental or center frequency and φ_{CE} the so called carrier-envelope phase (CEP). The latter is defined as the phase between the maximum of the electric field to the maximum of the envelope. In 2000, it became possible for the first time to access the carrier-envelope phase (CEP) φ_{CE} of the electric field [8]. In particular for ultrashort pulses approaching the single-cycle regime, the

maximum electric field strength varies dramatically if there is a change in the CEP from pulse to pulse [31].

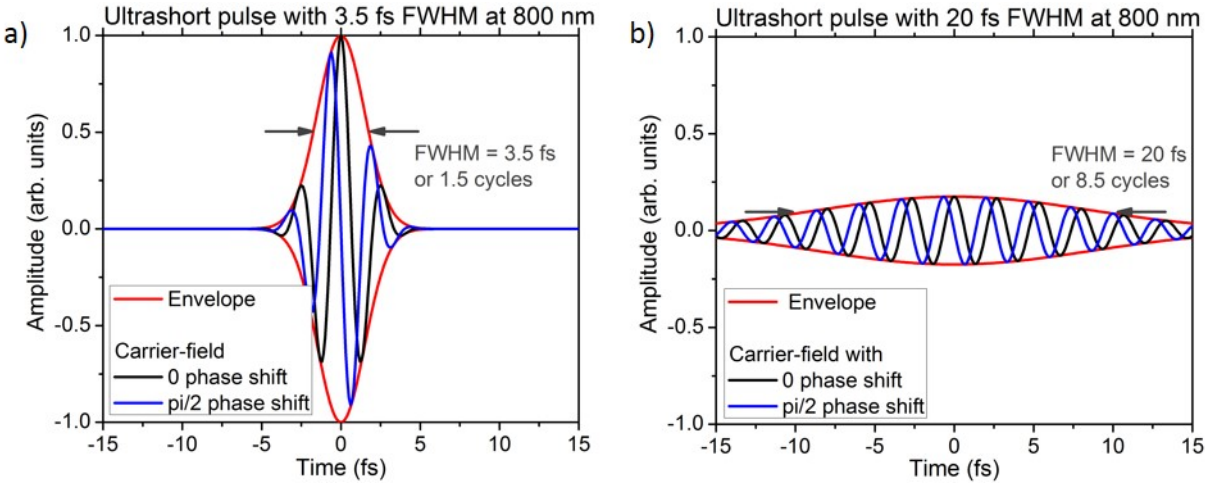

Figure 1-2: Plot of ultrashort pulses with FWHM pulse duration of 3.5 fs or quasi-single cycle (a) and 20 fs or multi-cycle filed (b).

Figure 1-2 shows example pulses with durations of 3.5 fs and 20 fs (FWHM) corresponding to 1.5 (quasi-single cycle pulse) and 8.5 optical cycles (multi-cycle pulse). In the figure, the pulse envelopes are colored in red and the pulse energies normalized. Assuming an energy of 1 mJ in each pulse, the peak powers of the quasi-single cycle and the multi-cycle pulses would be 285 GW and 50 GW, respectively. The electric fields with zero (black curve) and $\pi/2$ phase shift (blue curve) are displayed. First, it can be observed, that the highest field strength is given for zero phase shift. Secondly, the difference between the highest values for zero and $\pi/2$ shifts is much greater for the quasi-single cycle pulse. Generating pulses approaching the single-cycle limit as well as locking the CEP were major accomplishments in the field of ultra-fast laser science.

1.2 Amplification of Few-Cycle Pulses

Highly nonlinear optics requires large laser intensities. Thus, it is not only necessary to concentrate the energy in an ultrashort pulse but also to maximize the energy in the pulse. Chirped-

pulse amplification (CPA) was introduced in 1985 [32] to amplify pulses with sub-50-fs pulse duration [33]. Systems exceeding the 100 TW-level with more than 10 W average power have been presented [34] and TW-level Ti:sapphire-based CPA systems are commercially available. Traditional Ti:sapphire-based CPA is typically limited to pulse durations of >35 fs, due to the limited amplification bandwidth of the gain material, prohibiting the direct amplification of few-cycle pulses. External spectral broadening in a hollow core fiber with noble gas and post-compression can be employed to shorten the pulse duration and in 1997 the first compression to the sub-5-fs level was achieved utilizing this method [35]. Similarly, the nonlinear interactions occurring during filamentation can be employed to generate high energy few-cycle pulses [36].

Over the last decade, optical parametric chirped-pulse amplification (OPCPA) has improved in performance. It is seen as a highly promising scheme for the direct amplification of few-cycle pulses reaching high-intensities. Pulse durations as short as 4 fs have been directly amplified by OPCPA without the need for post-amplification nonlinear spectral broadening [37]. The current record in peak power from a table-top OPCPA is 16 TW [38] and the current record average power is 22 W [39]. OPCPA offers the ability to produce high energy and high average power in the few-cycle pulse regime, i.e. sub-10-fs for 800 nm center wavelength, and average power of several Watts depending on the configuration. However, OPCPA provides much greater flexibility in choosing the center wavelength for amplification from the visible to the mid-IR than CPA. As detailed later in Chapter 2, the available pump lasers currently limit the scalability of the OPCPA output power and pulse energy. In addition, the stability of an OPCPA system is largely dependent on its pump laser due to the nonlinear nature of the amplification process. Thus, high quality, picosecond pump lasers are a key requirement for laboratory-scale few-cycle OPCPA systems. The design and implementation of a high-performance and highly stable picosecond

pump lasers are two of the most challenging parts in OPCPA development. Several different laser technologies are employed for the pump beam generation, such as flashlamp-pumped solid-state rods [40], diode-pumped solid-state rods [41], diode-pumped cryogenically-cooled crystals [42], thin-disk [43] and fiber [39] amplifiers. These systems operate in largely different regimes in terms of pulse energy and repetition rate, making each most appropriate for different applications. For example, flashlamp-pumped, solid-state amplifiers provide high-gain with large aperture amplifiers generating up to J-level OPCPA pump pulses [38]. In contrast, fiber-based amplifier systems offer operation with high repetition rate and high average power but with OPCPA pulse energies limited to the 100-µJ-level [44].

The majority of the research conducted for this dissertation was directed towards the development of a laboratory-scale, few-cycle OPCPA facility. An important topic in this dissertation has been scaling both the output energy and average power of picosecond laser systems to drive few-cycle OPCPA systems at a higher performance level. The details of the solid-state amplifier chain are presented in this dissertation, including high average power [45] and ultra-high energy configurations [46]. In addition, initial investigations towards a high average power, 10 MHz OPCPA system are presented.

1.3 Few-Cycle OPCPA Facilities

In order to provide a robust platform for cutting-edge experiments, the CREOL Laser Plasma Laboratory (LPL) has invested heavily in the development of high energy, few-cycle, ultrafast laser systems. The focus of this dissertation is the OPCPA facility presented in Chapter 5 named HERACLES facility (**h**igh-**e**nergy, **r**epetition rate **a**djustable, **c**arrier-**l**ocked-to **e**nvelope **s**ystem). The few-cycle system is based on a traditional OPCPA in the visible to near IR consisting of an ultra-broadband Ti:sapphire oscillator and BBO OPAs. The pump is generated in a hybrid

ultrafast/fiber/solid-state MOPA system with diode-pumped, solid-state amplifiers as final amplifier stages presented in Chapter 4. The few-cycle OPCPA facility is anticipated to provide several mJ pulse energy with sub-10-fs pulse duration and several kHz repetition rate. The HERACLES facility was designed for applications [47] such as HHG and attoscience [48], filamentation [49] or CEP-dependent materials processing [50]. An early version of the system was presented in [51] and [52], and since then underwent several major re-designs towards improved output performance.

In addition to the HERACLES facility, two additional research projects are presented in this dissertation. Promising results with ultra-high energy amplifiers led to another research effort in the Laser Plasma Laboratory on ultra-high peak intensity, quasi-single cycle OPCPA. The design of a new OPCPA facility is presented in Section 4.5, named PhaSTHEUS (PHAse-Stabilized, Terawatt, High-Energy, Ultra-Short system). This facility design is anticipated to provide similar output to [38] featuring sub-5-fs duration with two-color pumping [53] and 100 mJ-level pulse energy [46].

On the other hand, the initial implementations of a high average power, 10 MHz OPCPA system is presented in Chapter 6. The seed and pump beam generation were based on a common high-energy ultrafast oscillator. The pump beam generation for this OPCPA system is based on multiple rod-type fiber amplifiers to maximize average power output [54]. The concept of multi-beam OPA pumping is introduced to further scale the average power and pulse energy in a 10 MHz OPCPA system.

1.4 Dissertation Outline

This dissertation follows the effort of our research laboratory to implement the high-energy and high-average power, few-cycle OPCPA facility HERACLES. Essential aspects, concepts,

implementations and improvements are discussed in detail in this dissertation. As emphasized earlier, the output of OPCPA systems is dictated by the pump laser. Thus, a major part of this dissertation focuses on the development of high-quality pump lasers with picosecond duration and high pulse energy, high average power or both simultaneously. The structure of the dissertation is explained in the following:

Chapter 2 is an overview of the field of ultrafast laser amplifiers. CPA and OPCPA systems are conceptually described along with selected chronological milestones. An overview on selected OPCPA pump laser technologies as well as recent developments and trends are given.

Chapter 3 provides essential aspects necessary to develop few-cycle OPCPA systems. It includes concepts and numerical investigations for more "traditional" laser amplification schemes, few-cycle dispersion management, CEP stabilization and optical parametric amplifiers.

Chapter 4 describes in detail the development and implementation of two high average power, high energy and picosecond laser systems based on diode-pumped, solid-state amplifiers. Power-scaling and energy-scaling are discussed, including initial experimental results. The design of a new OPCPA facility, PhaSTHEUS, is also presented.

Chapter 5 describes the implementation of major components of the HERACLES facility. It is designed to provide a sub-10-fs pulse duration with mJ-level pulse energy at few kilohertz repetition rate. The architecture, pump generation, few-cycle dispersion management, optical parametric amplifier and CEP-stabilization are presented. Several numerical and experimental investigations are discussed.

Chapter 6 contains the concept, numerical results and the initial implementation of a high average power, 10 MHz OPCPA system. The system utilized a Yb:KGW oscillator and nonlinear broadening methods to generate the seed beam. Pump beam generation utilizes on nonlinear

spectral compression in rod-type fiber amplifiers to obtain a high peak and average power output, which is discussed numerically and experimentally. The concept and challenges of multi-beam OPA are introduced.

Chapter 7 concludes the dissertation and gives an outlook.

Appendix A provides supporting material for this co-tutelle dissertation.

Appendix B provides the lists of references from the literature survey supporting Section 2. The key parameters of the OPCPA and the associated systems are listed.

Appendix C summarizes additional experimental findings with the high energy and high average power amplifiers obtained in a regime not directly related to the amplification of picosecond pulses. These investigations allow a better understanding of the employed laser amplifier modules.

2 OVERVIEW OF FEW-CYCLE PULSE AMPLIFICATION

Ultrashort pulses in the few-cycle regime are now routinely produced by commercially available, mode-locked laser oscillators [28]. The output pulse energy of such laser oscillators is typically in the nanojoule (nJ) range [29]; however, much higher pulse energies and intensities are required for wide range of applications. Over the last two decades, many high intensity laser systems have been developed. Many such systems are based on two concepts: chirped-pulse amplification [55] and optical parametric chirped-pulse amplification [56]. Overviews of the historical development and the guiding principles of both techniques are presented in the following two subsections. Both techniques are compared in Subsection 2.3. The following Subsection 2.4 gives an overview of selected published systems covering a broad range of operational parameters. A short historical overview and recent trends in relevant high energy, high average power, and picosecond laser technology are given in Subsection 2.5.

2.1 Chirped-Pulse Amplification

In the 1990s, the primary enabling technology for most of the high-power ultrafast laser systems was chirped-pulse amplification (CPA) as first reported in 1985 [32]. The concept is illustrated in Figure 2-1. Ti:sapphire is the most commonly used gain medium for ultrafast CPA as reviewed in [55]. In CPA, the output of an ultrafast laser oscillator, typically with pulses durations between 5 fs and 1 ps and nJ-energies at tens of MHz repetition rates, are stretched to pulse durations of several 100 ps. The pulse stretching is typically achieved using diffraction grating geometries [57], which decreases the peak power by a factor of 10^3 to 10^5. These stretched pulses are typically amplified by six to nine orders of magnitude (60 to 90 dB) in Ti:sapphire-based regenerative and/or multi-pass amplifiers. These amplifiers provide a single-pass gain

between 2 and 100 per pass with sub-Hz [58] to multi-kHz repetition rates [59]. The full extraction of the stored energy with the original ultrashort pulse duration would result in intensities exceeding the (surface) damage threshold of most of the used materials (Sapphire, Fused Silica (FS) glass, BK7 glass, etc.). In the case of Ti:sapphire, the amplifier stages are typically pumped by electronically synchronized, frequency-doubled Nd:YAG lasers with 5 to 10 ns pulse duration. Thereafter, the amplified pulses are recompressed by a grating or prism pair as presented by Treacy [60] or Fork and Martinez [61] resulting in ultrashort pulses with high intensities.

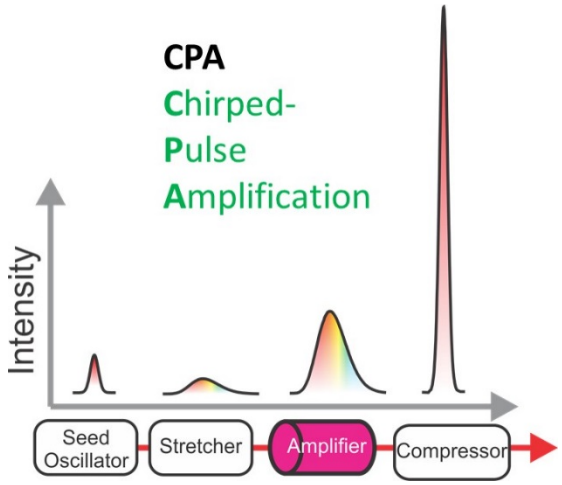

Figure 2-1: Simplified diagram of a chirped-pulse amplification (CPA) system.

In the CPA scheme, the pulse bandwidth is typically limited by the finite gain bandwidth of the employed material and spectral narrowing associated with high gain operation. For example, the gain bandwidth of Ti:sapphire at 800 nm is 75 nm (FWHM) but the obtained bandwidth after 6 to 8 orders of magnitude of amplification reduces to below 35 nm [62]. The transform-limited pulse duration $\Delta\tau$ corresponding to a certain bandwidth $\Delta\lambda$ can be calculated with Equation (1) and the expression [30]

$$\Delta\nu = \frac{c}{\lambda_0^2}\Delta\lambda\,. \tag{3}$$

For example, the 75 nm gain bandwidth of Ti:sapphire corresponds to a pulse duration of 12 fs. A decrease of bandwidth down to 35 nm corresponds to a longer duration of 27 fs. As comparison, the bandwidth corresponding to a transform-limited 50 fs pulse is 19 nm. Thus, conventional CPA based on Ti:sapphire is limited to the amplification of pulses with 35-50 fs transform-limited pulse duration. Nonlinear spectral broadening (coherent) beyond an octave with subsequent pulse compression and chirped-mirrors has enabled the generation of 3.5 fs pulse duration from CPA systems [63]. This approach utilizes the nonlinearities induced during the propagation of the transform-limited pulse through a hollow core fiber filled with a noble gas. This approach is limited to pulse energies of a few mJ due to the limited hollow core fiber (HCF) diameter and onset of damage [64] [65]. A noteworthy CPA record with up to 250 W average power was presented recently based on amplification in a Yb:fiber CPA system and nonlinear post-compression down to 25 fs [66].

2.2 Optical Parametric Chirped-Pulse Amplification

The nonlinear three-wave interaction in optical parametric amplification (OPA) can provide ultra-high gain per unit length, broad wavelength tunability, and a amplification bandwidth exceeding the typical gain specifications of Ti:sapphire. As detailed in Section 3.5, the phase-matching condition in OPA can support nearly octave-spanning spectral bandwidth and parametric gains as high as 10^6. Thus, OPCPA extends the concept of CPA, i.e. pulse stretching, amplification and compression, with the benefits (and challenges) of OPA [67]. It was first demonstrated in 1992 [68] and a review was presented in 2003 [56]. In 2006, the first few-cycle OPCPA laser facility

was presented [69]. Since then, numerous systems have been developed as overviewed in Section 2.4. An OPCPA scheme is shown in Figure 2-2.

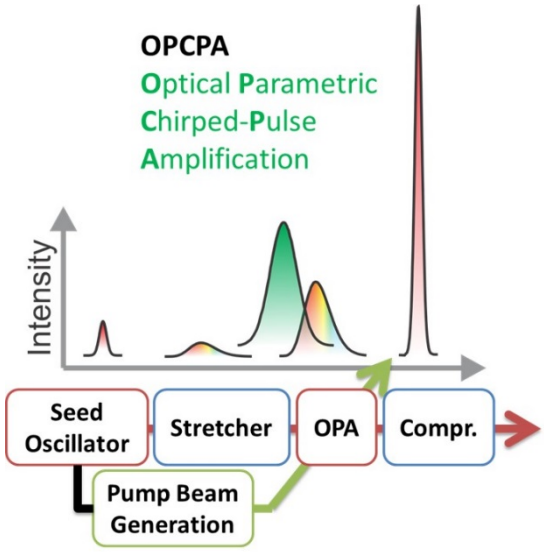

Figure 2-2: Simplified diagram of an optical parametric chirped-pulse amplification (OPCPA) system.

In order to take advantage of the ultra-broad amplification bandwidth in OPCPA, the seed source typically generates few-cycle pulses with CEP stabilization. These seed pulses are usually stretched to 0.5 to 100 ps and re-compressed by introducing dispersion from bulk materials [42] [70], chirped mirrors [39], grating/prism pair [71] [60] or grism pair [72] [73] and then delivered to the OPA stages. Due to the larger bandwidth and relatively large stretching factor, a more sophisticated dispersion management is needed than in traditional CPA. For example, the compressor must provide sufficient bandwidth to not truncate the pulse; therefore, bulk transmission optics are often utilized instead of diffraction gratings pairs [72]. Most OPCPA systems also feature devices with adaptive dispersion allowing fine-adjustments across the large bandwidth, such as an acousto-optical programmable dispersive filter (AOPDF) [40] or a spatial light modulator (SLM) based ultrafast pulse shaper [69].

The pump pulse is typically optically or electronically synchronized to the signal pulse within the necessary timing jitter. In each OPA, the energy is transferred from a narrow-band pump pulse with high energy to the broad-band seed pulse. Since no energy or heat is stored in the nonlinear medium as part of the parametric amplification, the OPA scheme is primarily limited by the pulse energy, average power, beam quality and stability of the driving laser source. Due to the nature of the nonlinear amplification process, the OPCPA pump laser needs to be highly stable in almost all parameters, such as pulse energy, wavelength, pulse duration as well as spatial and temporal pulse overlap. Fluctuations and jitter in any of these parameters are amplified by the OPA.

Two OPCPA facilities are currently being developed within the Laser Plasma Laboratory and are described throughout this dissertation. The HERACLES facility was designed for mJ-level pulses energies, few-cycle duration at kHz repetition rate [52]. The PhaSTHEUS facility (PHAse-Stabilized, Terawatt, High-Energy, Ultra-Short system) was designed for ultra-high pulse energy with quasi-single cycle duration [46]. Both are based on OPA in the visible to near-IR with BBO crystals and a pump beam generation based on solid-state amplifiers and ~100 ps pump pulse duration. For the high average power pump of HERACLES, diode-pumped solid-state rods were employed and the implementation is detailed in Sections 4.2 to 4.4. The pump generation scheme for PhaSTHEUS was designed based on large aperture, flashlamp-pumped, solid-state rods as presented briefly in Section 4.5.

2.3 Comparison between CPA and OPCPA

As previously mentioned, ultrashort pulses are typically amplified utilizing either CPA or OPCPA. Relevant properties for both approaches are collected for comparison in Table 2-1. Both approaches share that the pulses are stretched, amplified and compressed. The benefit of OPCPA

in the direct amplification with broader and tunable bandwidth is evident. The direct comparison from Table 2-1 also highlights the more demanding requirements on pump performance and stability.

Table 2-1: Comparison of key properties between ultrafast pulse amplification based on table-top CPA and OPCPA.

	CPA	**OPCPA**
First reported	1985 [32]	First system in 1992 [68] First facility in 2006 [69]
Amplification process	Stimulated emission	Optical parametric amplification
Central wavelength	800 nm (Ti:sapphire)	0.8, 1.6, 2.1, 3.5, 3.9, 6.0 μm
Typical bandwidth	<50 nm	Almost full octave (500 nm at 800 nm) [39]
Single-pass gain	2-10	$10^2 - 10^6$
Typical number of amplification stages	~20	1-3
Typical pulse duration	25-50 fs (for traditional Ti:sapphire CPA) [55]	5-10 fs at 800 nm [71] 10-15 fs at 2.1 μm [43]
Supports few-cycle duration via	Nonlinear spectral broadening	Large parametric gain bandwidth
Highest few-cycle pulse energy	mJ-level [65]	125 mJ [38]
Pump pulse duration	5-10 ns	0.5-100 ps
Optical-to-optical efficiency	30-40%	10-15%
Power fluctuations	<1% (RMS)	<5% (RMS)
Timing jitter	sub-ns	sub-ps [74] to 10 ps
Highest average power	50 W [59]	22 W [39]
Pulse-to-background contrast	Challenging (up to 10^{10} [75])	Ultra-high ($> 10^{14}$ [76])
Parasitic process	Amplified spontaneous emission (ASE)	Superfluorescence (SF)
Main technological challenge	Thermal management	Pump beam generation

2.4 Recent Advances of OPCPA Laser Systems

The design and performances of several OPCPA systems have been published and selected systems are summarized in Table 2-2. Early systems were based on Ti:sapphire technology [71] or flashlamp-pumped Nd:YAG [40] [69] pump systems with repetition rates of 1 kHz, 10 and 30 Hz, respectively. Subsequent OPCPA systems have utilized pumps based on a variety of technologies, such as diode-pumped solid-state rods [77], thin-disk [70], cryo-cooled [42] and fiber-based [78] amplifiers. Table 2-2 lists the key parameters of selected published OPCPA systems.

Table 2-2: Selected OPCPA systems reported in the literature. A few notable OPCPA records: The record peak power was 16 TW with 125 mJ pulse energy, the record average power was 22 W with 185 W pump power, the highest repetition rate was 1 MHz, the shortest pulse duration was 5.0 fs, and the lowest number of optical cycles was 1.5.

Year	Repetition rate	Pulse energy	Average power	Pulse duration	Cycles	Peak power	Center wavelength	Pump laser technology	Pump duration	Ref
2006	10 Hz	90 mJ	0.9 W	10 fs	3.8	9.0 TW	800 nm	Flashlamp	60 ps	[40]
2006	30 Hz	16 mJ	0.47 W	7.6 fs	2.9	2.1 TW	800 nm	Flashlamp	60 ps	[69]
2006	1 kHz	200 µJ	0.2 W	15 fs	3.0	13 GW	1.5 µm	Ti:sapphire	50 fs	[79]
2007	1 kHz	1.5 mJ	1.5 W	6.4 fs	2.4	230 GW	800 nm	Ti:sapphire	100 ps	[71]
2008	1 kHz	2.7 mJ	2.7 W	5.5 fs	2.1	490 GW	800 nm	Ti:sapphire	75 ps	[80]
2009	100 kHz	1.2 µJ	0.12 W	96 fs	9.0	13 MW	3.2 µm	DPSS	15 ps	[41]
2009	1 kHz	220 µJ	0.22 W	23 fs	3.1	9.6 GW	2.2 µm	DPSS	12 ps	[81]
2009	1 kHz	740 µJ	0.74 W	15.7 fs	2.2	47 GW	2.1 µm	DPSS	49 ps	[77]
2009	10 Hz	0.125 J	1.25 W	7.9 fs	2.9	**16 TW**	805 nm	Flashlamp	78 ps	[38]
2010	100 kHz	3.8 µJ	0.38 W	67 fs	6.3	56 MW	3.2 µm	DPSS	8 ps	[82]
2010	**1 MHz**	420 nJ	0.42 W	9.7 fs	3.6	43 MW	800 nm	Fiber	420 fs	[83]
2010	96 kHz	74 µJ	7.1 W	8.0 fs	3.0	9.3 GW	800 nm	Fiber	780 fs	[78]
2010	143 kHz	1.3 µJ	0.19 W	8.8 fs	3.3	150 MW	800 nm	Thin-disk	1.6 ps	[70]
2010	143 kHz	3 µJ	0.43 W	5.7 fs	2.0	530 MW	850 nm	Thin-disk	1.56 ps	[84]
2011	1 kHz	850 µJ	0.85 W	32 fs	4.6	27 GW	2.1 µm	Cryo SS	12 ps	[42]
2011	30 kHz	87 µJ	2.61 W	5.4 fs	2.0	16 GW	800 nm	Fiber	700 fs	[44]
2011	20 Hz	8 mJ	0.16 W	83 fs	6.4	96 GW	3.9 µm	Flashlamp	70 ps	[73]
2012	1 MHz	22 µJ	**22 W**	**5.0 fs**	1.7	4.4 GW	880 nm	Fiber	500 fs	[39]
2013	3 kHz	1.2 mJ	3.6 W	10.5 fs	**1.5**	114 GW	2.1 µm	Thin-disk	1.6 ps	[43]

The OPCPA systems listed in Table 2-2 are graphically displayed in Figure 2-3 in terms of average power against pulse energy for the different employed pump laser technologies. The plot reveals that the systems typically operate at the few W-level, where the OPCPA performance strictly follows the key characteristics of the employed pump technology (pulse energy and average power with ~10% efficiency). It indicates that the OPCPA process itself is currently not fundamentally limited in either pulse energy or average power. The aperture of the available OPA crystals is not limiting the current performance and active cooling or active thermal management of the OPA stages has not been necessary to date. Currently, scaling OPCPA to higher pulse energies and higher average power is dependent on scaling the driving laser source. For systems operating with high average powers, thermally induced distortions and crystal damage have been observed, attributed to the idler wave absorption and associated temperature gradients [39]. The use of larger beams with higher pulse energies mitigates these effects in the OPA stage reducing the temperature gradients while maintaining high pump peak intensity. The performance of recent visible few-cycle OPCPAs (16 TW peak power and 22 W average power) offer performances comparable with table-top Ti:sapphire-based CPA systems, which typically operate in a range from 10-100 TW peak power and 1-20 W average power. However, their higher complexity and relatively lower output stability associated with OPCPA systems prevent their “routine” application in research laboratories to date and there are currently no commercial systems. Nevertheless, the next generation of OPCPA systems is matured enough allowing this promising technology to be used in more ultrafast laboratories [67].

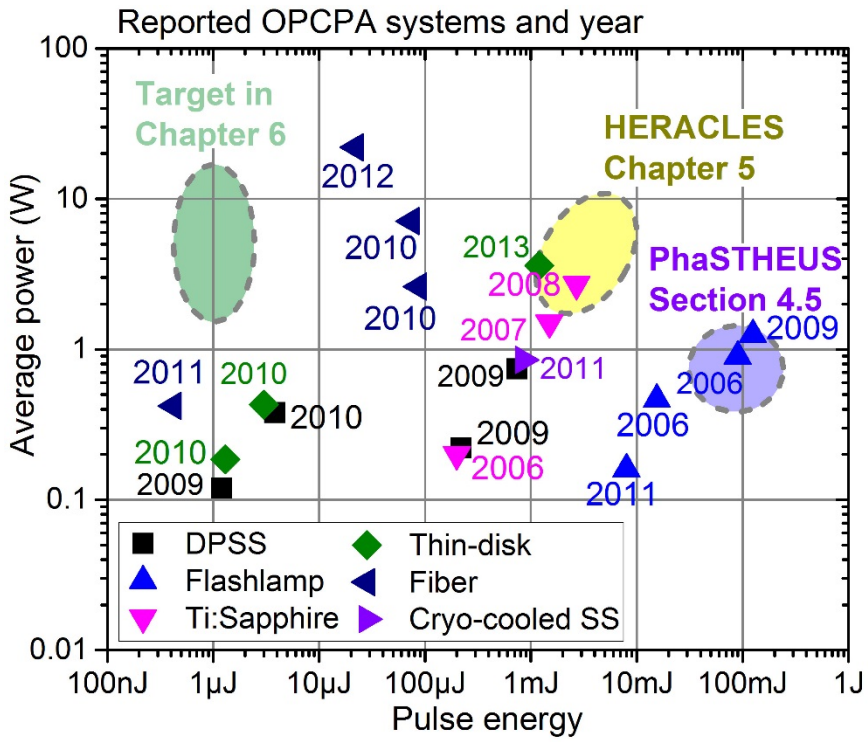

Figure 2-3: The plot shows the average power against the pulse energy of the OPCPA systems shown in Table 2-2. Three areas are highlighted which are in focus of this dissertation.

Three areas are highlighted in Figure 2-3. The yellow region (center) with label "HERACLES Chapter 5" describes the parameter range targeted with the here presented high energy and high average power OPCPA system HERACLES shown in Chapter 5. The purple region (right) with label "PhaSTHEUS Section 4.5" highlights the design range of the PhaSTHEUS facility which is designed to provide ultra-high pulse energies at modest average power described briefly in Section 4.5. The green region (left) with label "Target in Chapter 6" shows the anticipated range of operation of the high average power effort presented in Chapter 6 with OPCPA repetition rates at the MHz-level. The chapter also provides a discussion of the challenges associated with OPCPA systems in this range (~1 µJ pulse energy with 1-10 W average power).

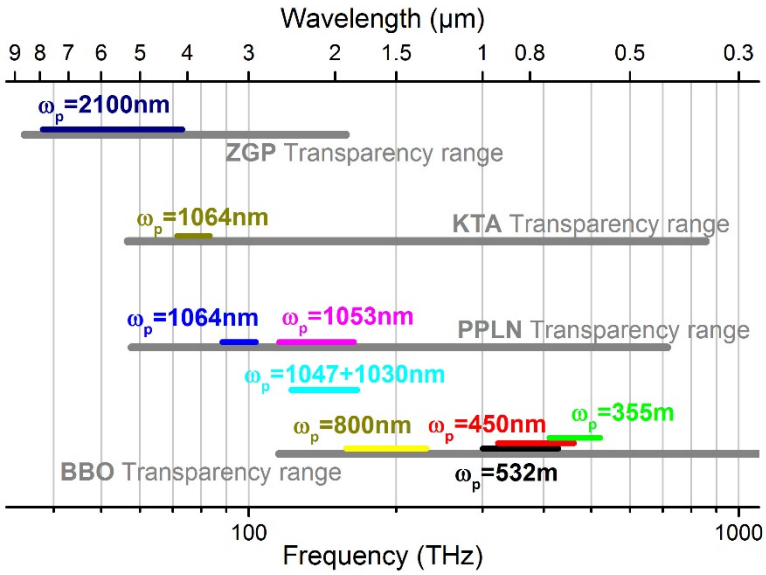

Figure 2-4: Operating wavelength ranges for the OPCPA systems listed in Table 2-2. The transparency ranges were found with the SNLO software package (AS-Photonics, LLC).

The OPCPA system listed in Table 2-2 operate with different pulse energies and repetition rates, as well as a variety of wavelengths ranges. Common wavelength ranges and the transparency range of employed nonlinear crystals are shown in Figure 2-4. The majority of systems with highest performance to date have been based on sources at 515 or 532 nm to pump the amplification of few-cycle pulses in the visible and near-IR with BBO as nonlinear material [40]. More recently, several systems have been demonstrated driven by 1030, 1053 or 1064 nm pump lasers and amplify few-cycle pulses at 2.1 μm center wavelength in PPLN [77] or Mg:O_2 crystals [81] OPAs. Similarly, OPCPA output with 3.2 μm center wavelength has been reported driven by a 1064 nm pump laser source has been reported [82] and cascaded OPA-stages have been utilized to produce a few-cycle OPCPA output at 6 μm center wavelength with mJ-level pulse energy [73].

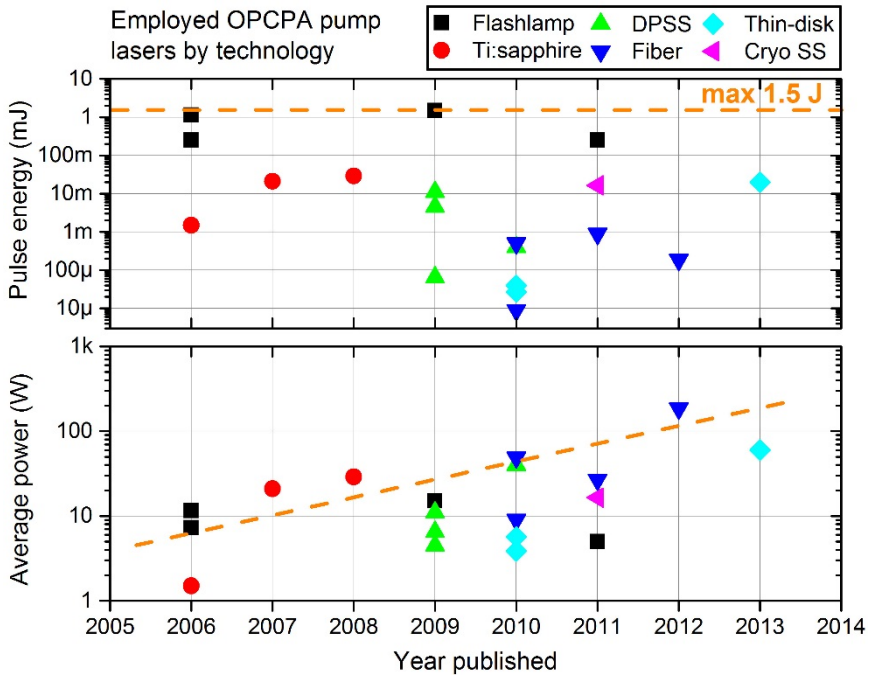

Figure 2-5: Historical trend of pump laser performance for the OPCPA systems listed in Table 2-2 graphically shown in terms of pulse energy and average power and differentiated underlying laser technology.

The pump laser sources for the OPCPA systems listed in Table 2-2 are presented in Figure 2-5 in terms of pulse energy and average power against the year of publication. To date, the maximum pump pulse energy was 1.5 J presented in 2009 [38] and the highest average power was 185 W in 2012 [39]. An increasing trend in average power of the employed pump laser systems can be found, which is supported by the recent progress made in thermal management of high average power amplifier systems such as thin-disk [43] and large mode fiber amplifiers [39].

The choice of pump laser technology is generally motivated by the application. For example, applications requiring ultra-high pulse energies, pump lasers with low repetition rates are used to maximize gain and pulse energy while reducing thermally induced effects. Flashlamp-pumped, solid-state amplifiers can generate pulse energies from tens of mJ to 1 J at repetition rates typically <100 Hz. One such system is presented in Section 4.5. If high pulse energy and high average power is necessary, diode-pumped solid-state amplifiers are utilized. The main part of the

research for this dissertation was dedicated to these systems and is presented throughout Chapter 4. Due to improved thermal management, fiber [78] and thin-disk amplifiers [70] enable the production of pulses at the μJ-level with more than 100 kHz repetition rate and conceptual and experimental investigations with such a fiber-based system are presented later in Section 6.

Over the past 5 years, systems operating at higher repetition rates have emerged based on progress in high power thin-disk regenerative amplifiers [43] and large mode area (LMA) fibers based on large-pitch photonic crystal fibers (PCF) [39]. CPA can also be utilized in the pump beam generation stretching the pulse to several ns and compressing to ~1 ps, taking advantage of the broader gain bandwidth of Yb- relative to Nd-based amplifiers. Due to this development, it can be seen from Table 2-2 that the pump pulse durations have been decreasing towards 0.5 ps leading to higher OPA pump intensities. Higher pump intensities provide increased parametric gain bandwidth leading to quasi-single-cycle pulses from the OPCPA systems. However, the temporal overlap between seed and pump pulse in the OPA requires a timing jitter of much less than seed and pump pulse duration. The latter can be challenging in pump beam generation schemes based on CPA and sub-1-ps duration [74]. From Table 2-2, one can see that the listed OPCPA systems operate in the few-cycle regime with output pulse durations typically around 2 optical cycles corresponding to 7 fs at 800 nm. The CPA-based pump beam generation has two drawbacks compared to a MOPA design: first, appropriately large aperture, solid-state amplifiers are not readily available and are currently developed in several research institutes [85] [86]. Second, the increased complexity and footprint tend to negatively impact system stability in terms of pulse energy, beam pointing, and timing jitter [74].

2.5 Recent Developments in Relevant Laser Technology

This section reviews recent progress in laser technology for OPCPA pumping. A literature study has been performed to identify trends based upon journal publications in the last 4 years (see Table B-2). The performance of the pump lasers of the systems presented in Table 2-2 (see Table B-1) were considered as well, and more detail is provided in Appendix B. Most of the systems listed in Table B-2 were not directly intended for the OPCPA pumping application and only a few have been reported with experiments involving OPCPA methods. The required performance for OPCPA pumping was assumed to be: <100 ps pulse duration, >1 µJ pulse energy, >1 W average power and >1 Hz repetition rate. The laser systems can be separated in MOPA systems (master oscillator, power amplifier), where the pulse duration remains fixed, and CPA systems, where the pulse is stretched, amplified and compressed.

Four characteristic performance levels are shown in Table 2-3 based on the values obtained during the experimental implementation of HERACLES. “Scaling Limit?” describes the performance anticipated from extending the current approach based on diode-pumped, solid-state rods to 4 mm diameter as presented in Section 4.4. The performance of the pump laser for PhaSTHEUS and the 10 MHz OPCPA (Chapter 6) are not specified as these efforts are still at a relatively early stage of development.

Table 2-3: Characteristic performances highlighted in the figures of this subsection.

Label	Pulse energy [mJ]	Average power [W]	Peak power [MW]	Presented in
Section 4.2	2.0	20	19.0	Section 4.2
Section 4.3	4.0	12	23.4	Section 4.3
Section 4.4	10.7	32	51.5	Section 4.4
Scaling Limit?	40	120	400	Section 4.4

Figure 2-6 plots the average power relative to pulse energy for selected MOPA and CPA systems. The plot reveals that high average powers >100 W are reached in either MOPA or CPA

configurations. Yb-based CPA systems typically have slightly higher energy extraction efficiency due to above saturation fluence operation lower quantum defect compared to Nd-based amplifiers. Additional losses in CPA systems arise from the grating compressor with typical values ranging from 60 to 75% transmission for commercially available holographic gratings [85] and 90 to 95% for dielectric gratings [42]. These additional losses seem to be overcome by the more efficient power extraction in Yb-based systems resulting in higher performance compared to the Nd-based MOPA systems. In general, these CPA systems are more complex and require a larger footprint due to the pulse stretcher and compressor assembly. Due to the increased complexity, pulse-to-pulse fluctuations, power fluctuations and timing fluctuations [74] are likely to increase along with an increased difficulty of operation.

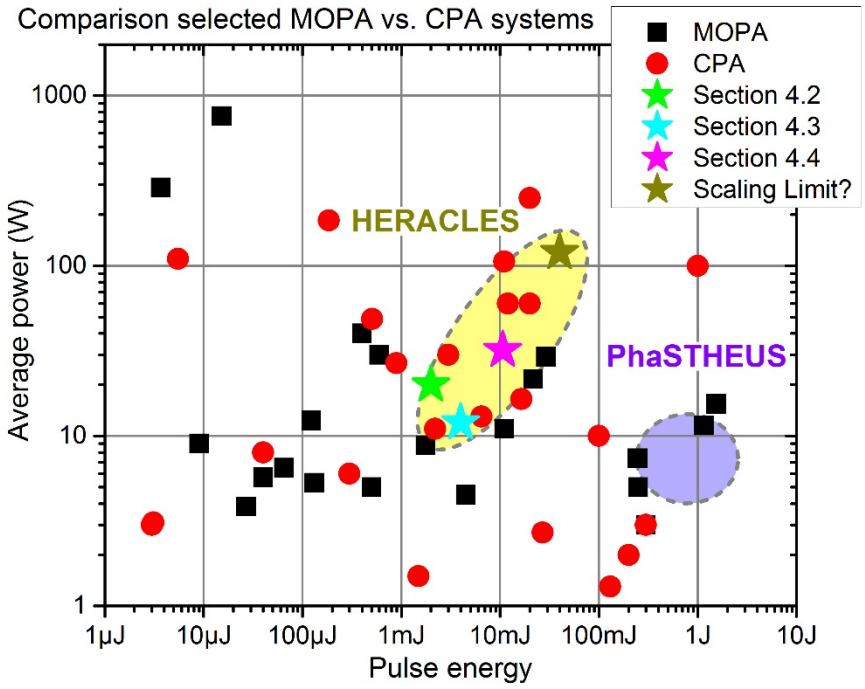

Figure 2-6: Performance comparison of MOPA and CPA systems listed in Table B-1 and Table B-2 in terms of average power and pulse energy.

The performances of the same systems are plotted in Figure 2-7 relative to obtained peak power and repetition rate. The peak power is generally larger in CPA schemes compared to MOPA

systems. In the case of Yb-doped solid-state amplifiers, the amplification bandwidth is ~3 nm corresponding to a transform-limited pulse duration of 0.5 to 1 ps. As a consequence, the pulse duration can reach sub-ps and therefore, the peak powers are generally higher in CPA systems.

For OPCPA, the optimal pump pulse duration is in the range of 1 to 10 ps. However, MOPA-like pump beam generation with >10 ps duration are well suited comprise for an OPCPA system such as HERACLES. The performances presented in this dissertation are comparable to other state-of-the-art MOPA systems. It should be noted that only a few of the systems listed in Table B-2 have been experimentally proven for OPCPA pumping.

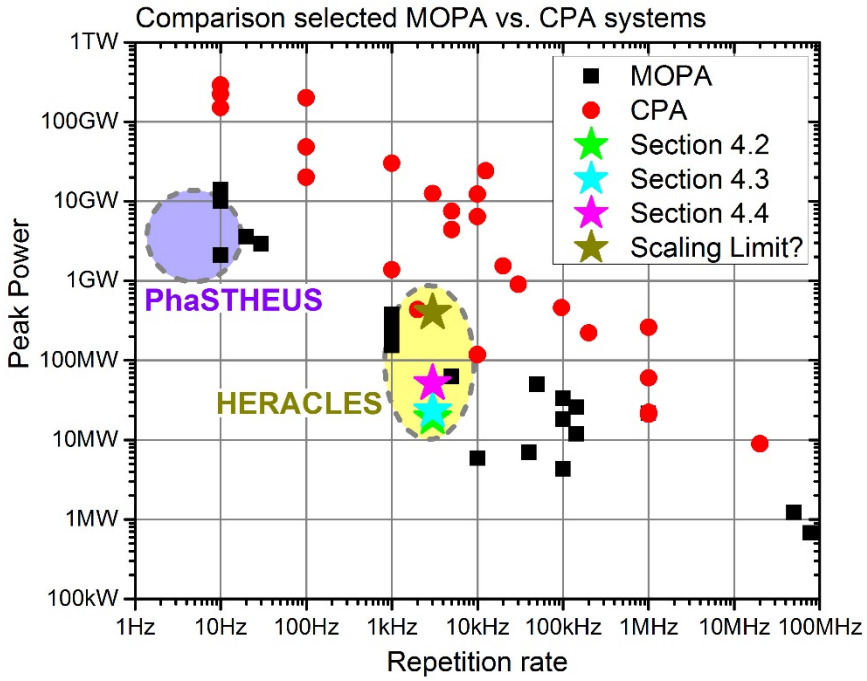

Figure 2-7: Performance comparison of MOPA and CPA systems listed in Table B-1 and Table B-2 in terms of repetition rate and peak power.

To gain insight into the current state-of-the-art performance of each laser technology, the MOPA and CPA systems were further separated in their key amplifier technology into the following categories: diode-pumped solid-state (DPSS), DPSS slabs, flashlamp-pumped solid-state, Ti:sapphire-based, thin-disk, fiber and cryogenically-cooled solid-state (cryo-cooled SS) amplifiers. Their performances are presented in Figure 2-8 for MOPA systems and Figure 2-9 for

CPA systems. The selected MOPA systems produce average powers between 5 to 50 W average powers typically with 0.1 to 10 mJ pulse energies. The flashlamp-pumped configurations provide an ultra-high pulse energy of >300 mJ at moderate average power. Ti:sapphire-based amplifiers are rather uncommon but a few of the first presented OPCPA systems were based on this technology. The additional cost of lasers to pump the Ti:sapphire gain medium makes this approach more costly and complex compared to other available technologies. Diode-pumped solid-state amplifiers based on Nd-doped rods are usually operated with repetition rates from 1 to 100 kHz with ~10 W average power and mJ-level pulse energies, similar to the amplifier chain later presented in Chapter 4.

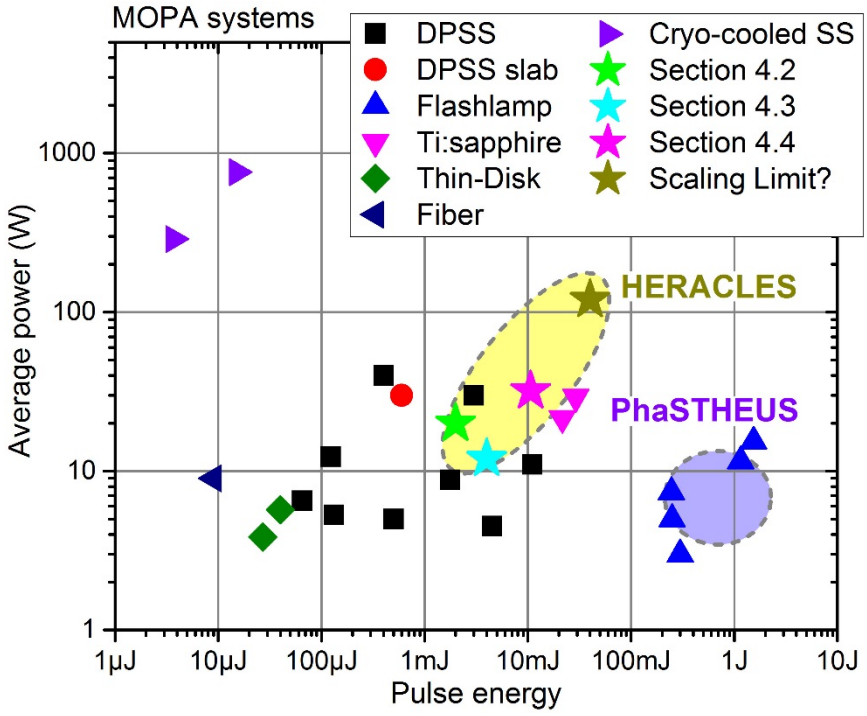

Figure 2-8: Performance comparison of MOPA systems listed in Table B-1 and Table B-2 in terms of average power, pulse energy and laser technology.

Figure 2-9 provides a comparison to the performance of CPA systems. The higher overall efficiency of the Yb-based CPA systems results in slightly higher obtainable output energies operating up to the 100 W-level compared to the MOPA systems. Fiber-based CPA systems offer

high average powers at moderate pulse energies as well as a robust design and stable beam quality. Additionally, cryogenically-cooled amplifier systems have been demonstrated with pulse energies of several tens of mJ and average powers beyond 100 W. Such systems are complex but this approach offers several advantages for further scaling [87] [88]. Recently, several systems have been demonstrated using pulsed diode pumping to maximize pump peak power, but reduce thermal stress, producing high average power (100 W) and high pulse energy (1 J) [89].

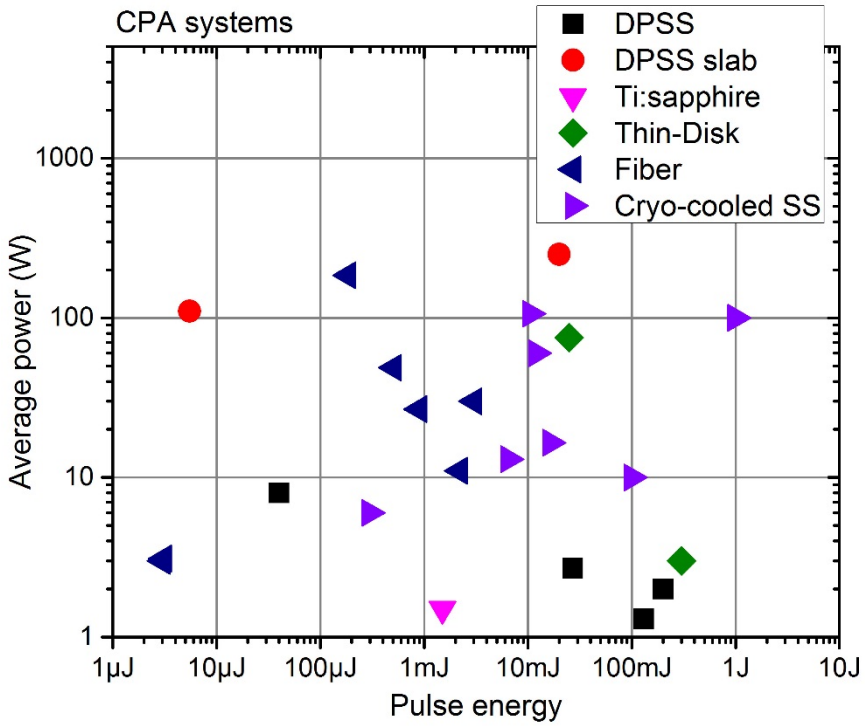

Figure 2-9: Performance comparison of CPA systems listed in Table B-1 and Table B-2 in terms of average power, pulse energy and laser technology .

The performances of the systems presented in Table B-2 typically exceed that of the pump lasers listed in Table B-1. As such, these advanced systems point the way to further improvements in OPCPA performance. A novel pump laser design has been presented recently based on burst mode operation of a CPA system leading to high repetition rate pulses within a low repetition rate pulse train [90].

2.6 Summary

In this chapter, the concepts of CPA and OPCPA have been presented along with a comparison of system performance based upon several historical milestones. The performance level and recent developments in OPCPA laser technology has been summarized, demonstrating that OPCPA is currently limited by the available driving pump laser systems. Thus, the current performance levels of such pump laser systems are presented and trends are identified. From this, it is possible to directly compare the performance of the systems developed as part of this dissertation relative to the state-of-the-art.

3 ESSENTIAL ASPECTS

The development of few-cycle OPCPAs as well as high-energy, high-average power, picosecond lasers assumes a broad background in physics, optics, and laser technology. While a complete treatment of all concepts related to these topics is beyond the scope of this dissertation, this chapter describes conceptually, theoretically and numerically some of the most crucial aspects. Associated aspects with the “traditional” amplification in solid-state amplifier are given in the first section. This is followed by a brief description of few-cycle pulses in Section 3.2. Dispersion and dispersion management is described in Section 3.3. CEP and its stabilization is introduced in Section 3.4. Finally, optical parametric amplification is covered in detail in Section 3.5.

3.1 Laser Amplifier Design Considerations

Three relevant aspects have to be taken into account when designing and operating a high energy, high average power amplifier stage. First, stimulated emission can be utilized to amplify laser pulses which can be described by equations given in the first subsection. Diode-pumped solid state lasers are based on high thermal load to amplify and extract as much energy as possible, which leads to thermally induced aberrations. Thus, the second aspect presented here is thermal lensing (Section 3.1.2), while the third aspect is thermally induced depolarization (3.1.3).

3.1.1 Amplification via Stimulated Emission

The most common method for laser amplification is via stimulated emission. The gain medium consists of a crystal or glass host doped with active ions such that a population inversion between the excited atomic level and its ground level can be realized. A photon propagating through such an inverted medium will cause an excited ion to emit another photon with the same energy and momentum as the initial photon, a process known as stimulated emission. On a

macroscopic scale this is perceived as gain or amplification of the optical input signal. This following section will provide an example of traditional amplification based on population inversion in diode-pumped, solid-state rods.

Figure 3-1 shows a commercially available laser amplifier module consisting of a 1 cm diameter, 12.5 cm long Nd:YAG crystal rod (Northrop Grumman Cutting Edge Optronics). The rod is side-pumped with up to 1.2 kW of average power from diode bars operating at a wavelength of 808 nm. The diode bars are arranged symmetrically around the amplifier rod resulting in a relatively uniform pump beam absorption.

Figure 3-1: Picture of a Nd:YAG amplifier module (Northrop Grumman Cutting Edge Optronics) with 1 cm rod diameter.

The performance of an amplifier module is modeled based upon [91] starting with the small signal gain, which is the maximum possible gain for a given absorbed pump distribution. Practically, the net gain obtained from an amplifier is often much less than the small signal gain due to the onset of gain saturation as well as intrinsic optical losses. The small signal gain G [91] is given by the equation

$$G = \exp(g_0 l)\,, \tag{4}$$

where g_0 is the gain factor per unit length and l the length of the amplifier medium. The following expression [92] decomposes the exponent $g_0 l$ in several parameters

$$g_0 l = \sigma_E \tau_{fl} \frac{\lambda_p}{\lambda_l} \frac{P_{abs}}{V} \frac{l}{h\nu} = \sigma_E \tau_{fl} \frac{\lambda_p}{\lambda_l} \frac{P_{abs}}{A\, h\nu}, \quad (5)$$

where σ_E is the emission cross-section, τ_{fl} is the fluorescence lifetime, λ_p and λ_l are the pump and lasing wavelength, P_{abs} is the absorbed pump power, V, l and A are the geometrical parameters of the pumped volume and $h\nu$ the lasing photon energy. The ratio

$$\eta_{qu} = \lambda_p / \lambda_l \quad (6)$$

is called the quantum efficiency and the value

$$QD = 1 - \eta_{qu} \quad (7)$$

is called quantum defect (QD). Equation (5) shows the dependence of the gain on the absorped pump power and the cross-sectional area of the gain volume, where:

$$g_0 l \propto P \quad (8)$$

$$g_0 l \propto 1/r^2 \quad (9)$$

It is common to increase the beam and amplifier module size to extract higher pulse energies and average powers. Equation (8) and Equation (9) show that the value $g_0 l$ scales inversly with cross-sectional area.

The saturation fluence defines the fluence value at which the gain has reduced to 1/e of its initial value due to saturation. If high gain is desired from an amplifier it needs to be operated far below the saturation fluence. If high extraction efficiency is desired the amplifier should be operated above the saturation fluence. The saturation fluence F_{sat} is given by the equation

$$F_{sat} = E_{sat} = \frac{h\nu}{\sigma_E + \sigma_A}, \quad (10)$$

where σ_A is the absorption cross-section at the lasing wavelengths. Table 3-1 shows relevant paramters for selected gain materials. The amplifiers used in this for the majority of this dissertation are based on Nd:YAG and Nd:YVO_4.

Table 3-1: Optical properties of selected gain materials [91]. Amplifiers based on Nd-doped YAG and Vanadate are used throughout this dissertation.

	Laser wavelength	**Typical gain bandwidth**	**Fluorescence lifetime τ_{fl}**	**Emission cross-section σ_E**	**Saturation Fluence**
Nd:YAG	1064.1 nm	0.6 nm	230 µs	$28 \times 10^{-20} cm^2$	$0.66\, J/cm^2$
Nd:YVO4	1064.3 nm	1 nm	90 µs	$114 \times 10^{-20} cm^2$	$0.16\, J/cm^2$
Nd:YLF	1053 nm		480 µs	$12 \times 10^{-20} cm^2$	$1.57\, J/cm^2$
Yb:YAG	1030 nm	3 nm	951 µs	$21 \times 10^{-20} cm^2$	$0.92\, J/cm^2$
Ti:sapphire	790 nm	>75 nm	3.2 µs	$28 \times 10^{-20} cm^2$	$0.90\, J/cm^2$

The stored energy per unit length J_{st} can be calculated assuming cw pumping [91] with the following expression [92]

$$J_{st} = g_0 E_{sat} = \tau_{fl} \frac{\lambda_p}{\lambda_l} \frac{P_{abs}}{l}. \tag{11}$$

Assuming that the population inversion is fully depleted after each pulse, the expression for the absorbed pump power can be re-written to

$$P_{abs} = \alpha_p \, P_{pump} \, \frac{1\, Hz}{f_{rep}}, \tag{12}$$

where α_p is the pump absorption, P_{pump} the total available pump power and f_{rep} the repetition rate of the amplifier. In the case of quasi-cw pumped and pulsed pumped, the expression for the absorbed pump power can be re-written to

$$P_{abs} = \alpha_p \frac{E_p}{\tau_p} = \alpha_p P_{peak}. \tag{13}$$

It can be seen, that increasing the pump peak power significantly increases the stored energy and the obtainable gain. Given that the maximum average power is ultimately limited by thermal considerations, it becomes increasingly difficult to achieve sufficient gain and to extract the stored energy as the aperture diameter increases. By comparison, pulsed-pumped amplifier modules

(flashlamp- or diode-based) typically offer more than 10 times higher gain than cw pumped amplifiers and can be employed in such large aperture amplifiers.

Table 3-2: Example calculation for properties of the booster amplifier modules.

Parameter	Value
Small signal gain	1.38
Including 10% loss	1.24
Saturation Energy	520 mJ
Stored Energy	168 mJ

Using the above equations, example calculations were performed for the Nd:YAG amplifier module from Figure 3-1. The results are listed in Table 3-2 and the associated parameters are: 1 cm rod diameter, 10 cm rod length, 1.2 kW cw pump power with 80% pump absorption and 1 kHz repetition rate. From equation (4), (10) and (11), the small signal gain is found to be relatively low with a calculated increase in energy by 38% after one pass. Typically, amplifier must also overcome losses due to parasitic effects such as depolarization, abberated thermal lensing, hard-aperture clipping, undesired reflections, absorption, dust, etc. Assuming a loss of 10%, the net gain of this amplifier stage reduces to 24%. Thus, the presented 1 cm diameter, Nd:YAG amplifier module would not be optiaml for high gain amplification. For comparison, typical single- and multi-pass amplifier are designed with overall gain factors per path of $G > 2$ and correspondingly higher small signal gain. Thus, 2, 3 and 4 mm diameter amplifiers are utilized throughout this dissertation and the implementations of such systems are desribed in Chpater 4.

3.1.2 Thermal Lensing in Laser Amplifier Rods

Thermal lensing occurs in laser materials based upon a non-uniform temperature profile across the rod [93]. A uniform pump absorption is desired as it provides uniform gain through the amplifier module and thereby minimizes beam distortions. In general, the minimum amount of

heat generated in a laser medium corresponds to the quantum defect ($1 - 808\,nm/1064\,nm = 24\%$). Cooling of the material is realized through one or more of the side facets resulting in a non-uniform temperature distribution throughout the material. For common gain materials, like Nd:YAG, Nd:YVO_4 [94], Ti:sapphire [95] and Yb:YAG [96], the increase in heat associated with pump light absorption induces a refractive index change where the parameter dn/dT is positive resulting in a thermal lens with positive focal length (see also Appendix C). For cylindrical amplifier rods that are cooled along the circumference, the thermal lens resembles a very thick graded index lens. The strength of this lens can be approximated by [91]

$$F_{thermal} = M_{r,\phi}/P_{heat}\,, \tag{14}$$

where $M_{r,\phi}$ is a coefficient containing all material and geometrical parameter and P_{heat} is the heat load. Thus, for inefficient optical power extraction, the thermal lens is approximately inversely proportional to the absorbed pump power P_{pump}. Finite element analysis (FEA) is an excellent method to model thermal lensing, as shown in the following paragraphs.

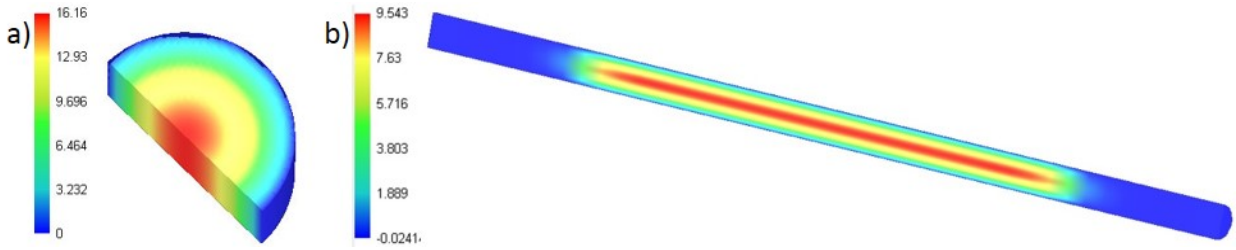

Figure 3-2: Thermal heat distribution of a side-pumped Nd:YAG with 3 mm diameter and 1 mm length pumped by 6 W (a) and 8.3 cm length pumped at the center 5 cm with 200 W (b).

Heat profiles were calculated for a 3 and 4 mm diameter side-pumped rod with FEA simulations using the software package LASCAD (LAS-CAD GmbH). Figure 3-2 (a) shows the thermal heat distribution in a 3 mm diameter, 1 mm long crystal pumped by 6 W at 808 nm with a maximum relative temperature increase of 16 K. Typically, the rod in a side-pumped laser amplifier module is only pumped in the center region along the optical axis while the end sections

of the rod are held for mounting. A second FEA simulation was carried out with a 3 mm diameter, 8.3 cm long rod pumped along the central 5 cm with 200 W. The heat distribution is shown in Figure 3-2 (b) and the maximum relative temperature increase was 9.5 K.

Based on these FEA simulations, the software package LASCAD enables the calculation of the average refractive index change across the rod diameter and results are shown in Figure 3-3. The refractive index change for a cylindrical 3 mm x 5 cm, Nd:YAG rod, side-pumped by 200 W is shown in Figure 3-3 (a) and a 4 mm x 10 cm, side-pumped by 400 W in Figure 3-3 (b). As a first approximation, a parabolic refractive index profile can be identified. A parabolic fit found via LASCAD corresponds to an idealized lens with 17 to 22 cm for the 3 mm diameter rod and 10 to 15 cm for the 4 mm diameter rod. Thus, a thermal lens of ~20 cm for the 3 mm diameter rod will be used later in this section as first approximation.

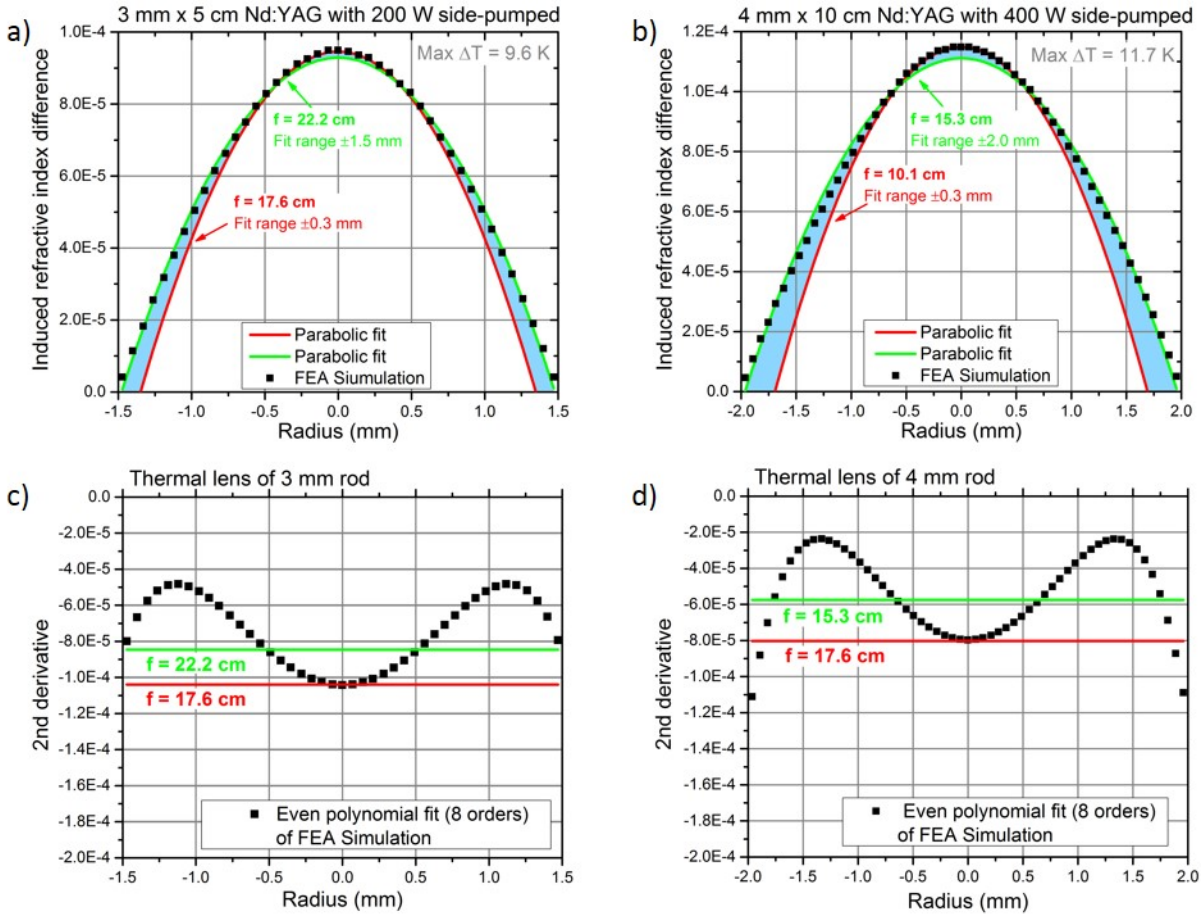

Figure 3-3: Refractive index change across the rod diameter with 3 mm (a) and 4 mm diameter (b) found with LASCAD (LAS-CAD GmbH) and FEA simulations. The second derivatives of the curves for the 3 mm (c) and the 4 mm diameter case (d) are shown.

The value of the focal length depends on the utilized fitting range: if only the center region ($r = \pm 0.3\,mm$) is used for fitting, the corresponding lens (red parabolic fit) is comparably stronger. When the full range is fitted (green parabolic fit) the lens is weaker. The difference between the fitted ideal lenses (red and green curves) is highlighted in blue in Figure 3-3 (a) and (b). It can be seen that the error between the fit curves is larger if the rod diameter increases from 3 mm diameter (a) to 4 mm (b).

Figure 3-3 (c) and (d) show the second derivatives of the induced refractive changes, where the points of the second derivatives of the FEA simulations are calculated based on even 8th order polynomial fits through the original data values. Based on this second derivative, an ideal lens is

represented as constant. Thus, the fitting curve for the values around the center ($r = \pm 0.3\ mm$) is shown in red and the fitting curve through the full range shown in green. It can be seen that the second derivative of the FEA simulations increases parabolic from the center while it decreases towards the outside due to higher order contribution. For a large distance away from the center approaching the radius of the rod, the FEA simulations become unreliable since it assumes fixed 0 degree relative temperature at the boundary (at $r = 1.5\ cm$ or $2\ cm$, respectively) with infinite heat removal capacity. The central quadratic increase, i.e. the deviation from an ideal lens, is used later in this section to describe the limitations of compensating thermal lensing.

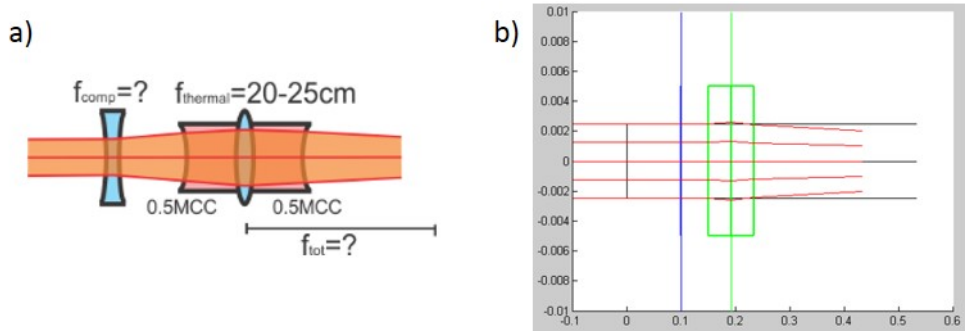

Figure 3-4: (a) Optical layout of the thermal lens compensation scheme. (b) Screenshot of the output from the implemented ray tracing code.

An ideal lens can be compensated with a negative lens of proper focal length. A paraxial ray tracing model was implemented in MATLAB (The MathWorks, Inc.) to estimate the parameters for an idealized thermal lens compensation scheme with the interfaces illustrated in Figure 3-4 (a). The first element is a negative lens with variable focal length, followed by a curved rod end, propagation in the rod with refractive index of the material, a thin lens in the center of the rod represents the thermal lens and the last interface is the curved end facet of the rod. Figure 3-4 (b) shows a screenshot retrieved from the implemented MATLAB (The MathWorks, Inc.) ray tracing code. In the first step, the effective lensing of the rod with curved ends, the thermal lens and no negative lens is estimated. Figure 3-5 plots the calculated total focal distance away from

the center of the rod in dependence of the thermal lens. Proper compensation of the ideal thermal lens is given for f = 31.6 cm (0.5MCC; shown in black) and 46.8 cm (0.75MCC; shown in red), respectively. Following the results of the FEA simulations, the thermal focal length of a 3 mm rod under ~200 W pumping is in the range of 17 to 22 cm. Thus, a negative curvature of 0.5MCC is not sufficient to completely cancel this thermal lens and an additional negative lensing effect is necessary to compensate.

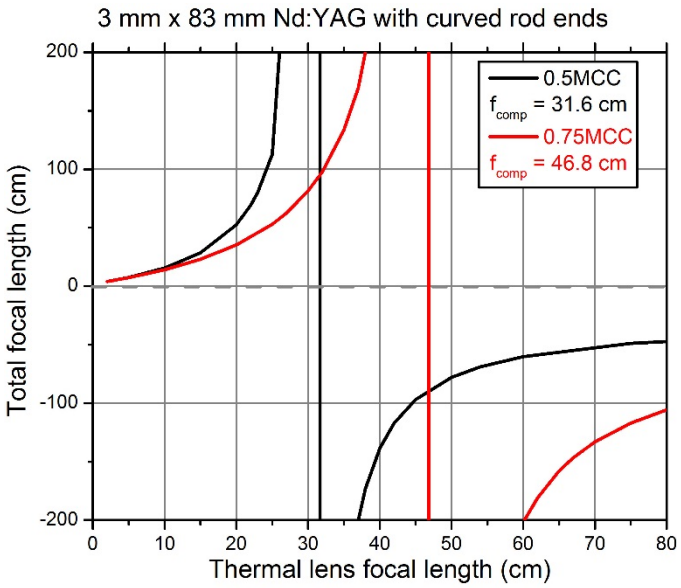

Figure 3-5: Calculated total lensing effect of the rod with curved end facets and varying thermal lens.

The ray tracing code was extended with a negative lens placed 5 cm in front of the amplifier rod. Figure 3-6 shows the total lensing effect of this system depending on the thermal lens. It can be seen that the combination of a negative lens of f = -40 cm with curved rod facets (0.5MCC) is able to compensate a thermal lens of f = 19.4 cm. This combination is employed later experimentally in Section 4.4.3.

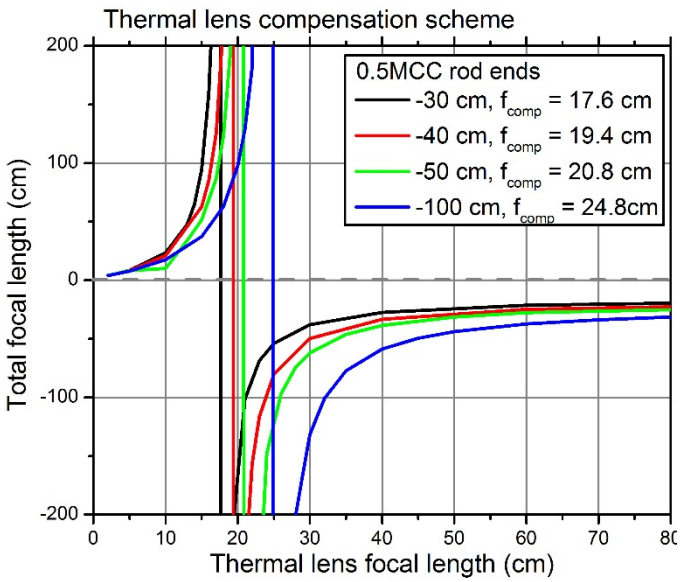

Figure 3-6: Calculated total lensing of the rod with curved end facets (0.5MCC), varying thermal lens and a negative lens of selected focal length placed 5 cm in front of the rod.

Unfortunately, the simulated refractive index change across the rod, shown in Figure 3-3, suggests that the approximation with an ideal lens only holds for the central region along the optical axis. The impact of the deviation of the thermal lens from an ideal lens is estimated conceptually in the following. The ABCD matrix formalism was extended by Siegman [30] to a medium with radially parabolic refractive index profile and is shown in the following. The transfer matrix of an optical system in the ABCD formalism is given by the general expression

$$\mathrm{M} \cdot \mathrm{x} = \begin{pmatrix} A & B \\ C & D \end{pmatrix} \cdot \begin{pmatrix} h \\ u \end{pmatrix}, \tag{15}$$

where M is a transfer matrix, x the ray tracing vector, ABCD the matrix elements of a transfer matrix, h the radial height of the ray and u the angle to the optical axis of the ray. For a distance Δl in a medium of refractive index n_0 the propagation is given by the transfer matrix

$$\mathrm{D} = \begin{pmatrix} 1 & \Delta l/n_0 \\ 0 & 1 \end{pmatrix}. \tag{16}$$

For a medium with radial refractive index distribution following

$$n(r) = n_0 - n_2 r^2/2\,, \tag{17}$$

where n_2 is the second order refractive index coefficient, the transfer matrix is given by [30]

$$\mathrm{R} = \begin{pmatrix} 1 & 0 \\ -n_2 \Delta l & 1 \end{pmatrix}. \tag{18}$$

To model the thermal lens in the ray tracing implementation, the matrices D_i following Equation (16) and R_i following Equation (18) allow to divide the crystal numerically into slices of length Δz with transfer matrix R_i and D_i. This ABCD matrix is implemented in the previously mentioned ray tracing code to provide conceptually insight into the thermal lensing compensation configuration found in Figure 3-6. Figure 3-7 (a) shows the output with a combination of a negative lens in front of the amplifier, curved rod facets and constant n_2. This configuration shows the ideal lens behavior and is fully compensated, i.e. the output beam is collimated.

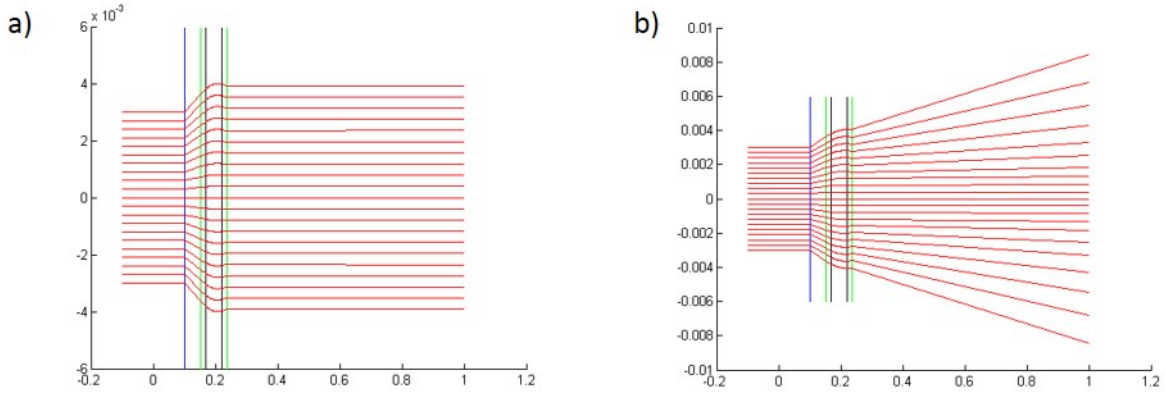

Figure 3-7: (a) Screenshots of the ABCD ray tracing code with axis in meter with thermal lens corresponding to an ideal lens with collimated output. (b) A higher order refractive index variation results in a partially diverging output beam.

However, the implemented ray tracing approach makes several important simplifications. In particular, spherical aberration and higher order refractive index changes are not considered. The latter is conceptually shown in Figure 3-7 (b), when the fourth order refractive index change n_4 is numerically included in the approximation of Equation (18). This fourth order refractive index dependence is found in the central region of the simulated refractive index profile across the

rod diameter as shown in Figure 3-3 (c) and (d). As can be seen in Figure 3-7 (b), the outer most rays diverging even when the center region is well collimated [97]. This behavior was seen experimentally as described in Section 4.4.3 and can limit the experimentally obtainable beam quality.

3.1.3 Thermally Induced Depolarization

The non-uniform temperature distribution in the pumped laser medium, such as Nd:YAG, results in non-uniform stress. The induced stress in solid-state rod amplifiers can lead to birefringence with radial and azimuthal components [93]. Thus, if a linearly polarized probe beam passes through such a medium, the different polarization components will experience different phase retardation [93] [98]. As an example, the depolarization effect and its compensation is exemplarily presented here for twin amplifier modules based on 3 mm diameter, 8.3 cm long, Nd:YAG rods.

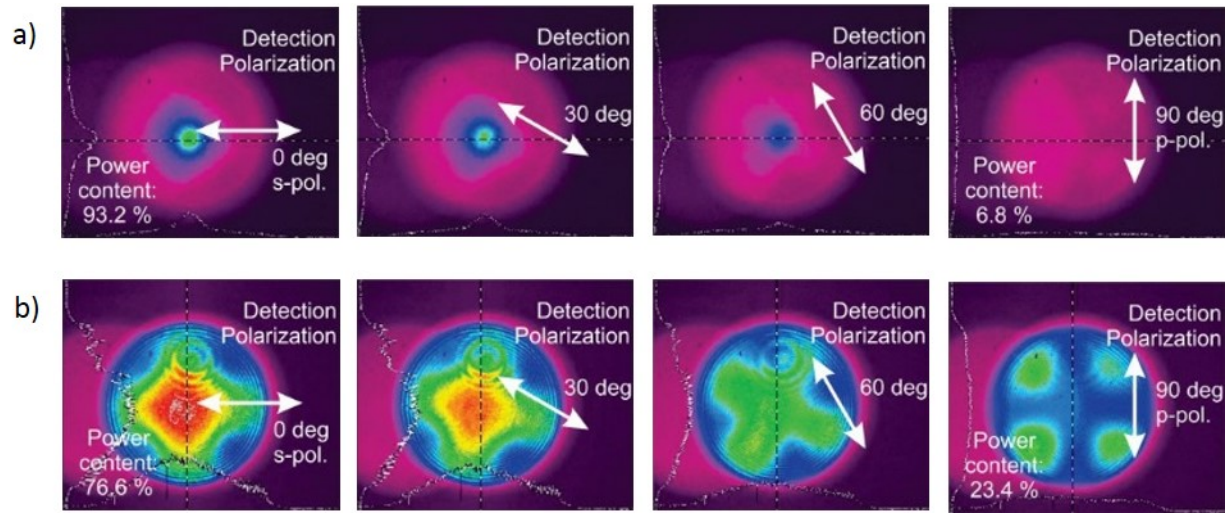

Figure 3-8: The beam profiles show the depolarization of a probe beam passing through a 3 mm diameter, Nd:YAG amplifier with small (a) and large fill factor (b). The detection polarization and power contents are indicated.

The depolarization behavior of a single 3 mm diameter, Nd:YAG module is investigated with a 1064 nm, s-polarized, cw probe beam. Figure 3-8 shows beam profiles relay imaged onto

the beam profiler (Spiricon, Ophir Optronics Solutions Ltd.) with the amplifier module under full thermal load (i.e. full pump power of up to 300 W at 808 nm wavelength) [93]. The detection polarization is controlled using a half wave plate and a thin-film polarizer in front of the beam profiler to study spatial profile and power content of the thermally induced depolarization process. It can be seen from Figure 3-8 (a) that with a small fill factor (i.e. small beam diameter) the depolarization loss is low with only 6.8% power content in the p-polarization (last profile in (a)). For an increased fill factor (b), the depolarization loss increases to 23.4% (last profile in (b)). The beam profiles in both p-polarization cases illustrate that the depolarization effects are stronger for the outer part of the beam. Similarly, the s-polarized beam profiles show that the beam deviates strongly from a symmetric Gaussian beam profile.

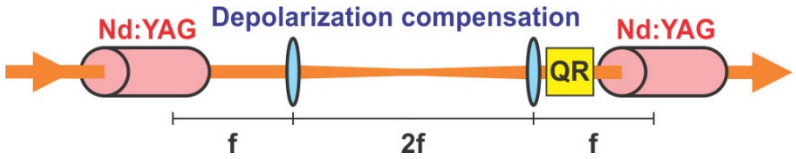

Figure 3-9: Depolarization compensation scheme based on twin amplifier modules and a 4f imaging scheme with 90 degree Quartz rotator.

The thermally induced depolarization effect can be canceled with 100% theoretical efficiency by using twin amplifiers. The compensation scheme consists of a 4f imaging scheme which 1:1-images a plane towards the end of a first module onto a plane at the front section of an identical amplifier module. Between the two modules, a Quartz crystal rotates the full beam polarization by 90 degree. Alternatively, one of the twin amplifier modules can be rotated by 90 degrees. Since the depolarization behavior can be assumed to be the same among twin amplifiers, the pass in the second amplifier will result in exactly the opposite depolarization effect leading to theoretically perfect compensation. Perfect compensation assumes perfect imaging, perfectly identical thermal load in the amplifier modules and that all rays follow the same path in the first and second amplifier. Experimentally, total depolarization loss tend to be <10% [99] due to small

difference in the twin amplifiers and their heat load (i.e. pump power minus extracted power). In addition, the compensation scheme assumes parallel rays through the amplifier modules. Experimentally, slightly different trajectories in the amplifier modules degrade the depolarization compensation efficiency (see Section 3.1.2) [99].

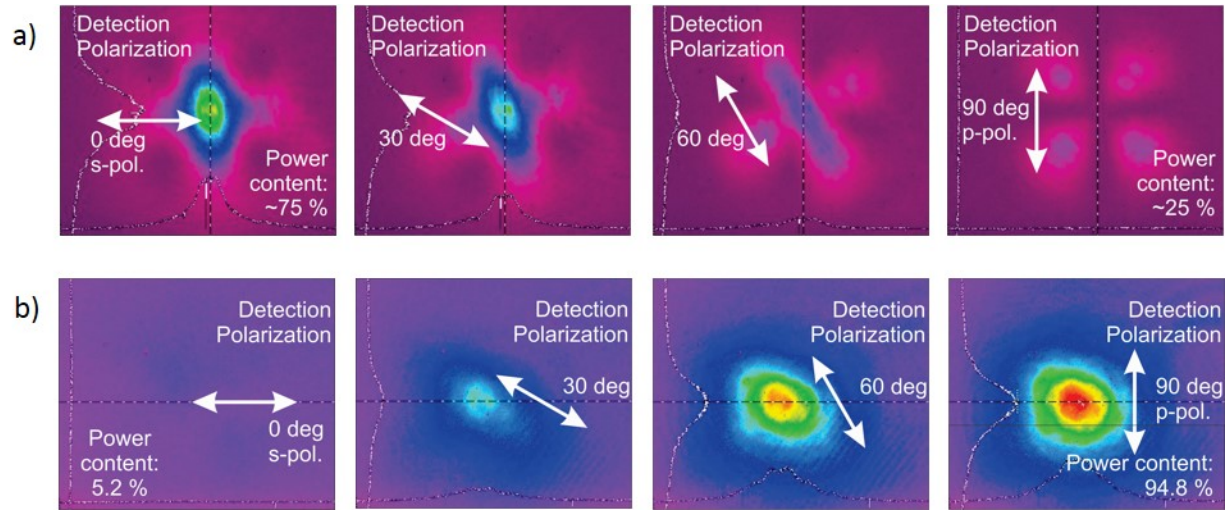

Figure 3-10: Depolarization study for the relay imaged, two module, booster stage with no Quartz rotator (a) and with Quartz rotator (b). The detection polarization and power contents are indicated.

The depolarization compensation, shown in Figure 3-9, was tested using two 3 mm diameter, Nd:YAG amplifier modules with thermal lens compensation (see Section 3.1.2) and a 1:1 relay imaging scheme. Figure 3-10 shows the depolarization and power contents of the cw probe beam (collimated output) after a single pass through two modules. When the 90 degree Quartz rotator (a) was not used, the depolarization compensation was not enabled and ~25% depolarization loss was observed as shown in the last profile in (a). The use of the Quartz rotator in (b) reduced the depolarization loss to 5.2% as shown in the first profile of (b). Consequently, the output polarization was rotated to p-polarization and the exiting beam profile showed good quality as shown in the last profile of (b).

The compensation of thermally induced depolarization is used in Section 4.4 for the implementation for a high energy, high average power, picosecond, booster amplifier stage based on twin, 3 mm diameter, Nd:YAG, amplifier modules. The presented concept is extended later in Section 4.4.4 for a single amplifier module [100] with 4 mm diameter.

3.2 Description of Optical Pulses

Ultrashort pulses are routinely generated by mode-locked laser oscillators with Gaussian or sech² pulse shapes. The description presented here follows the standard introduction given by [11], [30], [101] and [102]. The Gaussian electric field of an ultrashort pulse can be written as

$$E(t) = E_0 \exp\left(\frac{-(t-t_0)^2}{2\sigma^2}\right)\exp(i\omega_0 t)\,, \tag{19}$$

where E_o is the amplitude of the electric field, t_0 the center position of the pulse in time and ω_0 the center frequency. The width of the Gaussian envelope σ can be related to the FWHM pulse duration τ_p by the factor 2.35. The sech² pulse shape is expressed by

$$E(t) = E_0 \,\mathrm{sech}^2\left(\frac{t-t_0}{\tau_0}\right)\exp(i\omega_c t) = \frac{E_0\exp(i\omega_0 t)}{\cosh^2\left(\frac{t-t_0}{\tau_o}\right)}\,. \tag{20}$$

In the generation of an ultrashort pulse in mode-locked lasers, a large number of oscillating modes with frequency ν_m are created with high coherence and the same spectral phase ϕ_0. More than 100,000 equally-spaced modes are supported by the cavity, representing a frequency comb with mode spacing

$$\delta\nu = \nu_{m+1} - \nu_m = \frac{c}{2nL}, \tag{21}$$

where nL is the optical path length in the resonator. The corresponding electric field consists of the superposition of M adjacent longitudinal modes each with individual frequency ω_m and phase ϕ_m:

$$\tilde{E}^+(t) = \frac{1}{2}\tilde{\epsilon}(t)\exp(i\omega_0 t) \tag{22}$$

$$= \frac{1}{2}\epsilon_0 \exp(i\omega_0 t) \sum_{m=\frac{1-M}{2}}^{\frac{M-1}{2}} \exp\big(i(2m\pi\Delta t + \phi_m)\big).$$

For a free-running laser the value of the spectral phase ϕ_m is random, but in the case of mode-locking it becomes equal to a constant spectral phase ϕ_0 for all longitudinal modes. Further, the sum of Equation (22) can be analytically expressed by

$$\tilde{E}^+(t) = \frac{1}{2}\epsilon_0 \exp(i\omega_c t)\frac{\sin(M\pi\Delta t)}{\sin(\pi\Delta t)}. \tag{23}$$

The electric field shown in Equation (23) becomes similar to a pulse train with spacing between the pulses of $T_R = 1/\delta\nu$ in the limit of large M. Therefore, the mode superposition leads to an electric field where the entire radiated field is localized in an ultrashort instant. The duration of a single pulse is given by $\tau_p \approx 1/M\delta\nu$ and thus inversely proportional to the gain bandwidth given by $M\delta\nu = \Delta\nu$. The ratio

$$\frac{T_R}{\tau_p} = \frac{\Delta\nu}{\delta\nu} = \#modes \tag{24}$$

represents the number of longitudinal modes that are oscillating in phase and shaping the short pulse. This number can be very large, for example a 100 fs pulse with a period of 10 ns between the pulses requires 100,000 longitudinal modes.

3.3 Dispersive Devices

OPCPA and CPA require pulse stretching with stretched-to-compressed-duration ratio as high as 10,000:1. Dispersion has a larger impact on few-cycle pulses than on narrow-bandwidth picosecond pulses due to the large bandwidth. Therefore the dispersive contribution of each element needs to be carefully considered. A numerical code was implemented in the Laser Plasma Laboratory and has been steadily improved [103]. Several dispersive components can be included in the analysis, such as grism stretcher, Dazzler or AOPDF and bulk material such as FS, BBO and SF57. The code is also used for dispersion managements of traditional CPA systems with Martinez-like [57] or Öffner-like stretcher [104] and Treacy-like compressor [60]. The following section gives an overview of each device and its typical dispersion.

3.3.1 General Description of Dispersion

In particular for few-cycle pulses the dispersion – even air – needs to be considered. Any incoming pulse $E_{in}(t)$ passing through a dispersive media will experience a spectral phase $\phi(\omega)$ following the formalism in [101]. The outgoing pulse in the time domain is described by the Fourier transform of the pulse multiplied with the transfer function of the spectral phase

$$E_{out}(t) = \frac{1}{2\pi}\int E_{in}(\omega)\exp(-i\omega t)\exp\big(i\phi(\omega)\big)\,d\omega\,. \tag{25}$$

For example, the dispersion $\phi(\omega)$ accumulated while propagating through a medium with refractive index $n(\omega)$ and length L is given by

$$\phi(\omega) = k(\omega)L = \frac{\omega}{c}n(\omega)L\,. \tag{26}$$

The first derivative of this expression leads to an expression for the group delay (GD) ϕ' (or D_1), which is the delay that the pulse envelope experiences compared to a pulse that would not have propagated through the medium. This is also referred to as group velocity dispersion GVD:

$$GVD = \frac{\partial \phi(\omega)}{\partial \omega} = \phi'_m = \frac{\partial (kL)}{\partial \omega} = L\left(\frac{\partial k}{\partial \omega}\right)^{-1} = \frac{L}{v_g} = T_g = GD\,. \tag{27}$$

This physical quantity is of major relevance in the ultrafast regime. The second derivative is called the group delay dispersion (ϕ'', D_2 or second-order dispersion GDD):

$$GDD = \frac{\partial T_g}{\partial \omega} = \phi''_m = \frac{\partial^2 \phi(\omega)}{\partial \omega^2}. \tag{28}$$

It is often convenient to represent the spectral phase $\phi(\omega)$ as a Taylor expansion around the center frequency ω_0:

$$\phi(\omega) = \phi(\omega_0) + \left.\frac{\partial \phi(\omega)}{\partial \omega}\right|_{\omega_0} (\omega - \omega_0) + \frac{1}{2}\left.\frac{\partial^2 \phi(\omega)}{\partial \omega^2}\right|_{\omega_0} (\omega - \omega_0)^2 + \frac{1}{6}\left.\frac{\partial^3 \phi(\omega)}{\partial \omega^3}\right|_{\omega_0} (\omega - \omega_0)^3 + \cdots . \tag{29}$$

The higher order terms are called third-order dispersion (ϕ''', D_3 or TOD), fourth-order dispersion (ϕ'''', D_4 or FOD), and so on. In order to observe the shortest possible duration, i.e. a transform limited pulse, all these terms need to be equal to zero. In particular, higher-order terms are not negligible for pulses approaching the few-cycle regime with nearly octave-spanning spectrum. Precise dispersion management is required to achieve the shortest on-target pulse duration for any few-cycle pulses experiment.

Typically, the pulse duration of an ultrafast laser is of special interest. It can be shown [101] that an initially Gaussian pulse shape with temporal pulse duration of $\Delta\tau$ will broaden due to dispersion according to

$$\Delta\tau_{\text{out}} = \sqrt{\Delta\tau^2 + \left(4\ln 2\frac{\phi''}{\Delta\tau}\right)^2 + \cdots}. \tag{30}$$

This expression shows that the final pulse shape is not dependent on the first derivative of the spectral phase. Similarly, it can be shown that the instantaneous frequency – the frequency of the carrier – is not influenced by the first derivative of the spectral phase (i.e. the group delay). On the other hand, second-order dispersion, the second term in the Taylor expansion in Equation (29), alters the pulse shape and causes temporal broadening.

3.3.2 Ultrafast Dispersion Management

Several optical devices exist in the laboratory which can introduce dispersion to an optical pulse. The dispersive elements relevant to the HERACLES facility are described conceptually in the following.

- Bulk Material:

The most common case of dispersion is introduced during the propagation of a broadband pulse through transparent media such as glass or air. The effect of dispersion on an optical pulse can be treated in a few equations that apply for a variety of materials in a wide spectral range. The basis of this analysis relies on expression for the frequency (wavelength) dependent refractive index of a given material described by the Sellmeier equation [101]:

$$\text{n}(\lambda) = \sqrt{1 + \frac{G_1\lambda^2}{\lambda^2 - \lambda_1^2} + \frac{G_2\lambda^2}{\lambda^2 - \lambda_2^2} + \frac{G_3\lambda^2}{\lambda^2 - \lambda_3^2}}. \tag{31}$$

Values of the coefficients G_i and λ_i are available in the literature for common materials and have been extensively studied in the near infrared. The corresponding dispersion values can then be numerically calculated based on the Equation (26) and the Sellmeier Equation (31). Some

calculated dispersion coefficients are listed in Table 3-3. Typically, the second- and third order dispersion, far away of any electronic resonances in the medium, have positive values termed normal dispersion and the ratio between them is around 0.7. Thus, a pulse propagating through a normal dispersive material will experience positive linear chirp (quadratic phase). The lower frequency part of the spectrum will exit the medium faster than higher frequencies. Therefore, another mechanism is required to balance pulse distortions induced by dispersion and to recompress the pulses to its minimum (transform-limited) duration.

Table 3-3: Calculated dispersion coefficients for some materials at 800 nm and a length of 1 cm based on Equation (26) and the individual Sellmeier Equation (31),

	GDD/fs^2	**TOD/fs^3**	**4OD/fs^4**	**TOD/GDD**
Air	0.217	0.0092	-0.000001	0.04
BaF_2	380	196	-3.13	0.516
SF8	1370	880	162	0.642
SF10	1590	1040	230	0.654
SF57	2210	1550	336	0.701
Fused silica	361	275	-114	0.762

- Grating Stretcher and Compressor:

In 1969 Treacy [60] generated negative GDD for the first time using of a pair of gratings. As a consequence, it was possible to compensate for material dispersion and to compress a pulse. Later in 1984 Fork and Martinez [61], [57] demonstrated the first method to introduce negative GDD with low-loss by utilizing a pair of prisms at the Brewster angle. The CPA technique introduced in 1985 [32] is commonly based on a pulse Martinez-like pulse stretcher and compression in a Treacy-like geometry. In 1987, the combination of grating and prism pairs was used to externally compress a pulse down to 6 fs [105].

For grating and prism pairs, the introduction of negative GDD results from the angular dispersion of light, i.e. different spectral portions of the light travel along different optical paths. A grating pair is commonly utilized to stretch or compress pulses from durations in the

femtosecond regime to tens or even hundreds of picoseconds. The dispersion of a Treacy stretcher is given by [101]

$$\phi'' = \frac{\partial^2 \phi}{\partial \omega^2} = \frac{8\,\pi^2\,c}{\omega^3\,d^2}\frac{2\,\Delta x}{\cos^3(\theta)}, \tag{32}$$

where d is inverse groove density g, Δx the normal distance between the gratings and θ the diffraction angle. In the case of Martinez-like stretcher geometry, the introduced dispersion equals exactly the negative of Equation (32), where Δx is the difference between the focal length and distance between grating and imaging lens. Δx can be chosen to be positive or negative and thus, positive or negative dispersion can be introduced with a Martinez-like stretcher.

- Acousto-optic Programmable Dispersive Filter:

Pulses with duration of less than 100 fs are strongly affected by dispersion due to their large bandwidth. For example, if the path in air to the experiment was increased by 1 m, a 6 fs pulse with a bandwidth of 150 nm at 800 nm (i.e. the oscillator) would broaden in time from its transform-limit to 11 fs due to the dispersion. Highly nonlinear experiments would strongly suffer if the dispersion is not compensated properly. The majority portion of the dispersion can be accounted for in the ultrafast amplifier system and a compressed output can be implemented by proper aligned. However, an adaptive method is necessary in case of small mechanical drifts and variations as well as additional dispersion that cannot be considered prior or when aligning the ultrafast amplifier system.

Adaptive pulse shaping with a LCD spatial light modulator (SLM) can be utilized [69]. It is based on amplitude and phase modulation by placing the SLM into the Fourier plane in a dispersion-compensated 4-f Martinez-like stretcher. This configuration is called ultrafast adaptive pulse shaper. The SLM can fully control the amplitude and phase of the spectrum and thus, via the Fourier transform the pulse duration. The full pulse shaper device can be placed anywhere in the

beam but is most likely placed where the pulse energy is low. A drawback of the SLM-based method with its typically 640 pixels is the discrete modulation on the output spectrum and phase through each pixel. The Fourier transform of these discrete steps in spectrum would lead to unavoidable pre- and post-pulses. Also, the discretization due to the limited pixel number and the minimal phase change between consecutive pulse of 2π leads to a limited overall spectral phase that can be applied onto the pulse.

Another approach is based on an acousto-optical modulator (AOM), where a transducer creates a sound wave, which causes a periodic variation in the refractive index associated with the pressure wave. The variation in refractive index can be used to diffract an optical beam with efficiencies up to 80% without distorting the beam properties. Of particular interest in the field of ultrafast optics is the ability to control the spectral phase $\phi(\omega)$ of the diffracted optical beam. The acousto-optical programmable dispersive filter (AOPDF) called Dazzler (Fastlite) is able to introduce an additional group delay of up to 6 ps over a spectral bandwidth ranging from 550 to 1150 nm. The AOPDF is based on precise phase-matching of the optical and acoustical wave in the crystal and the difference dispersion in the birefringent crystal [106].

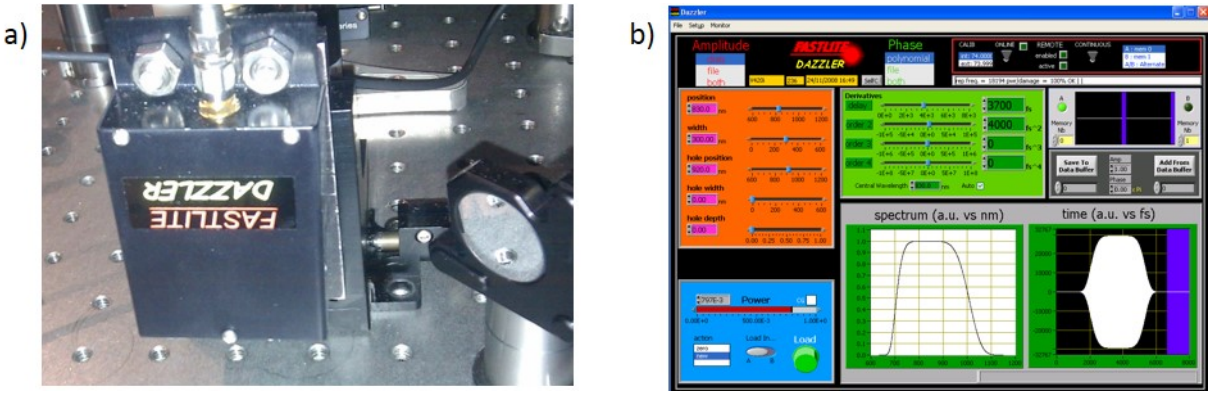

Figure 3-11: Picture of the Dazzler employed in HERACLES (a) and its software interface (b). A group delay difference of up to 6 ps can be compensated with the Dazzler device.

The Dazzler module, shown in Figure 3-11, allows adaptive control of the temporal shape of the laser pulse and supports an almost octave-spanning bandwidth. Such a dispersive filter can be employed in coherent control experiments to vary the spectral phase $\phi_i(\omega)$ of the diffracted beam in order to determine the best feedback from the experiment. If an algorithm is utilized to retrieve the best spectral phase of the diffracted pulse, many phases can be tested per second mainly depending on the time that it takes to achieve the feedback. For example, feeding back the signal strength of a nonlinear optical process such as second-harmonic generation allows to optimize for peak intensity.

- Grism Stretcher:

A grism stretcher utilizes the dispersive properties of a grating pair as well as a prism pair to introduce dispersion to an optical pulse. A sketch is shown in Figure 3-12. The method offers many degrees of freedom to tailor the dispersion. The following parameters have to be carefully chosen of the grism for tailored dispersion: prism apex angle α, prism material, prism length H, incident angle θ_{in}, groove density of the gratings, perpendicular grism separation G and the parallel grism separation S.

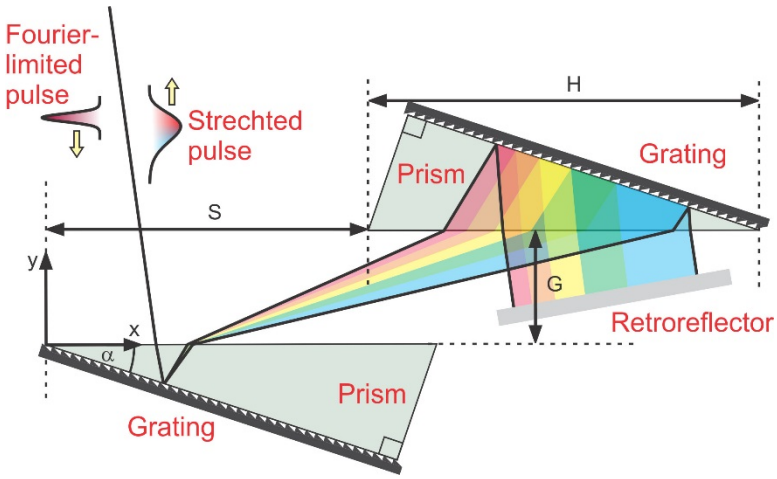

Figure 3-12: Sketch of the grism setup consisting of a pair of gratings and prisms.

The high number of parameters provides sufficient flexibility to match the dispersion of bulk glasses compressors. A grism stretcher and bulk glass compressor was suggested by Zheng et al. [107] as method to stretch and compress sub-10-fs pulses. The approach has been improved to sub-5-fs dispersion management [108]. The same approach has been followed for the dispersion management and is shown in Section 5.4.

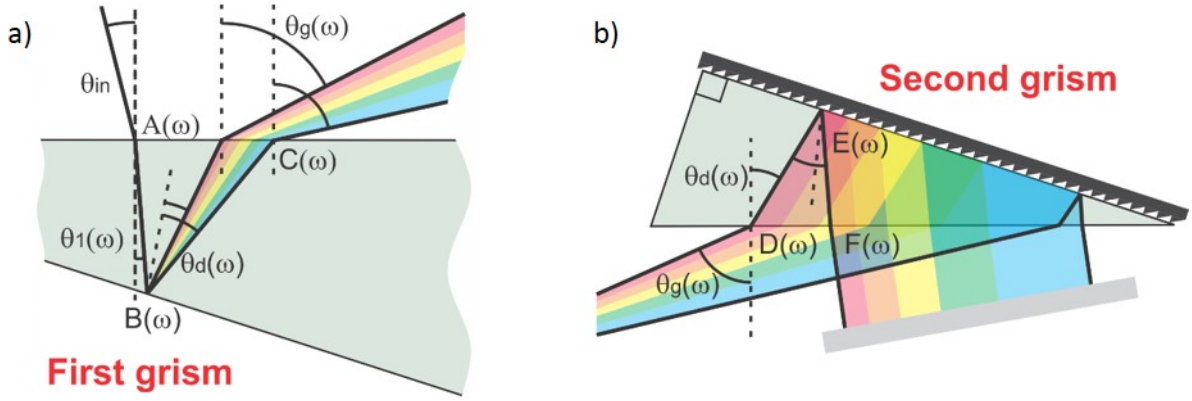

Figure 3-13: Sketches showing the distances, points and angles in the first grism (a) and the second grism (b) employed in the implemented ray tracing code.

Prior to the experimental implementation, the dispersion in OPCPA needs to be carefully designed. One particular challenge here is that several dispersive elements cannot be changed or chosen freely, such as the 4.5-cm-long TeO_2 crystal used in the Dazzler and three BBO crystals with ~5 mm length each. Designs for ultra-broadband laser amplifiers typically aim for a minimum amount of additional dispersion in the broadband beam as well as minimal optical path lengths.

The bulk compressor is usually chosen to be a highly dispersive glass with reduced optical path length. Other than increasing the number of passes, this bulk material offers no design flexibility. After this, the grism stretcher needs to be engineered to match the overall dispersion and needs to be carefully implemented. The parameters for HERACLES are shown in Section 5.4.

3.4 The Carrier-Envelope Phase

In 2000 Holzwarth et al. [8] presented the synthesize of a frequency comb for high precision spectroscopy. A mode-locked laser source emits an equally spaced frequency comb with frequencies

$$f_m = m\, f_{rep} + f_{CEP} \tag{33}$$

as seen in Section 3.2. The work of Theodor W. Hänsch and John L. Hall on measuring and controlling the offset frequency f_{CEP} was awarded the Nobel Prize in 2005. Initial publication where focused on ultra-precise spectroscopy, controlling the frequency offset relates directly to locking the carrier-envelope phase (CEP) [109].

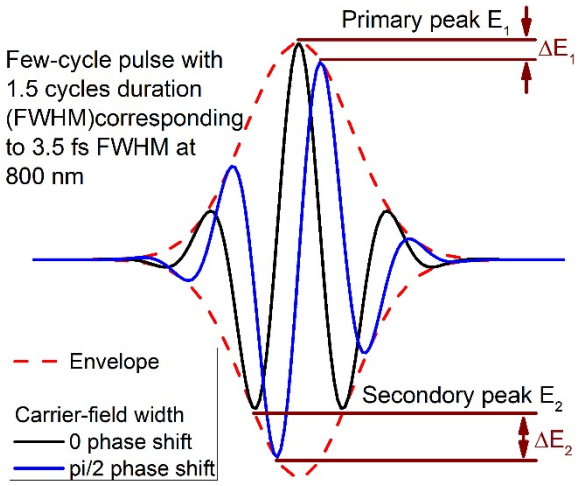

Figure 3-14: Few-cycle pulse with 1.5 cycle duration (red envelope). The electric field is shown with zero (black) and $\pi/2$ phase shift (red). The change in electric field strength for the primary and secondary peak is indicated.

For few-cycle pulses, the offset between the maximum electric field strength in the pulse with respect to the peak of the envelope is highly significant. Figure 3-14 illustrates the impact of different carrier-envelope phases φ_{CEP} on the electric field strength. The changes in electric field strength of the primary and secondary peak are indicated. For highly nonlinear experiments, the change of the primary peak is most interesting due to the direct response. It can be seen that the highest electric field strength can be achieved in the experiment when the CEP φ_{CEP} is 0 or

multiple of 2π, thus, the peak of the electric field coincidences with the peak of the envelope. For experiments such as the generation of isolated attosecond pulses, where a threshold electric field intensity is given, the secondary peaks are also important [31]. It can be seen from Figure 3-14 that the change of electric field strengths is more drastic on the secondary peaks.

3.4.1 Measuring the Carrier-Envelope Offset Frequency

The position of the peak electric field strength with respect to the envelope are related to each other through [109] [11]

$$2\,\pi\,\mathrm{f_{CEP}} = \omega_{CEP} = \frac{\Delta\varphi_{\mathrm{CEP}}}{T_R}, \tag{34}$$

where T_R is the round trip time in the resonator. It is not possible to measure the CEP frequency directly since the spectrum contains no energy in the region close to zero frequency. In the common approach, a frequency comb (Equation (22)) with frequencies f_m can be frequency-doubled to the spectrum $\tilde{E}^{(SH)}(\omega)$, which contains frequencies given by a simple multiplication of Equation (33) by two:

$$2\,\mathrm{f_m} = 2\,m\,f_{rep} + 2\,f_{CEP}\,. \tag{35}$$

If the fundamental spectrum is broad enough, it will also contain frequencies with

$$\mathrm{f_{2m}} = 2m\,f_{rep} + f_{CEP}\,. \tag{36}$$

Mixing the combs of $2f_m$ (Equation (35)) and f_{2m} (Equation (36)) results in a beat note at the difference frequency

$$2\mathrm{f_m} - f_{2m} = f_{CEP} \tag{37}$$

and therefore relates directly to the CEP frequency, which typically lies in the MHz frequency range. If sufficient signal power is available, a commercial MHz frequency analyzer can measure

the exact frequency of this tone from which the CEP φ_{CEP} or its changing rate $\Delta\varphi_{CEP}$ can be retrieved.

3.4.2 Locking and Controlling of the CEP

The CEP frequency, given by

$$\mathrm{f_{CEP}} = \frac{\Delta\varphi_{CEP}\ mod\ 2\pi}{2\pi} f_{rep}\ , \tag{38}$$

can be locked to a well-known ratio (typically 1:4) of the repetition rate. The techniques are typically based on a slight change of the optical path length in the cavity [110] [111] [112], while keeping other properties of the cavity as constant as possible. Mechanical drifts due to environmental parameters such as air pressure, crystal temperature, etc., must be small so the laser and the f-to-2f interferometer are typically enclosed and thermo/mechanically stabilized. For example, Helbig et al. [109] investigated the long-term CEP stabilization of a few-cycle Ti:sapphire laser oscillator that was actively CEP-stabilized by an AOM and presented a residual timing jitter of 10 as or 0.025 rad rms CEP noise.

After locking the CEP, the maximum of the electric field strength is still at a random but fixed position with respect to the peak of the envelope at the position of the experiment. An additional CEP shift $\Delta\varphi_{CEP}(L)$ can be introduced when the pulse is passing through a medium of length L [48] according to

$$\Delta\varphi_{\mathrm{CEP}}(L) = 2\pi L \left.\frac{\partial n}{\partial\lambda}\right|_{\lambda_l}\ . \tag{39}$$

Therefore, along the optical path from the CEP-stabilized oscillator to the experiment, the optical pulse acquires an accumulated CEP shift. By adding or removing dispersive path length, the

absolute position of CEP can be controlled at the exact position of the experiment. To change the CEP by a phase of π, a dephasing length of

$$L_{deph} = \frac{1}{2}\left(\frac{\partial n}{\partial \lambda}\Big|_{\lambda_l}\right)^{-1} \tag{40}$$

is needed. For typical transparent optical materials at a visible carrier wavelength λ_L, this dephasing length corresponds to tens of micrometers. Such a small dephasing length also means that active compensation of CEP drifts introduced by temperature changes, pressure fluctuations or vibrations in the laser system and experiment itself is needed. The latter is especially crucial since a small amount of vibrations transferred to a grating-based stretcher/compressor lead to CEP drifts and an increase in CEP rms noise. In addition, active compensation of CEP drifts via a composite glass plate [113] or an AOPDF [114] have been demonstrated.

3.5 Non-Collinear Optical Parametric Amplification

Non-collinear OPA is a technique to amplify ultrashort pulses with ultrabroad bandwidth [56]. This section gives the theoretical background and some numerical examples to illustrate key properties in OPA. A picture of a laboratory OPA setup is shown in Figure 3-15.

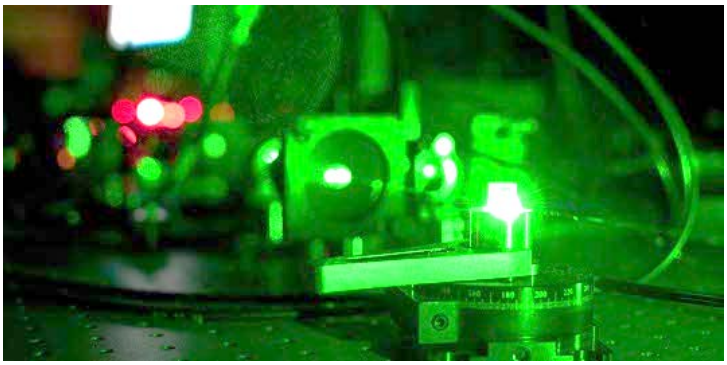

Figure 3-15: Picture of an OPA in the laboratory with the green pump laser beam propagating through the BBO crystal with dimensions 10 mm x 10 mm x 5 mm.

Optical parametric amplification is based on nonlinear polarization. Nonlinear optical materials with non-centrosymmetric crystal structures exhibit a polarization $\boldsymbol{P}$ when subject to an external electric field $\boldsymbol{E}$, given approximately by a Taylor expansion [115]. The second order term, a nonlinear polarization term,

$$P_i^{nl} = \epsilon_0 \chi_{ijk}^{(2)} E_j E_k \tag{41}$$

gives rise to the three-wave-mixing effect known as optical rectification. The well-known effects second-harmonic (SHG), sum-frequency (SFG) and difference-frequency (DFG) generation are direct consequences of this second-order nonlinear polarization. For all the wave-mixing combinations, the momentum conversation principle

$$\hbar \boldsymbol{k}_p = \hbar \boldsymbol{k}_s + \hbar \boldsymbol{k}_i \,, \tag{42}$$

and energy conversation principle

$$\hbar \omega_p = \hbar \omega_s + \hbar \omega_i \tag{43}$$

are considered. In OPA, an intense pump beam with higher frequency (index p) transfers energy to a lower frequency beam called signal (index s). A third beam is generated called the idler (index i) to satisfy momentum conversation via Equation (42) and energy conversation via Equation (43). Its frequency is given by the condition

$$\omega_i < \omega_s < \omega_p \,. \tag{44}$$

According to the general nomenclature, the signal frequency can obtain values ranging from $\frac{\omega_p}{2}$ to ω_p and the idler can vary from $\frac{\omega_p}{2}$ and lower. A typical geometry for optical parametric amplification (OPA) is sketched in Figure 3-16 for a noncollinear scenario: A high intensity, high freqency pump is overlaped with a low-energy lower frequency signal pulse in an optically nonlinear cystal. During OPA, energy is transferred from the pump to the signal pulse and an idler beam is generated as a direct consequence of momentum and energy conversation. The process

efficiency depends critically on many factors including the intensities, the incident angles, the orientation of the crystal axis, the material used and the frequencies of pump, signal and idler.

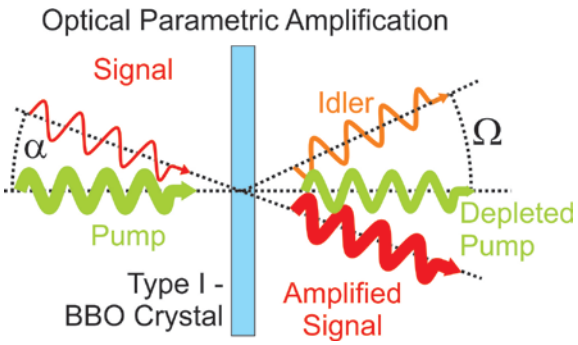

Figure 3-16: Sketch of the geometry in optical parametric amplification.

In the general case where a pump, a signal, and an idler beam are propagating with different group velocities $v_g = d\omega/dk$ in an optically nonlinear crystal, a set of coupled differential equations describing the parametric amplification process can be derived [56]

$$\frac{\partial A_s}{\partial z} + \frac{1}{v_{gs}}\frac{\partial A_s}{\partial \tau} = -i\frac{\omega_s d_{eff}}{n_s c_0} A_i^* A_p \exp(-i\Delta k z) \tag{45}$$

$$\frac{\partial A_i}{\partial z} + \frac{1}{v_{gi}}\frac{\partial A_i}{\partial \tau} = -i\frac{\omega_i d_{eff}}{n_i c_0} A_s^* A_p \exp(-i\Delta k z) \tag{46}$$

$$\frac{\partial A_p}{\partial z} + \frac{1}{v_{gp}}\frac{\partial A_p}{\partial \tau} = -i\frac{\omega_p d_{eff}}{n_p c_0} A_s A_i \exp(i\Delta k z)\,. \tag{47}$$

In this set, $A(z,t)$ represents the envelope of the electric field of the signal, idler and pump, ω the center frequency, v_g the group velocity, n the refractive index of the material, c_0 the speed of light, Δk the wave-vector mismatch given by

$$\Delta k = k_p - k_s - k_i\,, \tag{48}$$

d_{eff} is the effective nonlinear optical coefficient, an intrinsic property of a given crystal, and depends on the propagation direction relative to the crystal orientation and the polarization of the laser. The wave-vector mismatch is commonly termed phase-matching which highly ultimately

determines the obtainable gain and bandwidth in OPA and other nonlinear frequency conversion processes (shown in the following).

A few assumptions can be utilized to simplify these equations [56]. First, under the condition of perfect phase-matching ($\Delta k = 0$) the exponential expression vanishes. Second, for collinear cw (single frequency) beams, the time derivative in Equation (45), (46) and (47) can be dropped. This is due to the fact that the time derivative is introduced for the case of ultrashort pulses, where the group velocity mismatch (GVM) between pulses matters. In particular, the GVM between pump and signal sets a limit on the interaction length of the OPA process in the optically nonlinear medium. On the other hand, signal and idler need to fulfill the phase-matching condition and thus, GVM between them sets a limitation to the phase-matched bandwidth. Third, if no pump depletion is assumed an expression for the signal beam intensity can be expressed by [56]

$$\mathrm{I_s(L)} \cong \frac{1}{4}\mathrm{I_{s,0}}\exp(2\Gamma \mathrm{L})\,. \tag{49}$$

In this expression, L represents optical path in the nonlinear material and Γ the nonlinear gain coefficient which scales according to

$$\Gamma \propto \sqrt{I_p} \tag{50}$$

relative to the pump intensity I_p. The parametric gain can be extracted from Equation (49) to be

$$\mathrm{G} \propto \exp(2\Gamma \mathrm{L})\,. \tag{51}$$

Thus, the parametric gain is highly dependent on the pump intensity and interaction (i.e. crystal) length. Figure 3-17 shows the calculated parametric gain via equation (49) for the parameters of BBO [116]. High parametric gain of 10^6 can be achieved in only a few mm interaction length when pumped by an intensity of 10 to 100 GW/cm².

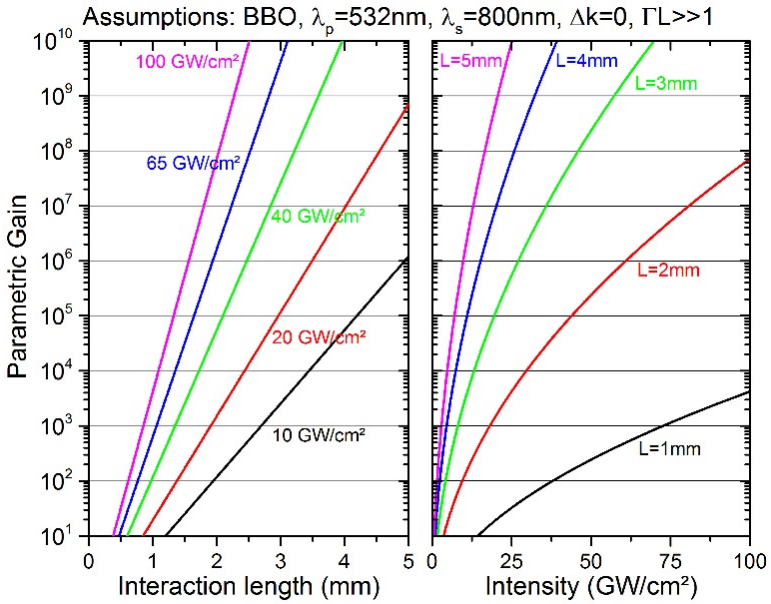

Figure 3-17: Parametric gain calculated via equation (49) for BBO for several different pump intensities and OPA interaction lengths.

The wave-vector mismatch for different frequency components has to be considered when extending the formalism to a broadband signal pulse. To achieve broadband phase matching, it is necessary to introduce an additional degree of freedom by separating the pump and signal with an angle α, resulting in an angle Ω between the signal and the idler as shown in Figure 3-16. In this particular case, the phase-matching conditions changes to [56]

$$\Delta k_{par} = k_p \cos\alpha - k_s - k_i \cos\Omega = 0 \tag{52}$$

$$\Delta k_{perp} = k_p \sin\alpha - k_i \sin\Omega = 0 \tag{53}$$

for the momentum-mismatch projected on the directions parallel and perpendicular to the signal wave vector. The angle Ω between the signal and the idler beam is determined by the geometry allowing further analysis [56] to determine the best angle α, where phase-matching for a certain signal wavelength λ_s

$$\alpha = \arcsin\left(\frac{1 - a^2}{1 + 2\,a\,b + b^2}\right) \tag{54}$$

where

$$a = \frac{v_{gs}}{v_{gi}} \tag{55}$$

and

$$b = \frac{n_s \lambda_i}{n_i \lambda_s}. \tag{56}$$

The angle between the wave vector of the pump beam and the optical axis of the nonlinear crystal is called phase-matching angle θ_m (angular phase-matching). Both angles θ_m and α together can be used to adjust the wave-vector mismatch Δk_{par} and Δk_{perp} to achieve maximum gain and/or amplification bandwidth and is studied in the following sub-sections.

3.5.1 Phase-Matching in BBO

In the HERACLES facility OPA is used to obtain few-cycle OPCPA output. Phase-matching is crucial during amplification. The standard phase-matching curves are calculated with the software package SNLO (AS-Photonics, LLC) and presented in Figure 3-18. The calculations were based on BBO as nonlinear material at a pump wavelength of 532 nm. A typical acceptance angle range is indicated based on laboratory experience showing the typical gain bandwidth ranging from 725 to 1050 nm. It can be seen in Figure 3-18 that the phase-matching curve with an angle α of 2.5 degrees offers a larger flat portion around 800 nm than the 2.3 degrees that can be used as well. The case of 2.3 degrees offers the larger bandwidth considering the typical angular acceptance width as indicated in on the plot of Figure 3-18, resulting in the broadest parametric amplification bandwidth, i.e. broadest phase-matching for a certain crystal length, a typically called “magic angles”.

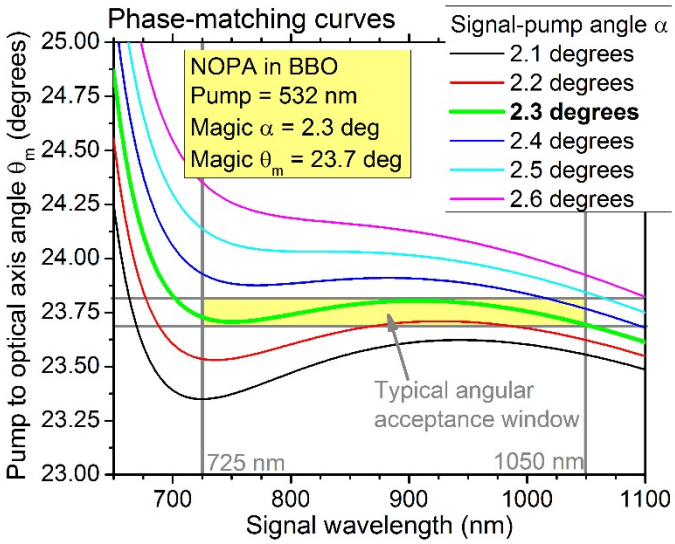

Figure 3-18: OPA Phase-matching curves with 532 nm pump wavelength (SH of 1064 nm wavelength). The magic angles, typical acceptance angle and parametric gain bandwidth are indicated in the figure.

As part of an experiment described later in this dissertation (see Chapter 6), it is important to mention the case of degenerate OPA. Degenerate OPA is often chosen for its simplified since collinear alignment. The phase-matching curve for this case was calculated and shown in Figure 3-19. The calculations are based on BBO as nonlinear medium and a pump wavelength of 1030 nm. A gain bandwidth of tens of nanometers can be achieved depending on the OPA crystal length. Shorter crystals can be employed if high pump intensities are utilized usually achieved with sub-ps pulse durations.

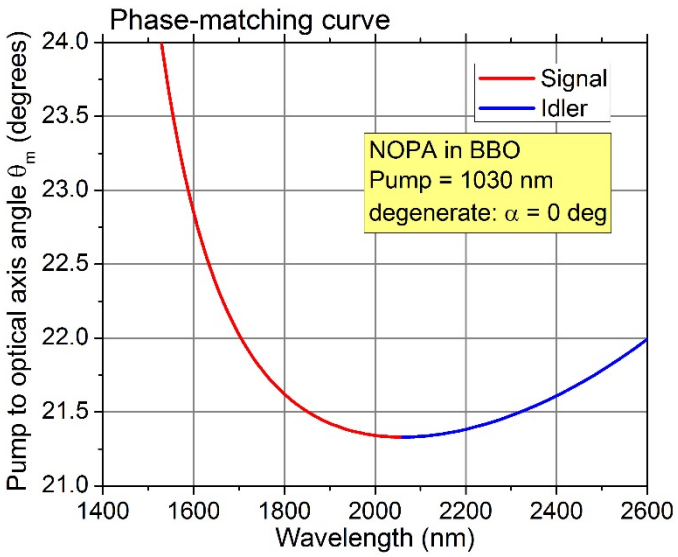

Figure 3-19: Phase-matching curves of degenerate OPA in BBO with 1030 nm pump. The broadest bandwidth can be generated around the minimum of the curve at 2.1 µm.

3.5.2 Origin of Fluctuations

One of the challenge during the implementation of a high-energy, few-cycle, OPCPA facility is the need for highly-stabile OPCPA output for long-term experiments. The stability of the OPCPA output is mainly given by the OPA stage. Following Equation (49) or Equation (51) for the approximated parametric gain, a few sources of noise and fluctuations can be identified, such as:

- Pump intensity/energy fluctuations. The parametric gain and its saturation are nonlinearly dependent on the pump intensity. This is of special concern in the first OPA stage, where a parametric gain of 10^6 or more needs to be achieved and maintained. Slight peak intensity fluctuations will lead to large output fluctuations. Also, the optical parametric phase (OPP) introduces additional intensity dependent dispersion as shown in [117].
- Pump duration fluctuations. For non-transform-limited pulses, a change in chirp rate influences the pump intensity and the instantaneous pump wavelength. As a consequence, the spectral output of the signal beam can be distorted given by momentum and energy

conversion as well as the phase-matching condition. Unsuccessful compression and additional background can be a consequence.

- Pump and signal overlap fluctuations. A poor overlap results in a dramatic change of parametric gain as well as output spectrum. Overlap instabilities can be reduced by utilizing larger beam sizes as well as increasing the seed to pump diameter ratio.

Many factors influence the output stability of OPA, which directly impact the OPCPA output stability. A high-quality pump laser is the key to provide stable OPCPA output. Chapter 4 discusses and addresses a few instability issues and solutions through the assembly steps towards a high-quality pump for the HERACLES facility.

3.5.3 Limitations with Small Beam Diameters

OPA pump pulses with more than 10 ps duration and sub-mJ pulse energies exhibit a peak power that is potentially too low for efficient OPA. In order to raise the pump peak intensity and allow sufficient parametric gain, the pulses need to be focused to small beam diameters of 50 to 100 µm. For example, a 65 ps pump pulse with 100 µJ pulse energy would need to be focused to 120 µm spot diameter to achieve a pump intensity of 15 GW/cm². However, when focusing Gaussian beams to such small spot sizes, the divergence angle of the beam becomes large, severely limiting the distance over which the intensity remains high enough for large parametric gain, associated with the Rayleigh range and the overlapping distance.

The Rayleigh range is the propagation distance after which a focused Gaussian beam with waist diameter w_0 has expanded to $\sqrt{2}w_0$ and therefore its peak intensity has dropped by a factor of two. For a diffraction limited Gaussian beam, it is given by the expression [30]

$$z_R = \frac{\pi w_0^2}{\lambda}, \tag{57}$$

where λ is the utilized pump wavelength. Thus, if the full Rayleigh range, given by twice the length of Equation (57), is on the order of the desired OPA interaction length, an intensity variation is the result that varies across the interaction length by a factor of 2. To achieve a quasi-uniform intensity distribution across the interaction length, the Rayleigh range should be many times longer than the employed nonlinear crystal. This can be achieved with large focused beam sizes obtained by a long focal length. As a consequence of the finite Rayleigh range, the obtainable parametric gain can be limited when operating with small beam sizes. In addition, the overlapping distance is limited by the finite size of the two beams [118]. Both effects were modeled and calculated results are presented in the following paragraphs.

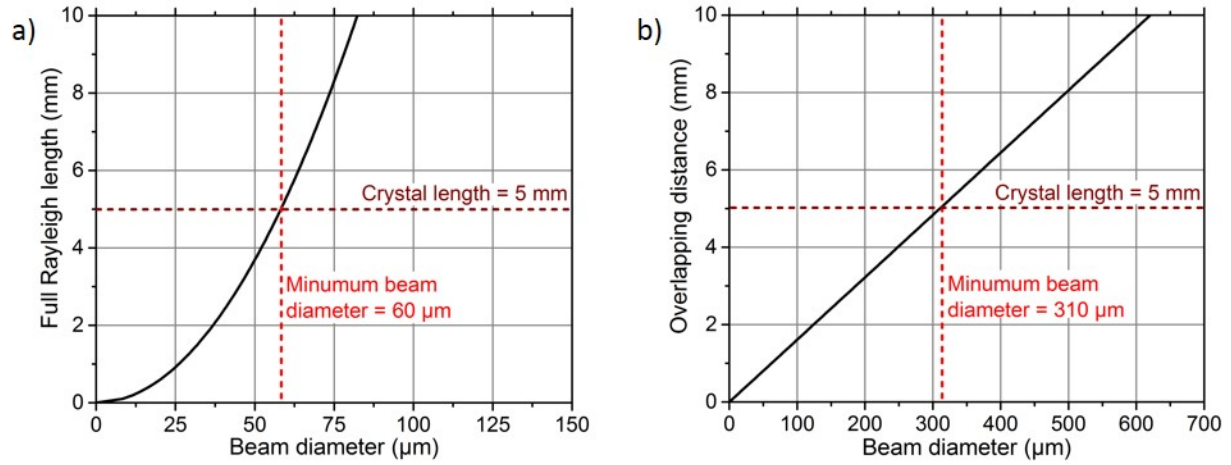

Figure 3-20: Full Rayleigh range (a) and overlapping distance (b) against beam diameter. A 5 mm crystal length is indicated with the corresponding minimum beam sizes.

The influences of the beam diameter onto the Rayleigh range and overlapping distance are shown in Figure 3-20 for a set of parameters relevant to the HERACLES facility. Assuming a 5 mm-long crystal, the minimum beam diameter to match the Rayleigh range was found to be 60 µm calculated for 532 nm wavelength. However, for such tight focusing, the beams would separate spatially after approximately 1 mm, as Figure 3-20 (b) shows. The minimum beam diameter in this

example, is therefore dictated by the overlapping distance. A minimum spot size of 310 µm is necessary in order to keep the beams spatially overlapping for the entire 5 mm crystal. Both effects become less severe for larger beam sizes and negligible for focused beam diameters exceeding 600 µm. Thus, in the presented case, pump beam sizes much larger than 310 µm are desired in order to achieve a quasi-uniform intensity distribution in the crystal and good beam overlap.

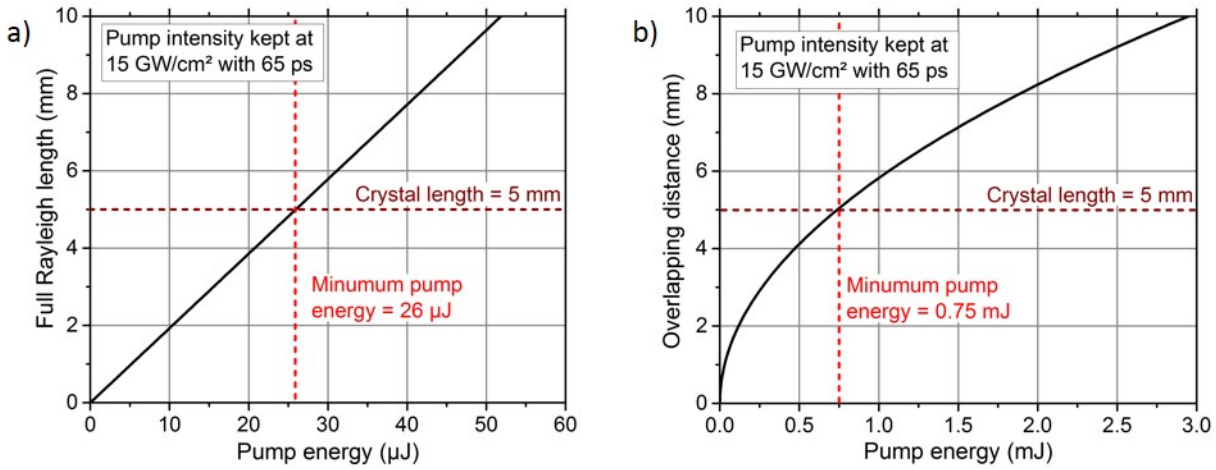

Figure 3-21: Full Rayleigh range (a) and overlapping distance (b) as function of pump energy with maintained focused pump intensity of 15 GW/cm² and 65 ps pulse duration. A 5 mm crystal length is indicated with the corresponding minimum beam sizes.

The influences of Rayleigh and overlapping distance are further investigated with respect to minimal required pulse energy with parameters relevant to the HERACLES facility. In the model, a focused beam intensity of 15 GW/cm² was maintained with a pulse duration of 65 ps and pulse energy and spot diameter adapted accordingly. Thus, the required pulse energies, as presented in Figure 3-21, can be related to the full Rayleigh range and the overlapping distance. Examples are indicated in Figure 3-21: a pulse energy of 26 µJ is necessary, for a peak intensity of 15 GW/cm² assuming 65 ps duration and a Rayleigh length of 5 mm. On the other hand, 0.75 mJ pulse energy is required to obtain an overlapping distance corresponding to 5 mm. Thus, the overlapping distance is again the limiting parameters in this study.

In another example, if only 500 µJ pump pulse energy is available with 65 ps pulse duration, the Rayleigh range condition is largely satisfied. However, the effective overlapping distance is reduced to 4 mm as indicated in Figure 3-21 (b). As a consequence, the obtainable parametric gain from this stage is highly reduced due to the shorter overlapping distance. Similarly, if the pump pulse energy is only 100 µJ the effective OPA interaction length is reduced further to 1.8 mm. On the other hand, a higher pulse energy leads to an increase of overlapping distance. For example, an 8 mm overlapping distance can be achieved for a pulse energy of 2 mJ, and this limiting effect can be generally neglected beyond 10 mJ. Thus, in the presented case, pump pulse energies much larger than 1 mJ are desired.

The set of parameters for the calculations shown in Figure 3-20 and Figure 3-21 were chosen to match the obtained values in the HERACLES facility. The required pulse energies are highly dependent on the chosen pulse duration, the focused peak intensity and the crystal lengths. This study could be extended in the future to other OPA setups. These calculations/results provide conceptual insights onto OPA limitations with finite beam sizes and give a performance estimate applicable for the HERACLES facility. Pulses at the mJ-level are used to pump the OPA stage in case of the HERACLES system, as presented later in Section 5.5. These pulse energies are at the lower limit for the 5 mm OPA overlapping distance degrading obtainable parametric gain. In addition, small beam sizes are more prone to beam pointing fluctuations, which was a key consideration during the implementation of the HERACLES facility and the topic is discussed throughout this dissertation.

3.5.4 Two-Color Pumping

In this section, an advanced OPA method based on pumping the OPA stages by two beams with different photon energies is conceptually discussed and considered for implementation in the

PhaSTHEUS OPCPA facility. Two-color pumping for OPA has the advantage of increasing the amplified bandwidth to enable sub-5-fs pulse durations at 800 nm center wavelength. It is based on OPA pumped by both the second-harmonic and third-harmonic of a near-IR laser. The gain bandwidth from the first OPA stage can be extended with a second OPA stage towards the blue part of the spectrum. Figure 3-22 shows a schematic of the two-color pumping procedure. The method has been experimentally demonstrated with a fundamental pump pulse duration of 1.5 ps and an OPCPA output duration of sub-3-fs [119]. It was also presented with a long pump pulse duration of 78 ps; although, the OPCPA output was not compressed but the experimentally obtained spectrum corresponded to a transform-limited duration of 4.5 fs [53].

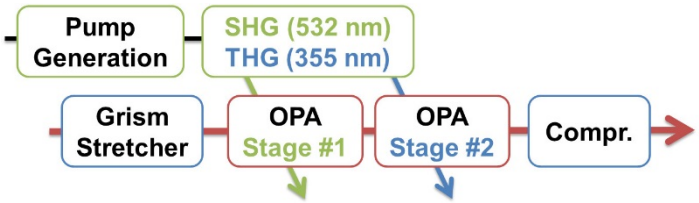

Figure 3-22: Schematic overview of the two-color pumping scheme in OPCPA.

Phase-matching curves are calculated for pumping with the TH wavelength of 355 nm and are shown in Figure 3-23. The typical gain bandwidth for pumping with ~60 ps pulse duration is 575 nm to 725 nm. The magic angles, which are the angles to obtain the broadest phase-matching condition, for the two-color scheme are listed in Table 3-4.

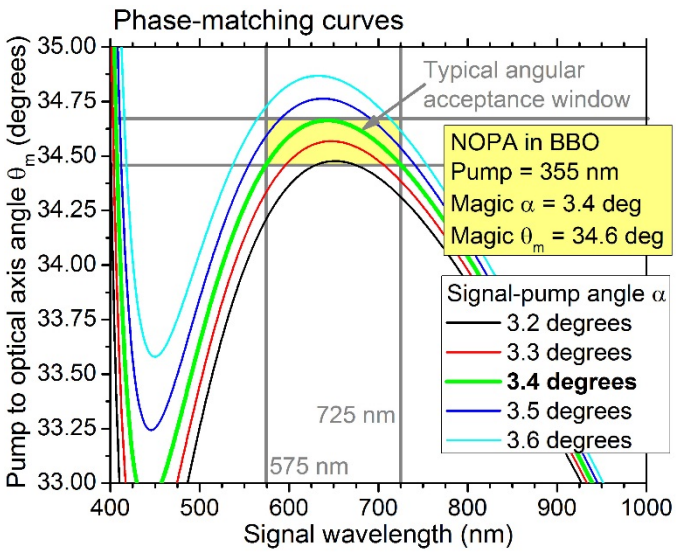

Figure 3-23: OPA Phase-matching curves with 355 nm pump wavelength (TH of 1064 nm pump wavelength). The magic angles, typical acceptance angle and parametric gain bandwidth are indicated in the figure.

As a result, two color pumping allows the direct amplification of almost octave-spanning ranging from 575 to 1050 nm. The number of OPA stages is doubled to typically four, which increases largely the complexity of the setup. Overall output fluctuations, pulse contrast and operational complexity are highly affected by the increased number of OPAs. In addition, the overlapping parametric gain bandwidths lead to problems when operating both OPAs in saturation. Ultra-high OPA gain eventually leads to signal and idler re-conversion to a pump photon causing decreased overall efficiency.

Table 3-4: Magic angles and gain bandwidth for two-color pumping based on 1064 nm fundamental wavelength.

Harmonic of 1064 nm	**Pump wavelength**	**Magic α**	**Magic θ_m**	**Gain bandwidth**
SH	532 nm	2.3°	23.7°	725 – 1050 nm
TH	355 nm	3.4°	34.6°	575 – 725 nm

3.6 Summary

This chapter describes essential aspects of DPSS amplifiers and few-cycle OPCPA. Different schemes for traditional laser pulse amplification are presented and related challenges are discussed. Dispersion and few-cycle dispersion management is the basis for the generation of the sub-10-fs and sub-5-fs pulses in the visible/near-IR as described in Section 5.4. The common approach to CEP locking is described. The basic theory of OPA is established in this section and relevant parameters in HERACLES are discussed in detail including the limitations with small pump beam spot sizes. Using these considerations, the implementation and experimental results are shown in the following chapters.

4 DPSS LASER FOR OPCPA PUMPING

For our few-cycle laser HERACLES facility, the pump beam is generated using a hybrid ultrafast/fiber/solid-state chain. A high-quality pump laser is required to achieve efficient and stable OPCPA output. Modeling, implementation, and optimization as well as power and energy scaling of a high-quality OPCPA pump system are presented in this chapter. The first section discusses a few aspects of diode-pumped, solid-state rod amplifiers, which are important in the context of this dissertation. Section 4.2 describes the implementation of a high average power regenerative amplifier, which provided sufficient pulse energy at high repetition rates, but suffered unacceptably from severe beam pointing problems. It was found, that the poor beam stability of the pump beam generation propagated through the system and led to a highly unstable OPCPA output. As a consequence, another amplifier system was implemented operating at higher pulse energy based on improved laser amplifier modules and a slightly modified design. This effort is presented in Section 4.3. Section 4.4 shows the energy and power scaling of the diode-pumped, solid-state amplifier chain. The design and implementation of two booster stages is presented to obtain high pulse energy and high average power. Scaling to ultra-high pulse energies is presented in Section 4.5. Here, flashlamp-pumped, solid-state rods provided final amplification. Limitations, results, further scaling and the design of an ultra-high intensity OPCPA facility called PhaSTHEUS, which is based on these findings, are described in section 4.5. The section is concluded with a summary in Section 4.6.

For simplification, the scope of this chapter is reduced to the solid-state amplifiers of the pump beam generation and the amplifiers are related later in Chapter 5.3 to the OPCPA system. The solid-state amplifiers were seeded with a fraction of the bandwidth at 1064 nm from a sub-5-

fs oscillator followed by a fiber-based pre-amplifier (see Section 5.3.1). This ultrafast/fiber front-end was employed to seed the presented solid-state amplifiers in this chapter.

4.1 Basic Considerations

Diode-pumped, solid-state amplifiers allow the amplification of optical pulses with high-pulse energy and high-average power and are the basis of the presented amplifier line. The goal is a high-quality OPCPA pump beam with few mJ pulse energy and ~100 ps pulse duration. A few general design considerations are given in this section.

4.1.1 MOPA-like Design

The design of the amplifier can be simplified to a MOPA-like structure as shown in Figure 4-1. A Ti:sapphire oscillator and fiber pre-amplifier provided stable seed pulses for the solid-state amplifier stages. The output of this stage is further amplified in a regenerative amplifier and a single-pass amplifier, followed by a frequency-doubling crystal. These stages are described in Section 4.2 and 4.3 and the output performances of several stages are shown.

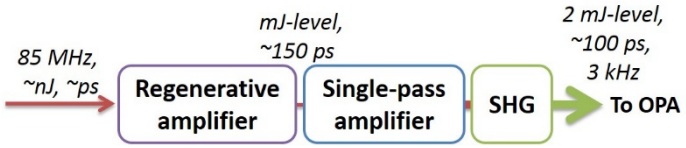

Figure 4-1: Schematic of the amplifier chain to generate the OPCPA pump beam.

4.1.2 Basic Concept of Regenerative Amplifiers

Regenerative amplifiers are commonly used to boost the pulse energy of an ultrashort pulse with duration ranging from 50 fs to 5 ns and energy ranging from nJ or pJ by about 6 orders of magnitude (or 60 dB) to the mJ-level or beyond. Figure 4-2 shows the principle layout of a regenerative amplifier. It consists of a resonating cavity (typically between the HR or VBG), a

Pockels cell, a quarter-waveplate and a thin-film polarizer to inject, trap and eject the pulse from the cavity. The output beam profile is strongly influenced by the cavity mode and care is taken to make the resonator operate in fundamental TEM_{00} mode.

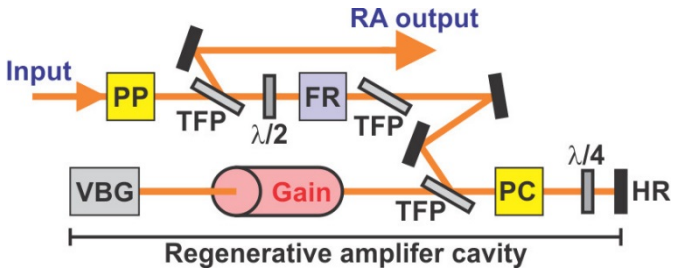

Figure 4-2: Layout of a regenerative amplifier. The optical pulse is injected/ejected from the cavity by polarization switching via the Pockels cell.

The timing of the switching Pockels cell can be adjusted so that the pulse can be held in the cavity until the amplification saturates and the gain (or population inversion) is depleted. Typically, the number of round trips is on the order of 20 to 50, at which point the output energy reaches the mJ-level. The distance between the polarizing elements and the end of the cavity needs to be larger than the switching time of the Pockels cell and the pulse duration, but is usually kept at the minimal length to achieve a robust resonator. For example, a minimum length between Pockels cell and cavity end of 75 cm corresponds to a switching time window of >5 ns, allowing more than enough roundtrop time for a pulse with 100 ps duration. For the presented amplifiers, the Pockels cell switching time was measured to be 3.76 ns for 90% rise or fall and 5.4 ns for full rise or fall. The optimal applied voltage was measured to be 4.52 kV (data sheet: 4.6 kV).

For operation closely above the threshold, a regenerative amplifier becomes a cavity-dumped system, where the pulse amplification does not reach saturation resulting in less extracted energy. This effect can be partially avoided by increasing the number of round trips to allow saturation. If the seed energy is below threshold, the system becomes effectively a Q-switched laser where the pulse in the cavity starts from spontaneous emission. This amplified spontaneous

emission (ASE) is unavoidable and a competing process in the regenerative amplifier. Lührmann et al. [120] estimated the minimum seed pulse energy for the reported regenerative amplifier to be 1 pJ. This system is comparable to the regenerative amplifiers presented in this work. The 1 pJ threshold gives an order of magnitude estimation for the minimum seed energy necessary for the here presented regenerative amplifiers.

4.1.3 VBG-Controlled Transform-Limited Pulse Duration

In order to further reduce unwanted ASE, a volume Bragg grating (VBG) is utilized in all regenerative amplifier systems presented in this dissertation. The employed VBG has a 50 pm (FWHM) reflection bandwidth (120 pm full width) centered at 1064.235 nm with 70% reflectivity and was chosen because of its availability at the time of implementation. The VBG is employed as a narrow-linewidth mirror effectively minimizing ASE built-up in the wavelength region outside of the VBG reflectivity band (similar to [121] and [122]). When used as a feedback element inside the regenerative amplifier, the supported linewidth can be reduced to tens of pm and the build-up/amplification of energy outside the supported bandwidth is suppressed. The VBG has an additional effect of forcing the regenerative amplifier to operate at 1064.2 nm, even though Nd:YVO_4 is used as the gain material.

The regenerative amplifier was seeded with a low energy pulse (10 pJ) and not transform-limited ~20 ps pulses. A picture of an intra-cavity VBG is shown in Figure 4-3 (a). It narrowed the spectrum and tailored a transform-limited pulse with 100 ps-level duration. Figure 4-3 (b) shows a numerically simulated spectrum of a pulse in the regenerative amplifier cavity after each round trip. A reflection from a VBG with 300 pm FWHM Gaussian-shaped reflectivity was assumed for each round trip. It can be seen that the spectrum rapidly narrows to below the VBG reflectivity FWHM within a few round trips and further continues to narrow.

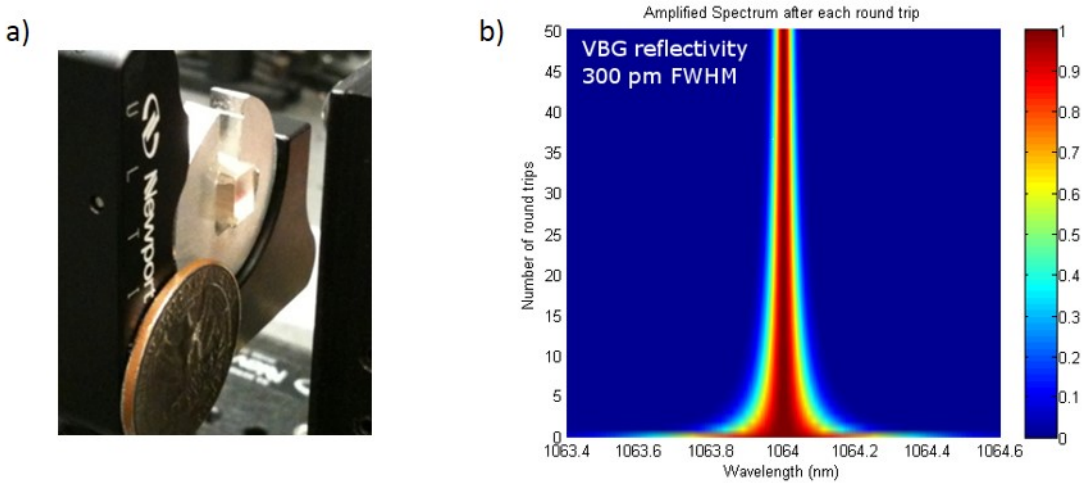

Figure 4-3: (a) Picture of the utilized VBG. (b) Normalized spectrum after each pass showing exemplary the linewidth narrowing with an intra-cavity VBG.

The effect of an intra-cavity VBG on the linewidth was numerically studied and is shown in Figure 4-4 (a) for several reflectivity bandwidths. In the case of a VBG reflectivity of 300 pm, the output linewidth dropped below 100 pm after 9 round trips. After 25 round trips the linewidth was ~60 pm and after 50 round trips it was ~40 pm. A similar trend can be found for the presented cases of 150, 100, 70 and 50 pm FWHM VBG reflectivity. Thus, the output linewidth is dependent on the utilized VBG reflectivity FWHM as well as the number of round trips. This linewidth has to be carefully chosen since the regenerative amplifier output linewidth sets approximately the output linewidth of the overall pump beam generation in the presented scheme. Any change in VBG reflectivity FWHM or number of round trips influences the output linewidth.

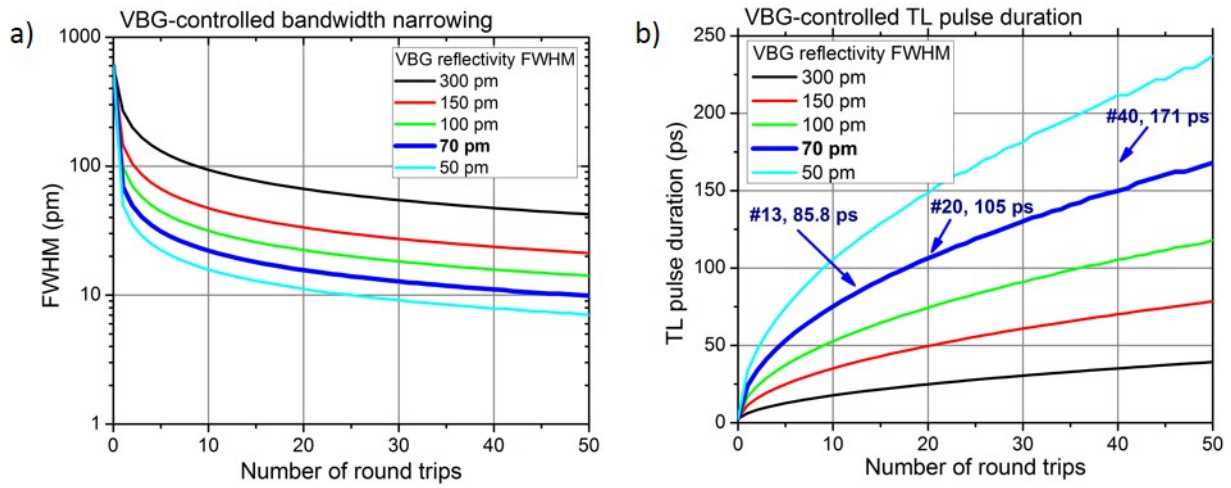

Figure 4-4: Linewidth (a) and transform-limited pulse duration (b) for several number of round trips in a regenerative amplifier with a VBG as cavity mirror.

After several roundtrips within the regenerative amplifier cavity, the linewidth is reduced to below 100 pm and can be assumed to be transform-limited. The output pulse duration is shown in Figure 4-4 (b) for intra-cavity VBGs with several reflectivity bandwidths. It can be seen that the output pulse duration can reach values from 17.8 ps for 10 round trips with 300 pm VBG reflectivity to ~240 ps for 50 round trips and 50 pm. The 106.3 ps in the case of 70 pm FWHM reflectivity after 20 round trips increase to 108.8 ps after one additional round trip or 130.2 ps after 10 additional round trips, respectively.

Experimentally, the utilized VBG had 70% reflectivity, reflectivity FWHM of 50 pm and an aperture of 5 mm x 5 mm with 1 cm length. The number of round trips in the regenerative amplifier were always chosen to result in complete energy extraction from the gain material and thus, highest output pulse energy. Three operational points are indicated in Figure 4-4 (b) which were obtained with this VBG: 85 ps[123], 106 ps (Section 4.2) and 171 ps (Section 4.3).

4.1.4 Laser Material Comparison: Nd:YVO_4 and Nd:YAG

A regenerative amplifier model was implemented based on the equations found in Section 3.1.1. A comparison is given for Nd:YVO_4 and Nd:YAG. Both materials were available for a regenerative amplifier with an aperture size of 2 and 3 mm and a pump power 150 and 300 W, respectively. The key parameters, that differ strongly between the two materials, are the emission cross-section at 1064 nm ($\sigma_{Nd:YVO4} = 114 \cdot 10^{-20}\ cm^2$ and $\sigma_{Nd:YAG} = 28 \cdot 10^{-20}\ cm^2$) and the upper state (fluorescence) lifetime ($\tau_{Nd:YVO4} = 90\ \mu s$ and $\tau_{Nd:YAG} = 230\ \mu s$). Figure 4-5 shows the modeled small signal gain at different repetition rates for both materials in a regenerative amplifier, which agrees with experimental values ($ssg_{Nd:YVO4} = 5.5$ and $ssg_{Nd:YAG} = 2.5$). The plot shows that for Nd:YVO_4 the larger cross-section led to an increase in small signal gain and the shorter upper state lifetime led to high gain in the range of 1 to 10 kHz. Thus, Vanadate seems better suited as amplifier material especially for higher repetition rates. In addition, Vanadate is naturally birefringent which effectively suppresses thermally induced depolarization of the beam. Nd:YAG on the other hand was more readily available, especially for larger crystal dimensions. Thermally induced depolarization becomes a problem for high pump densities with up to 35% non-uniform depolarization of the beam [99]. This portion can be reduced with advanced compensations schemes to below 5% (see Section 3.1.3).

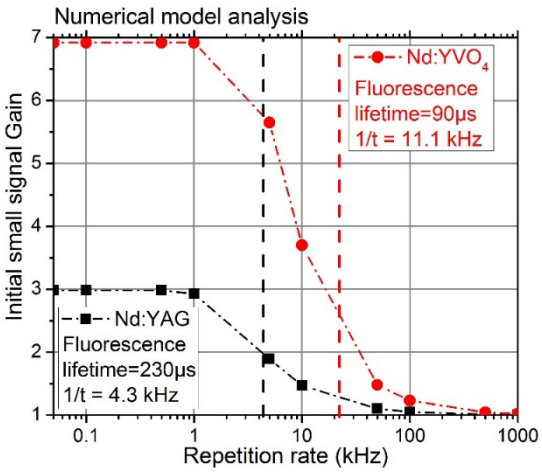

Figure 4-5: Calculated small signal gain at different repetition rates for Nd:YVO_4 and Nd:YAG.

The amplification performances of both materials were numerically analyzed and is shown in Figure 4-6. As seen earlier, Vanadate showed high small signal gain, which decreased when approaching the frequency corresponding to the inverted upper state lifetime ($1/\tau_{fl}$). Figure 4-6 shows the calculated extracted energies and average powers at different repetition rates for a hypothetical regenerative amplifier based on Nd:YVO_4 with 2 mm diameter and 150 W pump power (a) or Nd:YAG with 3 mm and 300 W (b). The parameters were chosen based on commercially available amplifier systems, which are typically pump power-limited by the fracture limit of the material. Based on the results shown in Figure 4-6, extraction of the highest pulse energy at high average power and moderate number of rounds trips is possible for repetition rates close to the inverse of the fluorescence lifetime. It can be seen that the hypothetical obtainable output pulse energy, which is the stored energy when operating close to saturation, is higher for Nd:YAG due to the higher pump power.

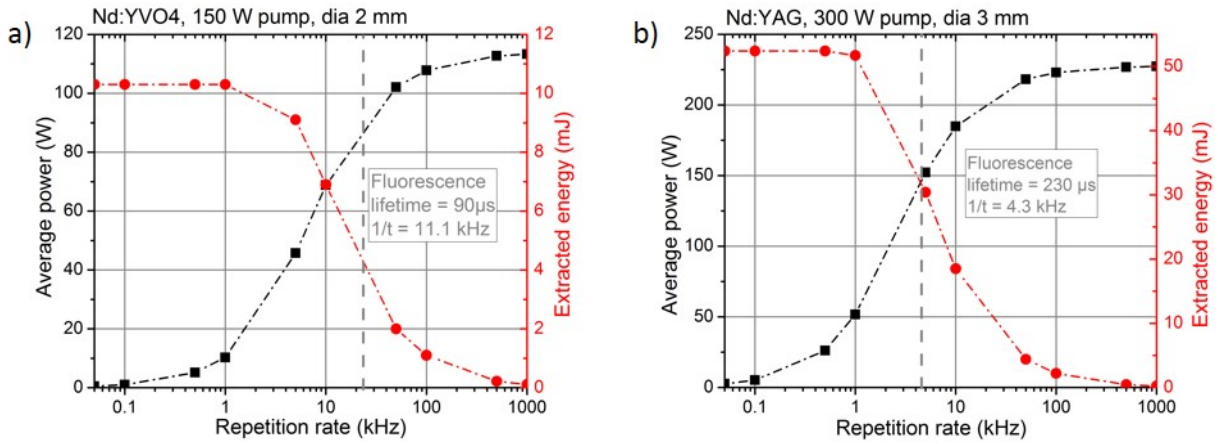

Figure 4-6: Calculated average power (black) and pulse energy (red) of a hypothetical regenerative amplifier based on Nd:YVO_4 (a) and Nd:YAG (b).

Based on the above considerations, Nd:YVO_4 was initially chosen in the regenerative amplifier to obtain high repetition rate (~10 kHz) output. A setup based on a Nd:YVO_4 amplifier was implemented and is discussed in the following section (4.2). As seen from Figure 4-6, a regenerative amplifier based on Nd:YAG was estimated to provide high pulse energy around 3-4 kHz repetition rate with modest average power. A setup based on a Nd:YAG amplifier was implemented and is detailed in the Section 4.3.

4.2 High-Average Power Regenerative and Single-Pass Amplifier

The high average power amplifiers were based on a regenerative and a single-pass amplifier with Nd:YVO_4 laser amplifier modules. Nd:YVO_4 as amplifier material offers relatively high gain and natural birefringence. The design goal of the presented amplifier chain after frequency doubling to 532 nm was an output pulse energy of a few mJ with 50 to 100 ps duration and high average power. The implementation and results are presented in the following paragraphs.

4.2.1 Regenerative Amplifier

A 2 mm diameter Vanadate-based amplifier module was used inside the regenerative amplifier. An initial version of this amplifier stage was reported previously and provided an output energy of 0.6 mJ at 1 kHz at modest pump powers [123]. The system was followed by a single-pass Nd:YVO_4 amplifier, which produced up to 2.2 mJ pulse energy. The beam profile was cleaned through a spatial filter before frequency doubling to 532 nm wavelength with a final output of ~1 mJ pulse energy and 85 ps duration.

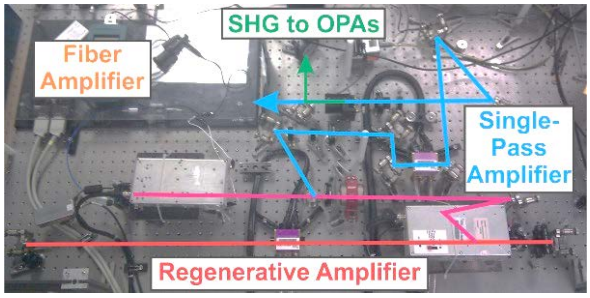

Figure 4-7: Picture of the regenerative and single-pass amplifier assembly in the laboratory.

Compared to the performance previously reported [123], the cavity of the regenerative amplifier was modified in this work and pumped at a higher power level. A picture of the high average power amplifier system is shown in Figure 4-7. The repetition rate was increased from previously 1 kHz to up to 10 kHz providing slightly higher pulse energies and more than ten times more average power. Figure 4-8 (a) shows the typical performance of the regenerative amplifier at a repetition rate of 10 kHz. An output energy of 0.79 mJ was observed corresponding to 7.9 W average power at full pump current (20 A). The beam at high pump currents exhibited an excellent Gaussian profile as shown in Figure 4-8 (b).

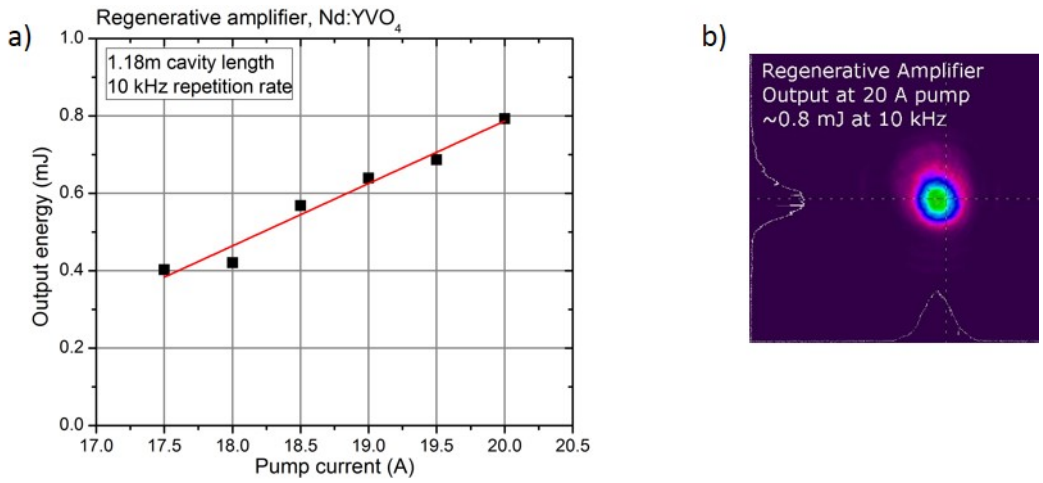

Figure 4-8: Measured output energy of the first generation regenerative amplifier operating at 10 kHz (a) and beam profile at the highest obtainable output energy (b).

The pulse energy built-up and the temporal pulse shape of the regenerative amplifier output were investigated with fast photo diodes and the recorded signals are shown in Figure 4-9. In the trace of the pulse built-up (a), one can observe the switching of the Pockels cell to trap the pulse in the cavity at $t_{in} = 70.83\ \mu s$. The pulse became visible at $t = 70.945\ \mu s$ and amplification approached saturation at $t = 70.96\ \mu s$. The pulse was kept in the cavity for a few more round trips to ensure full saturation of the amplification process and depletion of the population inversion in the used gain volume, which results in more stable output power and lower output pulse-to-pulse fluctuations. The pulse was extracted from the cavity at $t_{out} = 70.98\ \mu s$. Figure 4-9 (b) shows the pulse ejected from the regenerative amplifier. The clean main pulse can be seen, followed by another signal oscillation corresponding to the impulse response of the fast photo diode. No pre- and post-pulses were observed with the photo diode measurement, which leads to the conclusion that the pulse-to-background contrast exceeded 100:1.

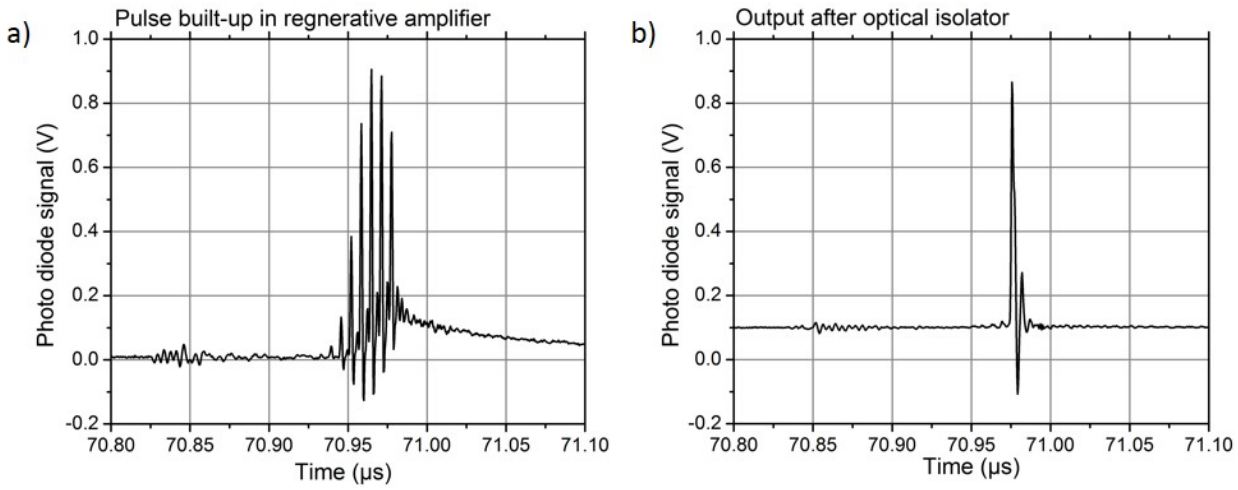

Figure 4-9: Measured pulse built-up in the regenerative amplifier (a) and output pulse (b).

The pulse duration was verified in an early experiment at a repetition rate of 1 kHz using a streak camera with sub-1-ps resolution as shown in Figure 4-10. The shape was well approximated with a Gaussian fit and the duration is measured to be 105 ps (FWHM).

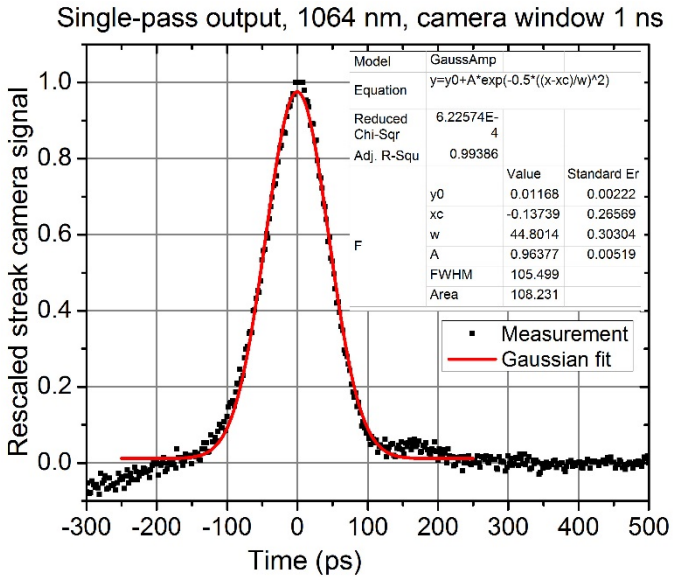

Figure 4-10: Pulse duration measurement with a sub-ps resolution stream camera of the pump beam at the fundamental wavelength of 1064 nm.

The output of the regenerative amplifier, with up to 7 W of average power, was frequency doubled using non-critically phase-matched LBO with 5 mm x 5 mm aperture, 20 mm length and heated to 148 C. A SH efficiency of up to 66% with 3.89 W and 0.39 mJ pulse energy was achieved

as shown in Figure 4-11 (a). This SH efficiency value is consistent with values reported in the literature ranging from 60 to 75% for ultrashort pulses with narrow spectrum as well as spatially and temporally Gaussian pulse shape [124]. The high efficiency and clean photo diode signal indicate a high pulse-to-background ratio as well as low ASE in the nanosecond to cw-like regime.

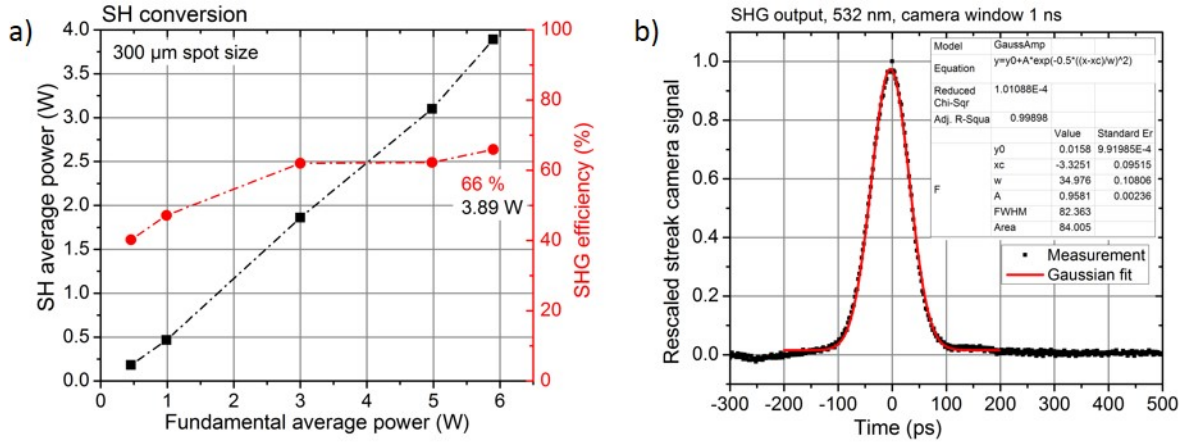

Figure 4-11: (a) Measured output power of the second harmonic generation of the regenerative amplifier output with up to 3.9 W and 66 % efficiency. (b) Measurement of the pulse duration of 82 ps with a streak camera.

The duration of the SH output pulses was also verified earlier at 1 kHz repetition rate with a sub-1-ps resolution stream camera. The duration was found to be 82 ps, as seen in Figure 4-11 (b). Following the squared root intensity dependence for pulses with Gaussian temporal shape, the 82 ps SH pulse duration corresponds to a 116 ps fundamental pulse duration, which is slightly longer than the measured 105 ps pulse duration.

4.2.2 Single-Pass Amplifier

Further power scaling of the output of the regenerative amplifier was investigated with a Vanadate-based single-pass amplifier. The module was identical to that utilized in the regenerative amplifier. The output of the regenerative amplifier (0.79 mJ at 10 kHz) presented in the previous section was used as seed for this Vanadate amplifier. A sketch is shown in Figure 4-12. Compared

to earlier investigations at 1 kHz, the routing and beam shaping to the single-pass amplifier was adapted for the regenerative amplifier output at 10 kHz.

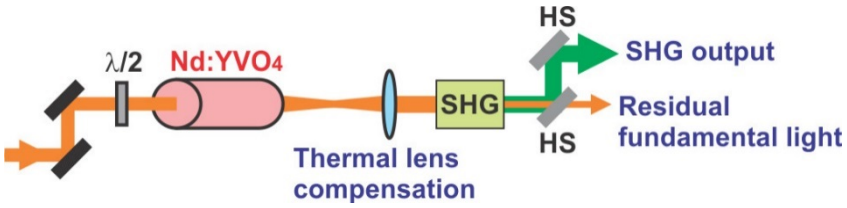

Figure 4-12: Sketch of the single-pass amplifier based on 2 mm diameter Nd:YVO_4 and the SH conversion.

The single-pass amplifier was routinely operated beyond 18 W average power corresponding to 1.8 mJ pulse energy at 10 kHz. Figure 4-13 shows the performance for up to 20 A, where a current of 24 A corresponds to a maximum of 175 W pump power. It was possible to increase the energy to beyond 2 mJ by increasing the pump current to 23 A, although this is not shown in Figure 4-13.

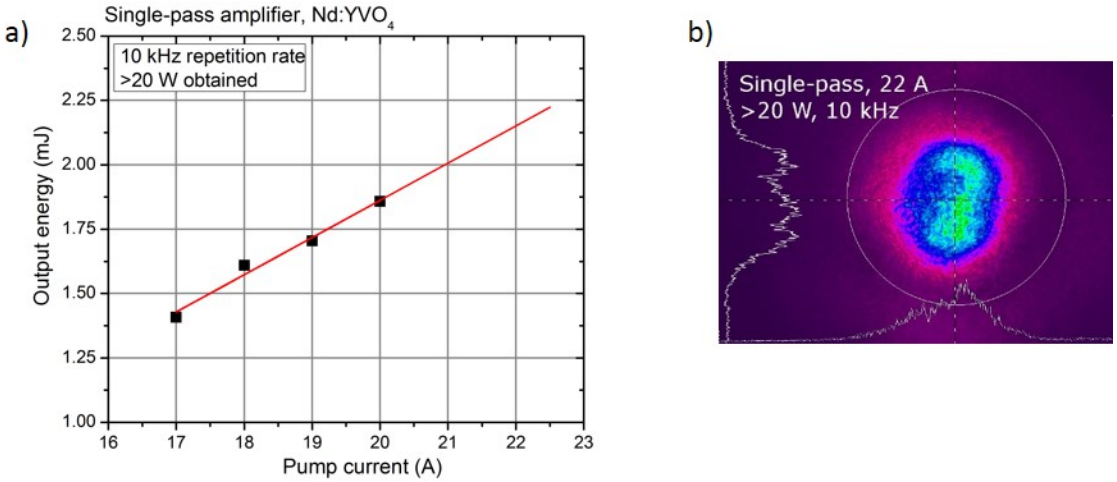

Figure 4-13: Measured output energy of the single-pass amplifier at several pump currents with linear fit extrapolating the trend to 23 A (a) and beam profile at highest output power (b).

This amplifier system was used for initial experiments for OPCPA pumping. It was found that a focused diameter of 110 µm (FWHM) was necessary to achieve significant parametric gain (>40 GW/cm²) in the OPCPA system. In this focusing geometry, the centroid position of the

focused pump beam fluctuated by >90 µm (St. Dev.). In contrast, the movement of the seed beam was estimated to be <25 µm, which was at the detection limit. As a result, the amplified signal pulses after the OPA were highly instable in amplitude and spectrum due to the fluctuating spatial overlap between seed and pump beams. The origin of the high beam pointing fluctuation was mainly found to be intrinsic to the design of the Nd:YVO_4 laser amplifier modules. For example, a cw, low-power, stable probe beam showed strong beam pointing fluctuations after passing through the used amplifier modules alone (see Appendix C). Because of the poor beam pointing performance of the presented amplifier chain, a major re-design was performed involving more robust amplifier modules, stronger opto-mechanical components and shorter optical path lengths. The design and implementation of this system is described in Section 4.3.

In a separate investigation, a set of piezoelectric-motorized mirrors were implemented after the output of the system [125], [126]. With a computer-controlled feedback loop, the beam was compensated for low frequency instabilities (limited to <30 Hz) mainly resulting from mechanical drifts, temperature variations and/or air turbulences. However, this pointing stabilization scheme was not able to fully suppress the fluctuations originating from the presented system.

4.2.3 Overall Performance and Stability

The high average power regenerative and single-pass amplifier performed at up to 2 mJ at 10 kHz repetition rate. The pulse contrast was high with >100:1 and the pulse duration was estimated with 105 ps. The corresponding peak power was 19 MW. Second harmonic generation as investigated for the regenerative amplifier (700 µJ at 10 kHz and 1064 nm) with up to 66% efficiency, 390 µJ pulse energy at 532 nm. The SH pulse duration was estimated to be ~82 ps and the corresponding peak power was 4.8 MW. The performance level of the Nd:YVO_4-based

amplifier stages was competitive to the values found in the literature [124] [127], but with higher complexity due to the synchronization to the sub-5-fs oscillator for OPCPA applications.

The obtained pulse energy and average power level were well suited to drive an OPCPA system. However, it is found that the output beam showed high beam pointing fluctuations leading to intolerably instable OPCPA output. The problem was identified to arise mainly from the utilized amplifier modules. Therefore, more robust amplifier modules were employed in another amplifier chain providing even higher pulse energies. This second amplifier system is presented in the following section.

4.3 High-Energy Regenerative and Single-Pass Amplifier

A second regenerative amplifier was implemented providing high pulse energy based on a commercial Nd:YAG amplifier module with 2 mm diameter. The output of the regenerative amplifier was further amplified by a single-pass amplifier based on an updated Nd:YVO_4 module, which was mechanically stronger built compared the previously-used modules to allow low noise amplification. This updated Nd:YVO_4 module showed highly improved performance with respect to the introduced beam pointing fluctuations (see data in APPENDIX C). The design goals of the amplifier chain were to match closely the power performance of the previous generation and to reduce the beam pointing fluctuations to a minimum in order to improve the stability for OPCPA pumping.

4.3.1 Design Changes of the Regenerative Amplifier

The regenerative amplifier was modified to decrease beam pointing and power fluctuations. The cavity length was reduced to increase the resonator stability to a total cavity length of 0.98 m (6.54 ns round trip time). The distance between the Pockels cell and the end of

the cavity was minimized to 0.83 m corresponding to 5.5 ns switching time. The center of the amplifier module was placed 27.5 cm from the end of the cavity (VBG). A LASCAD model was used to estimate the mode diameter in the regenerative amplifier and a screen shot of the LASCAD model (LAS-CAD GmbH) is shown in Figure 4-14.

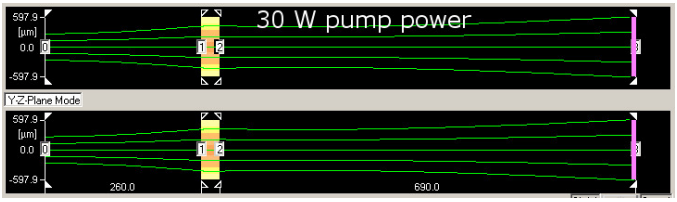

Figure 4-14: Screenshot of the LASCAD cavity model for the Nd:YAG regenerative amplifier.

Using the LASCAD built-in finite element analysis (FEA) tool and assuming a pump power of 50 W, a thermal focal length of the Nd:YAG amplifier of $f_{th} = 20.3\ cm$ was simulated. The focal length for a given pump power from the FEA simulations deviated slightly from the experimental found values. Thus, the simulated resonator stability allows only conceptually insights where the power calibration might deviate from experimental values.

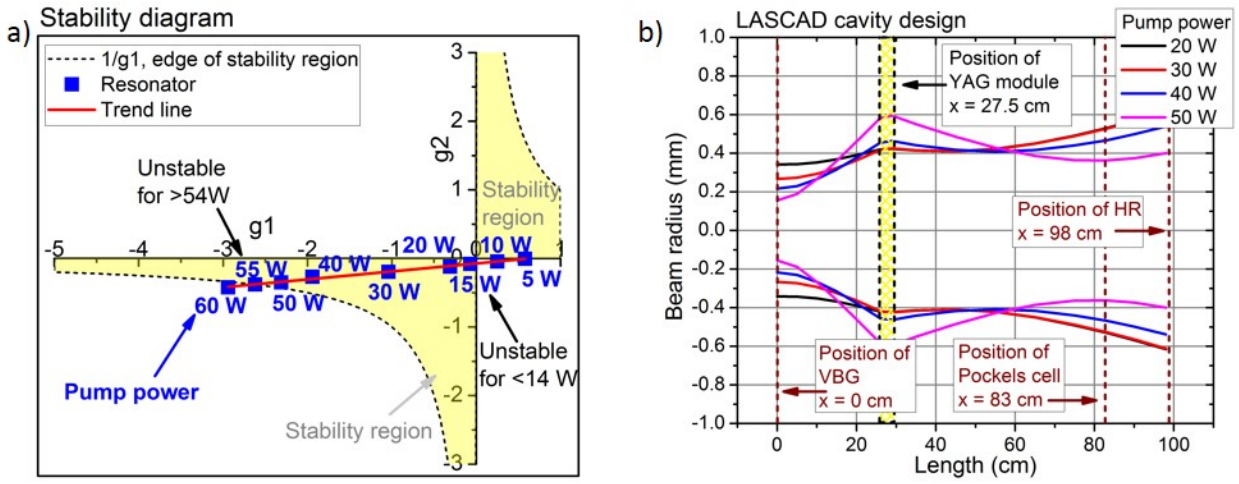

Figure 4-15: (a) Stability diagram of the LASCAD cavity design with stability curve of the resonator (red). (b) Modeled cavity mode diameter for several pump powers.

The resonator was modeled in LASCAD for several pump power levels. The stability diagram for different pump powers are shown in Figure 4-15 (a). The modeled resonator was stable

in the simulation for pump powers from 14 to 54 W, while the resonator was still stable in the experiment beyond 100 W pump power. The mode radius is plotted in Figure 4-15 (b) for several pump powers across the stability range. It can be seen, that the mode radius varied in the Nd:YAG crystal positioned at 26 cm from 0.42 at 0.6 mm, in the Pockels cell positioned at 83 cm from 0.53 to 0.36 mm, at the VBG positioned at 0 cm from 0.34 to 0.15 mm and at the HR mirror positioned at 98 cm from 0.62 to 0.40 mm. The aperture within the cavity was limited physically by the Nd:YAG rod and the BBO Pockels cell both with 2 mm diameter. With a beam diameter ($1/e^2$) of 0.84 to 1.2 mm in the YAG module and 1.24 and 0.80 mm in the Pockels cell, the fundamental mode was not clipped. Higher order modes typically have a larger beam radius and would experience clipping in the resonator, thus, the resonator can be seen as mainly supporting the TEM_{00} (or LP_{01}) mode.

4.3.2 Regenerative Amplifier

Nd:YAG has a longer upper state lifetime of 230 µs compared to Nd:YVO_4, which corresponds to a frequency of 4.3 kHz. As a consequence, the operational repetition rate of the regenerative amplifier was reduced from 10 kHz to achieve sufficient small signal gain (see Section 4.1.4). A picture of the setup is shown in Figure 4-16 displaying the boxed regenerative amplifier, the linear cavity, the injection/ejection optics as well as the electronics for the Pockels cell and the pulse picker.

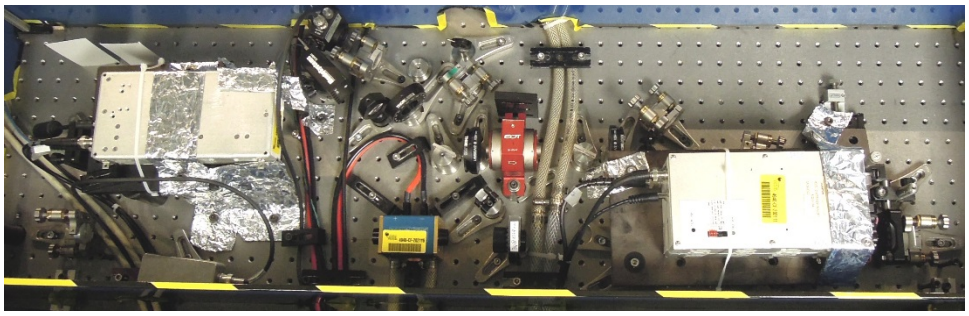

Figure 4-16: Picture of the regenerative amplifier based on Nd:YAG with 2 mm diameter.

Figure 4-17 (a) compares the output pulse energy of the regenerative amplifier based on Nd:YAG with the previously presented regenerative amplifier based on Nd:YVO_4 (shown in Section 4.2.1). The highest obtained pulse energy from the Nd:YAG regenerative amplifier was 1.96 mJ at 1 kHz. The drop in pulse energy for higher repetition rates can be attributed to the decreased gain, decreased saturation energy, as well as the increased loss due to the increased number of round trips (70 % VBG reflectivity). A repetition rate of 3 kHz was chosen for operation as it provides the best compromise between high average power and high pulse energy (1.44 mJ). The beam profile was recorded at this repetition rate and is shown in Figure 4-17 (b). The beam profile distortions, namely the two minor side peaks as well as the slightly elliptical shape, are attributed to reflections arising from the used thin-film polarizer and half wave plate.

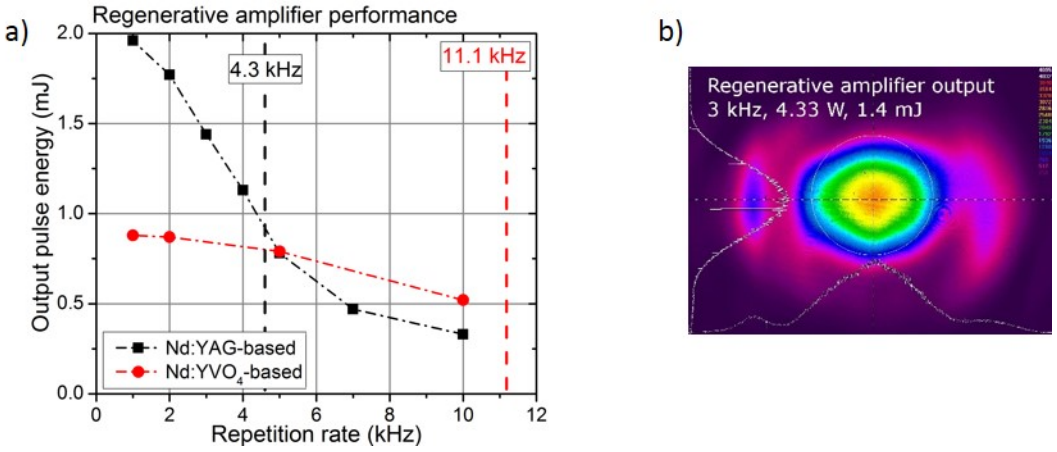

Figure 4-17: (a) Performance of the Nd:YAG regenerative amplifier (black) at different repetition rates compared to the Nd:YVO_4 (red). (b) Measured beam profile at 3 kHz repetition rate.

The short-term pulse stability of the regenerative amplifier was investigated. The output pulse was recorded with a fast photo diode and statistics of the pulse amplitude taken over several seconds. Table 4-1 shows the resulting pulse stability (RMS) for several reference timings, which correspond to the time when the Pockels cell was switched and the pulse extracted from the cavity. The calculated number of round trips is listed as well as the measured average power and the corresponding pulse energy at 3 kHz repetition rate. It can be seen that the highest pulse energy was achieved after 35 round trips with a pulse stability of 1.8%. For 34 round trips, the amplification was not saturated and early ejection of the pulse led to high pulse fluctuations of 19%. In addition, onset of bifurcation occurred, where not all pulses are effectively amplified [128]. This regime was avoided by increasing the number of round trips and stable output pulses were obtained for 35 and more round trips. Since output stability is important for the OPCPA pumping application, a number of round trips larger than 34 had to be chosen. On the other hand, a number of round trips close to saturation could have been chosen to obtain high energy since the pulse energy drops after saturation due to the 70% VBG-reflectivity. Thus, 36 round trips in the regenerative amplifier were seen as a good compromise between high pulse energy and pulse stability.

Table 4-1: Measured short term pulse stability of the regenerative amplifier output for several reference timings.

Reference timing [µs]	**Number of round trips**	**Average power [W]**	**Pulse energy [mJ]**	**Stability [RMS]**
70.25050	34	3.90	1.30	19%
70.25775	35	4.32	1.44	1.8%
70.26500	**36**	**4.04**	**1.35**	**1.7%**
70.27150	37	3.62	1.21	1.7%
70.27900	38	3.20	1.1	2.1%
70.28600	39	2.83	0.94	2.2%

The long-term power stability of the regenerative amplifier was investigated and is shown in Figure 4-18 (a). The measured mean was 4.68 W with a standard deviation of 0.20 W or 4.3% (RMS) over 45 minutes. The mean is plotted in Figure 4-18 (a) as red line and one can observe an increasing trend of the output power found after ~20 min. In addition, it was found that the number of round trips for saturation (35 round trips in Table 4-1) moved during the operation of the system potentially due to warm-up effects. The statistics over the last minute indicated a RMS noise of 3.1%. In absolute numbers, the mean of 1 minute increased from ~4.5 W to ~4.9 W over 45 minutes. This increase in average power was seen experimentally and was attributed to slight thermal drifts.

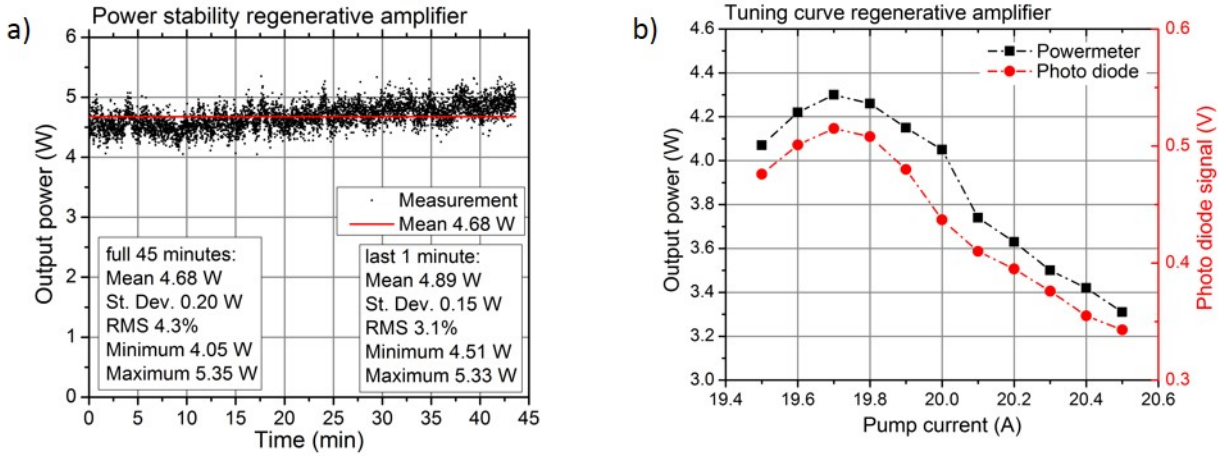

Figure 4-18: Measured long-term power stability of the regenerative amplifier output (a) and tuning characteristic of the regenerative amplifier (b).

A solution to stabilize this drift was investigated based on implementation of an active feedback loop. In a first version, a fast photo diode monitored the moving average and an algorithm adapted pumped power of the fiber pre-amplifier to obtain stable output from the regenerative amplifier. This method of feedback followed the approximately linear relationship between the fiber pre-amplifier pump power and its output (see Figure 5-12). In a second version, the photo diode signal was used to provide feedback and change adaptively the pump current of Nd:YAG amplifier module. Figure 4-18 (b) shows the feedback characteristics for this case: If the pump

current was decreased from 20 A to 19.8 A, the output power increased from 3.8 to 4.2 W. On the other hand, if the pump current was increased to 20.2 A, the regenerative amplifier output decreased to 3.4 W. The relationship between change in pump current and change of output power was highly depending on the current operation condition (i.e. warm-up time, output power, pump level, etc.). Since the sign, trend and magnitude of the change was not predictable only an adaptively controlled feedback-loop was able to suppress the long-term power drift. In summary, both feedback techniques allowed to successfully stabilize the long-term drift of the regenerative amplifier output resulting in a RMS stability of <4%. An additional solution to stabilize for the long-term drift would be to utilize a water-cooled breadboard under the footprint of the amplifier (1.2 m x 0.3 m), which was not attempted. Another method to stabilize the output power is to adaptively vary the output power with an exeternal closed-loop light-valve [129]. The disadvantage of the latter method is the reduced output power.

The beam pointing fluctuations of the regenerative amplifier was investigated and estimated to be 27 µrad (Std. Dev.) with the Nd:YAG amplifier module and the shortened cavity. In comparison, the Nd:YAG module by itself introduced in a measurement a beam pointing fluctuation of >100 µrad (see data in Appendix C). The large difference between these values was the result of the resonator geometry, which determines the modal behavior of the system and effectively reduces the output beam pointing fluctuations.

4.3.3 Single-Pass Amplifier

The updated (low-noise) Vanadate amplifier module was investigated in a single-pass amplifier configuration following the Nd:YAG-based regenerative amplifier. The typical amplifier characteristics at 3 and 5 kHz repetition rate are shown in Figure 4-19 (a). The highest obtained average power was ~12 W at 3 kHz and 11.4 W at 5 kHz. In the following results, the repetition

rate was 3 kHz to obtain higher pulse energy. The system provided routinely 3.2 mJ pulse energy at 3 kHz repetition rate (9.7 W average power). Figure 4-19 (b) shows a beam profile measured at 3 kHz with Gaussian distribution in the center and a surrounding plateau.

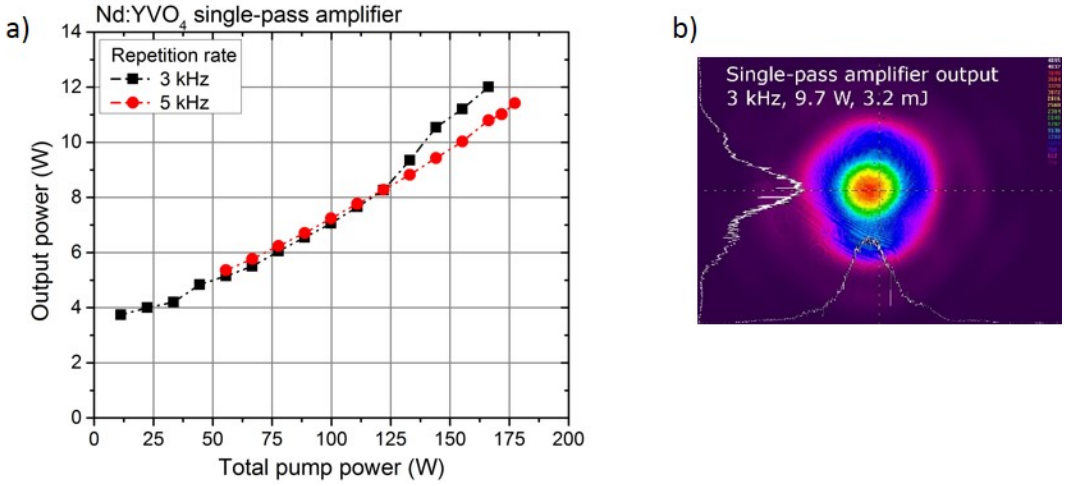

Figure 4-19: Performance of the single-pass amplifier (a) and beam profile at the highest pulse energy at 3 kHz (b).

The temporal shape of the output pulse was recorded with an autocorrelator and a fast photo diode. The autocorrelation had Gaussian shape and corresponded to a deconvoluted pulse duration of 171 to 211 ps as shown in Figure 4-20 (a). The increase in duration compared to Section 4.2 was attributed to the increased number of round trips in the regenerative amplifier (40 compared to 20) and the corresponding VBG-based narrowing effect. The temporal output trace was measured with the fast photo diode is shown in Figure 4-20 (b). The main pulse can be clearly identified with minor post-pulses of ~3% amplitude of the main pulse. The origin of the post-pulse was mainly attributed to depolarization occurring in the highly-pumped Nd:YAG crystals (see Section 3.1.3 and Appendix C). A compensation scheme was not implemented here in order to avoid increasing the complexity of the regenerative amplifier cavity, which could compromise reliability or stability of the overall system.

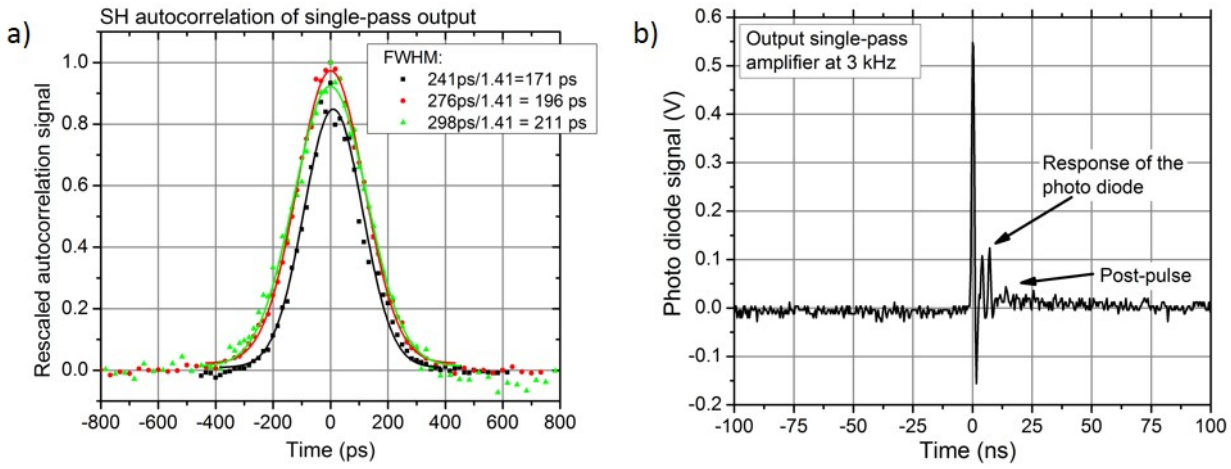

Figure 4-20: (a) Intensity autocorrelation of the single-pass output during different investigations. (b) Recorded output with a fast photo diode.

The output pulse of the single-pass amplifier was frequency-doubled using the previously mentioned (see Section 4.2.2) LBO crystal and the average power output is shown in Figure 4-12. The SH efficiency was 60% corresponding to a conversion of a pulse energy of 3.2 mJ at 1064 nm wavelength to 1.9 mJ at 532 nm. The average power at 3 kHz was 5.8 W. The LBO crystal was followed by two harmonic separators, which removed the power at the fundamental wavelength. The residual fundamental light (3.05 W) was captured in a beam dump. The SH beam of this stage was further directed through a light valve to the OPA setup as described in Section 5.5 for OPCPA pumping experiments.

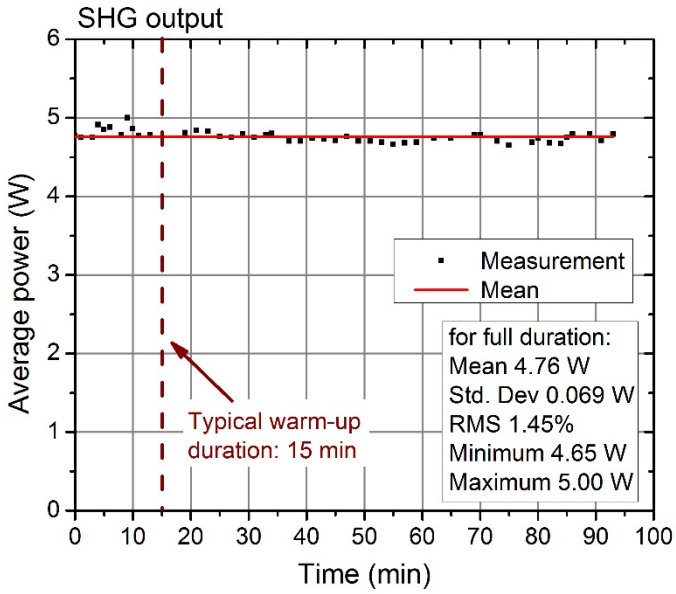

Figure 4-21: Long-term power measurement of the SHG output after harmonic separators.

The long-term measurement, shown in Figure 4-21, verified the power stability of the SHG output measured after the harmonic separators and the light valve. Over ~100 minutes the power stayed approximately constant around 4.76 W. Time was given to the system to warm up during the measurement, which mainly caused the slight noise during the first 20 minutes of the measurement in shown Figure 4-21. The approximate RMS power stability was measured to be 1.45% estimated with a thermal power meter and a recording interval of 1-2 minutes.

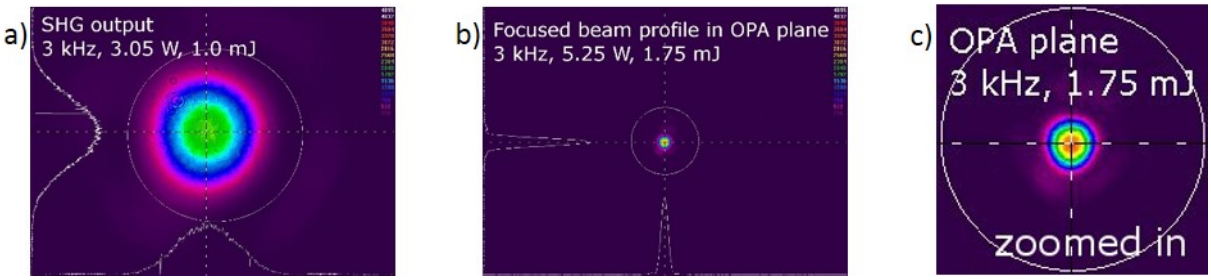

Figure 4-22: Beam profiles of the second harmonic beam after collimation (a) and focused at the OPA plane (b). The beam profile in (c) is zoomed in due to the small focus size.

Beam profiles of the second harmonic output are shown in Figure 4-22. The profile (c) corresponds to the collimated beam after harmonic separators and the light valve. An excellent Gaussian beam profile can be seen. The profiles (b) and (c) correspond to the focused beam ($f =$

$50\ cm$) at the plane of the OPAs conforming an excellent Gaussian shape and used in OPCPA pumping experiments shown in Section 5.5.1.

4.3.4 Performance Summary and Comparison

The presented combination of regenerative and single-pass amplifier routinely delivered 3.2 mJ pulse energy at 3 kHz repetition rate and 1064 nm wavelength. The pulse contrast was slightly compromised with a minor post-pulse attributed to depolarization effects in the Nd:YAG amplifier. The pulse duration after the single-pass amplifier was measured to be 171 ps, which is longer compared to the first Nd:YVO_4-based regenerative amplifier system. The longer duration resulted from the increase in number of round trips in the regenerative amplifier and the VBG-based narrowing effect. The corresponding peak power was 18.7 MW. The performance level of only the Nd:YAG-based regenerative amplifier stage was competitive to the values found in the literature [130] [131], but it also provides synchronization to the sub-5-fs oscillator for OPCPA pumping.

The output of the regenerative amplifier was frequency-doubled to 532 nm with up to 60% efficiency. The efficiency was slightly lower, compared to the 66% conversion efficiency in first system. This was attributed to the post-pulse with lower SH efficiencies. Up to 1.9 mJ pulse energy was measured after SHG. Assuming a SH duration of $(171/\sqrt{2} =)$ 121 ps the corresponding peak power was 7.9 MW. It was found that the beam pointing stability was greatly improved relative to the first system and were low enough to enable stable OPA output as shown later in Section 5.5. Thus, the described amplifier system represents a high-quality pump laser, which was utilized for the demanding application of OPCPA pumping.

4.4 Power-Scaling with DPSSL Technology

Further scaling of the energy and average power of the pump beam is described in the following subsections. First, general energy limitations arising from the B-integral and the optical damage threshold are investigated. This is followed by a subsection introducing the concepts of thermal lens and depolarization compensation. Based on these considerations, two booster amplifier stages were designed and implemented as presented in Subsection 4.4.3 and 4.4.4 [45]. The system schematic is shown in Figure 4-23, with the final amplifier seeded by the output of the regenerative and single-pass amplifier presented in the Section 4.3.

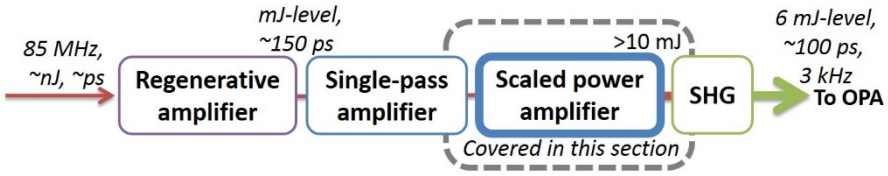

Figure 4-23: Schematic of the designed MOPA stage including the scaled power amplifiers with OPCPA pumping as target application.

4.4.1 Damage Threshold and B-Integral Limitations

Two parameters play a key role for direct energy scaling. The first consideration is the optical damage threshold of typical AR coatings. Typical manufacturer specification is a threshold of 20 J/cm² for a 10 ns pulse corresponding to an intensity of 2 GW/cm². It has been empirically found that the damage threshold scales in terms of pulse duration and wavelength by a square root scaling law [132]. If the anticipated pulse duration is 100 times shorter, the damage threshold fluence reduces by the squared root of 100 or a factor 10. Similarly if the center wavelengths is divided by 2 (i.e. frequency-doubling), the damage threshold reduces by the squared root of 2. Table 4-2 scales the threshold of 20 J/cm² for 10 ns (common value by manufactures) to several pulse durations. Table 4-2 illustrates the scaling law based on 20 J/cm² for 10 ns with several

shorter pulse durations and a wavelength of 1064 and 532 nm. The Damage intensity is calculated as well.

Table 4-2: Typical optical damage threshold according to the squared root scaling law [132] assuming 20 J/cm² for 10 ns pulses (common value by manufactures).

Pulse duration	Wavelength [nm]	Damage threshold fluence [J/cm²]	Damage threshold intensity [GW/cm²]
10 ns	1064	20	2
1 ns	1064	6.3	6.3
100 ps	**1064**	**2**	**20**
10 ps	1064	0.63	63
10 ns	532	14.1	1.41
100 ps	532	1.41	14.1

This discussion about the operational intensity assumes an amplifier line based on ~100 ps pulses at 1064 nm. If the beam profile is not perfectly Gaussian or flattop, strong intensity modulations can occur potentially locally exceeding the damage threshold. An operating intensity of several times lower than the damage threshold should be utilized. Based on the calculations and the literature values, the damage threshold intensity was estimated to be ~20 GW/cm², thus an intensity of 4 GW/cm² was regarded as safe operational intensity. Large aperture systems have been presented operating with 1 cm rod diameter, 70 ps, [73] and 250 mJ pulse energy resulting in a peak intensity of 4.5 GW/cm². Another system has been presented [133] operating at 40 mJ pulse energy, 48 ps pulse duration and 6.6 GW/cm² intensity with a 4 mm diameter rod. Thus, an increase of the operational intensity from 4 to 6 or 8 GW/cm² may be feasible assuming a good Gaussian or flattop beam profile can be obtained reliably from the amplifiers. Table 4-3 summarizes the damage threshold energy for 100 ps pulses if the full rod diameter is used or only 75% of the diameter.

Table 4-3: Pulse energy corresponding to a damage threshold fluence of 0.5 J/cm² for 100 ps or 4 GW/cm².

Rod diameter [mm]	**1**	**2**	**3**	**4**	**5**	**6**	**6.35**	**10**
Operational energy with full rod diameter [mJ]	3	12.5	28	50	78	113	125	310
Operational energy with 75% fill factor [mJ]	2.3	9.4	21	37	59	85	95	235

The second parameter, associated with pulse energy scaling, is the accumulated B-integral. It is given by the equation [30]

$$\mathrm{B} = \frac{2\pi}{\lambda} \int_0^L n_2(x) I(x)\, dx\,. \tag{58}$$

The B-integral is a measure of the nonlinear phase accumulated during propagation through a medium. In ultrashort pulse amplifiers, this B-integral is a critical value and is usually engineered to be below 1, such that the accumulated nonlinearities are negligible. If the B-integral is $\sim\pi$ severe beam distortions can be induced and/or self-phase modulation (SPM) leading to spectral broadening causing to unwanted spectral components. In addition, self-focusing can lead to surface and bulk damage within the amplifier. Table 4-4 shows the nonlinear refractive index of Nd:YAG and Nd:YVO_4. It can be seen that the nonlinear refractive index value for Nd:YVO_4 is ~15 times larger than for Nd:YAG.

Table 4-4: Nonlinear refractive index of Nd:YAG and Nd:YVO_4 at 1064 nm wavelength.

	Nonlinear refractive index n_2	**Reference**
Nd:YAG	$6.5 \cdot 10^{-20}\ m^2/W$	[134] [135]
Nd:YVO_4	$1 \cdot 10^{-18}\ m^2/W$	[136]

The B-integral expression from Equation (58) was adapted for exponential amplification with constant n_2, initial intensity I_0, gain per distance g and length of the amplifier module L:

$$\mathrm{B} = \frac{2\pi\, n_2 I_0}{\lambda} \int_0^L \exp(g\, x)\, dx = \frac{2\pi\, n_2\, E_0}{\lambda\, \tau\, A\, g} [\exp(g\, L) - 1]\,. \tag{59}$$

Examples are given in Table 4-5 for high gain amplifiers in single- or double-pass geometry. The output energy was set to the operational energy for each rod diameter, the length kept at either 5 or 10 cm and the input energy chosen so that the B integral of 1.5 at maximum. In order to reach the intended operational energy, high gain amplifier modules (gain of >4) are required. For rods of large aperture and length, such modules are usually either quasi-cw diode-pumped or flashlamp-pumped. The latter is discussed in an amplifier scheme in Section 4.5.

Table 4-5: B-integral estimates for high gain (>4) amplifier modules based on Nd:YAG.

Rod diameter [mm]	**1**	**2**	**3**	**5**	**6.35**	**10**
Assumed input energy E_{in} [mJ]	0.5	1	0.5	2	3	10
Assumed gain	4.6	9.4	42	30	32	24
Calculated output energy E_{out} [mJ]	2.3	9.4	21	59	95	235
Operational energy with 75% fill factor [mJ]	2.3	9.4	21	59	95	235
Propagation length [cm]	5	5	10	10	10	10
Estimated B-integral	1.21	0.96	1.25	1.38	1.35	1.45

The situation changes if low gain modules are used shown in Table 4-6. The decreased gain and increased length of the modules lead to higher intensities across the gain medium. In order to keep the B-integral around 1.5, the obtainable output energy is significantly reduced to well below the potential operational energy: for example, for a 5 mm diameter rod with a gain of 2.0, the obtainable output energy is 26 mJ instead of the 59 mJ associated with a gain of 30.

Table 4-6: B-integral estimates for low gain of 2-4 per amplifier module based on Nd:YAG.

Rod diameter [mm]	**1**	**1**	**2**	**2**	**3**	**5**	**6.35**	**10**
Assumed input energy E_{in} [mJ]	0.9	0.35	3	1.4	4	13	14	25
Assumed gain	2.3	4	2.5	4	2.5	2.0	2.0	2.0
Calculated output energy E_{out} [mJ]	2.3	1.4	7.5	5.6	10	26	28	50
Operational energy with 75% fill factor [mJ]	2.3	2.3	9.4	9.4	21	59	95	235
Propagation length [cm]	5	10	5	10	10	10	15	20
Estimated B-integral	1.52	1.55	1.26	1.55	1.49	1.54	1.54	1.48

For Nd:YVO_4, shown in Table 4-7, the obtainable pulse energy decreases further due to the ~15 times larger value of n_2. Table 4-6 shows exemplary calculations keeping the gain at 4, length of module with 3 cm and the B-integral around 1.5. For example, the obtainable output energy from a 5 mm diameter, Nd:YVO_4 module (7.2 mJ) is ~3.5 times smaller than for a comparable Nd:YAG module (26 mJ).

Table 4-7: B-integral estimates for low gain of 4 per amplifier module based on Nd:YVO_4.

Rod diameter [mm]	**1**	**2**	**3**	**4**	**5**
Assumed input energy E_{in} [mJ]	0.07	0.3	0.65	1.1	1.8
Assumed gain	4	4	4	4	4
Calculated output energy E_{out} [mJ]	0.28	1.2	2.6	4.4	7.2
Operational energy with 75% fill factor [mJ]	2.3	9.4	21	37	59
Propagation length [cm]	3	3	3	3	3
Estimated B-integral	1.43	1.45	1.48	1.41	1.47

In summary, the B-integral condition ($B < \pi$) limits the energy scaling based on diode-pumped, solid-state amplifiers with Nd:YAG or Nd:YVO_4 and 100 ps pulses. For example, the scaling limit seems to be reached with 4 mm diameter amplifiers and 40 mJ pulse energy. The implementation of energy and power scaling with diode-pump amplifiers are presented in the

following sections and the energy scaling with flashlamp-pumped amplifiers is covered in Section 4.5.

4.4.2 Thermal Lens and Depolarization Compensation

Thermal lensing is induced by a refractive index gradient due to the pump absorption in a medium. The topic is introduced and discussed in detail in Section 3.1.2, along with a compensation scheme. In addition, diode-pumped, solid-state, rod amplifiers show depolarization behavior as described in Section 3.1.3. The thermal lens and the depolarization compensations schemes can be combined and several laser systems have been successfully demonstrated providing high energy and high average power, nanosecond pulses from DPSS amplifiers (for example in [97]). In the following, a booster amplifier stage is designed and implemented using negative lenses. This is expected to offer comparable performance to another compensation scheme based on only positive lenses [137], which is not implemented due to the larger complexity (more optical components).

A ray tracing code for a booster amplifier stage with twin amplifier modules was developed and an example trace is displayed in Figure 4-24. The thermal lens compensation scheme including a negative lens in front of the first amplifier and an additional negative lens after the second amplifier. The depolarization compensation scheme was based on a 4-f imaging configuration, the two identical laser amplifiers and a 90 degree Quartz rotator (not shown). This 1:1 imaging system imaged the rear principle plane of the first amplifier onto the front principle plane of the second amplifier. Figure 4-24 shows the ray tracing model of a configuration optimized for a thermal lens of f = 70 cm. The dimensions of thermal lens, amplifier modules and optical interfaces were chosen to match a booster configuration with an amplifier aperture of several mm diameter (6-10 mm); however this analysis is directly applicable to smaller aperture amplifiers (3-4 mm). It can be seen

from the ray tracing that a set of parallel rays incident from the left was first defocused by the negative lens, was re-collimated by the thermal lens, passed through the 1:1 telescope (4f imaging scheme), focused by the thermal lens and re-collimated. Thus, the output beam of the ray tracing model showed a perfectly collimated beam.

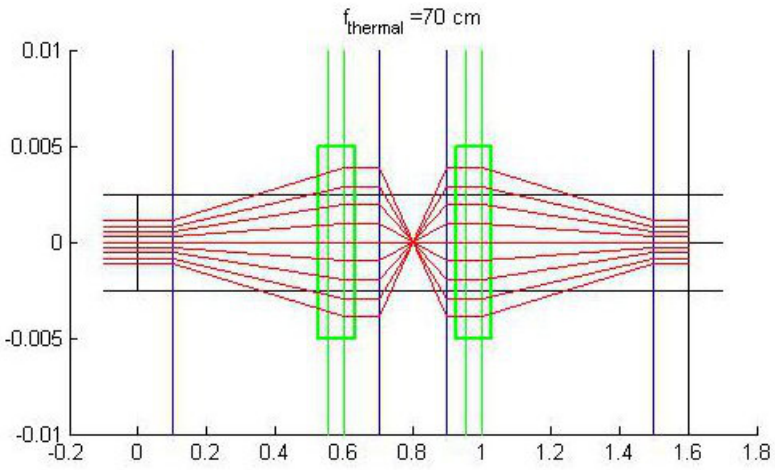

Figure 4-24: Ray tracing model of an optical system incorporating thermal lens and depolarization compensation scheme optimized for a thermal lens of f = 70 cm.

This scheme is optimized only around a working point defined by a certain pump power level since the thermal lens is depending on the heat load in the amplifier (see also Appendix C for experimental data). Figure 4-25 shows ray tracing scheme for the configuration implemented for a thermal lens of f = 70 cm but with a weaker (a) or stronger (b) thermal lensing effect. In the case of under-compensation (a), the output beam was diverging and in the case of over-compensation (b), the output beam was converging. The latter converging beam can potentially damage following optical elements.

The ray tracing model conceptually illustrates the underlying principle of the compensation scheme and was used to estimate beam sizes and distances for a given set of optics. The model only accounts for compensation with an ideal thermal lens within the paraxial approximation. Higher order aberrations were not considered and will ultimately limit the experimental

performance. It is shown in Section 3.1.2 that the thermal lens compensation scheme works best for rays closer to the optical axis and rays further away from the optical axis slightly diverge in this compensation scheme. Therefore, an experimental challenge exists in keeping the fill-factor as high as possible while obtaining a well-collimated Gaussian output beam.

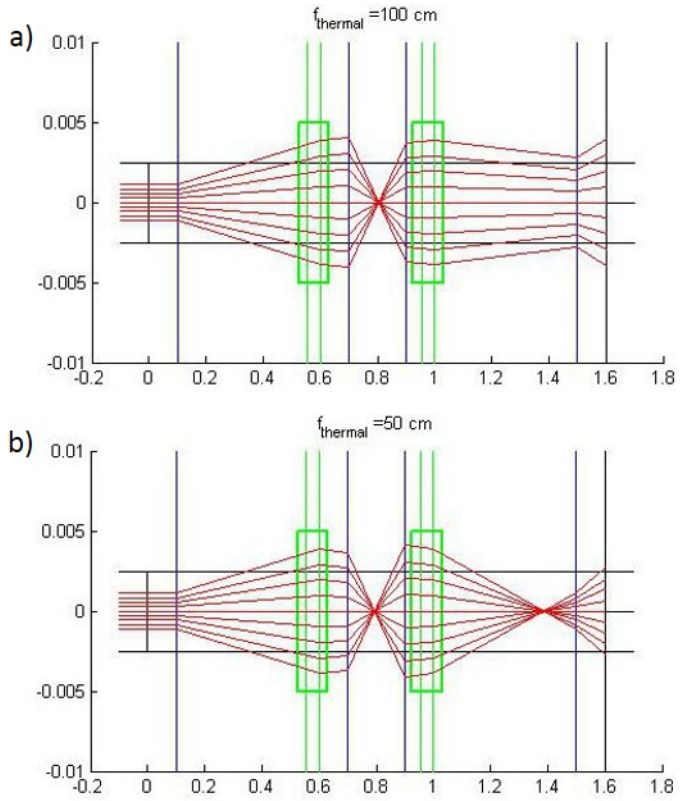

Figure 4-25: Ray-tracing model with under-compensated case due to a weaker thermal lens (a) and over-compensated case due to a stronger thermal lens (b).

Additional loss can occur due to the imperfect compensation of the depolarization behavior. Theoretically, the compensation scheme can perfectly cancel the depolarization effect but experimental systems typically exhibit a few percent depolarization loss (see Section 3.1.3).

4.4.3 First Power Booster Stage

A booster amplifier stage was implemented after the output of the high energy regenerative and single-pass amplifier system presented in 4.3. The line was designed following the guidelines

of the Section 3.1 with the compensation scheme described in the previous subsection. A set of twin amplifier modules was employed based on 3 mm diameter, 8.3 cm length, Nd:YAG, curved rod ends (0.5MCC) and with a maximum pump power of 300 W at 808 nm wavelength (see also Appendix C). The design of the amplifier stage is shown in Figure 4-26 and consisted of the two amplifier modules and compensation optics. In addition, the stage was double-passed to increase the obtainable output further, where pulse injection and ejection were based on polarization rotation.

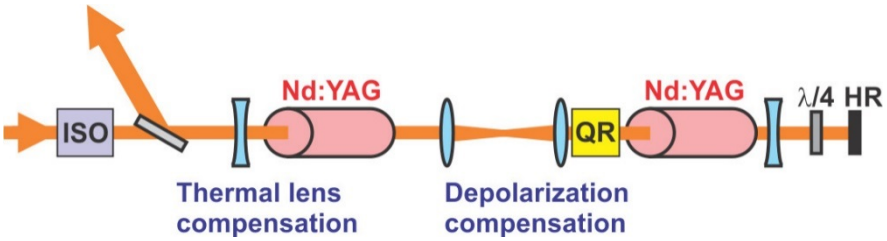

Figure 4-26: Sketch of double-pass booster amplifier stage based on twin amplifier modules with 3 mm rod diameter.

Initial investigations were conducted with a cw 0.1 W probe beam to avoid high peak power during the initial implementation. The proper implementation of the thermal lens and depolarization scheme was investigated in detail to allow highest extraction efficiency of the two booster stages. The first amplifier module provided an amplification factor (gain) of 1.81 (i.e. 81% power increase) with 0.123 W input and the second module another gain of 2.1. The single-pass gain of the total stage was accordingly 3.78 including potential optical losses due to the thermal lens and depolarization compensation optics. The beam pointing stability of the single-pass amplifier with cw probe beam was measured to be 102 µrad (Std. Dev.). Double-passing the amplifier stages led to a total gain of 11 to 13 corresponding to 1.3-1.6 W output depending on the negative lenses chosen for the thermal lens compensation. A picture of the amplifier stage is shown in Figure 4-27 (a).

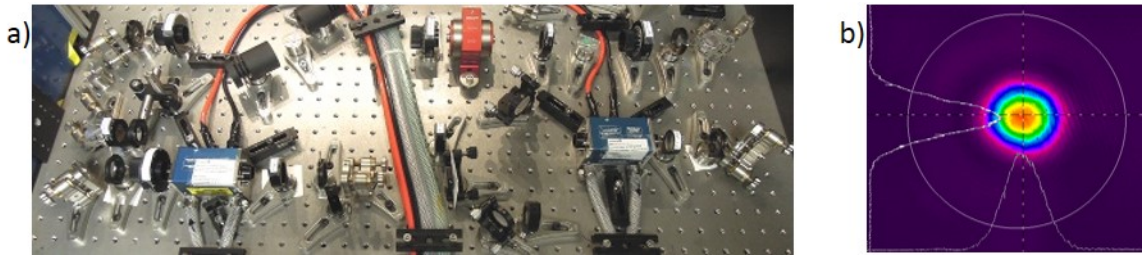

Figure 4-27: (a) Picture of the double-pass booster stage based on twin amplifier modules with 3 mm diameter. (b) Beam profile obtained of the double-pass at low power seeded with the picosecond beam at 3 kHz.

The booster stage was seeded by the output of the regenerative and single-pass amplifier presented in Section 4.3 at 3 kHz repetition rate, 1064 nm wavelength, 150-200 ps pulse duration as well as a beam input diameter of ~1.2 mm ($\pm 0.2mm$). Figure 4-27 (b) shows a beam profile obtained with the picosecond seed at low power after the booster stage was double-passed using a pair of f = -30 cm lenses for the thermal lens compensation. An excellent Gaussian beam profile was obtained in this configuration.

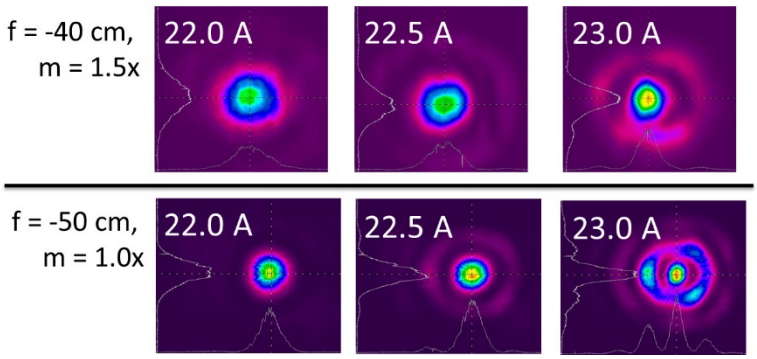

Figure 4-28: Characteristic beam profiles obtained during the gain optimization procedure.

During the investigations, it was important to maintain the beam profile to be uniform Gaussian and to ensure the ability to focus the output. Characteristic beam profiles are shown in Figure 4-28. It can be seen that the obtained beam profiles initially operated with 22 A pump current had good Gaussian shape following the input beam quality. The onset of diffraction occurred if the pump power was increased (beyond 23 A pump current). Following the findings from Section 3.1.2 and 4.4.2 and the concept shown in Figure 4-25, the onset of diffraction was

attributed to hard aperture clipping effects of the non-collimated portion of the beam in the double-passed stage. The severe beam distortions resulted in a non-negligible amount of energy outside of the Gaussian center, which degraded the peak intensity at focus. These findings highlight that the output beam profile of the booster stage was highly dependent on the thermal lens and needs to be monitored. A pump current of 22 A supported good Gaussian beam profiles with either pair of the f = -40 cm or the f = -50 cm lenses.

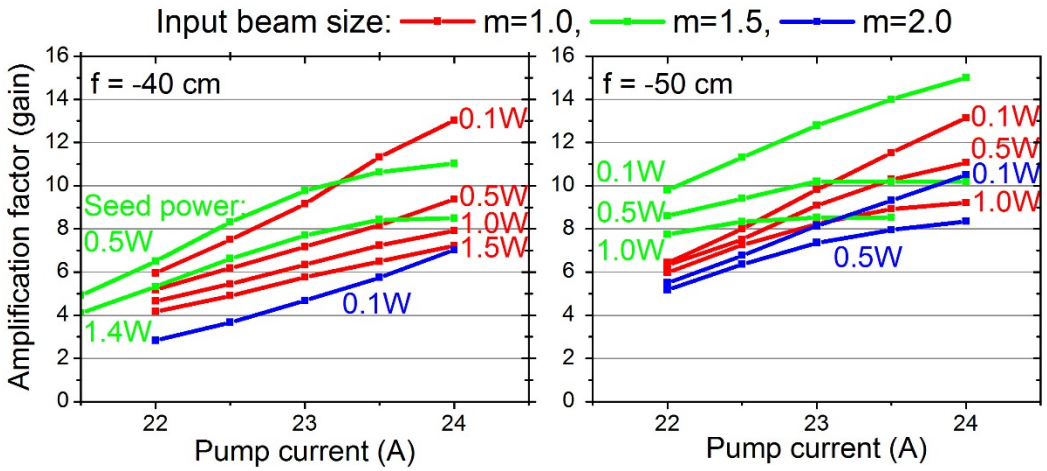

Figure 4-29: Obtained amplification factors of the double-passed booster stage for two negative lens combinations, several input beam size magnifications and power levels.

The obtainable gain from the double-passed stage was optimized changing two parameters as shown in Figure 4-29: first, the input beam size was varied with a telescope in front of the stage with magnification factor m. Second, the strength of the negative lenses was changed for the thermal lens compensation. The fill factor and the thermal lens compensation scheme were optimized using this procedure to experimentally obtain the highest gain from the stage. Several configuration were implemented with lenses of focal lengths from -5 to -50 cm. Figure 4-29 shows the results for a pair of negative lenses with f = -40 cm or f = -50 cm, which resulted in the highest gain. A magnification of m = 1.5 led in both cases to the highest obtainable gain, while the negative lenses of f = -50 cm resulted to the maximum gain of 15. It can be seen from Figure 4-29 that the

gain decreased due to saturation when the seed power was increased. The high gain of 15 led to the conclusion that fill factors in the twin amplifiers were highest and losses were lowest in this configuration. However, the corresponding beam profile, displayed in Figure 4-28, showed the effects of diffraction with severe impact on the beam profile and potentially on the ability to focus the beam and peak intensity degradation. Thus, a trade-off was made experimentally between the good Gaussian beam profiles at 22 A pump current and the high gain at 23 A.

The optimum thermal lensing compensation configuration with f = -40 or -50 cm agreed well with the findings of Section 3.1.2. The thermal lensing for the 3 mm diameter amplifier module was estimated to be in the range from 17 to 25 cm depending on the absorbed pump power as shown previously in Figure 3-3 (a). As presented in Figure 3-6, a thermal lens of 17-25 cm with curved rod ends (0.5MCC) was best compensated with a negative lens of -40 or -50 cm. This range agreed well with the findings of Figure 4-29.

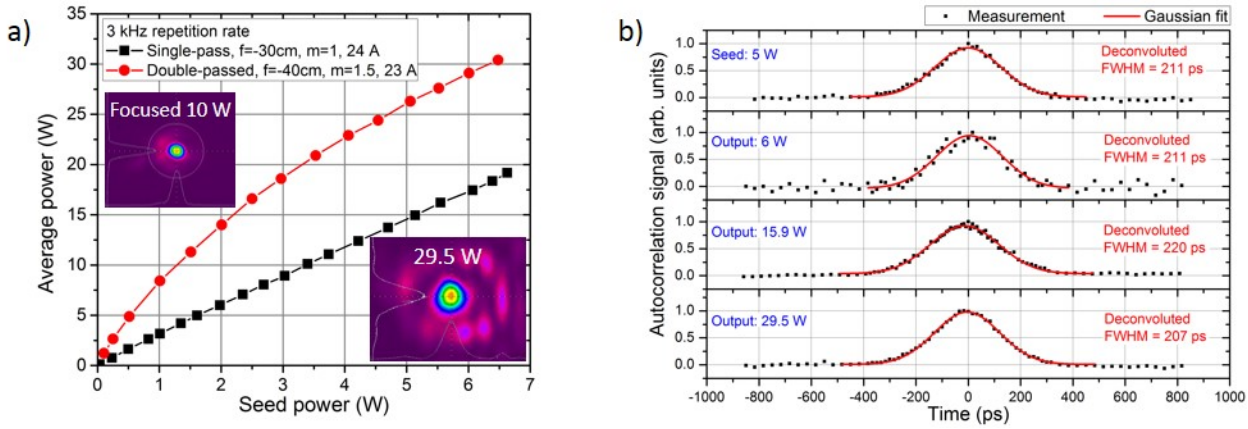

Figure 4-30: Amplification characteristics of the booster configuration (a) and intensity autocorrelation measurement of the double-passed output (b).

The booster amplifier stage was further operated under high power conditions with a seed power of up to 6.5 W. The amplification characteristics were recorded and are shown in Figure 4-30 (a). A first configuration was tested in a single-pass geometry with a magnification of m = 1, f = -30 cm lenses and a pump current of 24 A. This single-pass configuration resulted in a high

average power of up to 19.2 W corresponding to 6.4 mJ pulse energy at 3 kHz repetition rate. This configuration can be seen as high average power test, not optimized for Gaussian beam profile. A second configuration was tested in double-pass geometry in optimized configuration with magnification of m = 1.5, f = -40 cm lenses and a pump current of 23 A. The highest recorded average power in Figure 4-30 (a) is 30.1 W. During the investigation an average power of up to 32.0 W was measured corresponding to more than 10 mJ pulse energy at 3 kHz repetition rate.

The pulse duration was estimated with an intensity autocorrelator before and after the booster stage and results are shown in Figure 4-30 (b). At the time of this measurement, the seed was found to have a duration of 211 ps which is slightly longer than the 171 ps from Figure 4-20 (a) potentially due to imperfect alignment of the intensity autocorrelator. The output of the booster amplifier was measured with the same autocorrelator configuration at low, medium and high average power by varying the seed power to the booster stage. No deviation from the ~210 ps input duration was found. Together with the measured >10 mJ pulse energy and the clean input pulses from the single-pass system (see Section 4.3.3), the estimated peak power of the system exceeded 50 MW. All autocorrelation traces were well approximated with Gaussian fitting curves allowing the conclusion of Gaussian shaped pulses. The consistency of pulse shapes and durations during the amplification indicated that nonlinearities were negligible.

4.4.4 Second Power Booster Stage

The first booster amplifier stage based on twin amplifier modules of 3 mm diameter was followed by a second booster stage consisting of a double-passed amplifier with a single 4 mm diameter module. This second booster stage is described here along with initial experimental results although it has not yet been fully optimized and implemented as picosecond amplifier. Figure 4-31 shows a schematic (a) and a picture (b) of the stage. The design of this booster stage

was similar to the 3 mm diameter stage, follows the guidelines in Section 3.1 and the compensation scheme described in subsection 4.4.2. In contrast to the twin amplifier modules employed in the previous stage, this booster amplifier was based on a single amplifier module with 4 mm diameter, 12.6 cm length, Nd:YAG with a maximum pump power of 600 W at 808 nm wavelength (see also Appendix C). As before, the thermal lens compensation was based on curved rod ends (0.5MCC) and a negative lens next to the amplifier module. The thermal lens of the 4 mm rod diameter was expected to be within the range from 10 to 20 cm depending of the pump power as seen in Figure 3-3 (b).

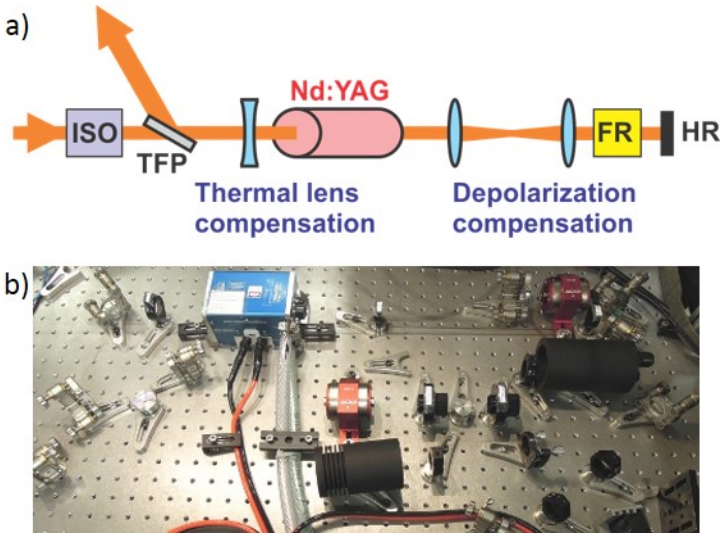

Figure 4-31: Sketch (a) and picture (b) of double-pass booster amplifier stage based on a single amplifier module with 4 mm rod diameter.

The second booster amplifier stage was studied in terms of the thermal lens and depolarization compensation. The total gain of the single-passed module with compensation optics was ~2 for both polarizations. Similarly to the first booster stage, the depolarization compensation scheme was based on a 1:1 relay imaging scheme and polarization rotation. In contrast to the first booster stage, a mirror reflected back the output of the 1:1 telescope effectively imaging the rear end of the single amplifier module onto itself. A double-pass through a 45 degree Faraday rotator

shifted the polarization by 90 degree. Experimentally, the depolarization compensation scheme was not quantified precisely but the compensation effect was observed and could have been qualitatively measured from the residual power rejected from the optical (directional) isolator.

Using a cw probe beam, Figure 4-32 shows the double-passed output beam profile for two different thermal lens compensation configurations. Operating with a compensation lens of f = -10 cm (a) led to a larger output beam profile, small diffraction rings and a double-passed gain of 3.4 corresponding to 0.4 W average power. A stronger negative lens configuration with f = -7.5 cm (b) resulted in a smaller beam profile but with noticeable diffraction around the Gaussian center as well as a lower output gain of 2.5.

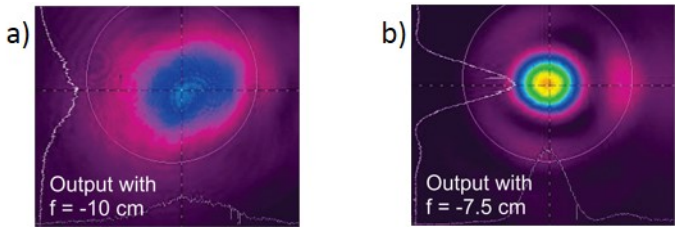

Figure 4-32: Beam profiles of the second booster stage with a cw probe beam and different thermal lens compensation configurations (not fully optimized configuration).

The optimized double-pass gain, a good output beam profile and the implementation as booster for the high energy pump beam generation have to be further investigated. However, these initial cw probe beam experimental results were promising and within the expected performance range. The principle of operation was successfully shown here for a low power, cw beam. The stage was intended to boost the energy from the previous stage by a factor of 2 and allow further increasing of the pulse energy and average power to pump the OPAs in HERACLES.

4.5 Ultra-High Energy-Scaling

The diode-pumped, solid-state amplifiers presented in the previous section are limited to a few tens of mJ pump pulse energy. Higher pulse energies with ps pulse duration require larger

beam diameters in the amplifiers to operate below damage and B-integral limits. Larger rod diameters are available up to 1 cm diameter with a few kW of optical pump power. An example measurement was taken with a 1 cm diameter rod pumped with up to 1.2 kW of optical power. The obtainable small signal gain per pass was measured to be 1.28 (see also Appendix C). In this example, the 28% power increase ignored depolarization and optical losses which occur typically in an amplifier stages. In general the small signal gain is proportional to the pump power but anti-proportional to the rod area (anti-proportional to the squared radius). Thus, a rod with 10 mm diameter needs to be pumped 25 times stronger to achieve a gain similar to a 2 mm diameter module (assuming the same doping concentration and length). The employed 3 mm diameter, Nd:YAG, amplifier modules described earlier are pumped with a maximum optical power of up to 300 W. In contrast, 10 mm-large aperture Nd:YAG amplifiers are available with up to 3 kW pump power, which is only a factor 10 increase in pump power, thus reducing the small signal gain in comparison. This limitation of the diode-pumped amplifier approach can be overcome when using multiple amplifier modules per pass or by increasing the number of passes per module. However, this requires ultra-low losses, which is challenging when thermal lens and depolarization compensation schemes are employed, and the B-integral needs to be limited to ~1.

A high single-pass small signal gain in a single large aperture rod currently requires pulse pumping such as achieved using flashlamps (Figure 4-33) or utilizing quasi-cw laser diodes. In both cases, either the flashlamp or the diode bars are operated in pulsed mode with low duty cycle. This approach sacrifices average power, but allows ultra-high pump peak powers and consequently high small signal gain. The reduced average power also results in weaker thermal lensing and depolarization.

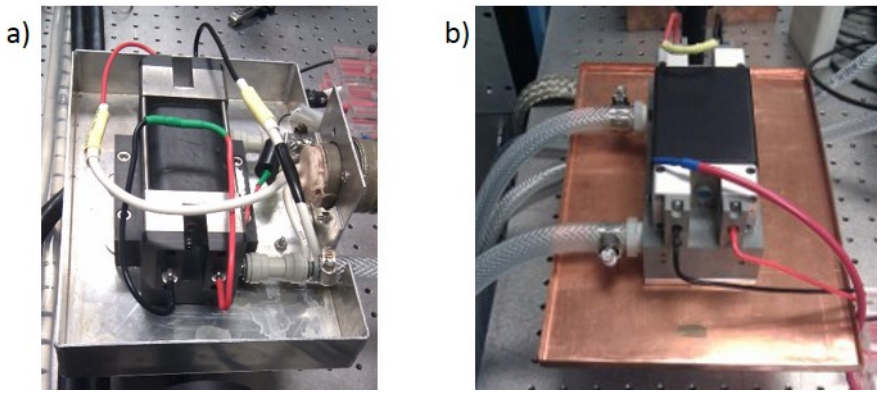

Figure 4-33: Picture of flashlamp-pumped, Nd:YAG modules for high pulse energy application with 6 mm (a) and 10 mm diameter (b).

The following sections describe the investigation on scaling the pump pulse energy beyond 100 mJ. Based on the investigations on flashlamp-pumped amplifiers the design of the PhaSTHEUS pump beam line is presented with the goal of providing 2 J pump pulse energy.

4.5.1 Scaling Limitations with ps Pulses

Flashlamp-pumped, solid-state amplifiers provide high-gain for large-aperture amplifiers. This pump method allows further scaling of the aperture of the rod amplifiers beyond what is possible with diode pumping, which in turn increases the obtainable output energy for nanosecond and picosecond pulses.

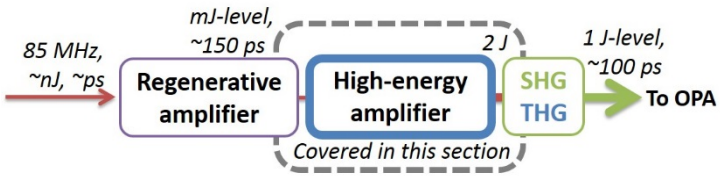

Figure 4-34: Sketch of the pump beam generation. The technical details of the high-energy amplifier (blue box) are presented in this Section 4.5.

The saturation fluence for an amplifier material is given by

$$\mathrm{F_{sat}} = \frac{h\,\nu}{\sigma_E + \sigma_A}, \tag{60}$$

which is constant for a certain material. The saturation fluence for Nd:YAG is $F_{sat} = 0.67\ J/cm^2$. Large-aperture Nd:YAG rods are commercially available with sizes up to 25 mm diameter. Table 4-8 compares the saturation energy given by

$$\mathrm{E_{sat}} = F_{sat}\,A \tag{61}$$

for different rod diameters.

Table 4-8: Comparison of saturation and operational energy (similarly to Table 4-3) for different diameters of Nd:YAG rods and 100 ps pulses.

Rod diameter [mm]	**6**	**10**	**12**	**15**	**18**	**25**
Saturation energy [J]	0.19	0.53	0.76	1.2	1.7	3.3
Operational energy for 100 ps [J]	0.11	0.31	0.45	0.70	1.02	1.96
Operational energy with 75% fill factor [J]	0.09	0.24	0.34	0.53	0.76	1.47

Typically, the stored energy of flashlamp-pumped systems with low repetition rate is much larger than the saturation energy. This is due to the large amount of energy provided by the flashlamps. Table 4-8 shows that in the case of 100 ps pulses the operational energy is limited by the damage threshold of the amplifier which is typically 20 GW/cm². The obtainable output energy is calculated to correspond to 4 GW/cm² for 100 ps, and corresponding values are given in the table for different rod diameters. The largest rod size of 25 mm diameter would give an output energy of 2 J if the full aperture was used with a flattop beam. If the fill factor is reduced to 75%, the output energy is decreased to ~1.5 J.

4.5.2 Results with Large-Aperture Amplifiers

A high-energy amplifier line was built as a proof-of-concept study employing large aperture Nd:YAG amplifiers previously utilized to generate a Joule-class output with nanosecond

pulses and a VBG-stabilized linewidth [138]. In this section, these amplifier heads were employed in a system operating in the picosecond regime with ~100 mJ-level output energy. The output of the HERACLES pump system [123], similar to the performance shown in Section 4.2, was used as seed source for the flashlamp-pumped amplifier chain operating at 1 Hz repetition rate. The results have been presented in [46]. An overview of the setup is shown in Figure 4-35.

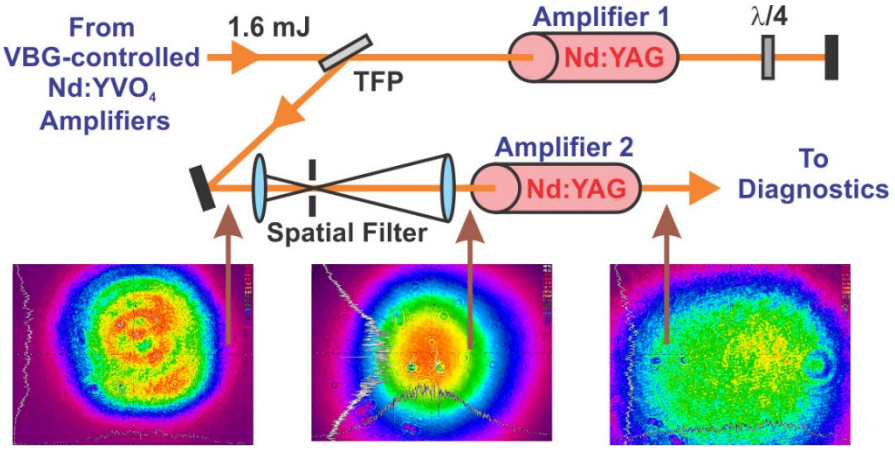

Figure 4-35: Schematic overview of the setup used to achieve 162 mJ pulse energy [46].

With a 1 mJ seed pulse energy, an output pulse energy of 75 mJ was obtained from first double-pass amplifier. After spatial filtering, an excellent Gaussian profile was obtained at the expense of a reduced pulse energy of 45 mJ. Further amplification to 162 mJ was achieved in a second 1 cm diameter Nd:YAG single pass amplifier. Figure 4-36 shows the output energy of each amplifier stage as a function of applied flashlamp voltage. No ASE pre- or post-pulses were observed on the temporal trace of a calibrated energy-meter.

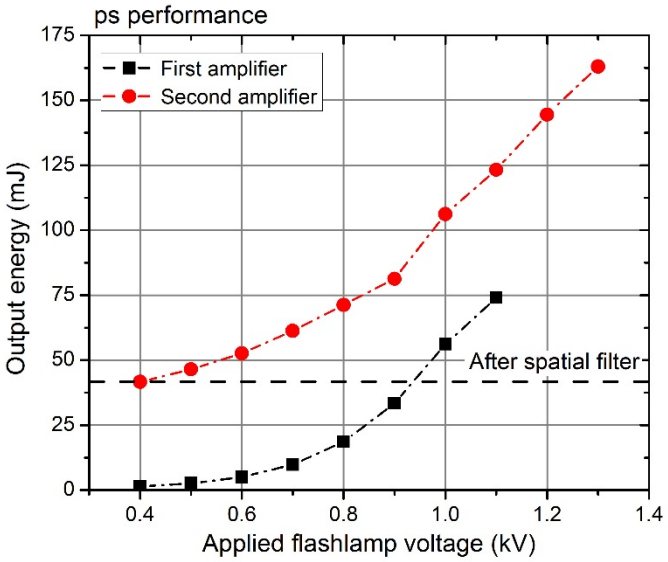

Figure 4-36: Amplification characteristics of the first (double-pass) and the second amplifier (single-pass) with picosecond pulses [46].

4.5.3 Outlook: Ultra-High Intensity OPCPA Facility (PhaSTHEUS)

Based on the presented experiments, a new OPCPA pump beam generation line was designed as shown in Figure 4-37. The design follows the experimental implementation shown in the previous chapter but is based on high energy amplification by flashlamp-pumped, solid-state amplifiers. Similar to the seed source used in the previous sections and presented in detail later in Section 5.3.1, a pre-amplifier based on Yb-doped fiber is employed to increase the pulse energy from a few-cycle oscillator from ~10 pJ at 1064 nm wavelength to the nJ regime while operating at the full repetition rate of 85 MHz. In the design, a pulse picker is used to decrease the repetition rate down to a few Hz for subsequent flashlamp-pumped amplification. These pulses are injected in the regenerative amplifier through an isolator configuration consisting of a thin-film polarizer (TFP), quarter-waveplate and Faraday rotator. The regenerative amplifier is based on a flashlamp-pumped, 3 mm diameter, Nd:YAG crystal and contains a VBG to narrow the spectrum to ~10 pm (similar Section 4.1.3). The performance of this amplifier was previously investigated in the Q-

switched regime and it produced more than 2 mJ pulse energy with 21 ns pulse duration and 22 pm linewidth [138].

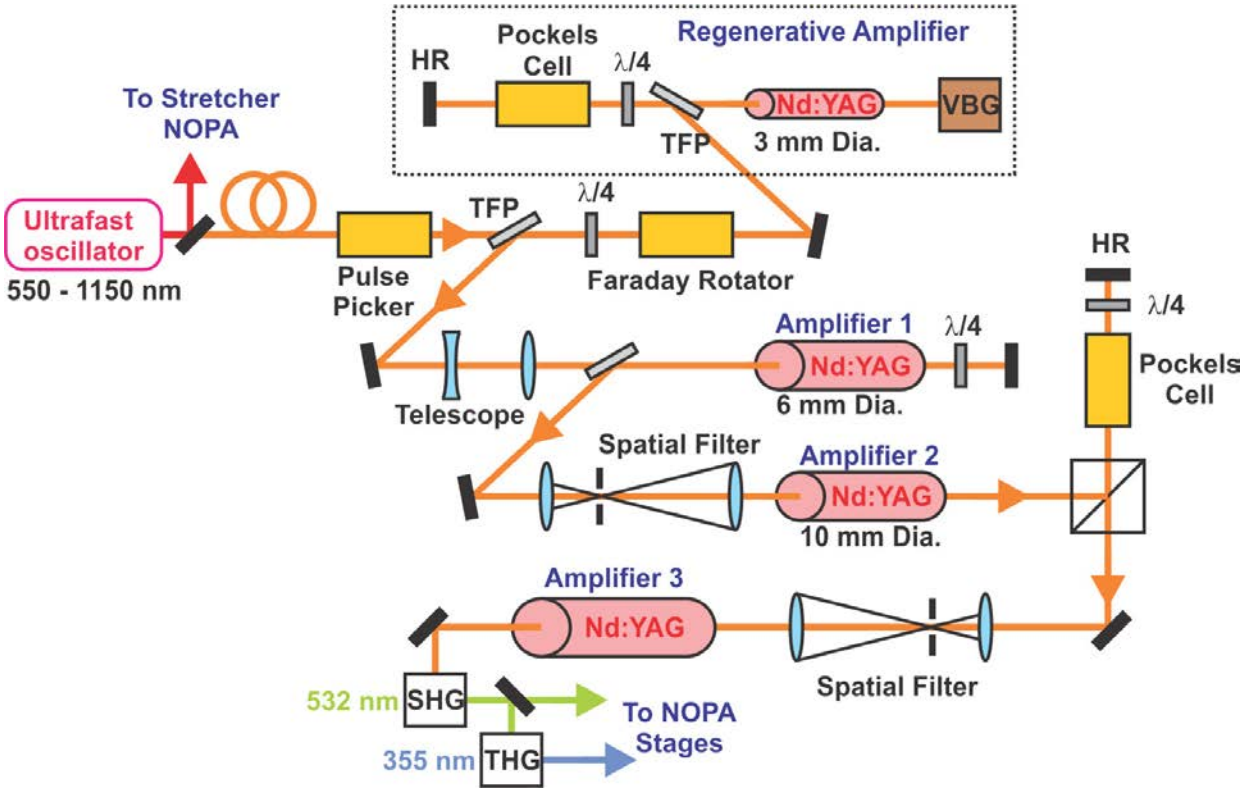

Figure 4-37: Sketch of the design of the ultra-high energy OPCPA pump beam generation line of PhaSTHEUS [46].

After the regenerative amplifier, a flashlamp-pumped, 6 mm diameter, Nd:YAG amplifier is utilized in double-pass geometry to increase the pulse energy from 1 mJ to 75 mJ. A spatial filter cleans the beam profile to obtain an excellent Gaussian beam profile. A flashlamp-pumped, 1 cm diameter, Nd:YAG rod is employed to increase the energy from 45 mJ to 160 mJ with ~100 ps pulse duration. Up to this point in the pump beam generation, the system is directly based on the experimental findings presented in this dissertation and in [46].

The presented design foresees electro-optical gating via a Pockels cell to “cut out” amplified-spontaneous-emission (ASE) to improve the pulse contrast along with a spatial filter to clean the beam profile to obtain the best possible beam quality [139] for final amplification to the

2 J-level with an anticipated 25 mm diameter, Nd:YAG amplifier. LBO crystals are utilized for second-harmonic generation to 532 nm wavelength and third harmonic generation to 355 nm with high efficiency up to 40% [53]. LBO crystal for the SHG applications are commercially available with an aperture size up to 25 mm, which is appropriate to support more than 2 J pulse energy with 100 ps pulse duration.

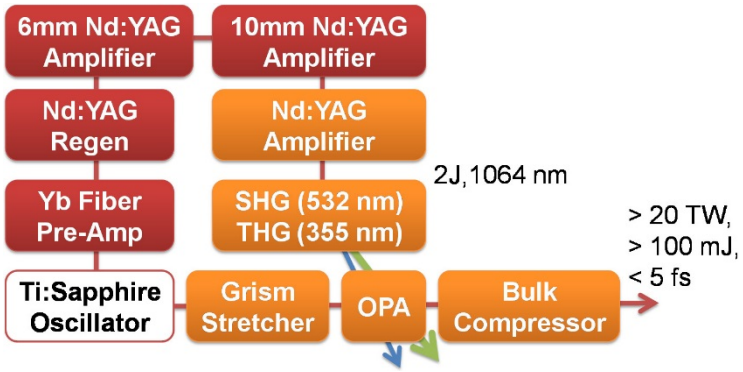

Figure 4-38: Schematic of the design of the PhaSTHEUS facility with the anticipated goal of 20 TW and sub-5-fs duration.

In addition to the experimental results described here, this approach for generating high energy picosecond pulses is supported by the literature. For example, a flashlamp-pumped, Nd:YAG rod amplifier chain with 1 cm rod diameter and 70 ps pulse duration has been presented in [73] with up to 250 mJ pulse energy. The operational intensity in the amplifiers was estimated to be ~4.5 GW/cm². Another system has been presented [133] operating at 40 mJ, 48 ps pulse duration and 6.6 GW/cm² intensity with a 4 mm diameter rod. An ultra-high energy system has been presented operating with 1.5 J output pulse energy and 110 ps duration with 18 mm diameter, Nd:YAG-based amplifiers [38].

The OPCPA facility shown in Figure 4-38 was named PhaSTHEUS (PHAse-Stabilized, Terawatt, High-Energy, Ultra-Short system) and the design, simulations and preliminary results are described in this section. The OPCPA output pulse energy was designed to reach 100 mJ with a sub-5-fs pulse duration at low repetition rates. The architecture for PhaSTHEUS follows the

implementation of HERACLES (see Chapter 5). The design of the pump beam generation for PhaSTHEUS is based on Nd:YAG amplifiers, similar to the presented experimental implementation for the HERACLES facility, but utilizes flashlamp pumping in order to achieve significantly higher pulse energies at lower repetition rate. Flashlamp pumping enables the use of large-aperture, solid-state rod amplifiers and increases the pump pulse energy to the presented more than 160 mJ. The described pump beam design is anticipated to reach J-level with 25 mm aperture amplifiers.

4.6 Summary

This chapter shows that solid-state amplifiers provided a reliable basis for a high-energy, high-average power system with ps pulse duration. Several considerations for regenerative amplifiers were presented in the first section.

The second and third section described two systems of amplifier chains based on a regenerative and single-pass amplifier and operated with few mJ-level pulse energy. The first system with high average power operated at 10 kHz repetition rate and at up to 2 mJ. A >100:1 contrast ratio, 105 ps duration and corresponding peak power of 19 MW were observed. The SHG process was investigated for this regenerative amplifier and a fundamental to SH conversion efficiency of up to 66% was measured. The corresponding SH pulse energy and duration were 390 µJ and 82 ps, respectively, resulting in a peak power of 4.8 MW.

Unfortunately, this system suffered from beam pointing fluctuations, which rendered it unsuitable for OPCPA pumping. The pointing instability was addressed in a system/amplifier re-design. This high energy system routinely operated with an output at 3.2 mJ pulse energy, 3 kHz repetition rate, 171 ps pulse duration and with a corresponding peak power of 18.7 MW. Minor post-pulses with small amplitudes were observed with a fast photo diode and were attributed to

slight thermally induced depolarization in the Nd:YAG amplifier. After SHG, the maximum pulse energy was 1.9 mJ and the pulse duration was estimated to be 121 ps pulse duration corresponding to 7.9 MW of peak power at 532 nm. The amplifier chain represented a high-quality pump laser to drive our HERACLES facility and initial experiments towards its implementation are shown in Section 5.3 and 5.5.

Two power booster stages were designed and implemented based on larger aperture Nd:YAG amplifier modules. The output of the last, high energy, regenerative and single-pass amplifier system was utilized for seeding of the first booster stage. Twin Nd:YAG amplifier modules with 3 mm diameter and up to 300 W pump power were employed with an optical scheme to compensate thermally induced lensing and depolarization. The optical scheme for the first booster stage was optimized with a cw probe beam and with the pulsed picosecond seed. After optimization, a small signal gain exceeding 10 was achieved. During the high power investigations, a maximum output power of 32.0 W was obtained corresponding to more than 10 mJ pulse energy. The pulse duration was estimated to be 207 ps with >50 MW corresponding peak power. The second booster stage was based on a single Nd:YAG amplifier module with 4 mm diameter and up to 600 W pump power. Similar to the first stage, compensation optics for thermal lensing and depolarization were implemented. The initial investigations with a cw probe beam show promising results in terms of obtainable gain and beam profile. These two power booster stages were designed to increase the available pulse energy and average power for the target application to drive an OPCPA system (HERACLES).

Ultra-high pulse energy investigations were presented and >100 mJ energy was obtained at a moderate operational intensity. Further scaling up to the J-level was addressed in a design of amplifier stages for ultra-high pulse energy utilizing large aperture rods. Following this route, a

design was presented for a full few-cycle OPCPA facility with ultra-high pulse intensities pumped by large aperture, flashlamp-pumped amplifiers providing an outlook for the OPCPA facility PhaSTHEUS currently under development.

5 FEW-CYCLE OPCPA FACILITY (HERACLES)

High-energy and high-average power, few-cycle pulses are a desired research tool for highly nonlinear experiments [48]. The HERACLES (**h**igh **e**nergy, **r**epetition rate **a**djustable, **c**arrier-**l**ocked-to-**e**nvelope **s**ystem) facility was designed to provide these pulses to enable novel experiments and the design of the facility was presented several times, for example in [140], [51] and [52]. The facility was intended to feature the generation of broadband pulses ranging from 725 to 1050 nm with pulse energies in the mJ regime at several kHz repetition rate and sub-10-fs pulse duration. Figure 5-1 shows a laboratory picture of the implemented facility during operation, where the green light was generated by the frequency-doubled high energy pump beam, whereas the red light (lower left corner) arose from the seed laser operating in the visible to near IR.

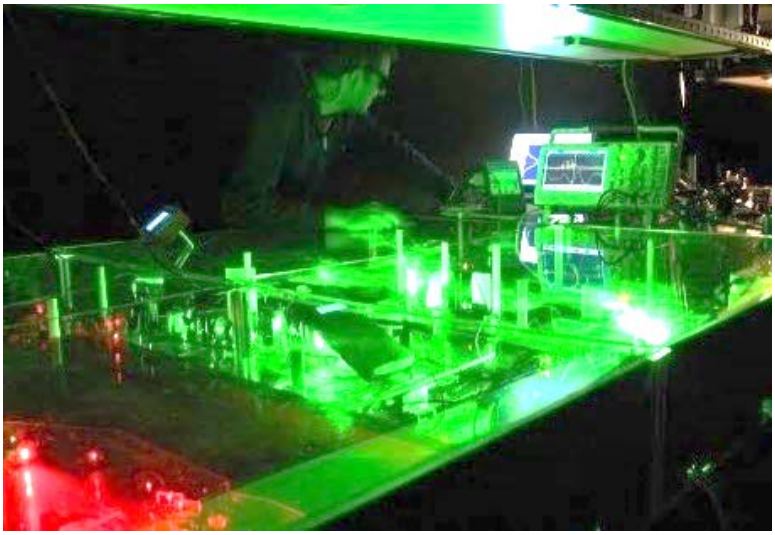

Figure 5-1: Picture of the current HERCALES facility during operation showing the green illumination from the pump beam generation and red illumination from the broadband seed laser.

5.1 OPCPA Architecture

HERCLES was based on a typical OPCPA architecture as most state-of-the-art systems shown in Section 2.4. A sketch with the layout is shown in Figure 5-2 similar to [52].

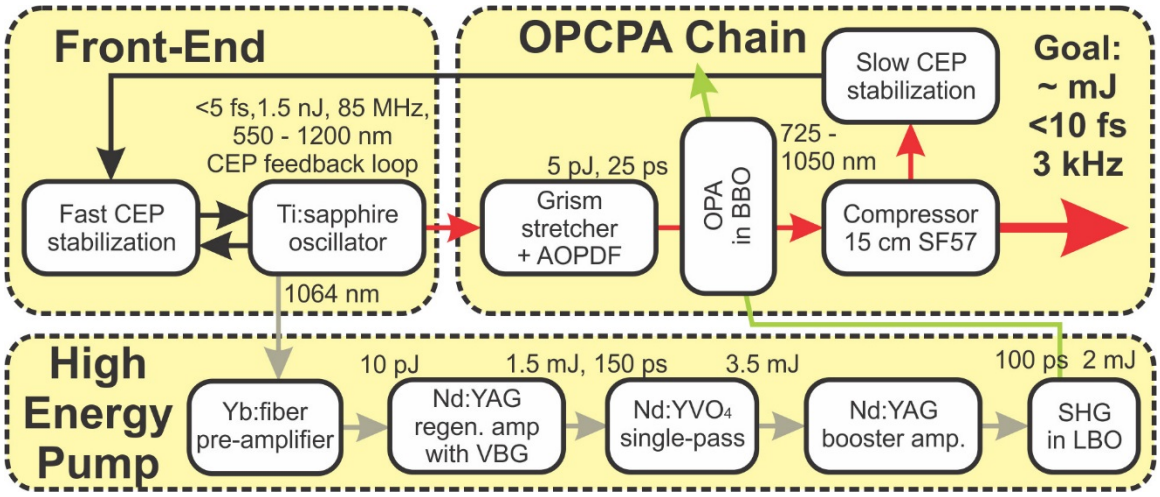

Figure 5-2: Sketch of the basic architecture of HERACLES with relevant performance data.

The front-end consisted of a CEP-stabilized, mode-locked, Ti:sapphire oscillator (Octavius 85M, MenloSystems Inc.), which generated an octave spanning spectrum corresponding to sub-5-fs pulses. Figure 5-3 (a) shows the measured output spectrum of the few-cycle Ti:sapphire oscillator ranging from <600 to >1100 nm on the 30 dB scale (red). The fast CEP stabilization scheme was based on utilizing the weak power in the wings of the spectrum at 570 nm and 1140 nm as presented in Section 3.4. A spatial filter consisting of curved mirrors and a pin hole was used to obtain the excellent Gaussian beam profile shown in Figure 5-3 (b). This few-cycle oscillator was the combined front-end of pump beam generation and OPCPA chain.

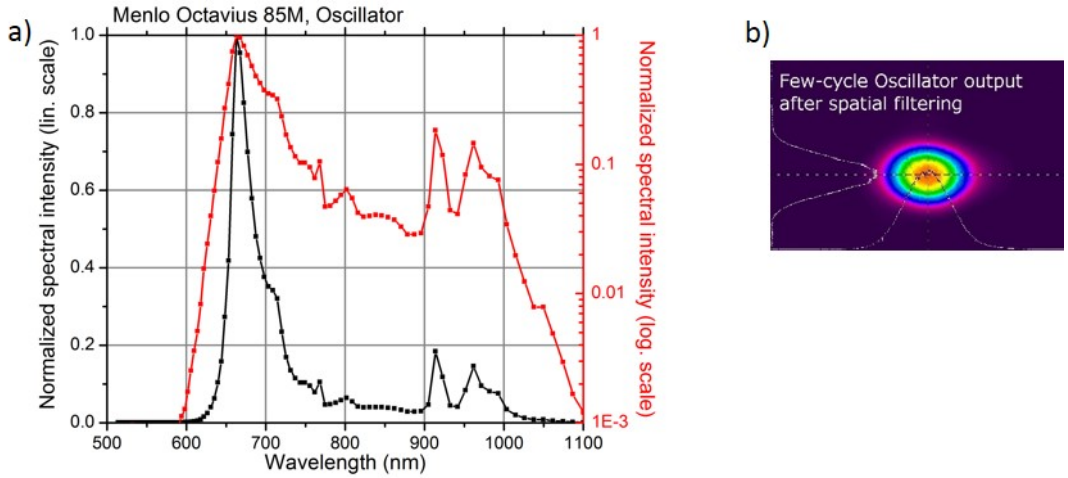

Figure 5-3: Recorded spectrum (a) of the ultrafast front end on a linear scale (black) and logarithmic scale (red) and spatial profile after spatial filtering (b).

As shown in the overview of Figure 5-2, the oscillator output was split equally to provide a broadband seed for the OPCPA setup and sufficient seed for the pump beam generation. The method also ensured precise optical synchronization between seed and pump pulses at the OPA stages. The broadband seed was stretched with a grism-based stretcher to 20 to 60 ps duration and overlapped synchronously with the derived pump pulse in the OPA stages. The pump beam, shown in the lower box in Figure 5-2, was generated via a hybrid ultrafast/fiber/solid-state amplifier architecture boosting the low pulse energy from the seed to the mJ-level as described in detail in Chapter 4 and later in Section 5.3. The few-cycle dispersion management is presented in detail in Section 5.4. The OPA efficiency with BBO is typically on the order of 10% with bandwidth spanning from 725 to 1050 nm as shown in Section 3.5 and [38]. The initial experimental implementation of the BBO-based OPA stages is shown in Section 5.5. The anticipated output pulse duration was around 8 fs given by the large gain bandwidth provided in the OPA and was anticipated to be compressed in 15 cm path length of SF57 bulk glass.

5.2 Temporal Characterization Devices

Two few-cycle pulse characterizations were implemented for the HERACLES facility. Typically, an optical pulse measurement device is employed that utilizes the optical pulse itself to measure its temporal duration by autocorrelation techniques [102], frequency-resolved optical gating (FROG) [141] or self-referencing spectral interferometry for measuring ultrashort optical pulses (SPIDER) [142]. Here, an interferometric autocorrelator (IAC) (Section 5.2.1) and 2DSI SPIDER (Section 5.2.2) were implemented to measure the duration of the few-cycle pulses from the oscillator and potentially the OPCPA output. An IAC can provide an almost real-time measurement of the approximate pulse shape which can be used for quick adjustments on the system. Meanwhile, a 2DSI SPIDER system is able to retrieve the full spectral phase across the spectrum from few-cycle pulse with low energy resulting in complete knowledge of the pulse shape.

5.2.1 Interferometric Autocorrelator

The duration of the oscillator output was measured with an interferometric autocorrelator and a picture of the setup is shown in Figure 5-4. This characterization device is described in detail in [102]. The optics of the autocorrelator were carefully chosen to minimize additional dispersion and support the octave-spanning bandwidth in the visible and near IR.

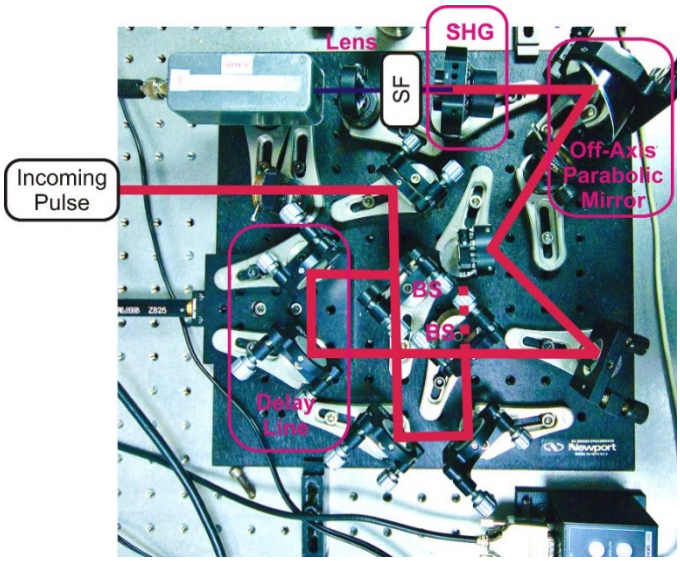

Figure 5-4: Experimental setup of the IAC implemented for temporal characterization of few-cycle pulses. The beam path is indicated by red lines.

A trace of the measured interferometric autocorrelation of the oscillator output is shown in Figure 5-5, corresponding to a pulse duration of less than 10 fs. The trace was taken with four additional bounces on chirped mirrors in order to compensate for the positive material dispersion of the oscillator (2.5 mm FS output coupler and external path in air). Residual chirp due to the lack of fine-tuning prevented perfect compression to the transform-limited pulse duration of 4.7 fs. The IAC was able to provide a quick measurement of the approximate pulse shape. The complete spectral phase and thus, pulse shape can only be retrieved by a FROG or SPIDER measurement. The latter was chosen for experimental implementation due to the direct nature of the phase retrieval and the ability to measure few-cycle pulses with low pulse energy.

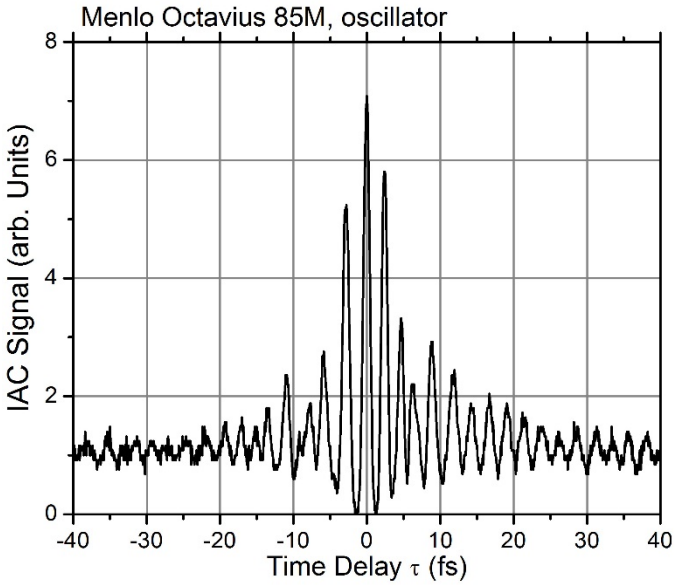

Figure 5-5: Measured autocorrelation trace of the ultrafast laser oscillator (Octavia 85M, Menlo System Inc.) indicating a duration of less than 10 fs.

5.2.2 2DSI SPIDER

Self-referencing spectral interferometry for measuring ultrashort optical pulses (SPIDER) was introduced by Iaconis and Walmslay in 1999 [142] and represents the major characterization technique for pulse characterization in the few-cycle regimes. SPIDER is able to measure the full spectral phase information and thus, allows to retrieve the exact temporal pulse shape. Over the last decade, several modifications and improvements of the original SPIDER scheme emerged. The underlying principal, which is common for all approaches, is discussed in the following. In the original SPIDER implementation [142], the femtosecond pulse is replicated twice by reflection from the front and back surface of a pellicle. In the regime of few-cycle pulses, conventional SPIDER suffers from this process: The pellicle method introduces distortions due to vibrations of the thin plate that can lead to interferometric noise in the setup as well as some unbalanced dispersion. This implementation problem can be overcome with zero-additional-phase (ZAP-) SPIDER [143], two-dimensional spectral shearing interferometry (2DSI) [144] or spatially

encoded arrangement (SEA-) for SPIDER [145] [146]. Because of the advantage to measure low energetic few-cycle pulses (~nJ) with modest average power (~100 mW), the 2DSI method was chosen and implemented experimentally.

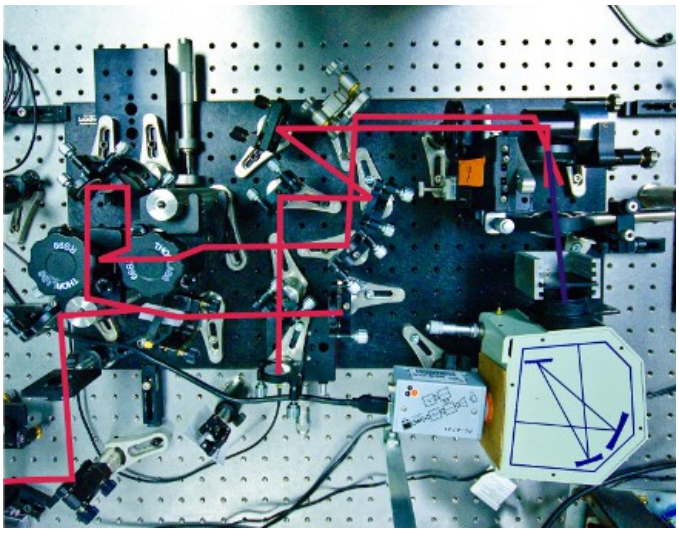

Figure 5-6: Picture of the implemented 2DSI SPIDER setup with highlighted beam path in red with input in the lower left corner.

A picture of the implemented setup is shown in Figure 5-6 and described in the following. In the implemented 2DSI setup, the Fresnel reflection from the front surface of a 3.9-cm-long SF8 glass block was utilized to create an undistorted replica of the few-cycle pulse. On the other side of the setup, the transmitted pulse experienced dispersion (5150 fs² plus higher orders) from the glass block, which caused the pulse duration to stretch to a longer duration of ~3 ps. A balanced Michelson interferometer was utilized to create two long pulses of this chirped pulse with a controllable delay with respect to each other (piezoelectric translation stage). The replica and the two long, chirped pulses were focused (f = 2.03 cm) in a type II nonlinear crystal (BBO), which allowed to obtain two upconverted pulses via SFG. The upconverted pulses had a slightly different spectrum centered at ω_c and $\omega_c - \Omega$ since they were mixed with different frequencies of the each long, chirped pulse. The interferogram between the upconverted pulses on a detector had encoded the spectral phase of the input few-cycle pulse. The latter was retrieved utilizing a spectrometer.

If the delay between the long, chirped pulses was changed slightly, the interferogram changed in relation to the spectral phase of the input few-cycle pulse. An automated feedback loop and algorithm was employed to vary the delay between the two long, chirped pulses, to obtain the interferogram and to retrieve the spectral phase information of the input few-cycle pulses.

The relationship between the spectral phase of the input few-cycle pulse and the interferogram is presented in the following. The interferogram $D(\omega_c)$ can be expressed by [144]

$$\begin{aligned} D(\omega_c) &= \left|E(\omega_c)\exp\left(i\phi(\omega_c)\right) + E_{replica}(\omega_c)\exp\left(i\phi_{replica}(\omega_c)\right)\right|^2 \\ &= \left|E(\omega_c)\exp\left(i\phi(\omega_c)\right)\right. \\ &\quad \left. + E(\omega_c-\Omega)\exp(i\phi(\omega_c-\Omega)-i\omega_c\tau)\right|^2 \\ &= \left|\tilde{E}(\omega_c-\Omega)\right|^2 + \left|\tilde{E}(\omega_c)\right|^2 \\ &\quad + 2\left|\tilde{E}(\omega_c-\Omega)\tilde{E}(\omega_c)\cos[\phi(\omega_c-\Omega)-\phi(\omega_c)-\omega_c\tau]\right|, \end{aligned} \tag{62}$$

where $E(\omega)$is the electric field of the pulses, $\phi(\omega)$ the spectral phase, ω_c the upconverted angular frequency, Ω the spectral shear between the upconverted pulses and τ the delay between them. The expression reveals that the spectral phase $\phi(\omega_c)$ is encoded in the interferogram $D(\omega_c)$.

The interferogram, as shown in Equation (62), has two terms with oscillations at zero frequency (dc) and at frequency ω_c (ac). A Fourier transform was employed in the implemented algorithm to filter the ac side bands. Applying a filter around the ac side band in the Fourier domain, using the inverse FFT (IFFT) and taking the argument revealed the spectral phase of the oscillations

$$\phi(\omega_c-\Omega)-\phi(\omega_c)-\tau\omega_c \equiv \theta_{red}(\omega_c)\,. \tag{63}$$

From the measured interferogram, the phase $\tau\omega_c$ can be eliminated and the reduced phase information $\theta_{\mathrm{red}}(\omega_c)$ obtained. The group delay can be approximated with

$$\tau_g(\omega) = \frac{\partial\phi(\omega)}{\partial\omega} \approx \frac{\phi_2 - \phi_1}{\omega_2 - \omega_2} = \frac{\phi(\omega - \Omega) - \phi(\omega)}{(\omega - \Omega) - \omega} = \frac{\phi(\omega) - \phi(\omega - \Omega)}{\Omega}. \tag{64}$$

The phase difference $\phi(\omega) - \phi(\omega - \Omega)$ represents a first order approximation to the group delay multiplied by the factor Ω. The exact information of the group delay can be acquired by the integration of Equation (63) and by the insertion of Equation (64)

$$\begin{aligned} \phi(\omega_c) &= \int_0^\infty \tau_g(\omega_c)\, d\omega_c \approx \int_0^\infty \frac{\phi(\omega_c) - \phi(\omega_c - \Omega)}{\Omega} d\omega_c \\ &= \int_0^\infty \frac{\theta_{red}(\omega_c)}{\Omega} d\omega_c . \end{aligned} \tag{65}$$

It is possible to perform a numerical integration of the phase $\theta_{red}(\omega_c)$ to extract the spectral phase $\phi(\omega_c)$. Alternatively, it is possible via concatenation to reconstruct the spectral phase [147]. Through both methods, the spectral phase $\phi(\omega_c)$ is obtained in the upconverted frequency space. Converting the upconverted to the fundamental frequency range is required to overlay the measured spectral phase. The involved frequency up-conversion process (SFG) can be written as

$$\omega_c = \omega_f + \omega_{cw}\,, \tag{66}$$

where ω_{cw} is the cw-like portion of the chirped pulse. The frequency shift ω_{cw} was estimated in this work by adding known dispersion to the pulse, and varying the assumed ω_{cw} in the algorithm until proper overlap between the expected spectral phase $\phi_m(\omega_f)$ and the net retrieved spectral phase $\phi_{meas}^{net}(\omega_f)$ was accomplished. This method was employed for experimental implementation in the following with good and reliable results. The retrieved spectral phase $\phi(\omega_f)$ is utilized to retrieve the pulse in time by a simple fast Fourier transform with the separately measured fundamental spectrum $I_f(\omega_f)$ according to [102]

$$I(t) = \left|\mathrm{FFT}\left\{\sqrt{I_f(\omega_f)} \cdot e^{-i\phi(\omega_f)}\right\}\right|^2 . \tag{67}$$

Experimental results are presented in the following.

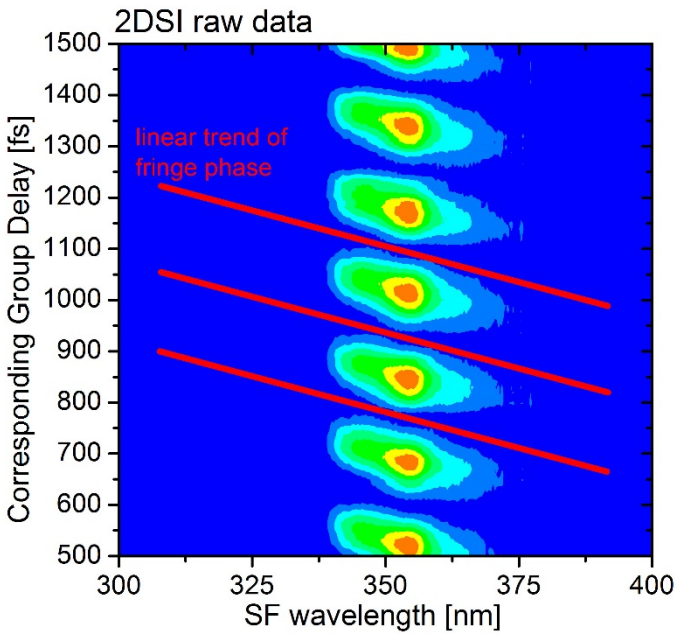

Figure 5-7: Raw data example of a 2DSI measurement showing the linear spectral phase of the fringes in the interferogram indicating dispersion.

An example trace of the 2DSI raw data is displayed in Figure 5-7 showing the interferogram generated by the few-cycle oscillator and exemplary additional dispersion. The fringes of the interferogram can be clearly seen in the range from 338 to 373 nm and a linear trend line approximates the phase of the fringes. A fast Fourier transform along the time axis τ revealed the fringe phase $\theta(\omega_c)$ and numerical integration or concatenation of $\theta(\omega)$ directly provided the spectral phase $\phi(\omega_c)$ with a calibration factor Ω. No absolute calibration of the traveled distance for the time delay between the long, chirped pulses in the Michelson section was necessary as long as the distance showed linear translation over more than two optical fringes. After converting the spectral phase from the upconverted frequencies ω_c to the fundamental frequencies ω_f, the pulse was retrieved via Equation (67). An example is shown in Figure 5-8 which illustrated the extracted phase information for an almost transform-limited pulse (black) and with BaF_2 (red) or FS in the beam path (green) as well as the separately measured fundamental spectrum (blue). It can be seen

that the phase information was well retrieved from 610 to 860 nm. Outside of this range, the pulse energy was below the detection limit of the device.

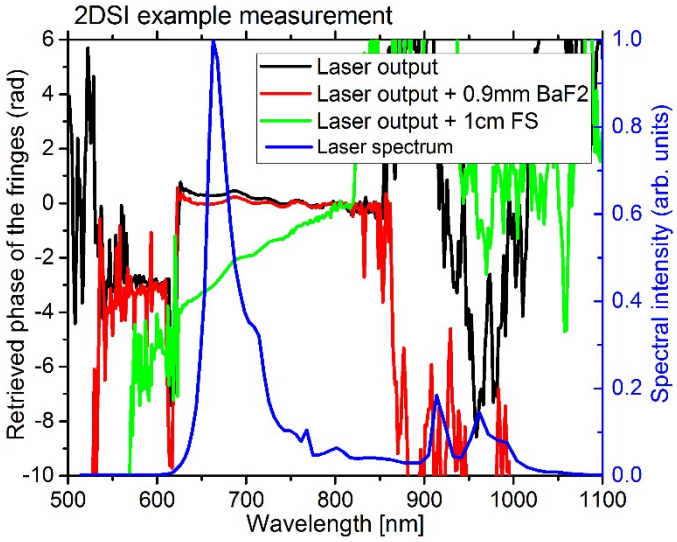

Figure 5-8: Example 2DSI absolute phase measurement of the laser output (black) as well as with additional dispersion of BaF2 (red) or FS (green). The spectrum is also shown (blue).

A measurement with the minimal spectral phase is shown in Figure 5-9. The graph shows traces for the few-cycle pulse with minimal spectral phase (black) as well as the net traces with 0.9 mm BaF_2 (red) and 1 cm Fused Silica (green) of additional dispersion. The retrieved phase of the oscillator showed the typical phase oscillations which were attributed to the chirped mirrors in the oscillator [148] [149]. The range, in which the phase is correctly retrieved, is limited in this measurement from 625 to 825 nm corresponding to the range were the power of the oscillator is concentrated (see Figure 5-3). The 2DSI device was designed to support the full bandwidth and measurement of few-cycle pulse durations and no additional dispersion was introduced by the device.

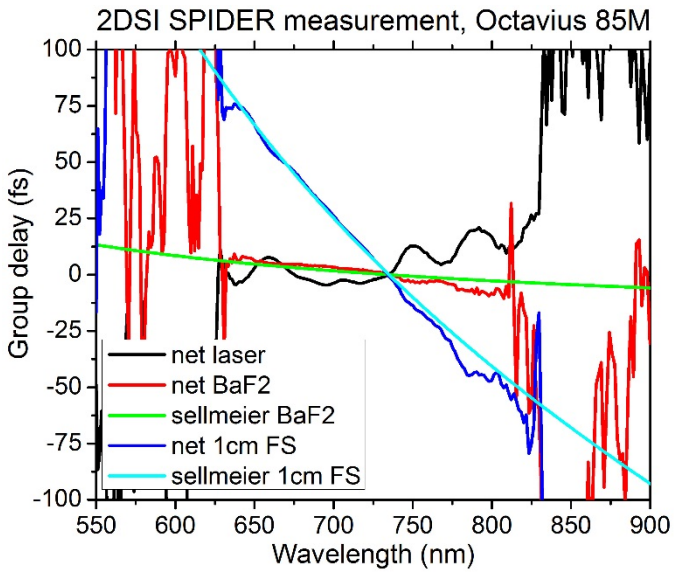

Figure 5-9: Measured group delay of the sub-5-fs oscillator via 2DSI with zero and some additional dispersion.

The accuracy of 2DSI was tested in the measurement shown Figure 5-9 by inserting a known amount of dispersion in the beam path (similar to [144]). The differences between the spectral phase retrieved in the case with minimal spectral phase (black) and with dispersion resulted in information of the net spectral phase introduced due to the material dispersion $\phi_{mat}^{net}(\omega)$. These measured spectral phases are compared in Figure 5-9 with the theoretical curves given by the Sellmeier equation (green and cyan). A good overlap was found between the curves of the experimentally found net phase and the theoretical dispersion. The presented test verified the accuracy and reliability of the implemented 2DSI SPIDER device.

5.3 Pump Beam Generation

The pump beam generation to drive the few-cycle OPCPA system, the HERACLES facility, was based on a hybrid ultrafast/fiber/solid-state amplifier architecture shown in Figure 5-10. The chain was seeded directly by the Ti:sapphire oscillator at 1064 nm (see Section 5.1). The first amplifier stage consisted of a fiber-based pre-amplifier which is detailed in Section 5.3.1. The

output pulses were amplified in a regenerative amplifier to the mJ-level, which was followed by a power amplifier and SHG. Both DPSS amplifiers have been detailed in Chapter 4 and the performance parameters of the initial investigations with the OPA are summarized in Section 5.3.2.

Figure 5-10: Sketch of the amplifier chain for the pump beam generation of the HERACLES facility.

5.3.1 Fiber-Based Pre-Amplifier

The first amplifier stage was implemented as a fiber-based pre-amplifier to increase the seed energy from the sampled wavelength portion at 1064 nm from the Ti:sapphire oscillator for the following amplifiers [123]. Figure 5-11 shows a sketch of the fiber amplifier stage, which consisted of a coupling lens (f = 11 mm), a 3-dimensioal linear stage for alignment of the fiber tip, an isolator, a WDM to couple the light of the 750 mW core-coupled diode (Alfalight, Inc.) into the Yb-doped active fiber (Nufern, Inc.), a bandpass filter at 1064 nm with a bandwidth of 3 nm, another isolator and a collimator. All fiber components were based on a polarization maintaining Panda 6/125/400 µm fiber (PM980). The first isolator prohibited ASE light from the active fiber to propagate back in free-space to the Ti:sapphire oscillator. The bandpass, which transmitted only a narrow bandwidth at 1064 nm, suppressed effectively the main ASE signal at 1030 nm. The second isolator prohibited light from the following amplifiers from being coupled back to the active fiber.

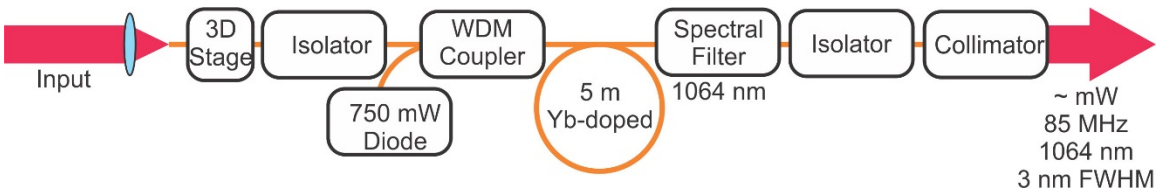

Figure 5-11: Sketch of the components in the fiber pre-amplifier. The amplifier was based on standard single-mode fiber components (PM980).

Figure 5-12 (a) shows the typical amplification characteristics obtained from the fiber pre-amplifier stage. The typical power coupled from the Ti:sapphire oscillator was measured at the output of the fiber amplifier and estimated to be around 4 µW corresponding to 47 fJ at 85 MHz. The ASE exiting the fiber system was characterized to be 54 µW without seeding. The output power increased to more than 850 µW at maximum seed power (4.6 µW coupled power), which resulted in a gain of 184 (or 22.5 dB). The corresponding pulse energy was 10 pJ at 1064 center wavelength with 3 nm bandwidth. Due to the fiber length and bandwidth, the output pulse duration was chirped to the ps-level.

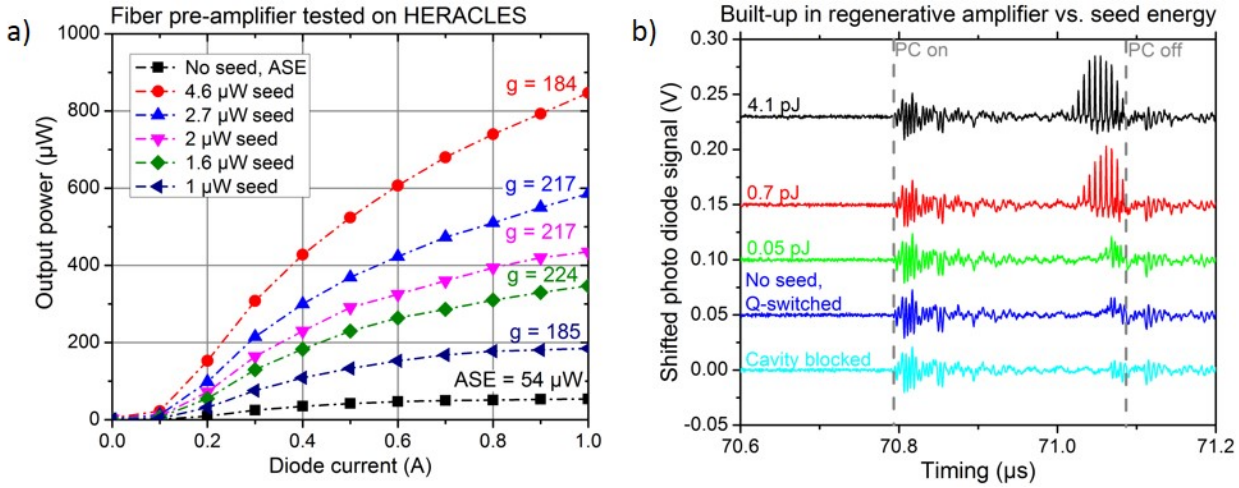

Figure 5-12: (a) Typical amplification characteristics of the fiber pre-amplifier for different seed powers. (b) Typical pulse built-up in the followed regenerative amplifier for several fiber amplifier outputs.

The characteristic threshold of the pulse built-up in the regenerative amplifier for different levels of coupled seed energy was investigated and presented in Figure 5-12 (b). A characteristic built-up trace similar to Figure 4-9 (a) can be seen in the case for 4.1 pJ seed energy (black) as well as 0.7 pJ (red). In the case of the latter the built-up took a few more round trips in the cavity to reach saturation and high pulse energy. A further decrease in seed energy (~0.05 pJ, shown in green) led to insufficient pulse built up and competition with the Q-switched pulse built-up. The Q-switched built-up can be seen in the case without seed, where the cavity was practically dumped

when the Pockels cell switched (reference timing: 71.084 µs). The last trace (cyan) was recorded with a blocked regenerative amplifier cavity and the electronic ringing due to the high voltage electronics can be seen. In conclusion, a coupled energy of 0.05 pJ marked the threshold for successfully seeding the regenerative amplifier. Such levels were routinely provided from the fiber pre-amplifier.

5.3.2 Performance of the DPSS Pump Beam Generation

The output of the fiber pre-amplifier stage was further amplified in the pump beam generation scheme shown in Section 4.3. The output parameters at 532 nm were 1.9 mJ pulse energy, Gaussian temporal pulse shape, 121 ps pulse duration (FWHM) and 3 kHz repetition rate with excellent Gaussian beam profile (see Section 4 for detailed discussion). The pump beam generation was designed to have high stability and minimal beam wandering of the focused pump beam at the position of the OPA stages. Long-term power drifts were eliminated with a closed-loop feedback system. The pulse-to-pulse fluctuations were minimized by operating the regenerative amplifier as close as possible to saturation. Other fluctuations, such as timing jitter and change in pulse shape as well as duration, were negligible. Thus, the DPSS amplifier stages provided an excellent output for pumping the OPCPA system with more than 5 W average power.

5.4 Few-Cycle Dispersion Management

CPA and OPCPA are based on pulse stretching, amplification and compression to achieve high output peak powers. The pump pulse duration is depending on the OPCPA design and typically ranging from 0.5 ps to 140 ps (see Appendix B). The seed pulse duration is typically chosen to match the pump duration ($\tau_{seed} \sim 0.7\ \tau_{pump}$). The here utilized grism stretcher and bulk compressor design is a robust method to provide tailored dispersion for stretched ps pulse durations

and an AOPDF is utilized for fine-tuning (see Section 3.3). A comprehensive code involving analytical equations as well as ray tracing methods to accurately simulate the dispersion management was implemented in the Laser Plasma Laboratory based on the principles presented in Section 3.3. Numerical results were briefly presented in [103] and [52]. This section describes extensively the basic principles of the dispersion management. It provides the numerically found parameters for the implemented sub-10-fs dispersion management in modified configuration compared to [103] and [52]. The numerical model was employed to numerically investigate the experimental configuration for sub-5-fs dispersion management and the results are presented in the following. The final subsection describes B-integral estimates for the bulk glass compressor obtained with the code available in the Laser Plasma Laboratory. These numerically found estimates show that a low B-integral can be maintained for 100 µJ and mJ-level few-cycle pulses with the experimentally implemented aperture of the bulk compressor.

5.4.1 Sub-10-fs Dispersion Management

Several constraints exist for the transform-limited duration of the pump beam and the stretched pulse duration of the broad-band seed beam. OPA can be performed with ns, ps or fs pulse duration but is typically dictated by the pump pulse duration available. In case of OPCPA, the duration ranges from 1 to 100 ps for MOPA- and is ~1 ps for CPA-like pump schemes. The pump pulse duration is a trade-off between reducing the peak power in the beam generation to avoid damage/nonlinearities and increase extraction efficiency as well as obtaining sufficient intensity at the OPA for parametric gain. For few-cycle seed pulses, it is desired to use shorter pulses with a low stretched-to-compressed duration ratio since it effectively reduces the need and tuning range for adaptive phase correction. The pump-to-seed ratio is a complex trade-off between the parametrically amplified bandwidth and the OPA efficiency and the compromise is based on

several constraints. Due to the nonlinear nature of the OPA process, the typically Gaussian temporal shape of the pump pulse, a temporal window of significant parametric gain is obtained, which is substantially narrower than the pump duration [150]. Two consequences arise from this. First, for a given pump duration the amplified signal bandwidth is larger for shorter pulse durations. This is a consequence of the (approximately) linear chirp, which causes the pulse content at the edges of the spectrum to experience dramatically less parametric gain compared to the center of the pulse/spectrum. Second, higher overall conversion efficiencies are obtained if the seed pulse overlaps well over the given pump duration. As a consequence, a fixed pump to signal duration ratio in the OPA stages hence must lead to a trade-off between amplified bandwidth and OPA efficiency. This trade-off can be optimized for all OPA stages [151], split over the OPA stages [150] or the pump pulse shape can be adapted [152]. All methods increase the complexity of the OPCPA system and are therefore not implemented in this work but mentioned for a complete overview. In addition, superfluorescence is generated in each OPA, which arises from spontaneous down-conversion of a pump photon into a signal and idler photon pair [153]. During the temporal window of significant parametric gain and in proper geometry, the SF can built up to a considerable amount and amplify in consecutive OPA stages [154]. In analogy to ASE, it can be minimized by decreasing the parametric gain of the OPA stage, by optimizing the temporal pump to seed ratio, or by spatial filtering.

The pump pulse duration for the HERACLES facility was anticipated to be at the 100 ps-level, as detailed in Chapter 4 and Section 5.3. The system presented in Section 4.3 operates with 121 ps but could be reduced to 50 to 100 ps by adapting the VBG-based narrowing effect if desired. For broadband, few-cycle pulses, the stretched pulse duration is typically kept <50 ps, thus a pump pulse duration of 85 ps was assumed in the following discussion. A 5 cm long piece of SF57 glass

was chosen as pulse compressor, where the number of passes was variable. Figure 5-13 shows the introduced group delay difference from 725 to 1050 nm for several path lengths in SF57 glass. For 15 cm path length, the group delay difference between 725 and 1050 nm was 24 ps or a ratio of 0.28 to the 85 ps pump duration. This ratio represented a good compromise between amplified bandwidth and efficiency [150] [151], and was chosen in the following discussion.

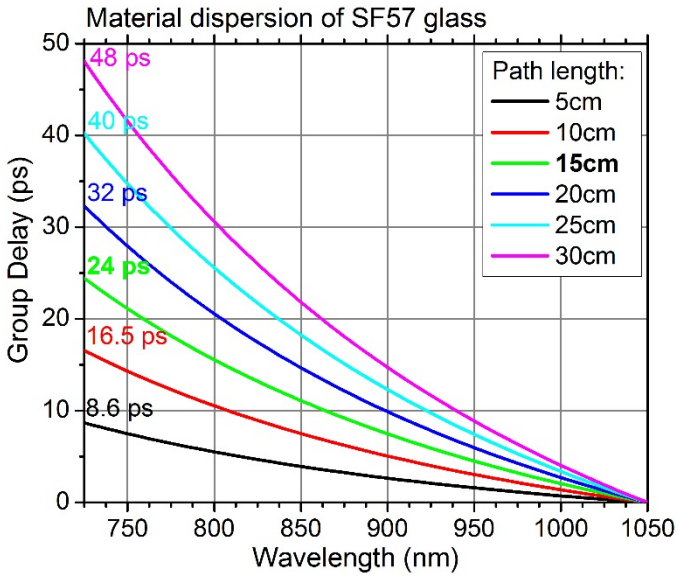

Figure 5-13: Estimated group delay between 725 and 1050 nm for several path lengths in SF57 glass.

Figure 5-14 shows a picture of the implemented grism (a) and a sketch (b) with the parameters found in the following discussion. A numerically derived apex angle of the prism was 18.0 degrees and the prisms were manufactured accordingly within a measured accuracy of ± 0.1 degrees. A set of parameters was found with the simulation for sub-10-fs dispersion management (SF57 compressor length = 15 cm, groove density 300 l/mm, SF11 prism material, grism separation G = 2.033 cm, grism shift = 3.1 cm, grism insertion of 1 cm and 6.8° angle of incidence).

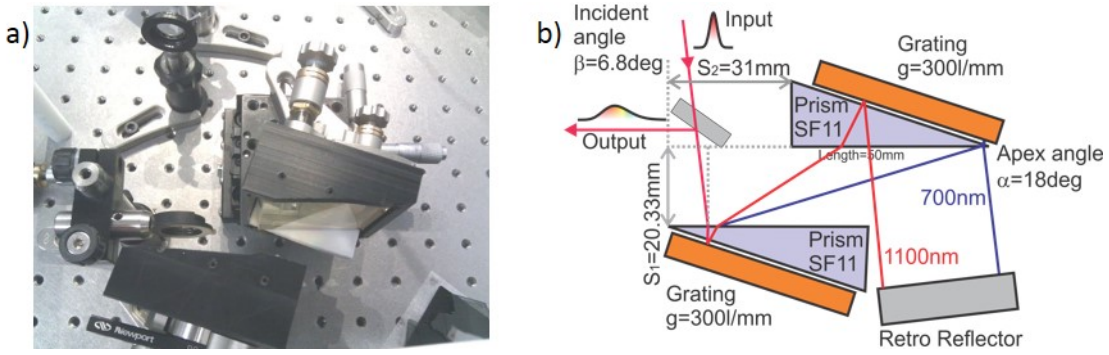

Figure 5-14: (a) Picture showing the grism setup used in the experiment. (b) Sketch showing the implemented geometry.

The calculated dispersion parameters for all considered elements are listed in Table 5-1. It can be seen that the grism introduces the largest amount of negative dispersion while the TeO_2 crystal of the AOPDF/Dazzler and the SF57 introduce the largest positive amount. The overall dispersion added up to zero second and third order dispersion, which the system was optimized for [107]. Higher orders were considered to be compensable with the capabilities of the AOPDF.

Table 5-1: Table of the calculated dispersion parameters for sub-10-fs dispersion management. The system was designed numerical for 0 fs^2 and 0 fs^3 residual dispersion.

	D2 [fs^2]	**D3 [fs^3]**	**D4 [fs^4]**
Grism	-48,000	-35,000	-144,000
Dazzler	-3,000	0	0
TeO_2	+20,000	+14,000	+7,000
BBO, FS	+1,000	+800	-300
SF57	+30,000	+21,000	+6,000
Residual	~0	~0	-131,000

The calculated residual group delay after the compressor is shown in Figure 5-15. Figure 5-15 (a) shows the full range, where the delay between 725 and 1050 nm corresponding to a range of 325 nm was 3 ps (gray area). The AOPDF (Dazzler U45-WB, Fastlite) can typically adjust for up to 6 ps of maximum group delay difference. A bandwidth of more than 100 nm was within a group delay difference of 100 fs due to the optimized zero second and third order dispersion. Figure 5-15 (b) shows the residual group delay plotted in a smaller temporal window of $\pm 20\, fs$. A bandwidth of 62 nm was found within a temporal window of $\pm 10\, fs$, which was larger than its

transform-limit of 15 fs (62 nm Gaussian bandwidth at 850 nm). A bandwidth of 49 nm was found within $\pm 5\ fs$ which was lower than its transform-limit of 19 fs, which is indicated in Figure 5-15 (b) by the gray area. Thus, it can be concluded that the output pulses could potentially be compressed in the presented geometry to sub-20-fs duration without adaptive spectral phase correction.

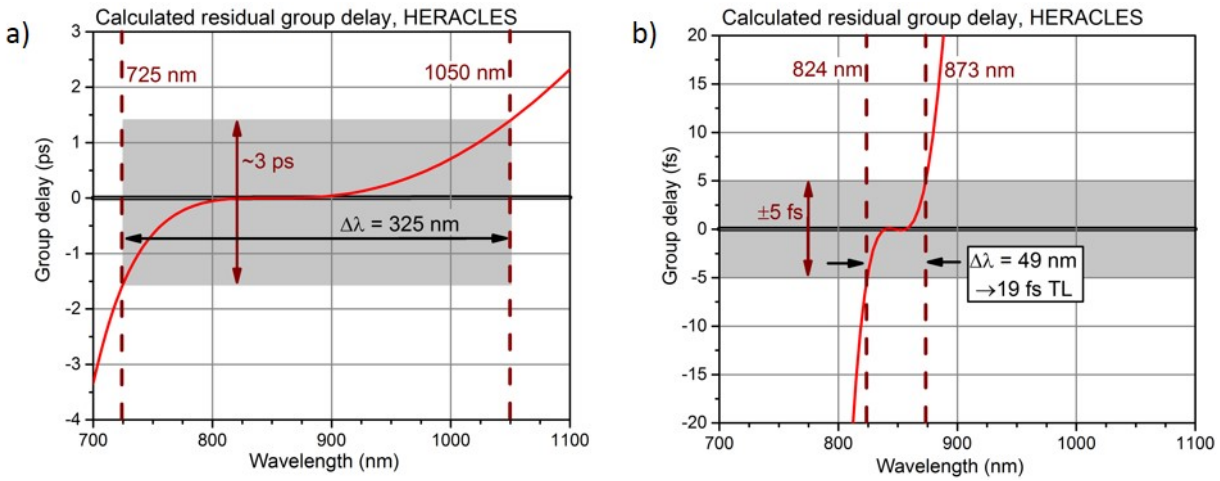

Figure 5-15: The plots shows the residual group delay of the OPCPA chain for the sub-10-fs dispersion management.

The presented approach was limited to a total range of ~350 nm, due to the sharp increase in group delay outside of the 725 to 1050 nm spectral range. The maximum group delay difference outside of this range exceeded largely the typical capability that the AOPDF can compensate of 6 ps. As a consequence, the grism stretcher, AOPDF and bulk compressor approach with optimization to zero second and third order dispersion was limited to ~350 nm bandwidth or sub-10-fs.

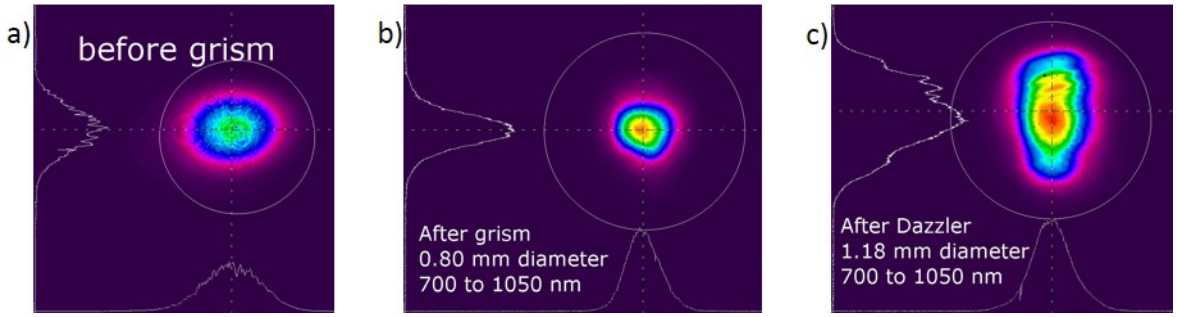

Figure 5-16: Measured beam profiles through the pulse stretcher system.

Beam profiles of the implemented grism stretcher and AOPDF were taken and are shown in Figure 5-16. Picture (a) shows the profile obtained before the grism with a slightly elliptically Gaussian profile. Picture (b) shows the profile after the grism and picture (c) shows the profile after the AOPDF/Dazzler. All beam profiles were sufficiently close to the diffraction limit and well-suited for seeding the OPA stage. The full transmission bandwidth of the grism/Dazzler configuration was verified and a broad amplification bandwidth is shown in Section 5.5.

5.4.2 Sub-5-fs Dispersion Management

Two-color pumping for OPA brings the opportunity to increase the amplified bandwidth to almost octave-spanning (see Section 3.5.4) ranging from 575 to 1050 nm if based on BBO and pumped at 532 nm wavelength. It enables an OPCPA output with sub-5-fs pulse duration and was considered in the design for the PhaSTHEUS project (see Section 4.5.3). In order to manage the additional spectral bandwidth, the dispersion management was extended compared to the previously shown sub-10-fs. The previous section showed that the sub-10-fs approach was limited to ~350 nm of bandwidth. A solution was offered by a different optimization routine, where, instead of optimizing the system for zero second and third order dispersion, the system was optimized for minimal residual group delay difference (similar to [108]). The method allowed the

AOPDF to operate within its 6 ps group delay compensation range enabling sub-5-fs dispersion management.

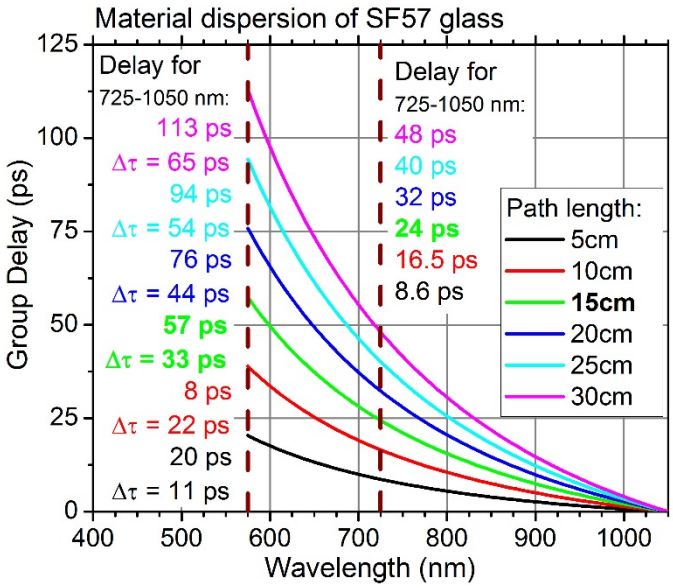

Figure 5-17: Estimated group delay from 575 to 1075 nm for different path lengths in SF57 glass.

As for the sub-10-fs dispersion management in Section 5.4.1, the compression was chosen to be in 15 cm path length of SF57 glass. Figure 5-17 shows the group delay curves estimated for SF57 for the range 575 to 1050 nm. The full group delay was 57 ps with 15 cm of SF57 (e.g. the delay between 550 to 1050 nm). Alternatively seen, the bandwidth from 725 to 1075 nm was temporally spread over 24 ps and the bandwidth from 575 to 725 nm over 33 ps. On the pump side, the assumed pulse duration of the SH at 532 nm was 85 ps and the corresponding duration of the TH at 355 nm was 70 ps. The chosen compressor length of 15 cm SF57 glass provided temporal overlap ratios of (24 ps/85 ps) 0.28 and (33 ps/70 ps) 0.47, respectively. The found values corresponded to a good trade-off between amplified bandwidth and efficiency [150] [151]. The found parameters for the sub-5-fs dispersion management are discussed in the following paragraphs.

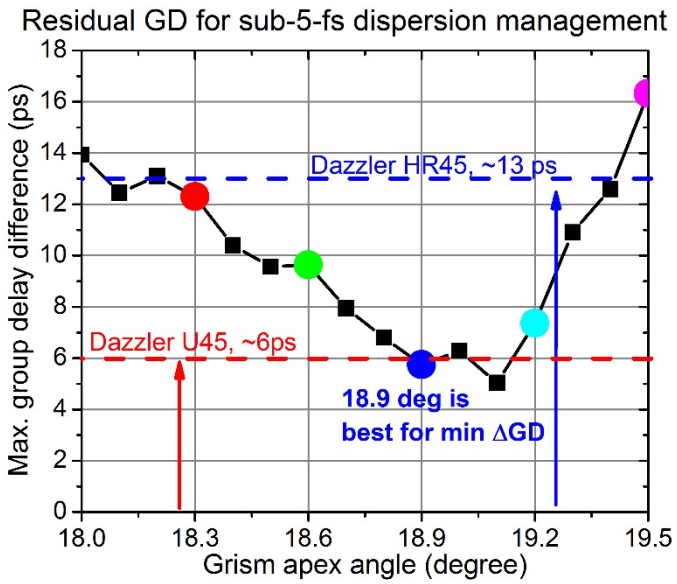

Figure 5-18: The plot shows the maximum group delay difference in the range of 575 to 1075 nm that the Dazzler needs to compensate.

The large bandwidth of ~500 nm required that the AOPDF operated at its full capabilities. Instead of optimizing the system for zero second and third order dispersion, the AOPDF was assumed to compensate for several ps group delay difference. Figure 5-18 shows the residual group delay difference between 575 to 1075 nm for several different grism apex angles. In this study, the compression was simulated in 15 cm of SF57. It can be seen that the minimal delay difference occurred between 18.9 and 19.2 degrees with less than 6 ps. Two horizontal lines are shown: the red dashed curve represents the maximum 6 ps delay that the Dazzler model U45 (Fastlite) can typically handle and the dashed blue line corresponds to the 13 ps delay that the Dazzler model HR45 (Fastlite) can typically compensate for. Besides the maximum group delay, the two Dazzler models differed in diffraction efficiency and spectral accuracy. The HR45 had lower diffraction efficiency as well as a lower dispersion resolution (i.e. number of points for $\phi(\omega)$ across the 650 nm bandwidth). Thus, it was preferred to utilize the model U45 if less delay was possible, however, the model HR45 gave a larger margin in maximum group delay and was considered to be employed in the design of PhaSTHEUS.

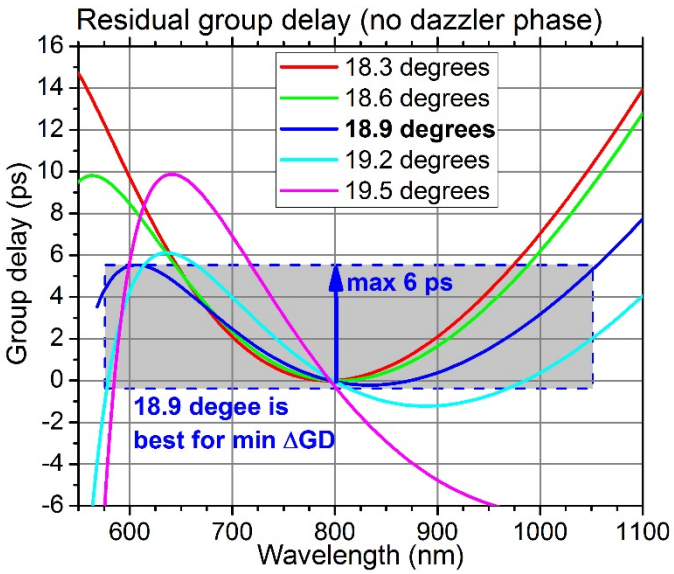

Figure 5-19: The plot shows the calculated shape of the residual group delay across the bandwidth.

Figure 5-19 shows the exact shape of the residual group delay for several grism apex angles, while Figure 5-18 only shows the maximum difference. The color code matches between both figures (Figure 5-18 and Figure 5-19). For an angle of 18.3 degrees, the shape of the residual dispersion was dominated by the second order term and the total range was above 12 ps. The curve of 18.9 degrees fitted within the 6 ps delay window of the common Dazzler, which enabled full compensation. A further increase in apex angle distorted the shape significantly. At an angle of 19.5 degrees, the maximum delay was beyond 15 ps and beyond the 12 ps of the Dazzler compensation range. 19.0 degrees gave the smallest amount of group delay that needed to be compensated but 18.6 allowed for the smallest prism side length as well as more uniform diffraction efficiency of the Dazzler. Thus, an apex angle of 18.9 degrees was considered to be the best compromise valuing the importance of minimum group delay slightly higher.

Table 5-2: Residual group delay dispersion for the case with apex angle 18.9 degrees and 15 cm SF57.

	D2 [fs^2]	D3 [fs^3]	D4 [fs^4]
Grism	-51,000	-4,500	-88,000
Dazzler	0	0	0
TeO2	+22,000	+15,000	+9,000
BBO, FS	+1,000	+800	-200
SF57	+33,000	+22,000	+7,000
Residual	+5,000	+34,000	-72,000

A set of parameters was found for which the AOPDF provided sufficient group delay compensation over the full bandwidth ranging from 575 to 1075 nm achievable with two-color pumping. The calculated dispersion values are given in Table 5-2. The optical path length through 1.5-cm long BBO and 4.5 cm-long TeO_2 crystals were assumed as additional material dispersion. It can be seen from Table 5-2 that the residual group delay had significant contributions from second, third and higher order dispersion. However, it was numerically shown that the AOPDF was able to compensate to sub-5-fs pulse durations in the mentioned geometry. The identified parameters for sub-10 and sub-5-fs dispersion management are summarized in Table 5-3.

Table 5-3: Grism parameters for sub-10 and sub-5-fs dispersion management.

	Sub-10-fs	Sub-5-fs
Bandwidth	725 – 1050 nm	575 – 1050 nm
Compressor length	15 cm SF57	15 cm SF57
Groove density	300 l/mm	300 l/mm
Prism material	SF11	SF11
Prism apex angle	18.00 degrees	18.9 degrees
Grism separation G	2.033 cm	4.5 cm
Grism shift	3.1 cm	10 cm
Grism insertion	1 cm	1 cm
Angle of incidence	6.8 degrees	0 degrees
Maximum GD difference for AOPDF	~3 ps	~6 ps

5.4.3 Pulse Compression in Bulk Glass

Pulse compression was performed with the tailored dispersion in 5 cm long SF57 bulk glass with a three-pass geometry resulting in a total optical path length of 15 cm SF57. A picture of the bulk glass is shown in Figure 5-20. This compression approach has been successfully presented experimentally in the literature for up to 125 mJ pulse energy and 7.9 fs duration or 16 TW peak power with four additional chirped mirrors [38]. B-integral estimates were of major relevance for the here presented bulk compressor to avoid nonlinear effects such as self-focusing. Exceeding a B-integral of π could potentially cause damage to the bulk material and affecting the beam profile. The B-integral was given by Equation (58) with $n_2^{SF57}(1.06\ \mu m) = 4.1 \times 10^{-19} m^2/W$ [155]. The limit is commonly kept below 1. The output of the HERACLES facility with the pump beam presented in Section 4.3 (1.9 mJ at 532 nm wavelength) corresponded to a potential OPCPA output of ~190 µJ pulse energy assuming the typical 10% OPA conversion efficiency [38]. In addition, the bulk glass compression stage had to be designed for the mJ-level output enabled by the next generation pump beam generation presented in Section 4.4. Thus, B-integral estimates were carried out and are discussed here for 100-µJ-level and few-mJ-level pulse energies.

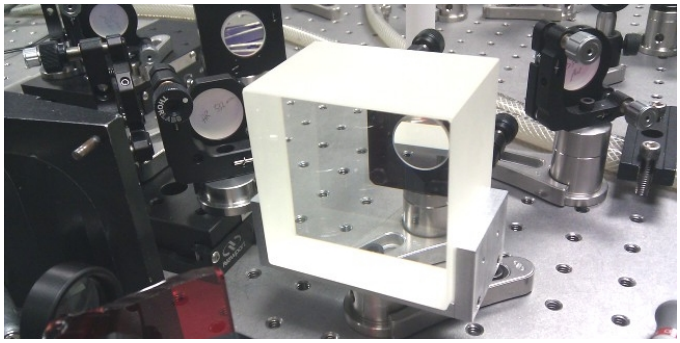

Figure 5-20: Picture of the SF57 bulk glass used for low loss, pulse compression. The thickness was 5 cm and the aperture 7 cm x 7 cm.

The estimated B-integral during the compression throughout the bulk material is given in Figure 5-21 for a low energy scenario up to 250 µJ. The beam size was chosen with 5 mm diameter

during the full compression. It can be seen from Figure 5-21 that the B-integral exceeded 1 for 250 µJ but was below 1 for the exemplary chosen energies of 10, 50 and 100 µJ. It can also be seen that the major contribution to the accumulated non-linear phase and B-integral were arising in the last 5 cm of propagation with an increase in the 100 µJ case (red curve) from 0.1 to ~1. In conclusion, a beam diameter of 5 mm supported numerically the compression within the B-integral limiting of pulse energies up to the 100-µJ-level.

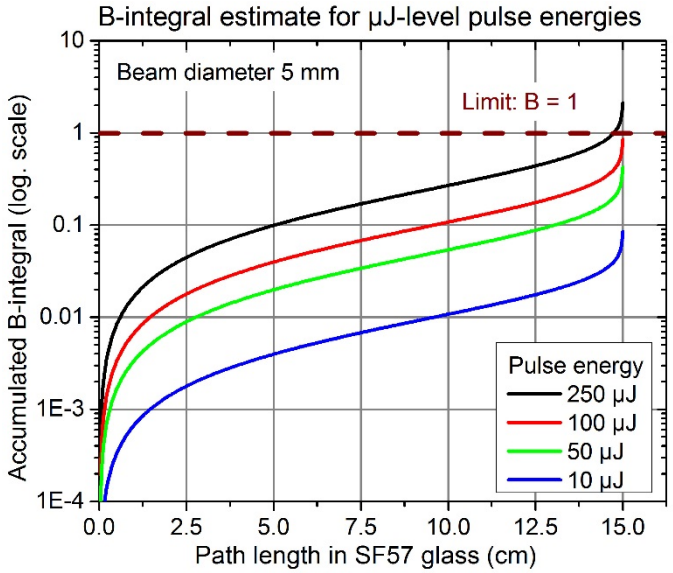

Figure 5-21: Relevant B-Integral estimates for the pulse compression in SF57 bulk glass with up to 250 µJ pulse energy and 5 mm beam diameter.

Compression of a pulse with energy largely exceeding 100 µJ required an increase in beam diameter to keep the accumulated B-integral below 1. Since the main contribution to the B-integral arises from the final section of compression, it was sufficient to increase the beam diameter for the last section of the propagation. Figure 5-22 shows the estimated B-Integral for exemplary compression of pulses with mJ-level energies, where the beam diameter was initially 2 cm (for the first 10 cm of propagation) and increased with a telescope to 4 and 6 cm (green, blue, cyan curves) for the last 5 cm section. It can be seen that the B-integral was ~0.6 in case of a pulse energy of 2 mJ, initial beam diameter of 2 cm and final beam diameter of 4 cm (green curve). The B-integral

estimate exceeded 1 in this case when the size was kept at 2 cm (black curve). Similarly, compression with 5 mJ energy and an initial beam diameter of 2 cm gave a B-integral estimate of <0.9 with a final diameter of 4 cm (blue curve) and <0.55 with 6 cm (cyan curve). The aperture of the SF57 bulk glass material is 7 cm x 7 cm, which could cause experimentally severe hard aperture clipping in case of the 6 cm beam diameter but would be sufficient for a diameter of 4 cm. Concluding, the B-integral for mJ-level pulse energies was kept numerically below the limit of 1 with the telescope approach and the 7 cm x 7 cm aperture.

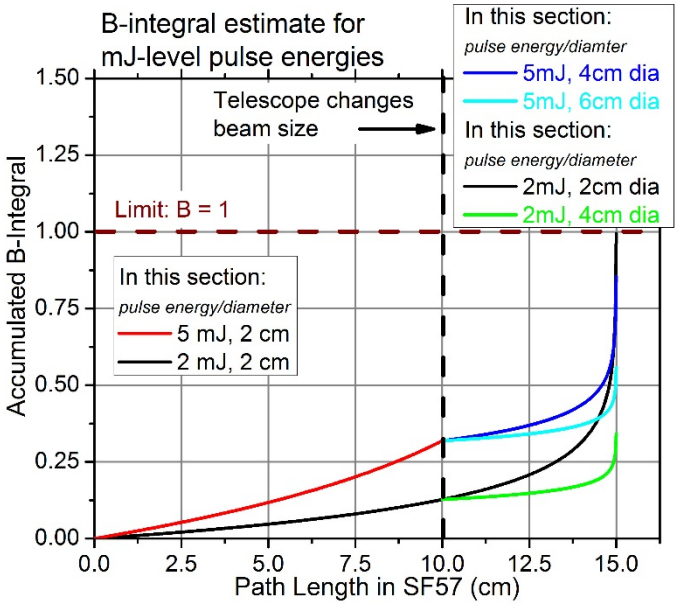

Figure 5-22: Relevant B-Integral estimates for the pulse compression in SF57 of up to 5 mJ pulse energy. The initial beam diameter was 2 cm followed by a telescope to increase diameter.

5.5 Non-Collinear Optical Parametric Amplifier

The OPA section of the HERACLES facility was experimentally investigated and the findings are described in the following. The amplification of the seed pulse was based on two OPA stages with 5-cm-long BBO. The presented experimental results in the following subsections were mainly obtained with the first OPA stage with the generated pump beam described in Section 5.3.

The following first subsection gives an overview of the utilized geometry and important properties of the pump beam. The second subsection presents experimental results.

5.5.1 OPA Geometry and Beam Properties

The OPA stages were seeded by the octave-spanning Ti:sapphire oscillator. Prior to the OPA, the seed pulses were stretched by the grism stretcher and AOPDF before incident on the BBO crystal with 5 mm length and 10 mm by 10 mm aperture. The pulse energy of the seed in the wavelength range from 700 to 1100 nm was estimated to be ~4 pJ with temporal distance of 24 ps between 700 to 1050 nm. A sketch of the OPA setup is shown in Figure 5-23 (a) and a picture of the laboratory setup in (b). Following the phase-matching parameters found in Section 3.5.1, the implemented magic angles were $\Theta = 23.7\ deg$ for the orientation of the crystal axis with respect to the surface normal, which incidents with the pump beam, and $\alpha = 2.3\ deg$ for the internal angle between pump and seed beam. The external angle between pump and seed was ~3.92 deg due to refraction on the BBO intersection.

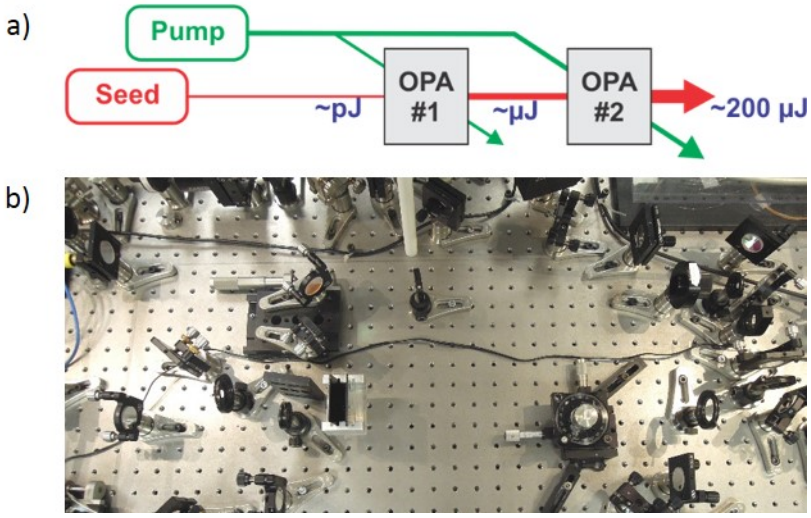

Figure 5-23: Sketch (a) and picture (b) of the two-stage OPA setup based on BBO as nonlinear crystals.

In a proof-of-principle study, the OPA configuration was experimentally implemented and briefly investigated based on the pump beam generation presented in Section 4.2. The available pump beam had an average power of 2.2 W at 532 nm wavelength and 10 kHz repetition rate. The obtained parametric gain at the first OPA stage was 10 with the pump beam focused to 130 µm diameter. The gain increased to 30 when focused to 100 µm and 100 with 77 µm diameter. The intensity in the last case corresponded to around 40 GW/cm² assuming ~200 µJ pulse energy and ~100 ps duration. The low parametric gain was mainly attributed to the small pump beam size and the effects presented in Section 3.5.3. As detailed in Section 3.5.3, the minimum pulse energy is 750 µJ to obtain an approximately uniform pump beam intensity and good overlap with the seed beam with picosecond pulses and 5 mm crystals. Thus, low parametric gain was the result. As a consequence of these finding, the pump beam generation was changed for a high energy system (shown in Section 4.3) with >1 mJ pump pulse energy as discussed in the following. This mentioned OPA stage with low pump pulse energy and low parametric gain was not investigated further.

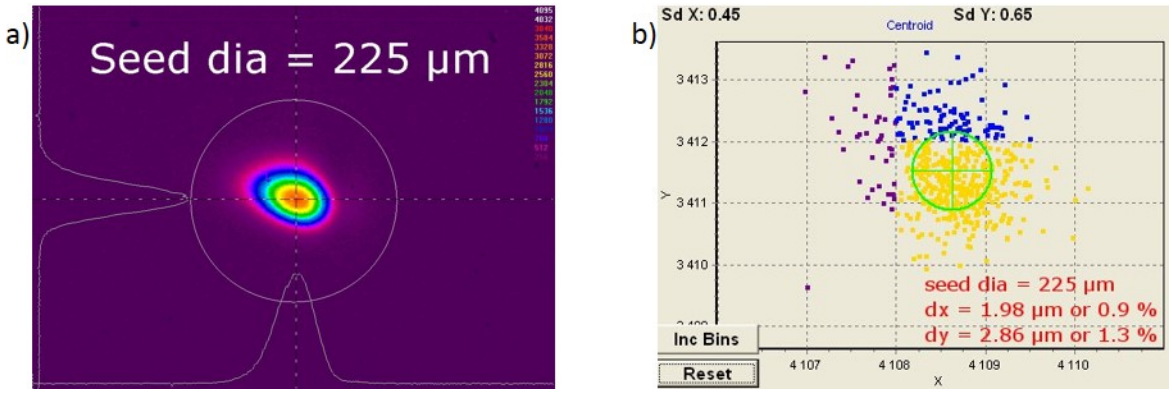

Figure 5-24: Beam profile of the focused seed beam (a) and the measured beam wandering (b) at the OPA plane.

In the following investigations, the pump beam was generated based on the high-energy DPSS amplifier presented in Section 4.3. The beam stabilities of the involved beams were investigated, which is discussed here. The focused beam profile and wandering of the seed beam

at the OPA plane were investigated and shown in Figure 5-24. The diameter of the seed beam was 225 µm with a beam wandering of 3.5 µm (Std. Dev.) or 1.6% of the beam diameter.

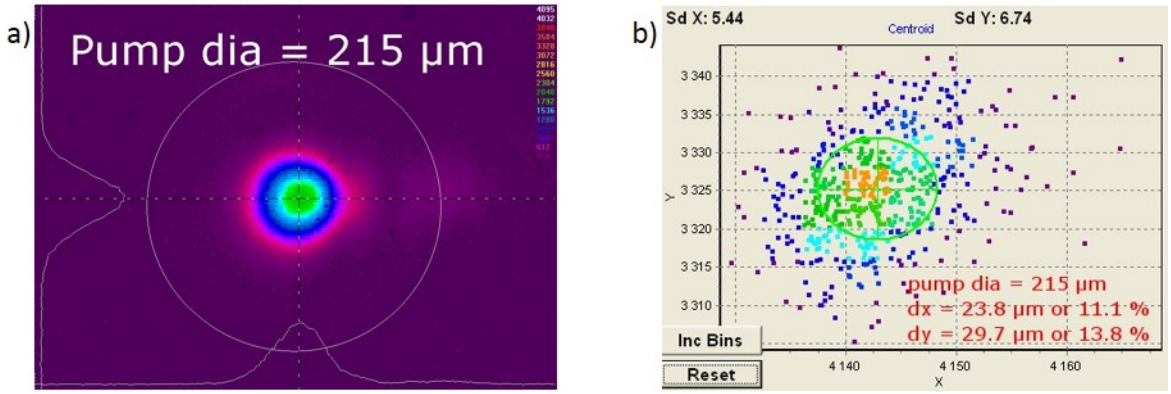

Figure 5-25: Beam profile of the focused pump beam (a) and the measured beam wandering (b) at the OPA plane.

The pulse energy of the pump beam was up to 1.9 mJ at 3 kHz repetition rate and 532 nm wavelength with an estimated pulse duration of 121 ps. The recorded beam profile and wandering at the OPA plane are shown in Figure 5-25. The focused beam size was kept similar to the seed beam diameter with 215 µm diameter, thus allowing pump intensities in excess of 40 GW/cm². The beam wandering was measured to be 38 µm (Std. Dev.) or 17% of the beam diameter. Although the beam wandering was already reduced in this second pump system from Section 4.3 compared to the one in Section 4.2, the measured beam wandering was still large enough to cause measurable OPA output fluctuations.

5.5.2 Experimental Results

In a proof-of-principle study, the superfluorescence was investigated. SF arises from the spontaneous down-conversion of a pump photon into a pair of signal and idler photons [153]. For high parametric gain, the SF can increase to a significant amount compared to the amplified seed [154]. The SF of the first OPA was briefly studied under non-optimized conditions. Figure 5-26 (a) shows the picture of the SF cone obtained after the OPA. In this configuration, the OPA was

detuned from optimized condition, which allows to observe simultaneously the smaller, non-amplified, seed beam and the superfluorescence cone as shown in Figure 5-26 (a). The elliptical shape of the SF hinted that the parametric gain could lead to distortions of the original seed profile, as seen in the following. A spectrum of the SF was recorded and showed a bandwidth of 88 nm (FWHM) centered at 810 nm in the case shown in Figure 5-26 (b). The spectrum of the SF was highly dependent on the tuned OPA geometry, as expected according to Section 3.5. Bandwidths of tens of nanometers were found ranging from almost 700 nm to more than 1000 nm, depending on the implemented phase-matching condition.

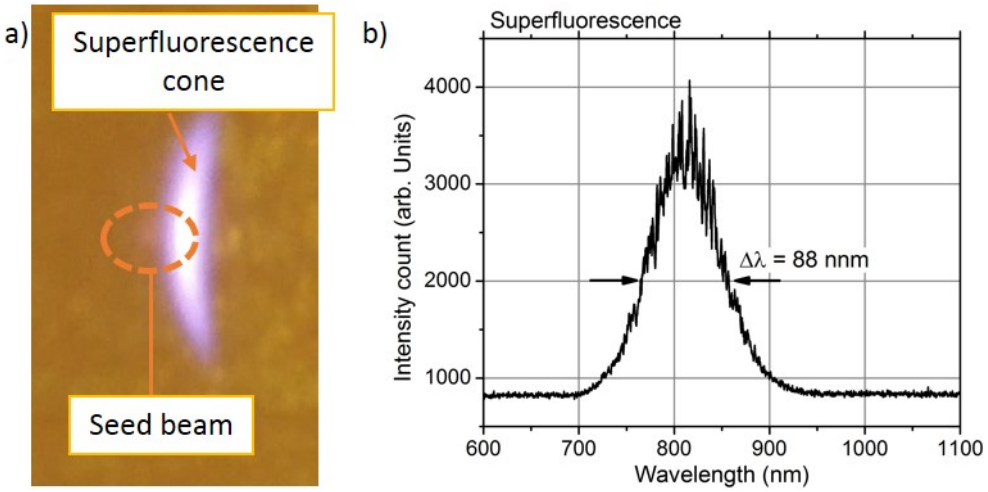

Figure 5-26: (a) Image showing the superfluorescence cone and the seed beam after the de-tuned OPA stage. (b) Recorded spectrum of the superfluorescence.

Shown in Figure 5-27 are the measured beam profiles of the seed signal (a) and amplified signal (b). The input beam profile was comparable to the profiles shown earlier in Figure 5-16 and exhibited slightly elliptical shape after passing through the AOPDF. After the parametric amplification, the beam profile showed a highly elliptical shape, which could potentially be cleaned with a spatial filter or shaped with cylindrical lenses. The amount of generated SF was measured to be negligible in this experiment compared to the amplified seed signal at the µJ-level.

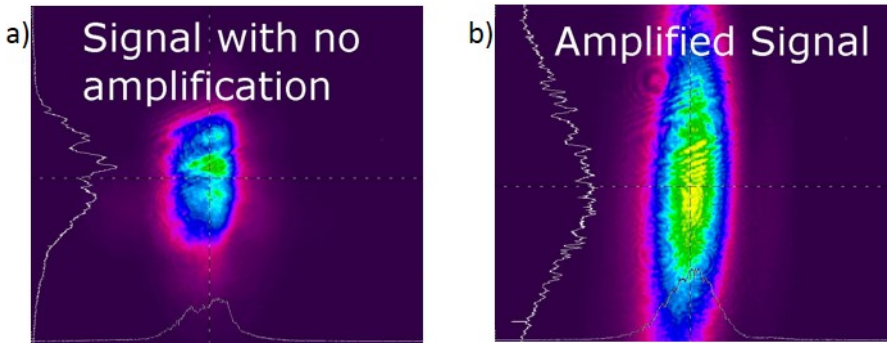

Figure 5-27: Obtained Beam profiles of the seed signal (a) and amplified signal (b).

The amplified pulse energy was studied in dependence of the OPA geometry and is shown in Figure 5-28. The small beam size of the pump beam resulted in an operating intensity which appeared to be close to the damage threshold of BBO. The latter can be found in the range from 32 GW/cm² for 8 ns pulses at 532 nm for bulk damage [156] to 7 GW/cm² for 250 ps for coating/surface damage (according to commercial manufacturer data). Thus, during operation potential damage could occur, particularly when the system was driven by high intensities to obtain high parametric gain or high conversion efficiency conditions.

As shown in Figure 5-27, the obtained parametric gain in the first amplifier was highly dependent on the pump beam focusing geometry. For example, if the beam was focused directly at the OPA plane (black curve) a moderate parametric gain of >6,000 was observed followed by damage at a pump energy of 0.41 mJ. In contrast, when focusing clearly in front of the OPA crystal (green) a gain of 5,000 was achieved at a pulse energy of 0.9 mJ without damage to the crystal. The highest gain was achieved in a range between these two with a gain of up to 9,000 (red curve). In this case, damage started to occur at 0.8 mJ pulse energy. In this experiment, it was not possible to estimate accurately and reliably the exact distance between focal point and OPA plane as well as the corresponding beam size. Estimates were given when possible.

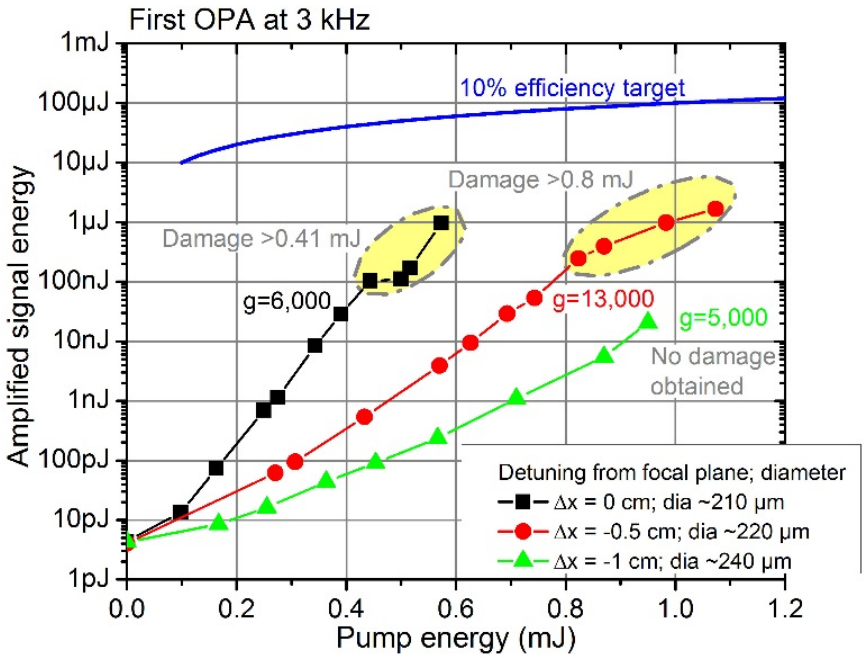

Figure 5-28: Amplified signal energy for different pump energies geometries.

In the presented geometry, the seed energy was amplified from ~4 pJ to the 10-µJ-level with a gain of approximately 10^4. Crystal damage was consistently obtained for pulse energies above the µJ-level due of the high pump intensity close to the BBO damage threshold. Onset of crystal damage occurred at higher intensities after seconds and at lower intensities after several minutes. Stable output power was obtained for each of the measured pump geometries in Figure 5-28 with energies of 29 nJ (black), 53 nJ (red) and 20 nJ. The corresponding pulse-to-pulse fluctuations were measured to be 22% for the first case (black), 20% for the second case (red) and 45% for the last case (green). The values for maximum and minimum pulse energy over 20 seconds were measured for the high gain case (black) with 63% minimum and 200% maximum energy.

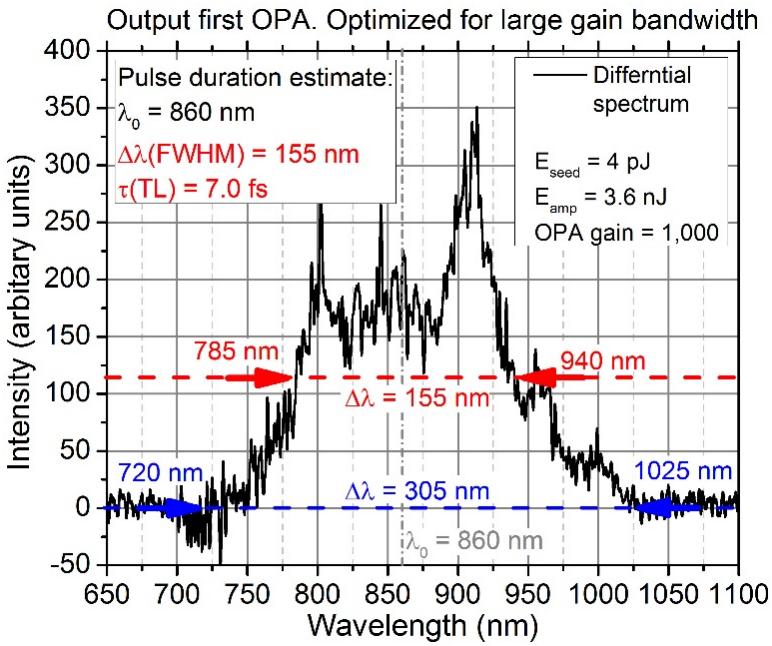

Figure 5-29: Recorded spectrum of the amplified signal indicating a bandwidth of more than 150 nm corresponding sub-10-fs TL duration.

The spectrum of the amplified signal was investigated at a modest gain of 1,000 and shown in Figure 5-29. The amplified spectrum showed a FWHM of 155 nm centered at 860 nm which corresponded to a transform-limited pulse duration of 7.0 fs assuming Gaussian pulses. The full amplified bandwidth ranged from 720 to 1025 nm overlapping well with the expected gain bandwidth in BBO ranging from 725 to 1050 nm.

5.6 CEP Control

The CEP control scheme implemented in HERACLES is shown in Figure 5-30 and was following the typical method described in Section 3.4. and [11]. The output of the Ti:sapphire oscillator was stabilized with a so-called 'fast' stabilization loop operating with ~100 kHz bandwidth, while the OPCPA output could be stabilized with a 'slow' stabilization loop operating at less than 100 Hz bandwidth.

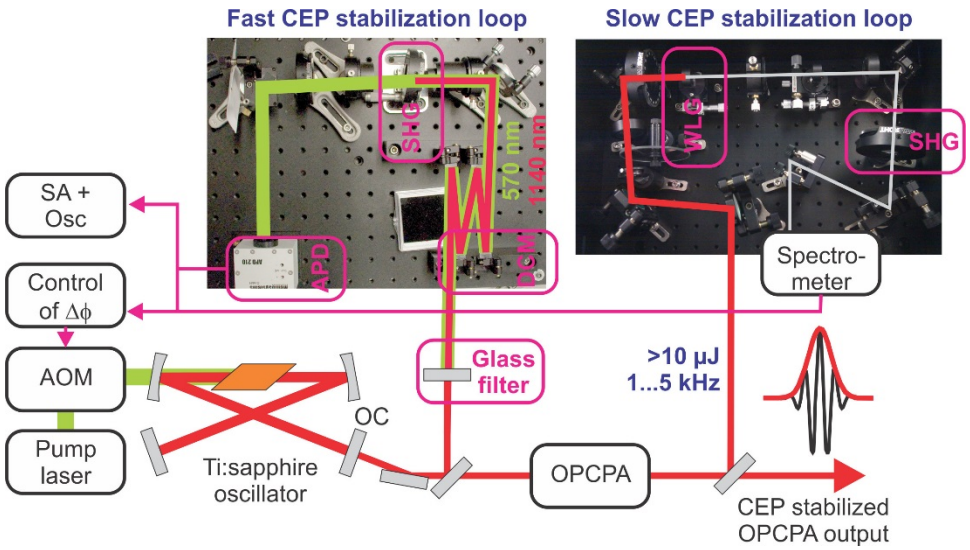

Figure 5-30: The sketch of the CEP locking method used in HERACLES for compensating of fast and slow drifts.

For the fast CEP locking method, a portion of the oscillator output was directed to a f-to-2f interferometer (MenloSystems, Inc.). The SHG of the signal at 1140 nm was frequency mixed with a portion at 570 nm. The resulting beat signal was detected with an avalanche photo diode (APD) and the beat tone referenced with the phase locking electronics (MenloSystems GmbH) to 1/4 of the repetition rate of the Ti:sapphire oscillator. The phase locking electronics detected slight deviations from this reference frequency and feedback was given to an AOM which modulated the pump intensity with a bandwidth of up to 1 MHz. These slight pump intensity modulations could change locally the temperature of the Ti:sapphire crystal and thus, change precisely the optical path length of the resonator. This fast feedback loop operated on a short time scale (>10 µs) limited by the ~100 kHz bandwidth of the phase locking electronics.

The slow CEP stabilization loop (APS800, MenloSystems GmbH) was available but not implemented due to the required compressed few-cycle pulse energy at the µJ-level. The scheme is described in the following. The fast stabilization scheme was anticipated to be seeded by the high energy, few-cycle OPCPA output. To enable the stabilization method, each input pulse was required to have a similar CEP, which is in contrast to the fast CEP stabilization and locking to 1/4

of the repetition rate. This requirement could be satisfied by proper pulse picking in the pump beam generation and OPA enabling the kHz pulse train to have similar pulse-to-pulse CEP. In the scheme, white light generation (WLG) was used for spectral broadening of the OPCPA output to obtain an almost octave-spanning spectrum. The CEP drift could be retrieved from the spectral interference pattern over several pulses of the fundamental and its SH. Any movement of the resulting interference pattern would indicate a slight change in CEP due to a drift in the OPCPA chain. A simple offset feedback signal would be applied to the AOM of the fast loop causing the OPCPA output to be stabilized and controlled to the desired CEP for further experiments.

5.7 Summary

Major components and employed methods used for the design and implementation of the few-cycle OPCPA facility HERACLES are presented conceptually, numerically and experimentally in this chapter. Key aspects, results and challenges are discussed. The OPCPA architecture of HERACLES, its ultrafast front-end as well as the utilized pump beam generation are described in detail. The concept of few-cycle dispersion management with bulk compression at the 100-µJ-level and few-mJ-level was numerically studied and is presented. The implemented OPA stage was investigated in detail based on the available 1.9 mJ pump pulse energy and conclusions about minimum energy requirements are discussed. An OPA output at the µJ-level pulse energy with a parametric gain of 10^4 was observed with an amplified bandwidth ranging from 720 to 1025 nm supporting sub-10-fs TL duration. The CEP locking method and its implementation is described. The HERACLES facility was designed to provide high-energy and high-average power, few-cycle pulses for highly nonlinear experiments.

6 TOWARDS HIGH-AVERAGE POWER, 10 MHz OPCPA

The literature study from Chapter 2.4 revealed that there is a performance gap from OPCPA systems operating at ultra-high repetition rates above 1 MHz. Two OPCPA systems have been reported operating at 1 MHz. The first system was mainly intended as proof-of-principle study of MHz OPCPA operating with sub-1-µJ pulse energy [83]. The authors of the second system were able to report the currently highest average power from OPCPA systems with 22 W and relatively high pulse energy of 22 µJ corresponding to a peak power of 4.4 GW [39]. The high performance of the latter was mainly enabled by previous improvements on the fiber-based amplifiers allowing a pump beam generation of 185 W average power. Thus, multi-MHz OPCPA would require overcoming a few technological challenges and therefore a few new concepts are introduced. An OPCPA system potentially resulting in the successful implementation of a 10 MHz OPCPA systems is presented in this chapter.

The research effort presented in this chapter was conducted at CELIA - “Centre Lasers Intenses et Applications” (the Center for Intense Lasers and Applications) at the University of Bordeaux 1 in Talence, France. The chapter begins with an introduction to multi-beam OPA pumping. Advantages and challenges of this technique as well as the anticipated OPCPA architecture are discussed in Section 6.1. The experimental investigations of the seed signal generation are presented in Section 6.2. Section 6.3 describes the implemented pump beam generation setup based on rod-type fiber amplifiers [54]. The early implementation steps of the OPA are treated in Section 6.4, followed by discussion about the limitations of the process in Section 6.4.2. The chapter is summarized in Section 6.5.

6.1 Architecture for Multi-Beam OPA

As found in Chapter 2, fiber-based CPA laser systems with relatively high pulse energy, high peak power, and high average power can be operated with 100 kHz to MHz repetition rates and show excellent pulse stability of which OPCPA system could benefit [78]. Thus, fiber amplifier-based systems show high potential for the implementation in high average power OPCPA pump lasers. The obtainable peak power is limited in these systems to the onset of nonlinearities [157]. The average power in high peak power fiber systems was recently shown to be limited by mode-instabilities leading to fluctuations in obtainable beam quality [158] [159]. Within these limitations, three noteworthy reported systems with record performances are named in the following. A fiber-based CPA system has been reported operating with 2.2 mJ output pulse energy, sub-500-fs duration and 3.8 GW peak power [160]. Another CPA systems was presented with 830 W average power, 640 fs pulse duration and a peak power of 12 MW [161]. An implemented OPCPA pump system was reported with 185 W average power, 710 fs pulse duration and 260 MW peak power [39]. In addition, it has been shown that the high stability of fiber-based CPA systems allows the coherent combination of several fiber-based amplifier channels into a single output with increased peak power of several GW [162] [14].

On the other hand, it has been shown that OPA with multiple pump beams can improve the OPCPA output performance. Employing two pump beams can increase the parametric amplification bandwidth [163] as well as the obtainable average power [164] compared to traditional OPCPA. Thus, combining the benefits of multi-beam pumping with the benefits of fiber-based CPA amplifier systems could make it feasible to generate 10 MHz OPCPA systems. Research elements directed towards 10 MHz OPCPA and multi-beam pumping with fiber-based pump beam generation are presented in this chapter. The architecture for the experiments towards

10 MHz OPCPA and multi-beam pumping is shown in Figure 6-1. The seed generation is presented in Section 6.2 and was based on supercontinuum generation in highly nonlinear fibers. The pump beam generation centered at 1030 nm was based on rod-type Yb-doped fiber technology and is covered in detail in Section 6.3. The OPA design foresaw to pump the OPA stage by up to three parallel rod-type fiber amplifiers corresponding to the available number of rod-type fiber amplifiers.

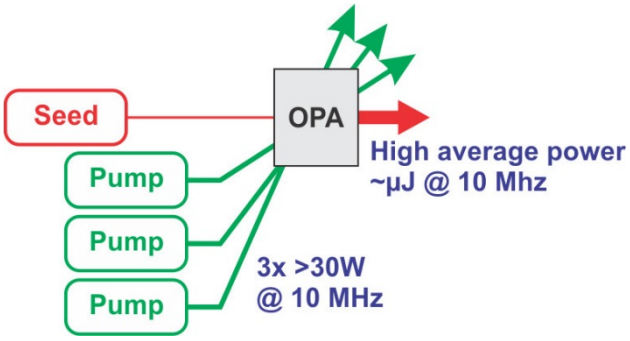

Figure 6-1: Sketch of the OPA pump beam combining scheme used in the experiment.

The front-end of the OPCPA architecture was a relatively high-energy, ultrafast oscillator which provided the seed pulses for signal and pump beam generations This front-end consisted of a two-crystal, Yb:KGW-based, long cavity, 10 MHz repetition rate oscillator (T-pulse, Amplitude Systemes). The maximum output average power was 4.5 W corresponding to a pulse energy of 450 nJ, centered at a wavelength of 1028 nm with a bandwidth of ~4 nm corresponding to a transform-limited pulse duration of 300 fs and approximately sech^2 temporal pulse shape. The relatively high pulse energy and peak power allowed the generation of significant nonlinear effects when, for example, tightly focused in highly nonlinear fibers without intermediate amplifiers. Thus, self-phase modulation (SPM) or soliton self-frequency shift (SSFS) were explored to generate a seed signal covering a wavelength range from 1.5 to 2.0 µm for the OPA stage.

6.2 Supercontinuum Seed from Highly Nonlinear Fibers

Operating at the pump wavelength of 1030 nm in the OPCPA system requires a seed pulse with longer center wavelength which has to be temporally synchronized with the front-end oscillator. The high energy, ultrafast pulses can be used to obtain nonlinear effects during their propagation in highly nonlinear fibers [165]. Coherent supercontinuum generation involving the nonlinear effects of SPM and soliton self-frequency shift (SSFS) can be potentially employed to obtain suitable OPA seed pulses in the range from 1.5 to 2.0 µm. The preformed numerical and experimental investigations towards this seed source are described in the following.

6.2.1 Analytical and Numerical Treatment

In this first section, important parameters are introduced in order to understand the processes occurring during the propagation of high peak power pulses in highly nonlinear fiber. The analytical discussion presented here follows directly the expressions given in a comprehensive review on the topic [166]. The peak power P_0 of an optical pulse can be represented by

$$P_0 = \frac{E_0}{2\,T_0}, \tag{68}$$

where E_0 is the pulse energy with the duration T_0 of the optical pulse defined for different pulse shapes by

$$T_0 = \frac{\tau_{FWHM}^{Gauss}}{1.65} = \frac{\tau_{FWHM}^{sech^2}}{1.76}. \tag{69}$$

The so-called dispersion distance L_D is given by the expressions

$$L_D = \frac{T_0^2}{|\beta_2|}\ and \tag{70}$$

$$L_D' = \frac{T_0^3}{|\beta_3|} \tag{71}$$

for second $|\beta_2|$ and third order dispersion $|\beta_3|$, respectively. During the propagation the nonlinear coefficient γ is an important measure of the nonlinear effects and given by

$$\gamma = \frac{n_2\ \omega_0}{c\ \alpha_{eff}}, \tag{72}$$

where n_2 is the nonlinear refractive index of the material, c the speed of light, α_{eff} the effective MFD and ω_0 the angular frequency. The nonlinear fiber length L_{NL} can be calculated by

$$L_{NL} = \frac{1}{\gamma\ P_0}, \tag{73}$$

providing an estimate on the propagation length until nonlinear effects become relevant.

It is well known that optical pulses can propagate like solitons under nonlinear conditions, where SPM and dispersion compensate each other. As a consequence of the soliton-like regime, the shape of the optical pulse is conserved during the nonlinear propagation. Thus, he pulses leaving the fiber can have ultrashort duration even after long propagation distances with a high amount of dispersion. Part of the here presented investigations consider the generation of soliton during propagation followed by SSFS. An important measure of the number and behavior of the generated solitons is given by the soliton number

$$N^2 = \frac{L_D}{L_{NL}} = \frac{T_0^2}{|\beta_2|}\frac{\gamma\ P_0}{1} = \frac{n_2\ \omega_0}{2\ c}\frac{E_0 T_0}{\alpha_{eff}|\beta_2|}, \tag{74}$$

which gives an estimate of the number of solitons potentially involved in the nonlinear interaction process during propagation. The expression can be reduced to

$$N^2 \sim \frac{E_0 T_0}{\alpha_{eff}\,|\beta_2|}. \tag{75}$$

From this expression, it can be seen that the soliton number N increases with increasing peak power but decreases with increasing effective MFD and dispersion. The distance after which soliton fission L_{fiss} occurs is given by

$$L_{fiss} \sim \frac{L_D}{N} \propto T_0\,. \tag{76}$$

The duration T_k of the k-th soliton is given by the expression

$$\mathrm{T_k} = \frac{T_0}{2N + 1 - 2k}, \tag{77}$$

which scales inversely with N. The peak power P_k of the k-th soliton is given by

$$P_k = \frac{(2N + 1 - 2k)^2}{N^2} P_0\,. \tag{78}$$

During the propagation, the soliton experiences a frequency shift called soliton self-frequency shift (SSFS) [166] given by the following equation for the k-th soliton

$$\Delta\nu_{\mathrm{R,k}} = -\frac{4\,T_R\,|\beta_2|\,z}{15\,\pi\,T_k^4}. \tag{79}$$

For the first soliton, the expression can be modified to

$$\Delta\nu_{R,k=1} \sim \frac{|\beta_2|\,(2N-1)^4\,z}{T_0^4}. \tag{80}$$

Based on these equations, the ratios between the initial pulse duration T_0, peak power P_0 and energy E_0 in comparison to the 1st order soliton were determined and are listed in Table 6-1. It can be seen that the first order soliton ($k = 1$) has highest pulse energy but longest duration. On the other hand, the peak power increases from 1-times towards 4-times the initial peak power for increasing soliton order k.

Table 6-1: Calculated ratios for the soliton of order k to the initial pulse for pulse duration, peak power and energy.

k	E_k/E_0	T_k/T_0	P_k/P_0
1	1	1	1
2	0.15	0.33	2.25
5	0.03	0.11	3.2
25	0.005	0.02	3.8
50	0.0025	0.01	3.9

Based on these analytical investigations, two contradictory conclusions can be found. A low soliton order N is preferred to achieve high pulse energy, which can be on the order of the initial pulse duration. In addition, the first soliton is preferred since the soliton-self frequency shift is largest (k=1). However, a higher N and larger second order dispersion $|\beta_2|$ are desired to achieve a larger shift.

To gain more insight, numerically simulations based on the commercially available software package FiberDesk (Fraunhofer Institute for Applied Optics and Precision Engineering IOF, Jena, Germany) were performed. Figure 6-2 shows an exemplary simulation for a case of a low soliton order N, short input pulse duration (50 fs) at 1030 nm center wavelength during propagation in 1 m of fiber. After a few cm of propagation the initial 50 fs pulse broke up and soliton fission took place. While the formed soliton propagated, soliton self-frequency shift occurred and the soliton center wavelength shifted from ~1.1 to >1.2 µm at the end of the propagation.

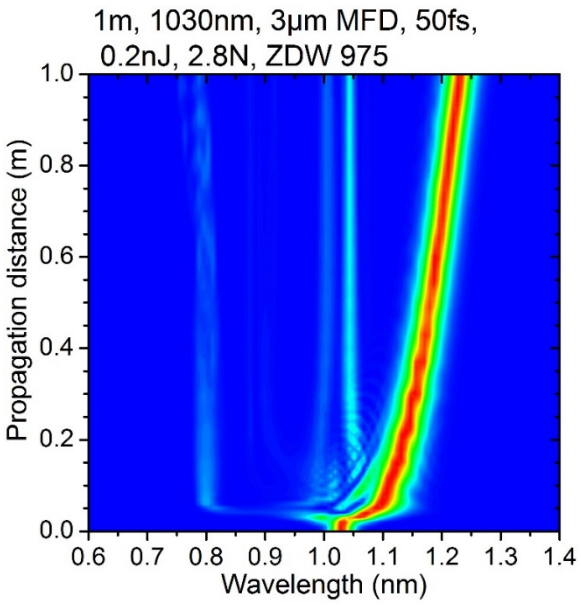

Figure 6-2: FiberDesk simulation of an exemplary propagation with low soliton order N and short pulse duration in 1 m of silica fiber.

Figure 6-3 shows selected spectrograms obtained from the same exemplary simulation. The color intensity of each spectrogram was normalized. At $z = 0\ cm$ (a) the initial, transform-limited 50 fs pulse can be seen. After a few cm of propagation (at $z = 3\ cm$, (b)) the pulse started to breakup and subsequently shifted towards longer wavelengths. After $z = 30\ cm$ (c), the soliton propagated due to the dispersion at roughly 1 ps temporal distance before the residual 1030 nm pulse. During further propagation, shown in (d), (e) and (f), the temporal separation of the soliton increased to 4 ps (at $z = 100\ cm$) and the central wavelength shifted to more than 1.2 µm. The presented case shows conceptually the process of SSFS. In addition, this graphical illustration of the nonlinear propagation retrieved from the simulations is not obtainable from experiments and thus, allows to gain further insights into the process.

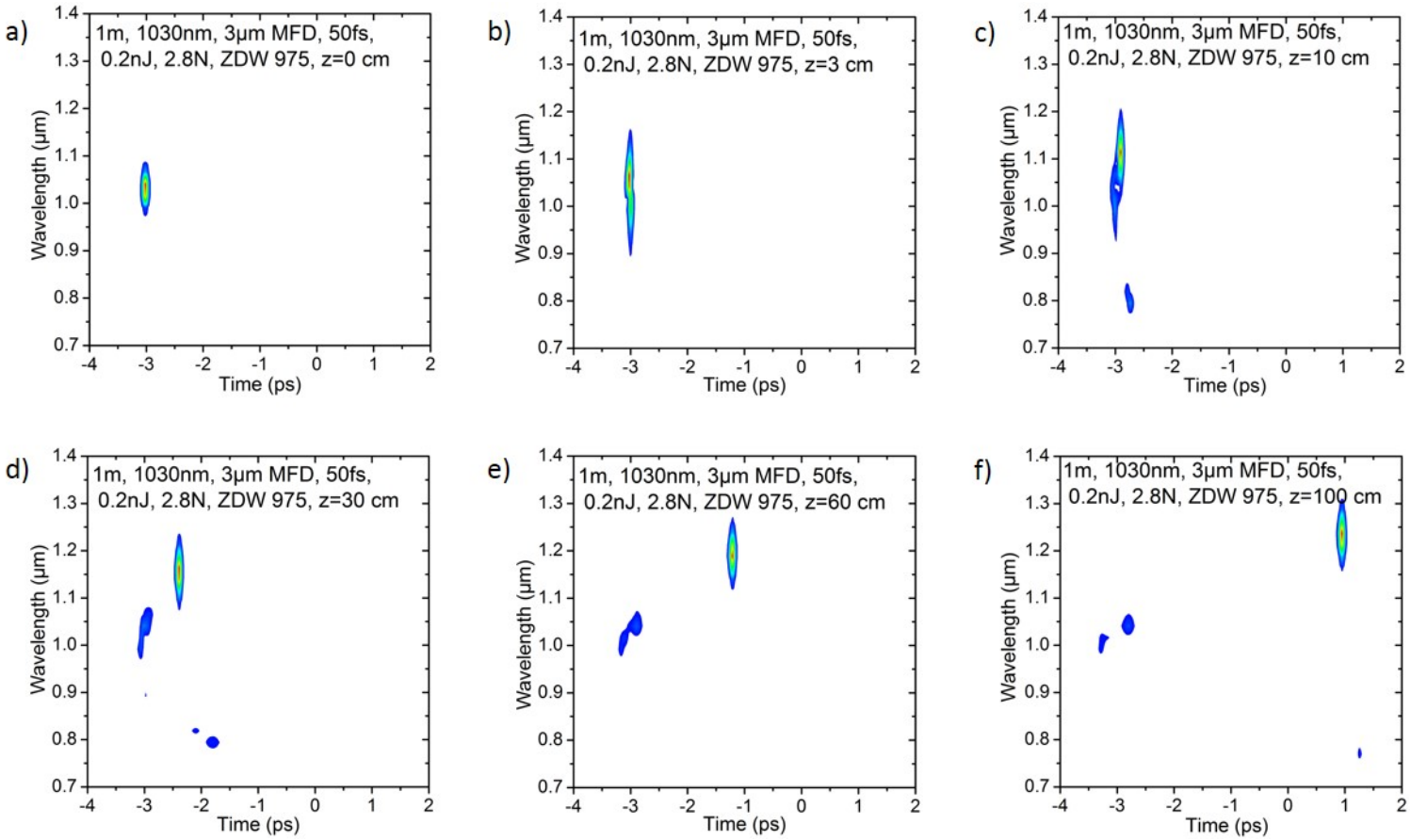

Figure 6-3: FiberDesk simulations of an optical pulse propagating under highly nonlinear conditions with low soliton order ($N = 2.8$). Spectrograms are given at the propagation lengths of 0 (a), 3 (b), 10 (c), 30 (d), 60 (e) and 100 cm (f).

Figure 6-4 illustrates a simulated case, where a high soliton order (N = 51.9) was chosen while MFD, nonlinearity and dispersion were kept to the same value as in the previously shown simulation of Figure 6-2. It can be seen in Figure 6-4 (a), that the initial 50 fs pulse broke up after a few cm of propagation into several soliton pulses. Figure 6-4 (b) shows the obtained first soliton (k = 1). A large frequency shift of this soliton to 1.65 µm center wavelength was observed and the soliton was temporally confined to ~100 fs. The overall output spectrum ranged from 0.6 to 2.25 µm in this simulation.

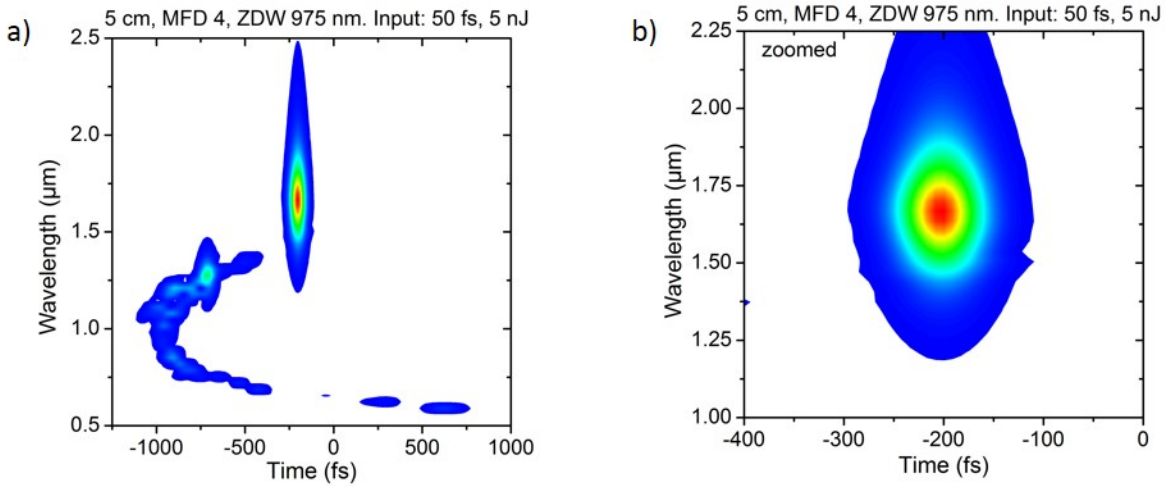

Figure 6-4: (a) FiberDesk simulation of an exemplary propagation with high soliton order N and short pulse duration. (b) Plot showing a zoomed view on the first soliton.

Concluding the numerical investigations, it seems feasible to obtain seed pulses via supercontinuum generation and fs pulses satisfying the OPA requirements with ps duration and center wavelength shifted towards 2 µm. Due to the limited experimental insight into the nonlinear propagation process, FiberDesk simulations allow to approximate the actual propagation conditions. Thus, the propagation simulations could be utilized with the experimental data and potentially be used to improve the experimental setup.

6.2.2 Experimental Results

In the following, the high energy, 300 fs pulses from the front-end at 1030 nm center wavelength and 10 MHz repetition rate were coupled into highly nonlinear fibers to obtain a nonlinearly broadened spectrum ranging into the mid-IR. Two highly nonlinear fibers based on a PCF structure from NKT Photonics A/S were available for the experimental study as well as a prototype fiber with ~3 µm MFD from Limoges University. Figure 6-5 shows a laboratory picture of the typical output of one of these fibers.

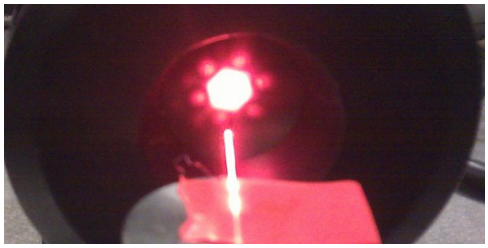

Figure 6-5: Laboratory picture of the output of a highly nonlinear fiber.

The investigation of efficient power coupling into these fibers was necessary in order to avoid damage to the input fiber facet due to the high peak and average power. The position and focal length of an additional lens in the beam path as well as the high NA coupling lens were varied to find the best coupling ratio. The combination of a lens of $f = 0.4\,m$ before the coupling stage and a high NA aspheric lens (Thorlabs, Inc.) with $NA = 0.68$ resulted in best coupling efficiency in the fiber. Typical values for the coupling efficiency for the 3 fibers under test were 25% for the 3 µm MFD proto-type fiber (termed “Limoges University fiber”), 34% for NL-3.7-975 and 15% for NL-2.8-840 (both NKT Photonics A/S). The datasheet of the fibers from NKT Photonics specified the core diameter to be 3.7 and 2.8 µm as well as the zero dispersion wavelengths (ZDW) of 975 and 840 nm, respectively.

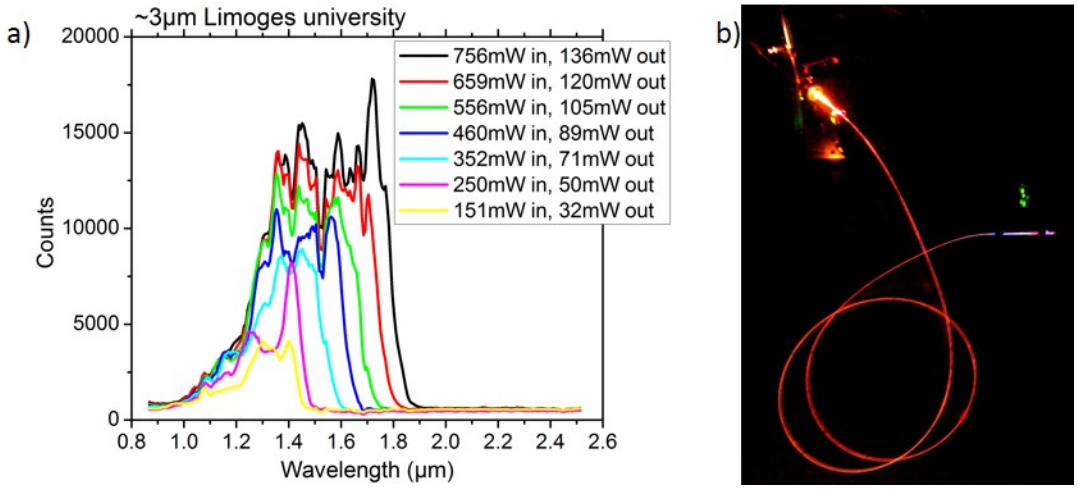

Figure 6-6: (a) Measured optical spectra for different input power levels with the fiber of ~3.0 µm core diameter. (b) Photograph of the setup during operation.

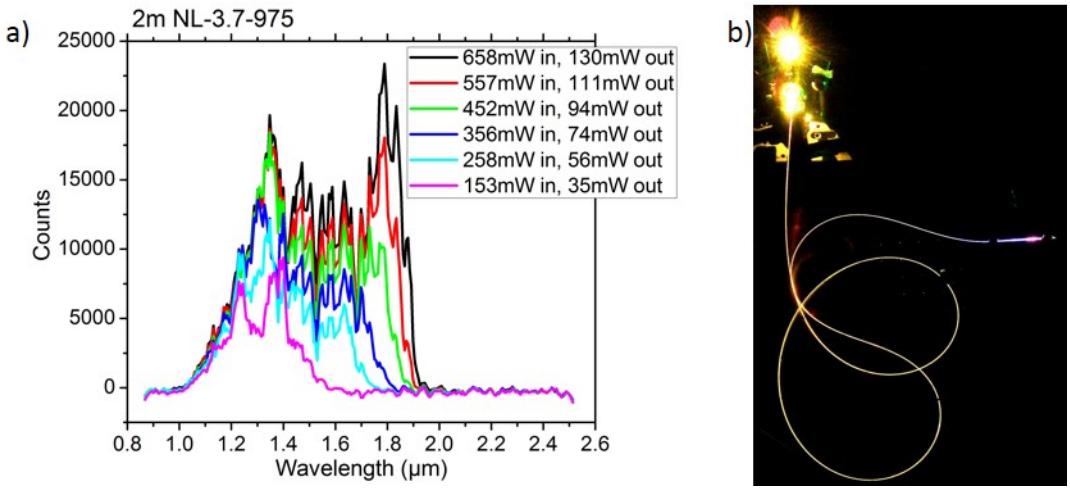

Figure 6-7: (a) Measured optical spectra for different input power levels with the fiber of ~3.7 µm core diameter and ZDW 975 nm. (b) Photograph of the setup during operation.

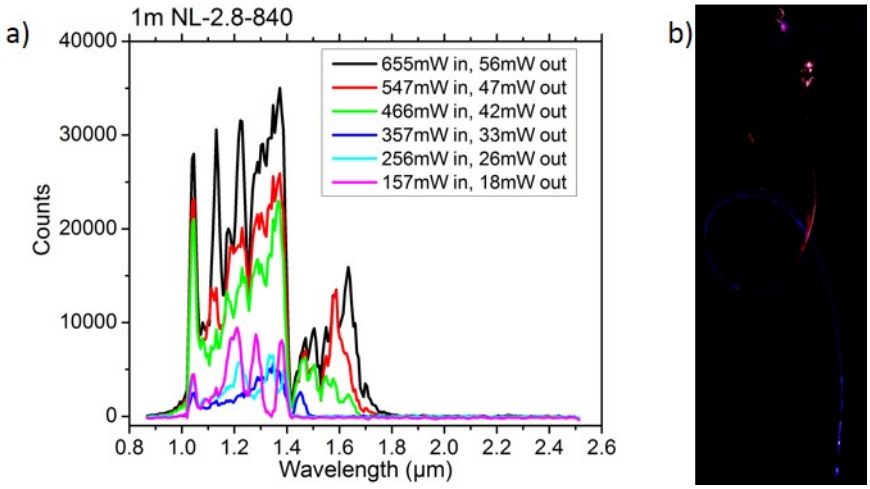

Figure 6-8: (a) Measured optical spectra for different input power levels with the fiber of ~2.8 μm core diameter and ZDW 840 nm. (b) Photograph of the setup during operation.

Figure 6-6, Figure 6-7 and Figure 6-8 show the measured output spectra of the three fibers under test (FUT) for different input power levels. As it can be seen from the plots, increasing the average power increased the long wavelength cut-off in all experiments. The longest wavelengths achieved were 1.9 μm for the Limoges University fiber, 1.95 μm for the NL-3.7-975 fiber and 1.7 μm for NL-2.8-840. The measurements show that the experientially obtainable wavelengths were almost ranging to the 2-μm-level. Note, that the NL-2.8-840 fiber showed damage at the highest average power level and was not investigate further at high power conditions.

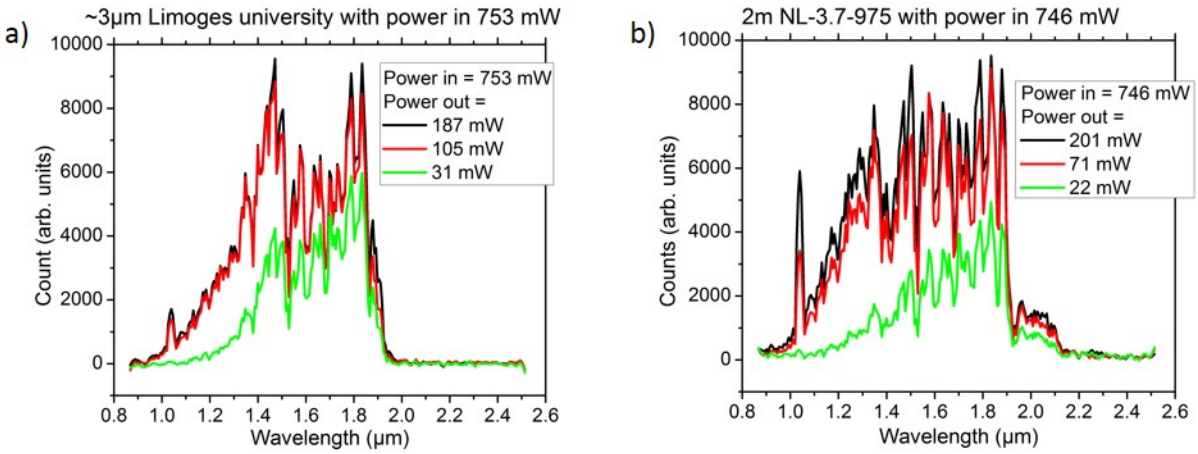

Figure 6-9: Output spectra measured with the Limoges prototype fiber (a) and the fiber with 3.7 µm core diameter (b) at highest input pulse energy (black). Colored glass filters were employed to estimate the power in the long wavelength spectral region (red and green).

Further, the pulse energies in the mid-IR range were estimated. Two different colored glass filters were employed to absorb almost all power outside of the wavelength range from 1.3 to >2 µm. Thus, the output power within the selected wavelength range can be measured. The pulse energies in this wavelength range assuming 10 MHz repetition rate were estimate to be 3 nJ for the Limoges University fiber and 2 nJ for the NL-3.7-975. Since the first OPA stage in the OPCPA architecture required approximately a few nJ of seed energy in this spectral range, each of these fibers were a good candidate for seeding the OPA.

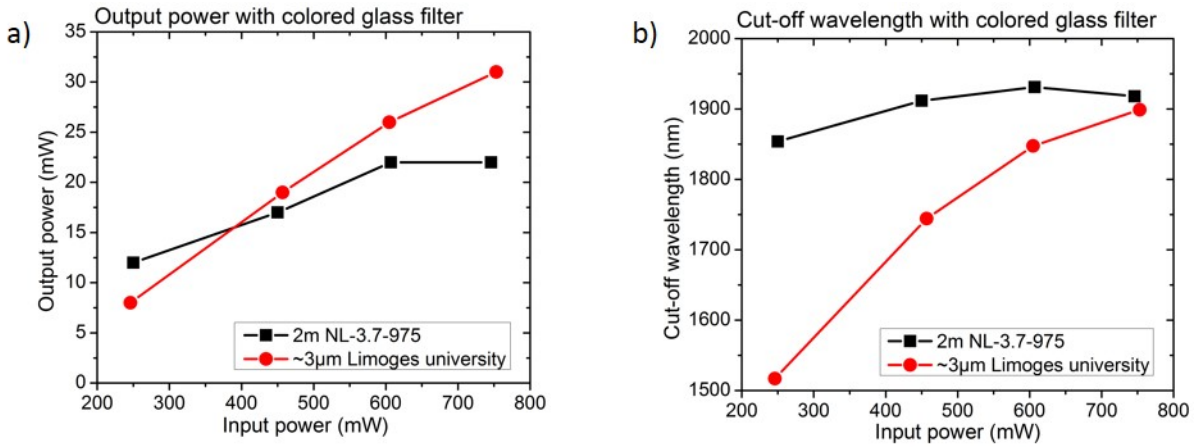

Figure 6-10: For the Limoges and the 3.7 µm core diameter fiber the pulse energy and spectral cut-off is shown.

Figure 6-10 shows the measured output power across the defined mid-IR range (a) and cut-off wavelength (b) for several pump powers. The 3 µm Limoges University fiber showed greater output power at the highest input power compared to the NL-3.7-975. For the highest input powers, the cut-off wavelengths of both fibers approached 1.91 µm. The 3 µm Limoges University was chosen for further investigations due to the higher output power.

Furthermore, the output was temporally characterized with a home-built cross-correlation between the supercontinuum output of the Limoges University prototype fiber and the transform-limited oscillator output. The used BBO crystal showed an output (full) bandwidth of only ~20 nm, which made it necessary to obtain two measurements at different fixed center wavelengths. The combined cross-correlation spectrogram, as shown in Figure 6-11 measured with 0.66 ps and sub-nm resolution, showed a continuum ranging from 1530 to 1690 nm spanning 12 ps in time. Longer wavelengths than 1.7 µm were not measured with the home-built cross-correlator potentially due to poor phase-matching, low sum-frequency efficiency or low fundamental peak power. No soliton structures with sub-ps temporal shape were observed in the supercontinuum with the cross-correlator. The NL-3.7-975 was expected to show a similar spatio-temporal characteristic but was not experimentally characterized with the cross-correlator.

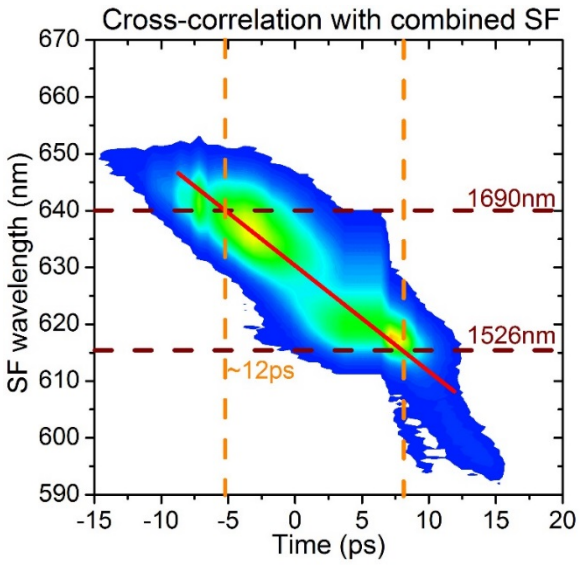

Figure 6-11: Cross-correlation between the supercontinuum output of the Limoges prototype fiber and the transform-limited oscillator output at 1030 nm and 300 fs duration.

In summary, each generated supercontinuum covered a broad wavelength range up to >1.9 µm wavelength. Pulse energies from 2 to 3 nJ were measured in the range from 1.3 to 2.0 µm. The temporal confinement was characterized to be 12 ps for the range of 1530 to 1700 nm. In conclusion, the supercontinuum generation seeded by the 300 fs oscillator and employing either the Limoges University fiber or the NL-3.7-975 fiber were determined suitable for the seed beam generation for the desired OPA application.

6.3 Rod-Type Fiber-Based Pump Beam Generation

Rod-type fiber amplifiers offer high average power operation with comparably large MFDs [167]. The here implemented OPA pump beam was derived from the front-end ultrafast oscillator. Due to its already high pulse energy and average power only a moderate amplification gain of less than 20 dB is required to obtain MW-level peak powers. This amplification is typically obtainable from a single high-gain amplifier stage. Thus, the design of the pump beam generation was based on a rod-type fiber amplifier with 80 µm core diameter and a mode field diameter at 1030 nm of

60 to 65 µm [168] [169]. The rod was pumped with an optical power of up to 140 W at 975 nm. The pump light was guided in the cladding, which had a diameter of approximately ~200 µm [54]. Figure 6-12 shows a sketch of the setup (a) and a laboratory picture at high pump power (b).

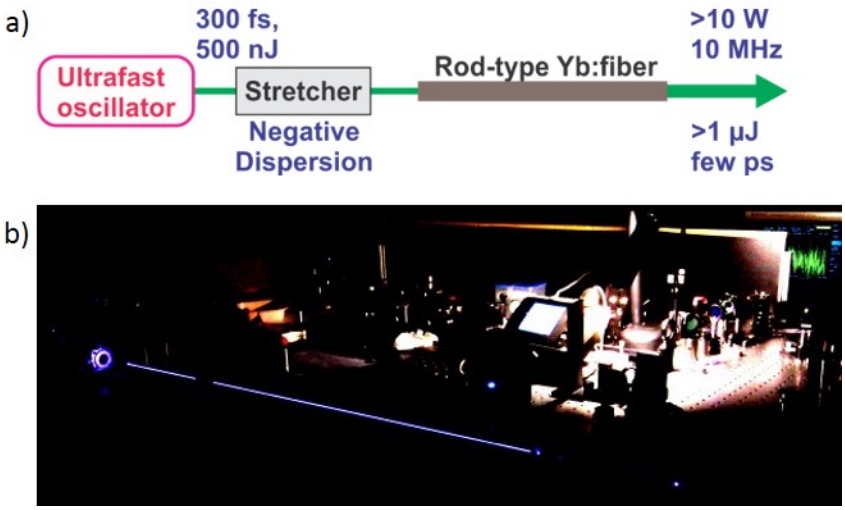

Figure 6-12: Sketch of the implemented pump beam generation (a) and photograph of the experimental setup during operation (b). The output is directed to the OPA stage.

6.3.1 Pulse Duration and High-Power Amplification

As shown in the sketch of the design of the pump beam generation in Figure 6-12 (a), a folded Martinez-like stretcher was implemented to allow adjustment of the pulse duration of the pulses launched into the rod-type fiber amplifier. The stretcher was experimentally characterized, which is described in the following. The Martinez-like stretcher consisted of a transmission grating ($g = 1740\ l/mm$) in first diffraction order (diffraction angle $\gamma = 60.5°$) and an imaging lens ($f = 7.5\ cm$) aligned in a double-pass geometry corresponding to four optical bounces on the grating. Figure 6-13 shows the measured output pulse duration for several stretcher distances characterized with a SHG autocorrelator. The minimum deconvoluted pulse duration was found to be $\tau_0 = 0.42\ ps$ (FWHM), which agreed well with the measured pulse duration before the stretcher of 0.43 ps. As it can be seen from the Figure 6-13, the pulse duration was adjustable from 10 ps with

negative dispersion to the transform-limited duration of 0.42 ps, where all dispersion in the beam including the Faraday isolator were compensated, to >4 ps with positive dispersion. A theoretical curve, presented in Figure 6-13 in red, was calculated with the help of Equation (30) and (32), which approximated well the Martinez-like stretcher.

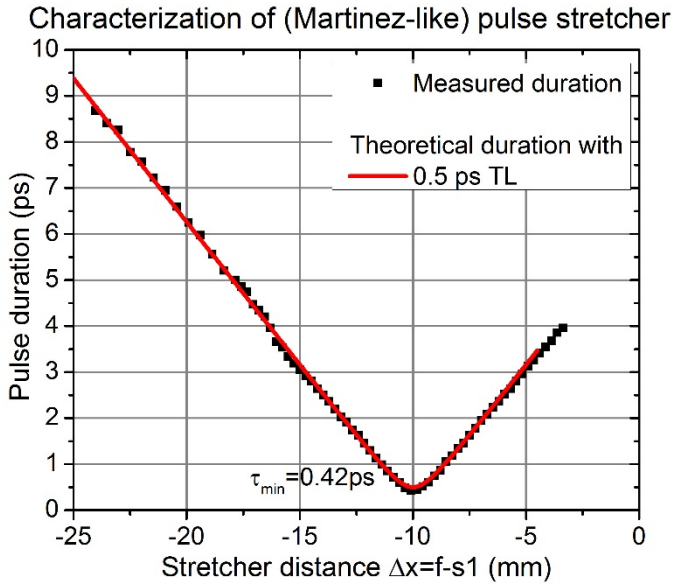

Figure 6-13: Measured pulse duration after the Martinez-like stretcher in dependence of the stretcher distance characterized with an SHG autocorrelator.

After the Martinez-stretcher, the pulses were launched into the rod-type fiber amplifier. For this initial experiment, the input pulse duration was chosen to be long resulting in comparably low peak power and negligible nonlinearities. This procedure allows to investigate the typical amplification characteristics of the rod-type fiber amplifier under low nonlinearities. The achieved output average powers were recorded for several levels of input power and are shown in Figure 6-14. The obtainable output power ranged from 30 to 37 W for a seed power from 0.3 to 1.2 W. A clear roll-off effect was observed for pump powers above 80 W and gain saturation effects were observed even with 25% of the highest seed power. Due to the short rod length of 0.9 m (typically 1.2 m), the end-pumped optical power was not completely absorbed in the experiment resulting in a degraded maximum obtainable power of 37 W (typically ~50 W). Recycling the residual pump

light could have further increase the optical efficiency and overall output power, but was not implemented.

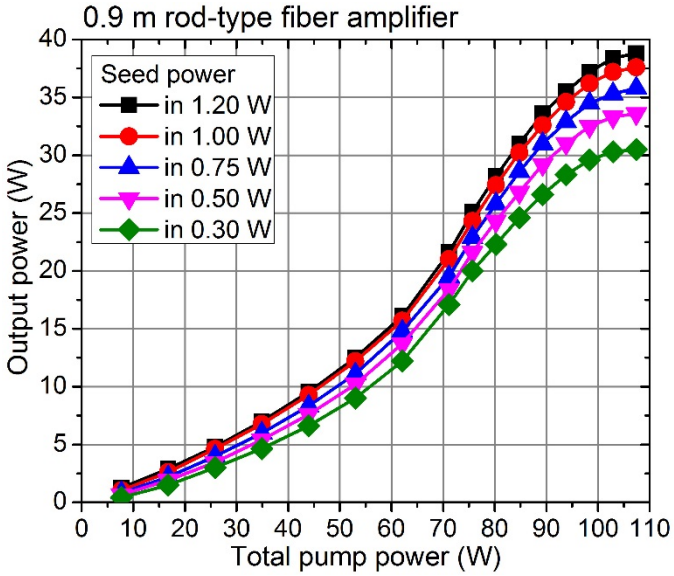

Figure 6-14: Typical amplification characteristics of the employed rod-type fiber amplifier. The maximum output power was ~37 W.

Up to 37 W optical power was observed from the rod-type amplifier at 10 MHz repetition rate. A change in input pulse duration had no significant effect on the obtainable output power with the exception of surface damage occurring for ultra-high optical intensities. Thus, optical pulses with up to 3.7 µJ were obtained from this stage. For the OPCPA pumping application it is beneficial to obtain the highest peak power as possible resulting in large parametric gain. The presented rod-type fiber amplifier stage was further investigated towards highest obtainable peak power, which is presented in the following subsection.

6.3.2 Nonlinear Spectral Compression

Obtaining a high peak power from fiber amplifiers can be challenging due to the small mode field diameter. For a given fiber geometry, the onset of nonlinearities are usually limiting the obtainable peak power [157]. During linear propagation in a fiber, the optical pulses experience

dispersion typically leading to longer pulse durations without compensation. On the other hand, if the pulse is slightly pre-chirped it can compress during propagation resulting in high intensities in the fiber causing the onset of optical nonlinearities, such as spectral broadening and pulse break-up, or even damage to the fiber. Another operational regime has been reported, in which the SPM under certain conditions can be utilized to narrow the spectrum during propagation resulting in a quasi-transform-limited pulse duration with high peak power [170]. This method is commonly termed nonlinear spectral compression and can result in transform-limited, high peak power pulses exiting the fiber amplifier without post compressor. Nonlinear spectral compression is studied in the following with numerical and experimental investigations.

Simulations were carried out using the software package FiberDesk to gain insight into the nonlinear processes occurring during the propagation with high peak power in a rod-type fiber. The results are shown in Figure 6-15 and described in the following. In all simulations the input pulse energy was set to 0.1 µJ corresponding to 1 W at 10 MHz and the output pulse energy to 35 µJ corresponding to the experimentally obtained performance from the rod-type fiber amplifier as shown in Section 6.3.1. The initial pulse duration was chosen to be 0.3 ps, the mode field diameter 70 µm and the fiber length 0.9 m. For the first investigation shown in Figure 6-15, the dispersion was varied over several orders of magnitude to illustrate the impact of the initial dispersion onto the nonlinear propagation. For the second investigation shown in Figure 6-16, the impact of the input dispersion in the regime of nonlinear spectral compression is shown. In this case, the dispersion was varied over only one order of magnitude and the output pulse duration and bandwidth were simulated. As a result, an operational point was identified with almost transform-limited output pulses in the regime of nonlinear spectral compression.

Figure 6-15 (a), (b) and (c) shows the change in the optical spectrum along propagation for different input dispersion cases ranging from positive to zero dispersion.

- For a large amount of positive dispersion, shown in Figure 6-15 (a), no change in the optical spectrum was observed and the input spectrum was maintained. The obtainable peak power was rather modest in this case due to the long input pulse duration.
- Figure 6-15 (b) shows the case for a dispersion of +400,000 fs^2 (the opposite sign of the case for the best spectral compression, as seen later). Here, the optical spectrum showed broadening and broke up towards the end of the propagation distance. The output temporal pulse shape exhibited two separate pulses corresponding to the two wavelengths peaks.
- Figure 6-15 (c) shows the case for a transform-limited 0.3 ps input pulse. As it propagated through the fiber, the pulse first spectrally broadened. Towards the end of the propagation/amplification, it experienced complex pulse break up and broadened even further. Due to the increased bandwidth and the linear chirp, this pulse broadened in time and resulted in a comparably longer pulse duration and reduced peak power.

Three selected cases of the negative dispersion regime were numerically studied and are shown in Figure 6-15 (d), (e) and (f). Due to the negative dispersion, the SPM effect during propagation initial narrowed the pulse spectrum, which was observed in all three cases.

- A small amount of negative dispersion was chosen for the case presented in Figure 6-15 (d). The corresponding spectrum of the pulse was first compressed due to the nonlinear spectral compression well within the propagation length at ~0.6 m.

Complex spectral broadening and pulse breakup was following due to the occurring high intensities, additional positive dispersion and onset of other nonlinearities. The output pulse shape was strongly distorted from a transform-limited pulse.

- The Figure 6-15 (e) shows the case, where the dispersion was chosen so that the nonlinear spectral compression occurred at the end of the propagation. The output pulse duration in this case was almost unchanged along propagation due to the spectral narrowing. This output pulse duration was close to be transform-limited and the shortest obtainable in the numerical experiments without external compressor. Thus, this case with best nonlinear compression represented the configuration with highest obtainable output peak power for the modeled fiber amplifier.
- A large amount of negative dispersion, as shown in Figure 6-15 (f), led in the simulations to insufficient spectral compression. A longer propagation distance would have been necessary for full nonlinear spectral compression. Due to the large initial chirp and the incomplete spectral compression, the output pulse duration was not transform-limited and longer compared to the previous case (e).

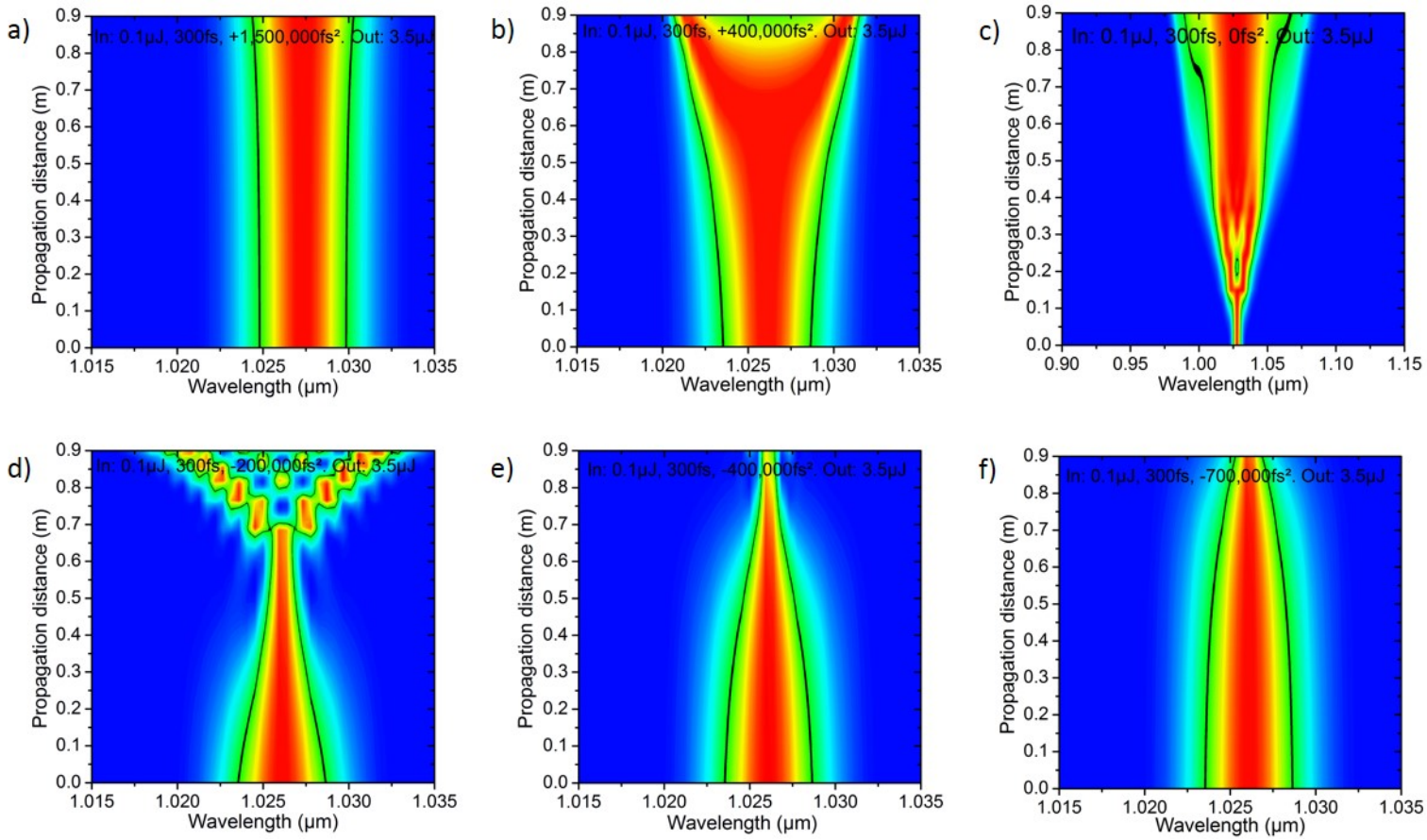

Figure 6-15: FiberDesk simulations carried out to gain insight into the dependence of input pulse dispersion and nonlinear propagation in fiber amplifiers. The top row shows the cases with a large amount of positive dispersion (a), a smaller amount of positive dispersion (b), as well as zero dispersion (c). The bottom row shows example cases for a small amount of negative dispersion (d), the amount of negative dispersion yielding to best nonlinear compression (e), and large amount of negative dispersion (f).

Based on similar FiberDesk simulations but with lower variation of the dispersion, the output spectral width and pulse duration was simulated in the regime of nonlinear spectral compression. The results are shown in Figure 6-16 (a) and the corresponding time-bandwidth products ($TBP = \Delta\tau\Delta\nu$) are given in (b). A negative dispersion of -0.2 ps² (or -200,000 fs²) led to spectral compression well within the propagation length followed by spectral broadening. In this regime, the TBP can be dramatically larger than for a transform-limited pulse. On the other hand, for a dispersion of -1,0 ps², the nonlinear spectral compression was insufficient and the output bandwidth close to the original bandwidth. Due to the chirped pulse duration, the TBP was large as well. The best spectral compression was found for a dispersion of -0.4 ps² resulting in 0.71 nm bandwidth (FWHM) and 3.6 ps duration (FWHM) corresponding to a TBP of ~0.7. Further fine-adjustment would have allowed to obtain output pulses closer to the transform-limit enabling highest peak powers, but was not investigated numerically. However, the concept is presented in detail and the values are applicable to the presented experiment within an order of magnitude.

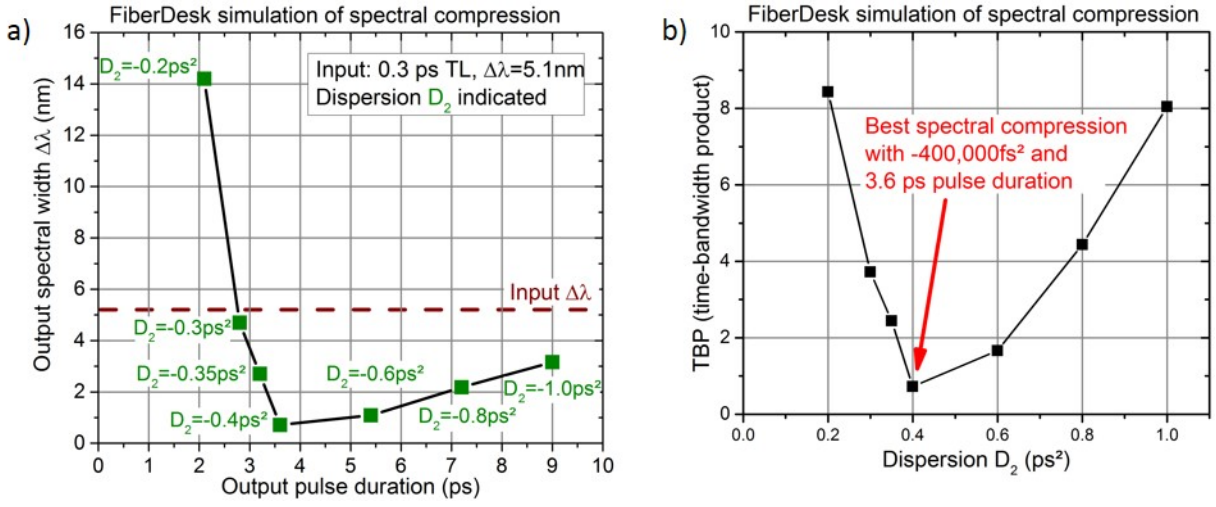

Figure 6-16: (a) Simulated output spectral bandwidth and pulse duration after nonlinear spectral compression for several input dispersions (noted in green) and (b) corresponding time-bandwidth product.

The nonlinear spectral compression was further investigated experimentally. The input pulse duration was changed with the calibrated stretcher and spectra were recorded for several durations with an OSA. Spectra were taken at full amplification for several stretcher configurations revealing the point of operation for best spectral compression. The resulting spectrum is shown in Figure 6-17 (a). During the investigations, the system was not changed thus the color intensity enables direct comparison between individual measurements. The stretcher distance was varied from -24 to -17 mm corresponding to an input pulse duration of 7.7 to 4.2 ps as indicated in Figure 6-17. Over the full range of measurements, the input bandwidth of ~3 nm was dramatically reduced to below 1 nm due to the nonlinear spectral compression during propagation and amplification. The red area corresponded to the highest obtained spectral power and thus, the best compression was found in the range from 7.1 to 5.4 ps input pulse duration.

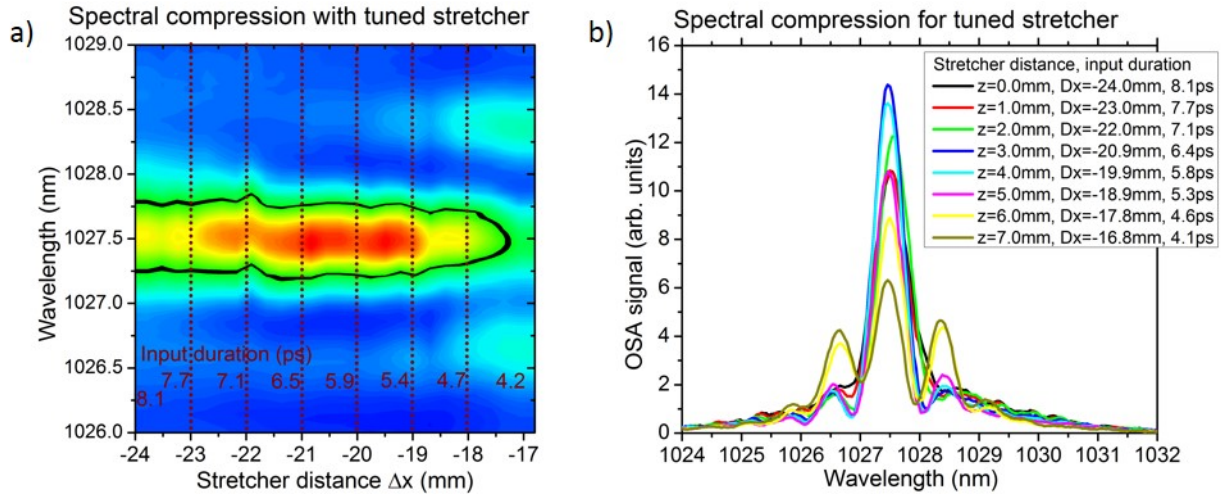

Figure 6-17: Experimental investigations of the nonlinear spectral compression after the amplification in the rod-type fiber amplifier with different input pulse durations shown as contour plot (a) and graph (b).

A few selected spectra are presented in Figure 6-17 (b). The graph shows that the case $\Delta x = -20.9\,mm$ resulted in the largest signal and cleanest pedestal. The input optical spectrum was compared to the spectrum of the amplified pulse for the case of best spectral compression, as shown in Figure 6-18. It can be seen that the initial FWHM of 2.94 nm narrowed to 0.58 nm. The

found parameters for the input pulse resulting in best nonlinear spectral compression are listed in Table 6-2.

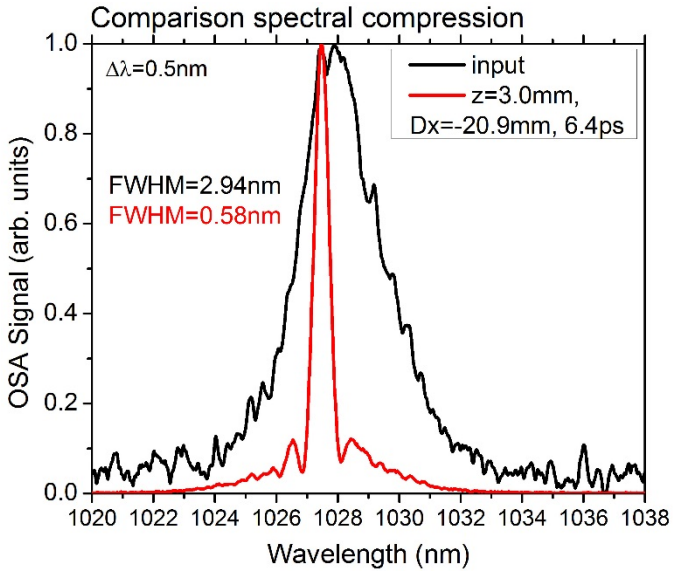

Figure 6-18: Comparison between the normalized unamplified spectrum (black) and the case of best spectral compression.

Table 6-2: Found properties of the pulses launched into the rod-type fiber amplifier with best nonlinear spectral compression.

Parameter	Value
Stretcher distance	$\Delta x = -20.9\ mm$
Measured center wavelength [nm]	1027.9 nm
Measured spectral bandwidth (FHWM)	2.94 nm
Corresponding TL pulse duration ($sech^2$)	0.38 ps
Measured stretched pulse duration	6.4 ps

The dependence of the spectral compression was further investigated experimentally. For this investigation, the output spectrum was obtained after propagation through the full rod-type amplifier but recorded for different levels of amplification. Figure 6-19 shows the investigation with an exemplarily chosen case of the nonlinear spectral compression. The maximum available pump current during the investigations was 54 A corresponding to 140 W optical pump power,

which was not fully absorbed in the amplifier. All recorded optical spectra from the output pulses experienced the full nonlinearities through propagation in the rod-type fiber but under different levels of amplification and occurring pulse energies. Note, that the 2D contour plot graphically represents a dramatically different physical process compared to the FiberDesk simulations earlier in this subsection, despite utilizing a similar appearance and color code. For the 2D contour plot shown in Figure 6-19, each spectrum was normalized after each measurement which allows the observation of a spectral compression after propagation through the full rod-type fiber for a fixed input duration but under different levels of amplification. It can be seen that, the initial spectrum already narrowed compared to the 3 nm input bandwidth due to the propagation in the rod-type fiber. This regime corresponds to the simulated case shown in Figure 6-15 (f). For an increased pump current, the spectrum narrowed further due to the increase in nonlinearity under higher amplification. Complete spectral compression was observed in the range from 30 to 35 A. In this range, the nonlinear propagation corresponds to the simulation case shown in Figure 6-15 (e). The experimental results showed that a further increase of amplification level beyond 35 A led to the onset of spectral broadening due to the increase in pulse energy corresponding to the case shown in Figure 6-15 (c).

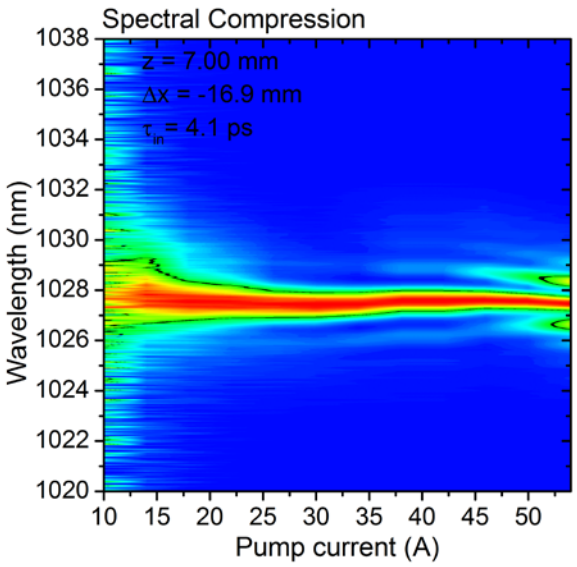

Figure 6-19: Measured output spectra of the rod-type fiber amplifier with nonlinear spectral compression under different level of amplification.

Note, that the physical resolution of the OSA measurements was investigated experimentally afterwards and seemed to be limited to >0.50 nm. In comparison, the narrowest obtained spectrum had 0.50 nm bandwidth. Thus, the obtained spectra seemed to be affected by limited spectral resolution of the characterization setup and the experimental spectra presented in Figure 6-17, Figure 6-18 and Figure 6-19 could have benefited from increased resolution. However, the effect of nonlinear spectral compression was clearly present and the narrowest bandwidth was expected to be on the order of ~0.3 nm.

6.3.3 Estimated Peak Intensity

The output of the rod-type fiber amplifier was characterized experimentally with a SHG autocorrelator. The deconvoluted FWHM duration was recorded for different optical pump powers as well as different calibrated input pulse durations and the results are presented in Figure 6-20. The pulse duration under low amplification below 15 W output average power already altered due to the additional dispersion and nonlinear spectral compression occurring in the rod-type fiber

amplifier. The autocorrelation shape in this low amplification regime matched that expected shape from the autocorrelation of a $sech^2$ pulse. Thus, the measured duration was seen accurate and the measured FWHM was accordingly divided by the autocorrelation deconvolution factor of 1.54 for a $sech^2$ pulse shape (or square-root of 2 for a Gaussian pulse shapes). An increase in pump power led a partial change in the central part of the autocorrelation shape due to the onset of the nonlinear spectral compression or other nonlinearities. The traces were not recorded explicitly and are not shown here. As a consequence, the deconvoluted pulse duration in the high amplification regime of Figure 6-20 lacks accuracy in the central region but might be employed as order of magnitude approximation. Thus, the pulse duration was estimated to be on the order of 10 ps or shorter for the best nonlinear spectral compression.

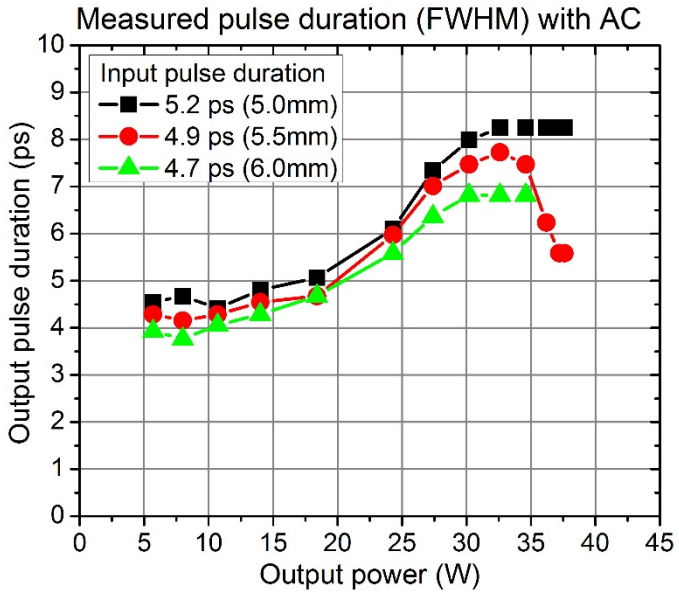

Figure 6-20: Deconvoluted pulse duration at different amplification and nonlinear spectral compression levels at the output of the rod-type fiber amplifier.

Based on these findings, peak intensity estimates were performed. Table 6-2 summarizes the parameters found for the input pulses with best spectral compression after the Martinez-like pulse stretcher. Table 6-3 shows the set of parameters found for the output pulses with best spectral compression. The peak power from the rod-type fiber was estimated to be larger than 370 kW.

Table 6-3: Found properties of the output pulses from the rod-type fiber amplifier with best nonlinear spectral compression.

Parameter	Value
Stretcher distance	$\Delta x = -20.9\ mm$
Measured center wavelength [nm]	1027.4 nm
Measured spectral bandwidth (FHWM)	<0.58 nm
Corresponding TL pulse duration	>2.68 ps
Estimated measured pulse duration	<10 ps
Measured average power	>37 W
Corresponding pulse energy	>3.7 µJ
Corresponding peak power	>370 kW

A few estimations of the peak intensity with different focused spot sizes were calculated and are listed in Table 6-4 based on the output parameters listed in Table 6-3. These values could be lower than the actual ones since the pulse duration was assumed as longest upper estimate. For example, if focused to 50 µm spot diameter, the corresponding estimated peak intensity was >18 GW/cm². A peak intensity exceeding 70 GW/cm² was estimated for a focused spot diameter of 25 µm, which seems experimentally feasible for the OPCPA application [83]. On the other hand, the limitations presented in Section 3.5.3 resulting from small beam sizes apply directly in this case. Thus, it might be experimentally challenging to extract high parametric gain with long (5 mm) OPA crystals, ~20 GW/cm² and <50 µm pump beam diameters.

Table 6-4: Intensity estimates for an optical pulse with >3.5 µJ energy and <10 ps duration for several focused beam sizes.

Diameter	Intensity
100 µm	>5 GW/cm²
50 µm	>18 GW/cm²
25 µm	>71 GW/cm²

A reference system was found in the literature with comparable specifications (~10 ps pump pulse duration, 20 GW/cm²-level peak intensity, ~1030 nm center wavelength, ~2 µm OPCPA center wavelength) but with higher pulse energy at the 10-mJ-level and larger beam diameters [42]. The reported values allow comparisons and proof-of-employability of the peak intensity resulting from the system described in this section for the OPCPA application. It was reported that a pump intensity of 20 GW/cm² can result in a calculated high parametric gain and amplification bandwidth of >350 nm at 2.2 µm center wavelength in MgO:PPSLT. The same authors reported on a parametric amplification from sub-1-µJ to 25 µJ with a bandwidth ranging over 405 nm (FWHM) utilizing such a pump system and OPA stage experimentally. Further, the authors employed 40 GW/cm² as pump intensity in their final high power OPA stage based on BBO as nonlinear material experimentally resulting in an amplification to 850 µJ with a bandwidth of 474 nm (FWHM). Thus, the minimum peak intensity estimates and the reference literature values suggest that the system described in this section provided sufficiently high peak power to serve as OPCPA pump laser system. However, the small beam sizes could make the experimental implementation challenging.

On the other hand, the only reported OPCPA systems operating with 1 MHz repetition rate employed peak pump intensities in excess of 100 GW/cm² [39] [83], which could be challenging to be obtained from the system described in this section when utilizing spot sizes larger than 20 µm. To increase the peak power or increase the beam diameter of the here presented system, the nonlinear spectral compression method could be replaced by a full CPA scheme with the addition of a Treacy-like grating compressor [168] [171]. A comparable system employing the full CPA scheme has been reported, able to generated 9 µJ pulse energy and 420 fs duration at 1 MHz repetition rate for OPCPA pumping [83]. Considering the parameters presented in Table 6-3, a

CPA scheme could potentially allow the compression of the amplified pulses to sub-500-fs duration with more than 2 µJ pulse energy (assuming 70% compressor transmission) resulting in more than 4 MW peak power. Thus, by employing a full CPA scheme, the peak power of the output pulses could be increased by 10 times, which would allow to either increase the peak intensity or beam diameters in the OPA stages.

6.4 High-Average Power OPA

To benefit from the high pump average power at 10 MHz, a high overall OPCPA efficiency is desired. The design of such an OPA stage is presented as well as relevant considerations for optical parametric amplification with µJ-level pump pulse energies and sub-10-ps duration. In addition, the high pump average power results in non-negligible absorption, which is investigated in the following subsection 6.4.2.

6.4.1 Design Considerations

The performance of seed and pump beam generation has been presented in the previous section. It was found that the energy of the supercontinuum seed was >2 nJ in the measured range from 1.3 to 1.91 µm. Considering the broad spectral range, the pulse energy might be below the 1 nJ-level for a typical amplification bandwidth of ~300 nm. The temporal confinement was characterized to be 12 ps for the range of 1530 to 1700 nm. On the other hand, the presented pump beam generation operated at up to 37 W average power corresponding to 3.7 µJ pulse energy and sub-10-ps duration. Thus, the spectral and temporal parameters of seed and pump pulses matched for OPA. The OPA operation close to the degeneracy condition (i.e. collinear OPA geometry) seemed feasible with corresponding seed/idler wavelengths of 2.06 µm.

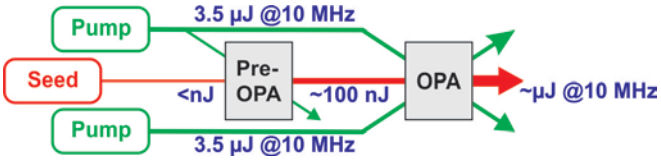

Figure 6-21: Sketch of the pre-OPA and multi-beam pumped OPA.

The overall amplification necessary to amplify the seed pulse would be more than three orders of magnitude from sub-1-nJ to the µJ-level, which would correspond to approximately 10% total OPA efficiency. Since it was intended to achieve high OPA efficiency and highest average power, the final OPA stage should be operated with lower parametric gain of 3-50 [44] [77]. Additionally, obtaining high parametric gain from the multi-beam OPA pumping scheme increases the complexity of the OPA stage and is more prone to fluctuations. Thus, a pre-OPA stage was designed to boost the seed energy from the sub-nJ-level to >100 nJ as shown in Figure 6-21. The implementation of this stage was started experimentally but not completed. No experimental data was available to support this section further and the setup is currently under further implementation based on the design and findings presented in this section.

6.4.2 High-Average Power Effects in BBO

Several nonlinear crystals can be chosen from for the OPCPA application [116]. Operating an OPA with high pump average powers (up to 50 W) and accordingly high seed/idler average powers (up to 5 W each) can lead to a non-negligible amount of absorbed power in the nonlinear material. Any absorbed power content results consequently in localized heating of the material. The employed focused beam diameters for low peak power beams can be on the order of 25 µm in order to obtain the high peak intensities necessary for significant parametric gain. As a result, a small heat affected volume can be identified along the beam path in the nonlinear material. It has been observed experimentally in CREOL and CELIA that tight focusing conditions in the OPA

with high average power can lead to bulk damage and micro-cracks. Recently, the temperature increase was investigated experimentally in a BBO-based OPA stage operated with high average power pump beam at 515 nm, a seed beam ranging from 600 to 1230 nm wavelength and a generated idler beam from 0.9 to 3.6 µm [172]. The authors reported a temperature increase of up to 148 C depending on the employed average power and wavelengths, with the main contribution originating from the longest involved wavelengths of the idler beam.

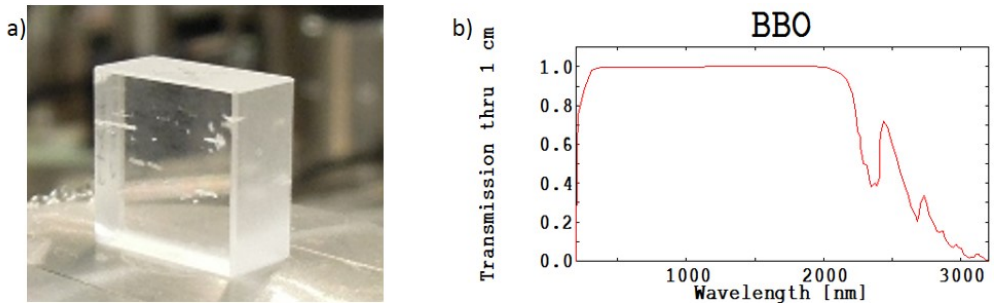

Figure 6-22: (a) Laboratory picture of a 0.5 cm long and 1cm x 1cm wide BBO crystal. (b) Transmission spectrum of 1 cm long BBO calculated with the software package SNLO.

Due its high nonlinear coefficients and commercial availability, BBO is the most commonly employed nonlinear crystal for OPA and a laboratory picture is shown in Figure 6-22 (a). The transmission spectrum of 1 cm BBO obtained with the software package SNLO is shown in Figure 6-22 (b). A high transmission window can be identified in the range from 200 nm to 2.1 µm. The occurring wavelength ranges in OPA and for the pump wavelength of 1030 nm are from 1.5 to 2.06 µm for the seed beam and from 2.06 to 3.2 µm for the idler beam. Values for the absorption are listed Table 6-5 and the corresponding absorption in 1 cm BBO is shown. It can be seen that absorption from the pump beam seems small (0.05%) compared to the idler beam which can exceed 20% at a wavelength of 2.55 µm. On the other hand, the occurring pump powers in the OPA are typically ~10 times larger than the powers of signal or idler beams. Thus, the main contribution to heat accumulation in BBO-based, non-collinear OPA pumped at 1030 nm can be

expected to arise from the idler absorption at >2.09 µm and a minor contribution from the absorbed pump beam. However, the picture changes at the degeneracy point, when seed and idler wavelengths are 2.06 µm. Here, the absorption values for pump, seed and idler are close to each other but the average power of the pump exceeds the power of signal or idler beams largely – especially, in the first OPA stage. Based on the previous discussion, the degeneracy geometry leads to minimal heat accumulation in the nonlinear material and is preferred for initial OPA experiments under high power operation.

Table 6-5: Absorption values reported in the literature and absorption estimates [173].

Wavelength	**Absorption value α**	**Absorption of 1 cm BBO**
1.03 or 1.064 µm	$0.0001\ cm^{-1}$	0.05%
2.09 µm	$0.07\ cm^{-1}$	3.5%
2.55 µm	$0.5\ cm^{-1}$	22%

FEA heat simulations were carried out, shown in Figure 6-23, to investigate the heating effect due to absorbed power assuming a cylindrical BBO section of 1 mm diameter and the pump beam propagating along the cylindrical axis. For the simulations, the degeneracy geometry pumped at 1030 nm wavelength was considered allowing to neglect signal and idler absorption. This condition is in particular relevant for a first OPA stage, were the pump power exceeds largely ($\gg 10$ times) the idler and signal beam power. The simulated heat profiles are shown in Figure 6-23 for 15 W (a) and 50 W pump power (b) and the maximum occurring temperature value was noted for each simulation on the color intensity scale. The pump beam size varied between 25 µm, 50 µm, 100 µm and 250 µm and the corresponding variation of heat affected zone was seen. The highest temperature increase was 61 K for the 25 µm pump beam diameter and 15 W pump power. The maximum temperature difference increased to up to 203 K for a pump power of 50 W. It can

be expected that stress in the material would result from this confined heat affected zone potentially causing damage to the crystal structure.

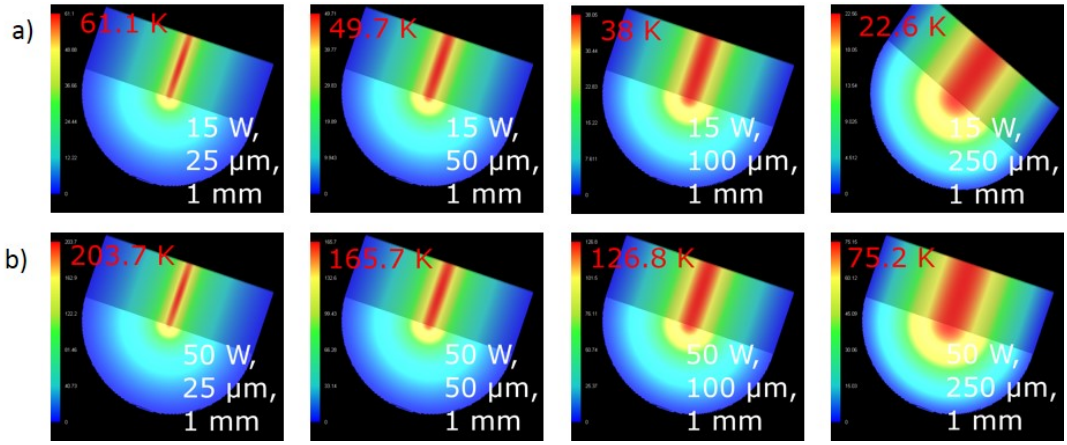

Figure 6-23: FEA heat simulation via LASCAD of a BBO-based OPA stage pumped with 15 W (a) and 50 W (b) at 1030 nm.

The maximum temperatures are plotted in Figure 6-24 showing a nonlinear increase with smaller beam sizes. A dramatic difference between the found temperatures at 15 and 50 W pump power was observed. Similarly, a large difference was observed between 25 and 100 µm pump diameter. To conclude, the FEA heat simulations suggests that operating with small beam sizes (<50 µm) and high average power (>10 W) heat accumulation can have a dramatic effect.

It is important to note that the simulated values had high uncertainty due to the estimation of the absorption at 1030 nm. The underlying literature values were only upper limit estimates and actual values can differ depending on the purity of the tested material. Thus, the simulated heat profiles are applicable within this comparative study to gain insight into the concept and to analyze trends. More data of the absorption vales, the temperature increases or the bulk damage in BBO with high average power beams and small beam diameters are necessary to achieve meaningful absolute temperature values or identify more trends. This study could be extended further to yield agreement with experimental results and gain further insight into the damaging process and occurring temperatures in BBO-based OPA.

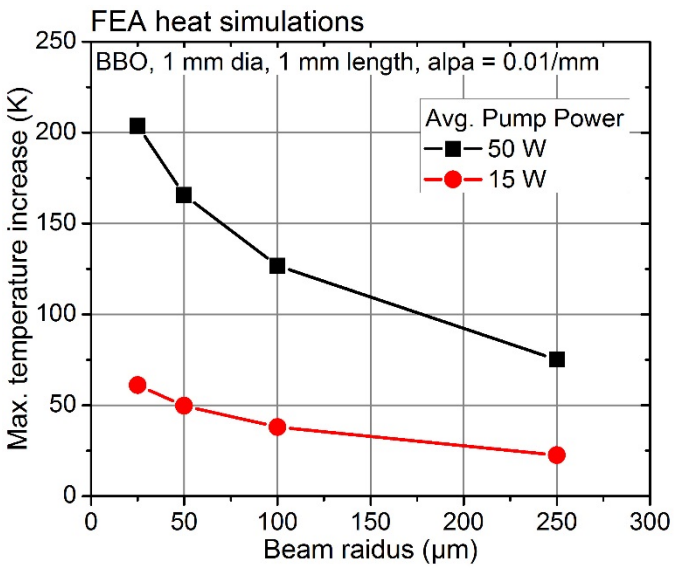

Figure 6-24: The maximum temperature increase found via the FEA heat simulations.

6.5 Summary

The research presented in this chapter was conducted at CELIA (Univeristé de Bordeaux 1, France) and was directed towards increasing the repetition rate of OPCPA systems towards the full repetition range of the oscillator front-end of 10 MHz potentially employing multi-pump beam OPA techniques. The 300 fs front-end was employed to generate seed pulses ranging into the spectral window from 1.3 to 2.0 µm. This frequency conversion in highly nonlinear fibers was studied numerically and experimentally, and sufficiently high pulse energies at the nJ-level is presented. The pump beam generation was based on a rod-type fiber amplifier generating 37 W average power and more than 370 kW peak power at 10 MHz. Estimates with the performance of seed and pump beam generation were obtained and a design towards the integration as OPCPA system is presented. In addition, FEA heat simulations are presented of the accumulated heat originating from the absorption of the high average power pump beam. The simulations indicated that small beam diameters can result in high maximum temperature increase in a small volume potentially leading to thermally induced stress, OPA performance degradations or damage. The

presented experiments, estimates and designs suggest that the implementation of OPCPA systems at 10 MHz seems feasible and other systems are expected to be reported soon in the literature.

7 SUMMARY AND OUTLOOK

High-energy and high-average power, few-cycle pulses are a desired research tool for highly nonlinear experiments. OPCPA is a promising ultrafast laser amplifier technique to generate these pulses and its performances in terms of pulse energy and average power is at a level directly competing with traditional Ti:sapphire-based CPA. OPCPA offers direct amplification of almost-octave spanning bandwidth enabling few-cycle pulse durations and CEP-stabilization. A historical overview of both techniques, CPA and OPCPA, is given in this dissertation. Important aspects of few-cycle OPCPA and DPSS amplifiers were discussed. Investigations were conducted and are presented conceptually, numerically and experimentally. Most of the research for this dissertation was focused on the design and implementation of the HERCALES laser facility. It is expected to provide an output pulse energy at the few-mJ-level with high repetition rate and few-cycle pulse duration. Two temporal characterization devices were implemented based on interferometric autocorrelation and the SPIDER method. Moderate pulse energy and sufficient bandwidth for sub-10-fs duration is presented experimentally an initial implementation of the OPA stage.

The development of several amplifier schemes in the high energy, high average power, and picosecond pump beam generation for the HERACLES facility are presented. These systems were based on diode-pumped, solid-state amplifiers and investigated not only for high performance but also for stability. A high-quality MOPA chain is presented operating with up to 3.2 mJ-level pulse energy, ~170 ps duration, and more than 10 W average power. The corresponding peak power was greater than 18 MW. SH of this stage was investigated resulting in 7.9 MW peak power and stable output power. Two 3 mm diameter DPSS amplifier were employed to scaling of this system to high power (>30 W) and high peak power (50-MW-level). Another effort is presented, in which the output was further scaled to ultra-high pulse energy (>160 mJ), which led to the design of an

ultra-high energy pump beam generation for a new OPCPA facility. This OPCPA facility, termed PhaSTHEUS, is anticipated to generate sub-5-fs, ultra-high peak intensities for novel highly nonlinear experiments.

Parts of the research for this dissertation were conducted at CELIA (Univeristé de Bordeaux 1, France) with the goal to investigate the potential of operating OPCPA systems at ultra-high repetition rates of 10 MHz with high average powers. The seed pulses were derived from a 300 fs front-end and spectrally converted in highly nonlinear fibers into the relevant wavelength window of 1.3 to 2.0 µm. A rod-type fiber amplifier was employed in the pump beam generation and generated 37 W average power and more than 370 kW peak power. Designs and estimates towards integration into an OPCPA system are presented as well as the concept of multi-pump beam OPA pumping. In the near future, increasing the repetition rate of OPCPA system beyond the current reported maximum of 1 MHz seems feasible with high average power fiber systems and novel OPA pumping schemes.

The discussed OPCPA systems operate in radically different regimes in terms of peak power, average power and repetition rate with few-cycle duration. Thus, these systems enable a wide range of experimental studies employing novel highly nonlinear experiments. The conversion of the visible driving fields via high-harmonic generation (HHG) is a target application. Depending on the employed systems, high energetic photon bursts (XUV) with attosecond duration can be the result with high pulse energies or high photon flux. These attosecond pulses can be further employed to probe the dynamics in atoms and molecules. The XUV photon burst can be utilized for high resolution imaging or even seeding of free-electron lasers. In CREOL, the HERACLES facility will be used for a variety of experiments in attoscience, ultrafast materials processing, filamentation, LIBS and coherent control.

APPENDIX A
ADDITIONAL MATERIAL FOR CO-TUTELLE PHD DISSERTATION

A.1 Scan of Signed Inter-Constitutional Agreement

INTER-UNIVERSITY AGREEMENT
ON
JOINT DOCTORATE SUPERVISION
BETWEEN
UNIVERSITÉ BORDEAUX 1
TALENCE, FRANCE
AND
UNIVERSITY OF CENTRAL FLORIDA,
ORLANDO, FLORIDA, USA

Considering the Ministerial Order of 25 09 1985 on the modalities related to the registration and submission regulations of works carried out in part or fulfilment of Doctoral requirements;

Considering the Ministerial Order of 25 04 2002 on Post Graduate studies;

Considering the Order of 18 01 1994 on the setting up of a joint doctorate supervision procedure between French and foreign universities;

Therefore, the Université Bordeaux 1 (hereafter referred to as UB1), Talence, France, and the University of Central Florida (hereafter referred to as UCF), Orlando, Florida, USA, on behalf of its Board of Trustees, authorize the preparation of doctoral dissertations at UCF for students from UB1 and their submission under the joint responsibility of both universities according to the following modalities:

Article 1:

This is a general agreement ("Agreement") covering multiple students who will come to UCF from UB1, or vice versa, to study in one of the available doctoral programs. A "Specific Agreement," a copy of which is attached hereto as Attachment 1, will be signed by the relevant and authorized individuals at each university for each student. The students who participate in this joint doctorate program, some of whom may receive doctoral degrees from UCF, will meet admissions requirements for the programs they enter and satisfy all graduation program requirements.

PARAGRAPH I: ADMINISTRATIVE MODALITIES

Article 2:

The research work related to the doctorate is carried out in both institutions, in exchange, the student benefits from the joint supervision regime from the day the student's Specific Agreement is signed and for a maximum duration of 3 (three) years. All formal coursework will be taken at UCF, although transfer coursework from UB1 will be accepted for the student based upon policies in the UCF Graduate Catalog and consistent with UCF accreditation requirements.

Article 3:

The candidate must register in both universities, but registration fees are only due to one university at a time. However, students from France who are completing doctoral degrees at UCF must take a minimum number of dissertation hours at UCF in order to fulfil degree requirements. Should a student from France not enrol in dissertation hours at UCF for a year, then they will be asked to complete a "Leave of Absence" form so that they are excused from taking dissertation hours during that time. During the preparation of the doctorate, the student will pay registration fees to the university in which the student is physically present to study and/or to do research.

The registration requirements for this doctorate are those set up by the two universities for all their Ph.D. students. The dispositions adopted by UB1 are those of the Order on Post Graduate studies (equivalent to a French *Diplôme d'Etudes Approfondies, "DEA"*) that is current at the time of signing this Agreement and is subject to the approval of the president of UB1, after he has consulted those in charge of the Doctoral Training Team and the Doctoral School to which the dissertation belongs. The registration requirements at UCF are clearly outlined in the Graduate Catalog at www.graduate.ucf.edu. All participants are responsible for obtaining health insurance for themselves and their dependents.

PARAGRAPH II: PEDAGOGICAL MODALITIES

Article 4:
The authorization and the conditions for the defence of the dissertation are those adopted by each university within the general framework of the validation and assessment of their dissertation. The requirements of UB1 are those included in the order of Post Graduate studies that is current at the time of signing. Procedures for satisfying the dissertation requirement are outlined in the Graduate Catalog of UCF at www.graduate.ucf.edu.

Article 5:
Both universities recognize the validity of the joint doctorate supervision agreement hereby set up and the validity of the dissertation to be defended. The publication, exploitation and protection of the doctorate dissertation, as well as the results of the research, will be pursued by the two laboratories involved in the subject and according to local procedures in each country. All intellectual property rights in the dissertation shall be governed by policies of both universities - UCF and UB1. However, if a UB1 student prepares his or her joint doctorate at UCF, or if the dissertation is prepared by a UCF student, UCF's policies shall govern and prevail in the event of a conflict. Ownership of intellectual property ("IP") generated by the student pursuant to the Agreement will be determined at the time of invention disclosure of the IP. Joint ownership will be agreed upon by and through a separate Inter-institutional agreement negotiated by both universities. UB1 and UCF shall be entitled, with approval of the student, to maintain a copy of the dissertation in their respective libraries.
Any and all doctoral dissertations and associated research generated in conjunction therewith shall be subject to unrestricted publication or dissemination, provided that such publication or dissemination will not compromise patent rights or inadvertently divulge proprietary information. Any pre-publication or dissemination review shall be limited to consideration of such patent rights and proprietary information concerns and shall be concluded within a period not to exceed thirty (30) days.

PARAGRAPH III: THE SUBMISSION OF THE DISSERTATION

Article 6:
The dissertation is submitted in one country only. If submitted at UCF, Orlando, Florida, USA, the student will be awarded a Ph.D. degree. UB1 recognizes the validity of the dissertation and therefore awards *le grade de docteur de l'Université Bordeaux 1*. The converse situation will also be accepted by both Universities, provided the regulations for attainment of the degree have been fulfilled at both universities.

Article 7:
The doctoral supervisor in France will be a full member of the UCF dissertation advisory committee. The dissertation advisory committee will be selected based upon policies of the UCF Graduate Catalog to evaluate the dissertation as partial fulfilment of degree requirements at UCF. In addition to the UCF dissertation advisory committee, the dissertation will be evaluated by a jury composed of scientific representatives of the two countries. This jury is nominated with the full agreement of the two partner universities. It is made of an equal number of scientific representatives of the two countries and includes members of the UCF dissertation advisory committee. One of the jury members must not belong to either of the two universities. This jury may be used to evaluate the awarding of the *grade de docteur l'Universite Bordeaux 1*.

Article 8:
If the dissertation is submitted at UCF, it will be written in English. A summary will be written in French.

If the dissertation is submitted at UB1, it could be written in French with a summary in English. If submitted at UB1 and then subsequently accepted by UCF as fulfilling requirements for the Ph.D., UCF will require the dissertation be written in English with a summary in French.

Article 9:
The registration regulations and the doctoral requirements for France comply with the Ministerial Order of 25 09 1985 already mentioned here above.

PARAGRAPH IV: AGREEEMENT RENEWAL, TERMINATION AND AMENDMENT

Article 10:
This Agreement shall remain in effect for a period of three years from its effective date. It may be renewed or amended at any time before the actual expiration date by a written agreement signed by authorized representatives of both parties.

This Agreement may be terminated by either party upon three (3) months prior written notice to the other party; however, termination shall not affect the participation of those students who have commenced their dissertation pursuant to the terms of this
Agreement. Those provisions pertaining to publication, IP and other provisions which by their nature survive termination or expiration, shall survive the expiration or termination of this Agreement.

UNIVERSITY OF CENTRAL FLORIDA
Orlando, Florida, USA

John C. Hitt, President

3/22/12
Date

UNIVERSITÉ BORDEAUX 1
Talence, France

~~Alain Boudou~~, President
DEAN LEWIS

11/04/12
Date

Legal content approved by:

UCF General Counsel's Office

3/14/12
Date

(2) two words crossed out; two (2) words added

ATTACHMENT 1
SPECIFIC AGREEMENT OF JOINT DOCTORATE SUPERVISION
BETWEEN
BORDEAUX 1 UNIVERSITY
AND
UNIVERSITY OF CENTRAL FLORIDA

All applicable provisions of the Inter-University Agreement on Joint Doctorate Supervision between Université Bordeaux 1, Talence, France, and the University of Central Florida, Orlando, Florida, USA ("Agreement") are expressly incorporated herein. As stated in the Agreement, ownership of intellectual property ("IP") generated by the student pursuant to the Agreement, will be determined at the time of invention disclosure of the IP, as stated in the Agreement. Joint ownership will be agreed upon by and through a separate Inter-institutional agreement negotiated by both universities.

Name of Doctoral Student: ***Andreas Vaupel***

The title of the research work is: Advanced ***Ultrashort laser development in the IR and mid-IR***

Duration of agreement: January 2011 – July 2013

Dissertation/dissertation supervisors: Martin Richardson and Eric Cormier

- Bordeaux 1 University:

  (name) Eric Cormier

  (DEPARTMENT AND TITLE) PROFESSOR, DEPARTEMENT OF PHYSICS

- University of Central Florida:

  (name) Martin Richardson

  (DEPARTMENT AND TITLE) Professor, Director Townes Institute, College of Optics

Signatures

Vaupel — Date: 03/13/2012
Student

E.C. — Date: 03/15/2012
Bordeaux Supervisor

M. Richardson — Date: 03/13/2012
UCF Supervisor

B. AUDOIN — Date: 04/04/12
Program Chair (Bordeaux)

Date: 3/14/12
Program Chair (UCF)

University of Central Florida

Townes Laser Institute
CREOL, the College of Optics & Photonics

To: **Ms Brigit Socolovert, Student Affairs**
Ms Olga Ivanova, International Student Affairs
University of Bordeaux 1,
351 course de la liberation,, 33405 Talence, France

From : **Martin Richardson,** ***Director, Townes Laser Institute,***
The College of Optics & Photonics, University of Central Florida,
4000, Central Florida Blvd, Orlando, FL32816-2700
tel: 407 823 6819, email: *mcr@creol.ucf.edu*

Professor Eric Cormier, ***Department of Physics & CELIA***
University of Bordeaux 1,
351 course de la liberation,, 33405 Talence, France
Tel : (054) 000-6186 email : *eric.cormier@celia.u-bordeaux1.fr*

Copy **Chateaubriand Fellowship Program**
Office for Science & Technology, Embassy of France,
4101 Reservoir Road NW, Washington DC 20007
Tel:202 944 6057 email: *huong.pham@diplomatie.gouv.fr;*
Isabelle.schoninger@ambafrance-us

Date: **November 30, 2011**

Subject: **Andreas Vaupel - Chateaubriand Fellow.**

Per documents previously submitted to your offices, Mr Andreas Vaupel has received a Chateaubriand Fellowship from the Embassy of France in Washington DC, to pursue a co-tiutelle Ph.D under the UCF-University of Bordeaux Co-tutelle Agreement.
Mr Vaupel will pursue his Ph.D under the joint supervision of ourselves (Richardson and Cormier), under the terms of this Agreement. He will perform research on a common research program in both institutions. In particular we plan for him to spend much the year of 2012 in Dr Cormier research group in CELIA, performing joint research. It is planned that he defend his Ph.D thesis at the University of Central Florida, under the terms of the Agreement.

Student, Andreas Vaupel — Date: 03/13/2012

Bordeaux Supervisor, Eric Cormier — Date: 03/15/2012

UCF Supervisor, Martin Richardson — Date: 03/13/2012

APPENDIX B
LIST OF COMPARED MOPA AND CPA LASER SYSTEMS

Table B-1: List of pump laser systems used in the reported OPCPA systems listed in Table 2-2.

Year	Repetition rate	Pulse energy	Average power	Pulse duration	Peak power	Center wavelength	Gain medium	Laser technology	Scheme	Ref
2006	10 Hz	1.15 J	11.5 W	110 ps	10 GW	1064 nm	Nd:YAG	Flashlamp	MOPA	[40]
2006	30 Hz	250 mJ	7.3 W	85 ps	2.9 GW	1064 nm	Nd:YAG	Flashlamp	MOPA	[69]
2006	1 kHz	1.5 mJ	1.5 W	50 fs	30 GW	800 nm	Ti:sapphire	Ti:sapphire	CPA	[79]
2007	1 kHz	21 mJ	21 W	141 ps	150 MW	800 nm	Ti:sapphire	Ti:sapphire	MOPA	[71]
2008	1 kHz	29 mJ	29 W	106 ps	273 MW	800 nm	Ti:sapphire	Ti:sapphire	MOPA	[80]
2009	100 kHz	65 µJ	6.5 W	15 ps	4.3 MW	1064 µm	Nd:YVO_4	DPSS	MOPA	[41]
2009	1 kHz	4.5 mJ	4.5 W	12 ps	380 MW	1053 µm	Nd:YLF	DPSS	MOPA	[81]
2009	1 kHz	11 mJ	11 W	49 ps	225 MW	1053 µm	Nd:YLF	DPSS	MOPA	[77]
2009	10 Hz	1.5 J	15 W	110 ps	14 GW	1064 nm	Nd:YAG	Flashlamp	MOPA	[38]
2010	100 kHz	400 µJ	40 W	12 ps	33 MW	1064 µm	Nd:YVO_4	DPSS	MOPA	[82]
2010	1 MHz	9 µJ	9 W	420 fs	21 MW	1030 nm	Yb-doped	Fiber	CPA	[83]
2010	96 kHz	500 µJ	49 W	1.1 ps	460 MW	1030 nm	Yb-doped	Fiber	CPA	[78]
2010	143 kHz	40 µJ	5.7 W	1.56 ps	25 MW	1030 nm	Yb:YAG	Thin-disk	CPA	[70]
2010	143 kHz	27 µJ	3.85 W	2.3 ps	12 MW	1030 nm	Yb:YAG	Thin-disk	CPA	[84]
2011	1 kHz	16.5 mJ	16.5 W	12 ps	1.4 GW	1029 µm	Yb:YAG	Cryo SS	CPA	[42]
2011	30 kHz	890 µJ	26.8 W	990 fs	900 MW	1030 nm	Yb-doped	Fiber	CPA	[44]
2011	20 Hz	250 mJ	5 W	70 ps	3.6 GW	1064 µm	Nd:YAG	Flashlamp	MOPA	[73]
2012	1 MHz	185 µJ	185 W	710 fs	260 MW	1030 nm	Yb-doped	Fiber	CPA	[39]
2013	3 kHz	20 mJ	60 W	1.6 ps	12.5 GW	1030 nm	Yb:YAG	Thin-disk	CPA	[43]

Table B-2: Selected MOPA and CPA systems from the literature for comparison to existing OPCPA pump lasers. Criteria: <100 ps, >1 µJ, >10 Hz, recently published.

Year	Repetition rate	Pulse energy	Average power	Pulse duration	Peak power	Center wavelength	Gain medium	Laser technology	Scheme	Ref
2004	40 kHz	130 µJ	5.3 W	19 ps	7 MW	1064 nm	Nd:YVO_4	DPSS	MOPA	[127]
2005	100 kHz	123 µJ	12 W	6.8 ps	18 MW	1064 nm	Nd:$GdVO_4$	DPSS	MOPA	[174]
2008	78 MHz	3.7 µJ	287 W	5.5 ps	670 kW	1029 nm	Yb:YAG	Cryo SS	MOPA	[175]
2009	20 kHz	300 µJ	6 W	195 fs	1.5 GW	1030 nm	Yb,Na:CaF_2	Cryo SS	CPA	[176]
2009	3 kHz	25 mJ	75 W	1.6 ps	15 GW	1030 nm	Yb:YAG	Thin-disk	CPA	[85]
2009	10 Hz	300 mJ	3 W	2 ps	150 GW	1030 nm	Yb:YAG	Thin-disk	CPA	[177]
2010	50 MHz	15 µJ	760 W	12 ps	1.2 MW	1030 nm	Yb:YAG	Cryo SS	MOPA	[96]
2010	2 kHz	6.5 mJ	13 W	15 ps	433 MW	1030 nm	Yb:YAG	Cryo SS	CPA	[86]
2010	10 kHz	3 mJ	30 W	25 ps	118 MW	1064 nm	Nd:YAG	DPSS	MOPA	[178]
2010	20 MHz	5.5 µJ	1.1 kW	610 fs	9 MW	1030 nm	Yb:YAG	DPSS Innoslab	CPA	[179]
2010	1 MHz	3.1 µJ	3.1 W	140 fs	22 MW	1030 nm	LMA Yb-doped	Fiber	CPA	[180]
2011	100 Hz	100 mJ	10 W	5 ps	20 GW	1030 nm	Yb:YAG	Cryo SS	CPA	[181]
2011	5 kHz	12 mJ	60 W	1.6 ps	7.5 GW	1030 nm	Yb:YAG	Cryo SS	CPA	[182]
2011	100 Hz	27 mJ	2.7 W	560 fs	48 GW	1030 nm	Yb:KYW	DPSS	CPA	[183]
2011	10 Hz	130 mJ	1.3 W	450 fs	290 GW	1030 nm	Yb:YAG	DPSS ceramic	CPA	[184]
2011	5 kHz	1.8 mJ	8.8 W	28 ps	62 MW	1064 nm	Nd:YAG	DPSS	MOPA	[131]
2011	10 Hz	200 mJ	2 W	900 fs	222 GW	1030 nm	Yb:YAG	DPSS	CPA	[185]
2011	10 kHz	500 µJ	5 W	85 ps	5.8 MW	1064 nm	Nd:YVO_4	DPSS	MOPA	[123]
2011	12.5 kHz	20 mJ	250 W	830 fs	24 GW	1030 nm	Yb:YAG	DPSS Innoslab	CPA	[186]
2011	50 kHz	600 µJ	30 W	12 ps	50 MW	1064 nm	Nd:YVO_4	DPSS slab	MOPA	[187]
2011	10 kHz	3 mJ	30 W	470 fs	6.4 GW	1030 nm	Beam combining	Fiber	CPA	[162]
2011	5 kHz	2.2 mJ	11 W	500 fs	4.4 GW	1030 nm	PCF Yb-doped	Fiber	CPA	[160]
2012	10 kHz	11 mJ	106 W	865 fs	12.3 GW	1018 nm	Yb:YLF	Cryo SS	CPA	[188]
2012	100 Hz	1 J	100 W	5 ps	200 GW	1030 nm	Yb:YAG	Cryo SS	CPA	[89]
2012	200 kHz	40 µJ	8 W	180 fs	220 MW	1043 nm	Yb:KYW	DPSS	CPA	[189]
2012	1 MHz	3 µJ	3 W	50 fs	60 MW	1030 nm	Beam combining	Fiber	CPA	[190]
2012	10 Hz	300 mJ	3 W	141 ps	2.1 GW	1064 nm	Nd:YAG	Flashlamp	MOPA	[191]

APPENDIX C
PERFORMANCES OF THE LASER AMPLIFIER MODULES

The presented ps pulse amplifier stages (Section 4) were based on several parameters of the used amplifiers, such as cw-output power, small signal gain, thermal lens, depolarization and beam pointing. This appendix chapter summarizes the characterization and the performance of the used laser amplifier modules.

C.1 Characterization Methods

The cw performance of the amplifier modules was investigated in simple flat-flat cavities and varying output couplers based on broad-band HR coatings or a 70%-reflective VBG. These cavities differed from the typical configuration the manufacturer was using but could allow estimates about the obtainable output performance. The transverse mode was highly multi-mode in these cavity resonators since the cavities were not optimized for largest fundamental mode.

More parameters were investigated based on a single-pass probe beam at 1064 nm. The small signal gain in this low power measurement gives an estimate about the obtainable gain when used in the ps amplifier scheme. Similarly, the thermal lens was measured with the probe beam and a beam profiler and estimated within an accuracy of a several cm.

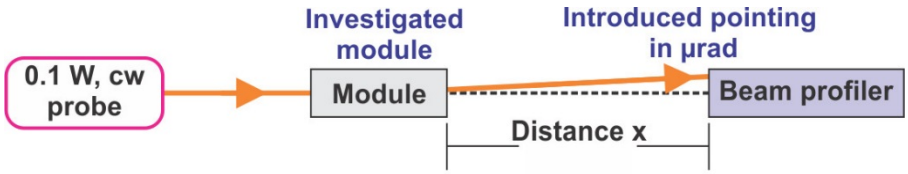

Figure C-1: Sketch of the optical setup used to investigate the beam pointing fluctuations.

Special care was taken to investigate the beam pointing fluctuations introduced by the utilized amplifier modules. Figure C-1 shows the typical scheme used for the investigations: A cw probe beam at 1064 nm with low average power and good spatial profile (Gaussian) was transmitted through the amplifier module. The propagation distance after the module was chosen to be larger than 50 cm to increase the angular resolution of the scheme. A beam profiler (Spiricon,

Ophir Optronics Solutions Ltd.) was used to record the wandering of the centroid (gravitational center of the beam profile) and measured the standard deviation of this position fluctuation. Given the pixel size (4.4 μm), the standard deviation was related to the angular deviation in μrad. It was found in all measurements that the initial probe beam had a pointing stability below the detection limit (typically less than 50 μrad), which was limited by the pixel size and the distance between the module and the beam profiler.

C.2 Characteristic Performances

Several laser amplifier modules based at the emission wavelength of Nd:YAG at 1064 nm were employed in this dissertation. The characteristic performances are listed in this section.

- Nd:YVO_4 amplifier module with 2 mm diameter (first generation):

In an earlier stage of HERACLES, the amplifier modules were based on the (called “first generation”) Vanadate modules (Northrop Grumman Cutting Edge Optronics). The rod used in the modules had a diameter of 2 mm, a pumped rod length of 3 cm with up to 180 W of pump power at 808 nm. Figure C-2 shows the cw output power in simple cavity cases and more than 30 W were obtained in most geometries.

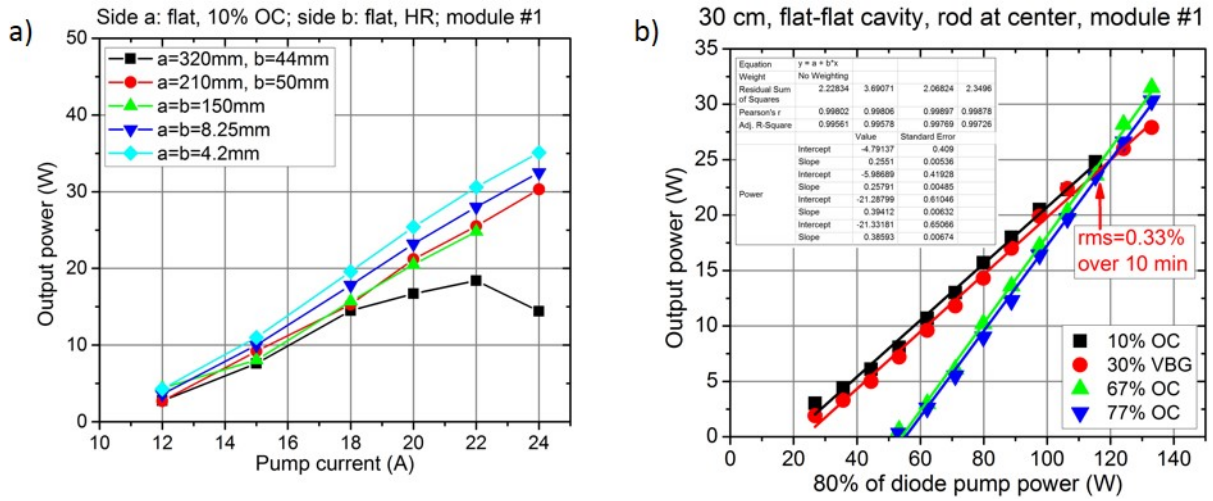

Figure C-2: cw performance of the first generation Vanadate module in simple laser cavities (a) and cw performance with a VBG and broadband OC (b).

Figure C-3 (b) show small signal gain and Figure C-4 (a) thermal lensing of the module. The Vanadate amplifier module typically had a high small signal gain of up to 4 and strong thermal lens with $f_{th} = 25\ cm$ due to the strong pumping.

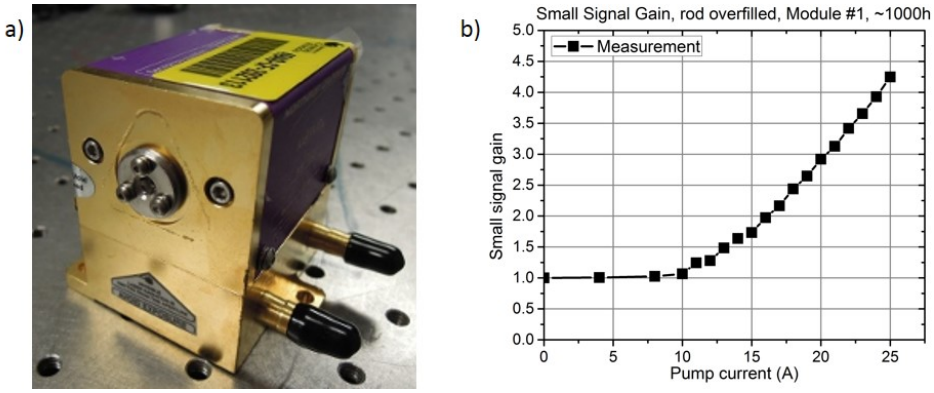

Figure C-3: Picture (a) and measured small signal gain for the first generation Vanadate module (b).

Some parameters were investigated analytically for comparison: The calculated small signal gain for this amplifier was 2.9 for a pump power of 100 W pump (80% absorbed), the stored energy $E_{st} = 5.5\ mJ$ and the saturation energy $E_{sat} = 5\ mJ$. For Vanadate, the upper energy limit was typically given by the B-integral and estimated to be around 3 mJ.

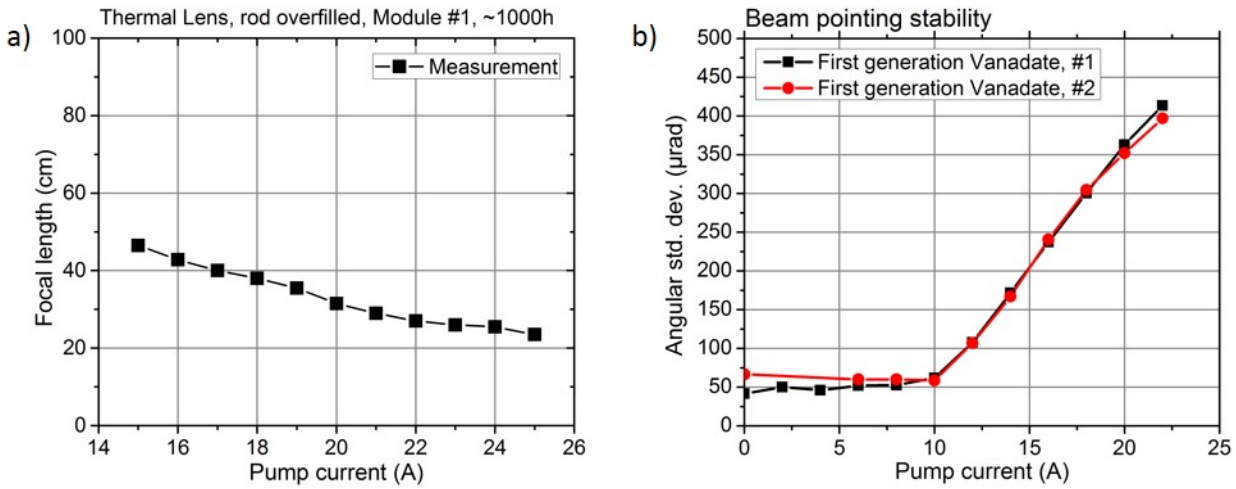

Figure C-4: Measured thermal lens (a) and pointing fluctuations (b) after passing the probe beam through the first generation Vanadate module.

As seen from Figure C-4 (b), the first generation Vanadate amplifier modules introduced severe beam pointing fluctuations under high thermal load. It was found that beam pointing fluctuations above 300 µrad would not be acceptable for the OPCPA applications since the focused beam at the OPA plane walked by more than the focal spot size. Especially for nonlinear optical effects, such as OPA with high parametric gain (10^6), this was not acceptable.

The introduced beam pointing fluctuations was explained by the manufactured in terms of poor mechanical stability of the crystal in the amplifier module. It was found that the turbulent water flow caused a small displacement of the crystal from the optical axis. The geometrical center of the thermal lens was then non-centered with respect to the optical axis. This moving lens effects led to a deviation of the original beam pointing direction for a stable on-axis probe. Since this process was instable, the pointing stability of the output beam was dramatically impacted. It was found that the effect became less severe when changing from YVO_4 to YAG due to the different mechanical mounting. The impact on the pointing stability was highest for the small 2 mm rod diameter and an increased rod diameter decreased the impact on the beam pointing stability.

- Nd:YVO_4 amplifier module with 2 mm diameter (second generation):

Similar to the first generation module, the second generation Vanadate module was tested under several conditions in order to ensure proper implementation as ps amplifier. First, a simple cavity was built to measure the cw performance of the module. The output power as shown in Figure C-5 (b) of the second generation (>50 W) improved compared to the first generation (> 35 W) potentially due to the reduced age of the pump diodes. The performance compared well with the specified performance; also a slightly different (flat-flat) cavity was used.

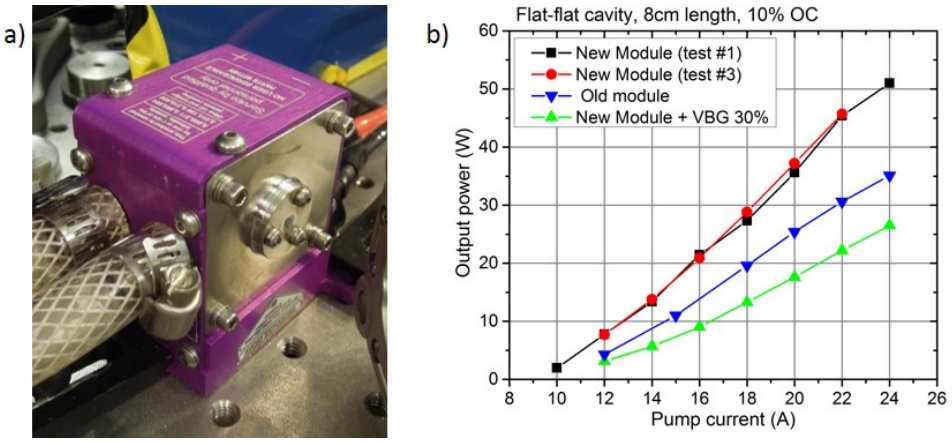

Figure C-5: Picture (a) and cw performance of the second generation Vanadate module in simple laser cavities (b).

Small signal gain showed comparable values to the first generation module and the specifications as shown in Figure C-6 (a). The induced beam pointing was moderate with <100 µrad as shown in Figure C-6 (b). In conclusion, the module was highly suitable as amplifier module in our OPCPA application and was implemented as single pass amplifier (see Section 4.3).

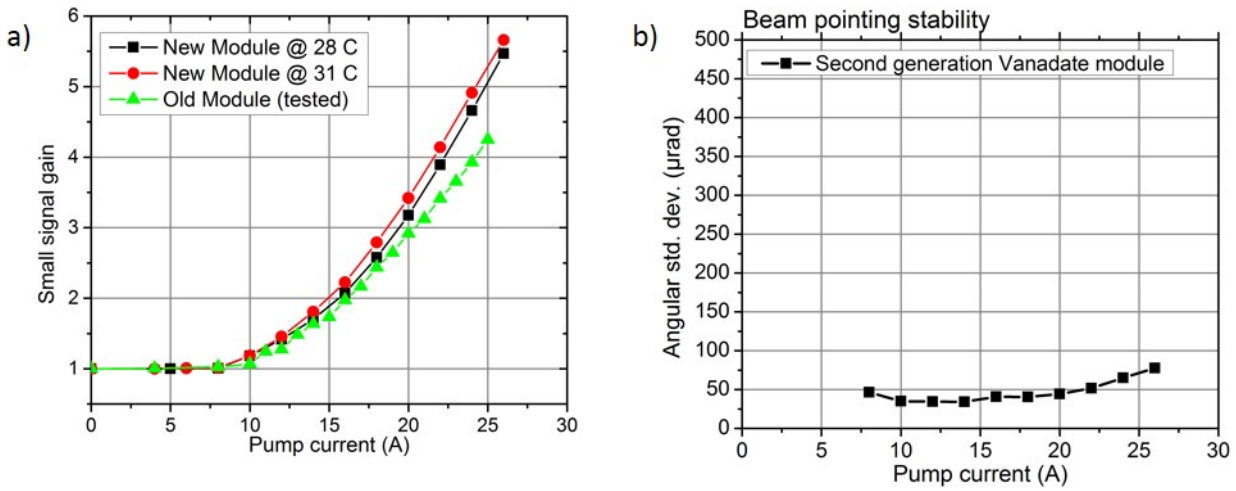

Figure C-6: Measured thermal lens for the second generation Vanadate module (a) and introduced beam pointing fluctuations (b).

- Nd:YAG amplifier module with 2 mm diameter:

The performance of a Nd:YAG laser module with 2 mm rod diameter was investigated. The cw performance is shown in Figure C-7 and was comparable to the second generation Nd:YVO_4 module up to 20 A with >30 W output. The small signal gain was measured to be >2.0 at 22 A and the results are shown in Figure C-8.

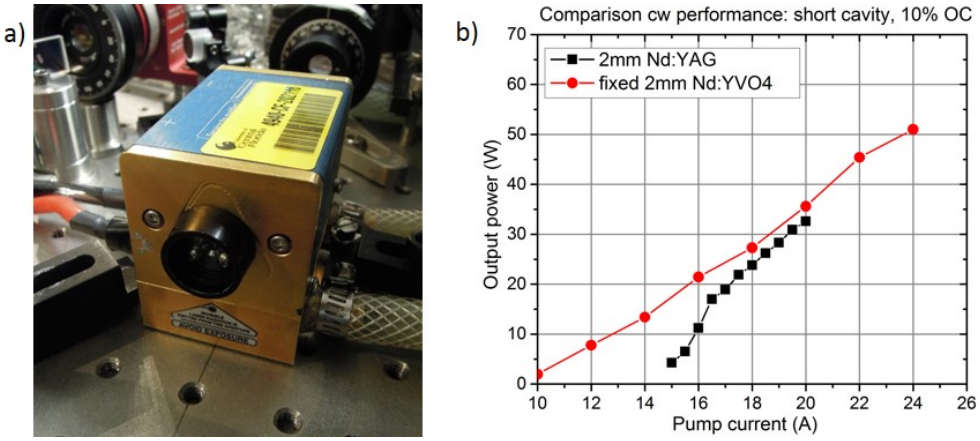

Figure C-7: Picture (a) and cw performance of the 2 mm diameter YAG module in a simple laser cavity (b).

Due to the pointing instabilities with the first generation Vanadate modules, the beam pointing induced by the YAG amplifier module was investigated as shown in Figure C-8 (b). As indicated in Figure C-8 the beam pointing fluctuations exceeded 100 µrad under strong thermal

load. A regenerative amplifier (Section 4.3.2) based on the YAG module was implemented. It was found that the output beam pointing fluctuations of the regenerative amplifier were low (less than 50 µrad) due to the resonant cavity.

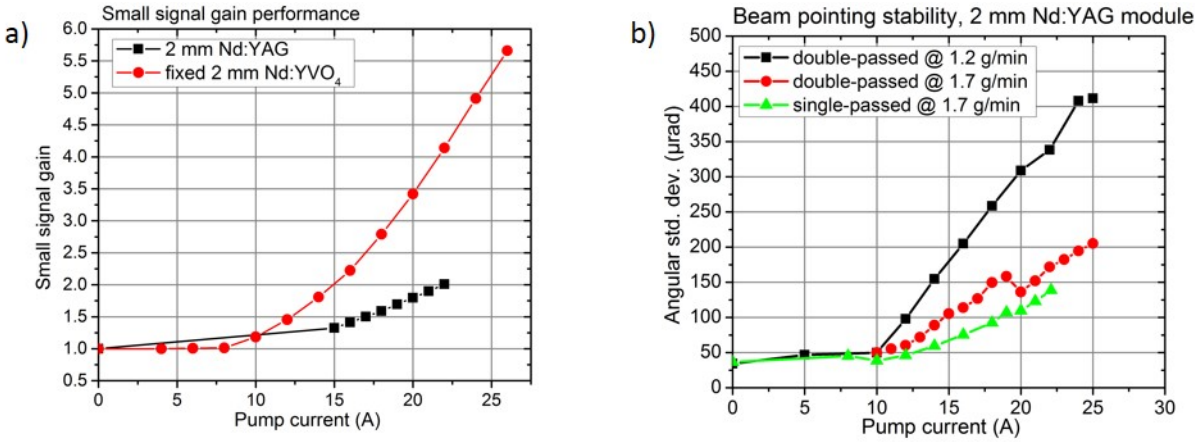

Figure C-8: Measured small signal gain (a) and introduced beam pointing fluctuations (b) for the 2 mm Nd:YAG module.

- Nd:YAG amplifier modules with 3 mm diameter:

  The performance of two Nd:YAG laser modules with 3 mm rod diameter was investigated. The cw performance of the modules is shown in Figure C-9 (b) and up to 94 W and 70 W was measured, respectively.

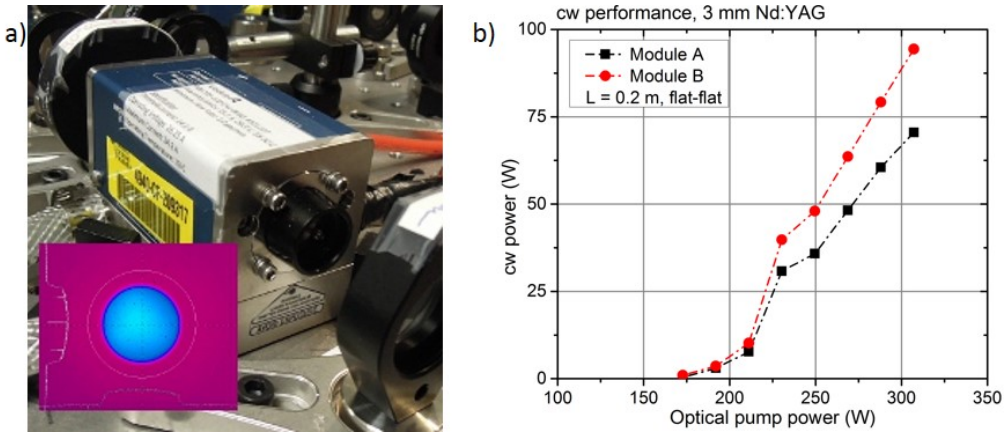

Figure C-9: (a) Picture of the Nd:YAG module with 3 mm diameter. (b) cw performance of two 3 mm diameter YAG modules in a simple laser cavity.

The small signal gain was investigated and values up to 2.2 are found, as is shown in Figure C-10 with a depolarization of up to 23.4%.

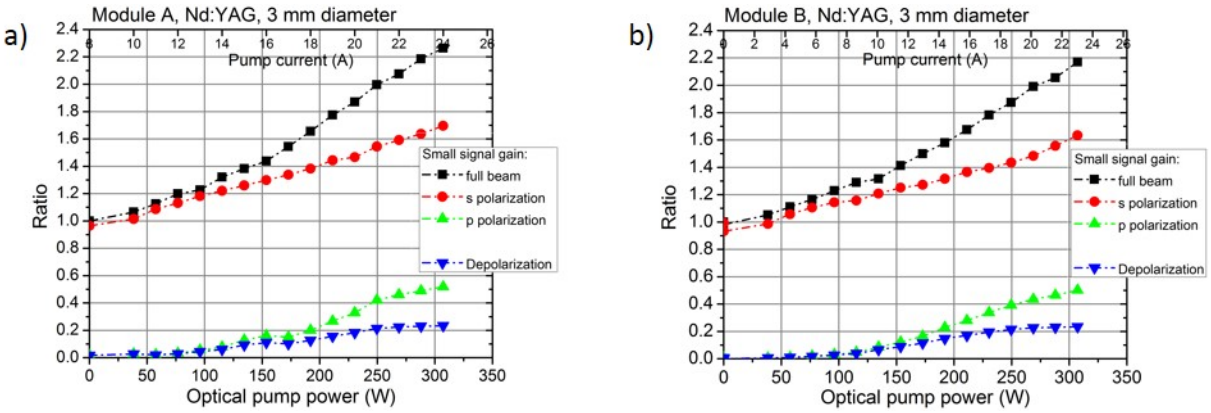

Figure C-10: Measured small signal gain for the Nd:YAG modules A (a) and B (b).

The introduced beam pointing fluctuations were studied and no influence (less than measurement limit of <50 µrad) was found as shown in Figure C-11.

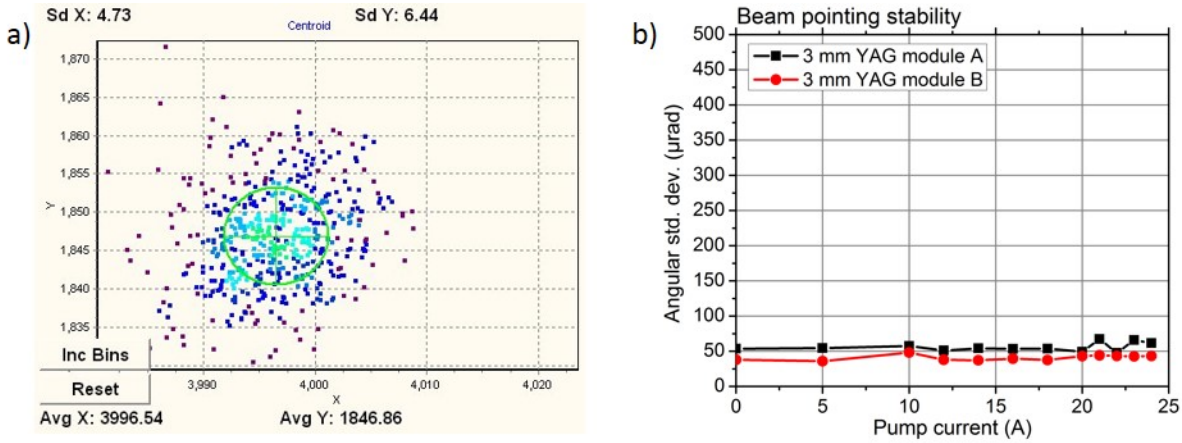

Figure C-11: Introduced beam pointing fluctuations (a) for the 3 mm Nd:YAG modules A and B (b).

- Nd:YAG amplifier module with 4 mm diameter:

The performance of a Nd:YAG laser module with 4 mm rod diameter was investigated. The cw performance of the module is shown in Figure C-12 (b) and more than 110 W was measured. The module was able to generate more than 240 W according to the manufacturer.

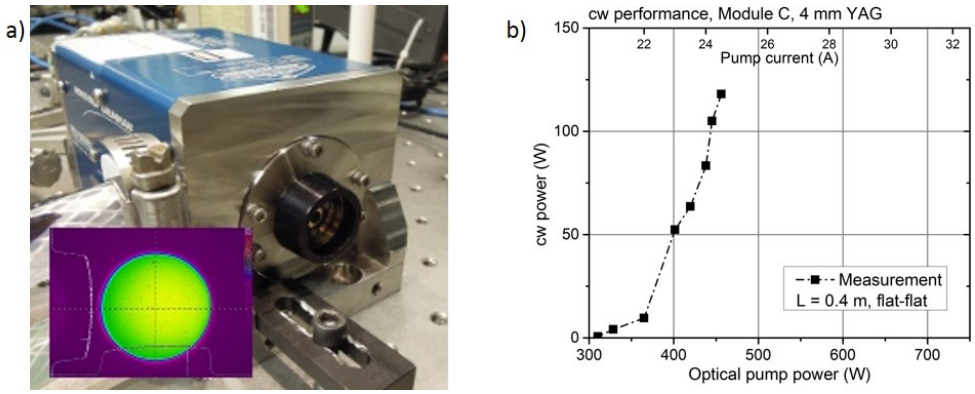

Figure C-12: Picture (a) and cw performance of a 4 mm diameter YAG modules in a simple laser cavity (b).

The small signal gain was measured to exceed 2.6 as shown in Figure C-11 (a) with a depolarization of up to 32%. The introduced beam pointing fluctuations were studied and no influence (less than measurement limit of <60 µrad) was found as shown in Figure C-11 (a).

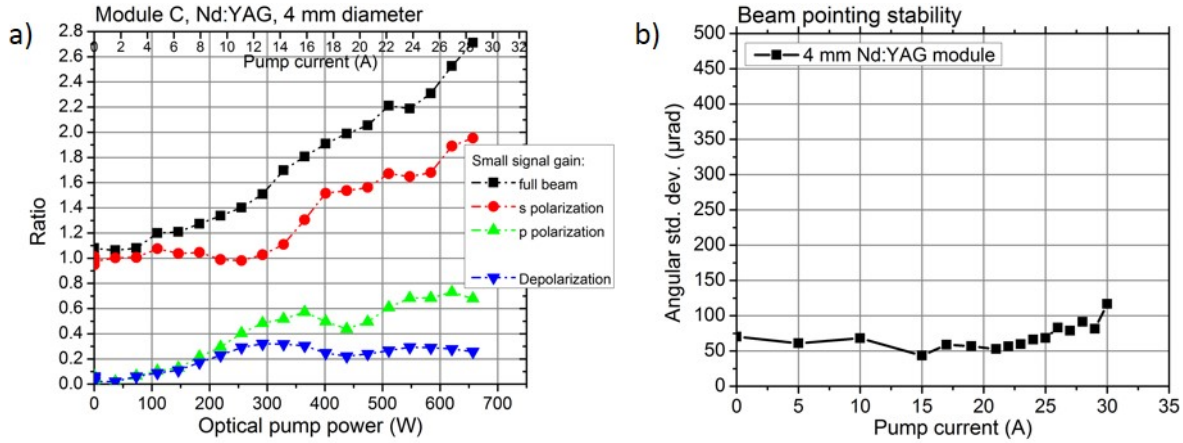

Figure C-13: Measured small signal gain (a) and introduced beam pointing fluctuations (b) for the 4 mm Nd:YAG module.

The depolarization process was investigated with a cw probe beam after a single-pass through the amplifier and relay imaging of the amplifier module onto a beam profiler. Figure C-14 shows the obtained beam profiles and the depolarization loss was measured to be 25.8% (last profile). Similarly as seen before, the depolarization was mainly affecting the outer part of the beam.

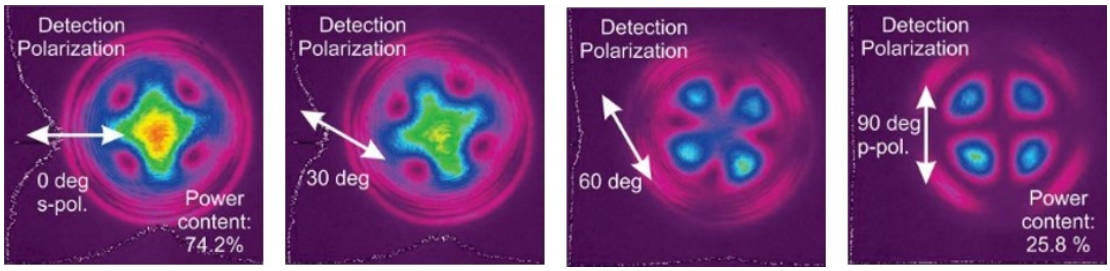

Figure C-14: The beam profiles show the depolarization of a probe beam passing through the 4 mm diameter Nd:YAG amplifier. Nd:YAG amplifier module with 10 mm diameter:

The large aperture, Nd:YAG modules were investigated similarly. The small signal gain (factor 1.28 at 36 A) are presented in Figure C-15 (b). Some parameters were investigated analytically: The calculated small signal gain was 1.38 for a pump power of 1.2 kW pump (80% absorbed), the stored energy $E_{st} = 168\,mJ$ and the saturation energy $E_{sat} = 520\,mJ$. For 1 cm diameter YAG, the upper energy limit was given by the damage threshold and estimated to be above 235 mJ.

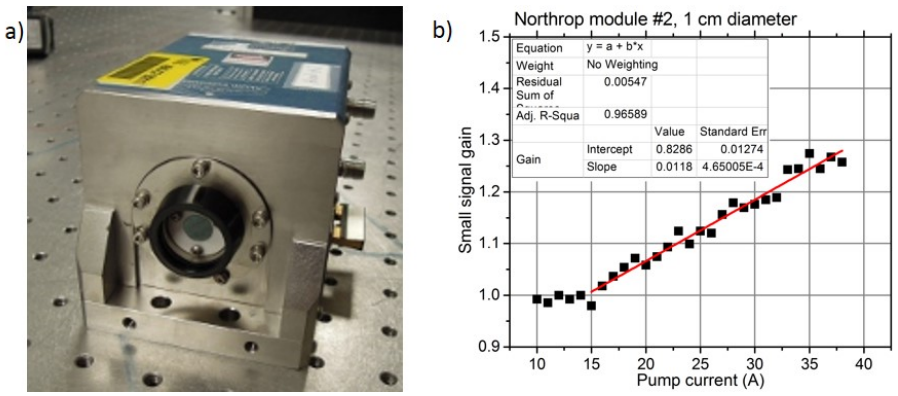

Figure C-15: Picture of the 1 cm diameter, Nd:YAG module (a) and measured small signal gain of the 1 cm diameter YAG module (b).

The thermal lens was measured and the results are presented in Figure C-16 (a). The large aperture modules showed no impact (less than measurement limit of <35 µrad) on the beam pointing fluctuations due to the increased mechanical stability as shown in Figure C-16 (b).

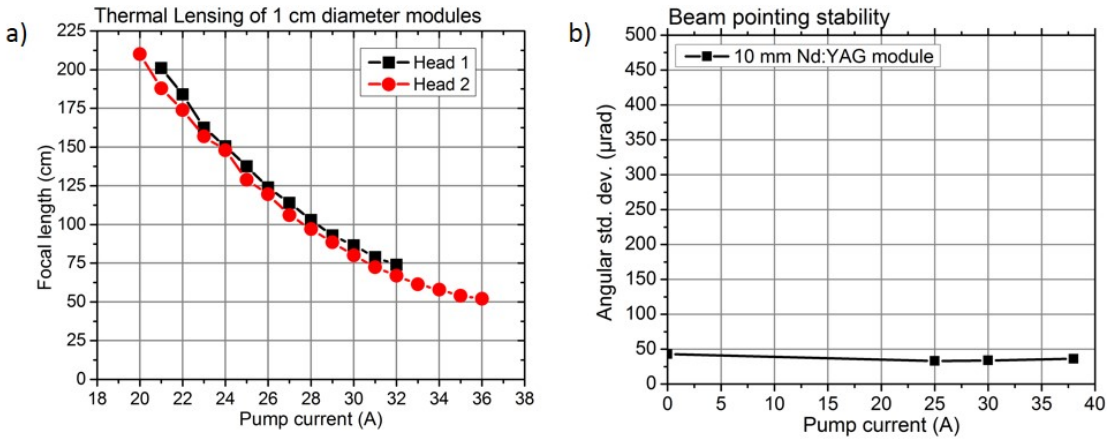

Figure C-16: Measured thermal lens (a) and introduced beam pointing fluctuations (b) for the 10 mm Nd:YAG module.

LIST OF REFERENCES

[1] U. Keller, “Recent developments in compact ultrafast lasers,” *Nature*, vol. 424, no. 6950, pp. 831–8, Aug. 2003.

[2] M. Ferray, A. L’Huillier, X. F. Li, L. A. Lomprk, G. Mainfray, and C. Manus, “Multiple-harmonic conversion of 1064 nm radiation in rare gases,” *Journal of Physics B: Atomic, Molecular and Optical Physics*, vol. 21, no. 3, 1988.

[3] P. Gonzales, R. Bernath, J. Duncan, T. Olmstead, and M. Richardson, “Femtosecond ablation scaling for different materials,” in *SPIE Proceedings Vol. 5458, Optical Micro- and Nanometrology in Manufacturing Technology*, 2004, vol. 5458, no. 407, pp. 265–272.

[4] A. Zoubir, C. Lopez, M. Richardson, and K. Richardson, “Femtosecond laser fabrication of tubular waveguides in poly(methyl methacrylate),” *Optics Letters*, vol. 29, no. 16, pp. 1840–2, Aug. 2004.

[5] H. Huang, A. Hu, P. Peng, W. W. Duley, and Y. Zhou, “Femtosecond laser-induced microwelding of silver and copper,” *Applied Optics*, vol. 52, no. 6, pp. 1211–7, Feb. 2013.

[6] D. Polli, M. R. Antognazza, D. Brida, G. Lanzani, G. Cerullo, and S. De Silvestri, “Broadband pump-probe spectroscopy with sub-10-fs resolution for probing ultrafast internal conversion and coherent phonons in carotenoids,” *Chemical Physics*, vol. 350, no. 1–3, pp. 45–55, Jun. 2008.

[7] T. Udem, R. Holzwarth, and T. W. Hänsch, “Optical frequency metrology,” *Nature*, vol. 416, no. 6877, pp. 233–7, Mar. 2002.

[8] R. Holzwarth, T. Udem, T. W. Hänsch, J. C. Knight, W. J. Wadsworth, and P. S. J. Russell, “Optical frequency synthesizer for precision spectroscopy,” *Physical Review Letters*, vol. 85, no. 11, pp. 2264–7, Sep. 2000.

[9] L.-S. Ma, Z. Bi, A. Bartels, L. Robertsson, M. Zucco, R. S. Windeler, G. Wilpers, C. Oates, L. Hollberg, and S. A. Diddams, “Optical frequency synthesis and comparison with uncertainty at the 10(-19) level,” *Science*, vol. 303, no. 5665, pp. 1843–5, Mar. 2004.

[10] P. B. Corkum, “Plasma Perspective on Strong Field Multiphoton Ionization,” *Physical Review Letters*, vol. 71, no. 13, pp. 1994–1997, 1993.

[11] Z. Chang, *Fundamentals of Attosecond Optics*. CRC Press, 2011.

[12] M. Hentschel, R. Kienberger, C. Spielmann, G. A. Reider, N. Milosevic, T. Brabec, P. Corkum, U. Heinzmann, M. Drescher, and F. Krausz, “Attosecond metrology,” *Nature*, vol. 414, no. 6863, pp. 509–13, Nov. 2001.

[13] E. Gagnon, P. Ranitovic, X.-M. Tong, C. L. Cocke, M. M. Murnane, H. C. Kapteyn, and A. S. Sandhu, “Soft X-ray-driven femtosecond molecular dynamics,” *Science*, vol. 317, no. 5843, pp. 1374–8, Sep. 2007.

[14] J. Boullet, Y. Zaouter, J. Limpert, S. Petit, Y. Mairesse, B. Fabre, J. Higuet, E. Mével, E. Constant, and E. Cormier, “High-order harmonic generation at a megahertz-level repetition rate directly driven by an ytterbium-doped-fiber chirped-pulse amplification system,” *Optics Letters*, vol. 34, no. 9, pp. 1489–1491, 2009.

[15] E. Goulielmakis, M. Schultze, M. Hofstetter, V. S. Yakovlev, J. Gagnon, M. Uiberacker, a L. Aquila, E. M. Gullikson, D. T. Attwood, R. Kienberger, F. Krausz, and U. Kleineberg, “Single-Cycle Nonlinear Optics,” *Science*, vol. 320, no. 5883, pp. 1614–7, Jun. 2008.

[16] J. Seres, E. Seres, A. J. Verhoef, G. Tempea, C. Streli, P. Wobrauchschek, V. Yakovlev, A. Scrinzi, C. Spielmann, and F. Krausz, “Source of coherent kiloelectronvolt X-rays,” *Nature*, vol. 433, no. 7026, p. E13; discussion E13–4, Feb. 2005.
[17] Z. Chang, “Controlling attosecond pulse generation with a double optical gating,” *Physical Review A*, vol. 76, no. 5, p. 051403, Nov. 2007.
[18] K. Zhao, Q. Zhang, M. Chini, Y. Wu, X. Wang, and Z. Chang, “Tailoring a 67 attosecond pulse through advantageous phase-mismatch,” *Optics Letters*, vol. 37, no. 18, pp. 3891–3893, 2012.
[19] P. B. Corkum and F. Krausz, “Attosecond science,” *Nature Physics*, pp. 381–387, 2007.
[20] M. Kling and F. Krausz, “Attoscience: An attosecond stopwatch,” *Nature Physics*, vol. 4, no. July, pp. 4–5, 2008.
[21] M. Uiberacker, T. Uphues, M. Schultze, a J. Verhoef, V. Yakovlev, M. F. Kling, J. Rauschenberger, N. M. Kabachnik, H. Schröder, M. Lezius, K. L. Kompa, H.-G. Muller, M. J. J. Vrakking, S. Hendel, U. Kleineberg, U. Heinzmann, M. Drescher, and F. Krausz, “Attosecond real-time observation of electron tunnelling in atoms,” *Nature*, vol. 446, no. 7136, pp. 627–32, Apr. 2007.
[22] R. L. Sandberg, A. Paul, D. A. Raymondson, S. Hädrich, D. M. Gaudiosi, J. Holtsnider, R. I. Tobey, O. Cohen, M. M. Murnane, and H. C. Kapteyn, “Lensless Diffractive Imaging Using Tabletop Coherent High-Harmonic Soft-X-Ray Beams,” *Physical Review Letters*, vol. 99, no. 9, p. 098103, Aug. 2007.
[23] G. Lambert, T. Hara, D. Garzella, T. Tanikawa, M. Labat, B. Carre, H. Kitamura, T. Shintake, M. Bougeard, S. Inoue, Y. Tanaka, P. Salieres, H. Merdji, O. Chubar, O. Gobert, K. Tahara, and M.-E. Couprie, “Injection of harmonics generated in gas in a free-electron laser providing intense and coherent extreme-ultraviolet light,” *Nature Physics*, vol. 4, no. 4, pp. 296–300, Mar. 2008.
[24] A. Pukhov, Z.-M. Sheng, and J. Meyer-ter-Vehn, “Particle acceleration in relativistic laser channels,” *Physics of Plasmas*, vol. 6, no. 7, p. 2847, 1999.
[25] S. C. Wilks, A. B. Langdon, T. E. Cowan, M. Roth, M. Singh, S. Hatchett, M. H. Key, D. Pennington, A. MacKinnon, and R. A. Snavely, “Energetic proton generation in ultra-intense laser–solid interactions,” *Physics of Plasmas*, vol. 8, no. 2, p. 542, 2001.
[26] M. Nishiuchi, A. S. Pirozhkov, H. Sakaki, K. Ogura, T. Z. Esirkepov, T. Tanimoto, A. Yogo, T. Hori, A. Sagisaka, Y. Fukuda, M. Kanasaki, H. Kiriyama, T. Shimomura, M. Tanoue, Y. Nakai, H. Sasao, F. Sasao, S. Kanazawa, S. Kondo, Y. Matsumoto, S. Sakai, C. Brenner, D. Neely, S. V. Bulanov, and K. Kondo, “Recent progress in particle acceleration from the interaction between thin-foil targets and J-KAREN laser pulses,” in *AIP Conference Proceedings*, 2012, vol. 133, no. May 2013, pp. 133–141.
[27] M. Veltcheva, A. Borot, C. Thaury, A. Malvache, E. Lefebvre, A. Flacco, R. Lopez-Martens, and V. Malka, “Brunel-Dominated Proton Acceleration with a Few-Cycle Laser Pulse,” *Physical Review Letters*, vol. 108, no. 7, p. 075004, Feb. 2012.
[28] R. Ell, U. Morgner, F. X. Kärtner, J. G. Fujimoto, E. P. Ippen, V. Scheuer, G. Angelow, T. Tschudi, M. J. Lederer, A. Boiko, and B. Luther-Davies, “Generation of 5-fs pulses and octave-spanning spectra directly from a Ti:sapphire laser,” *Optics Letters*, vol. 26, no. 6, pp. 373–5, Mar. 2001.
[29] L. Matos, D. Kleppner, O. Kuzucu, T. R. Schibli, J. Kim, E. P. Ippen, and F. X. Kaertner, “Direct frequency comb generation from an octave-spanning, prismless Ti:sapphire laser,” *Optics Letters*, vol. 29, no. 14, pp. 1683–5, Jul. 2004.

[30] A. E. Siegman, *Lasers*, First Edit. University Science Books, 1986.
[31] T. Nakajima and E. Cormier, "Effects of the carrier-envelope phase of chirped laser pulses in the multiphoton ionization regime," *Optics Letters*, vol. 32, no. 19, pp. 2879–81, Oct. 2007.
[32] D. Strickland and G. Mourou, "Compression of amplified chirped optical pulses," *Optics Communications*, vol. 55, no. 6, pp. 447–449, 1985.
[33] P. Maine, D. Strickland, P. Bado, M. Pessot, and G. Mourou, "Generation of Ultrahigh Peak Power Pulses by Chirped Pulse Amplification," *IEEE Journal of Quantum Electronics*, vol. 24, no. 2, pp. 398–403, Feb. 1988.
[34] K. Yamakawa and C. P. J. Barty, "Ultrafast, Ultrahigh-Peak, and High-Average Power Ti:Sapphire Laser System and Its Applications," *Selected Topics in Quantum Electronics*, vol. 6, no. 4, pp. 658–675, 2000.
[35] M. Nisoli, S. De Silvestri, O. Svelto, R. Szipöcs, K. Ferencz, C. Spielmann, S. Sartania, and F. Krausz, "Compression of high-energy laser pulses below 5 fs," *Optics Letters*, vol. 22, no. 8, pp. 522–4, Apr. 1997.
[36] C. P. Hauri, W. Kornelis, F. W. Helbing, a. Heinrich, a. Couairon, a. Mysyrowicz, J. Biegert, and U. Keller, "Generation of intense, carrier-envelope phase-locked few-cycle laser pulses through filamentation," *Applied Physics B*, vol. 79, no. 6, pp. 673–677, Sep. 2004.
[37] A. Baltuška, T. Fuji, and T. Kobayashi, "Visible pulse compression to 4 fs by optical parametric amplification and programmable dispersion control," *Optics Letters*, vol. 27, no. 5, pp. 306–308, 2002.
[38] D. Herrmann, L. Veisz, R. Tautz, F. Tavella, K. Schmid, V. Pervak, and F. Krausz, "Generation of sub-three-cycle, 16 TW light pulses by using noncollinear optical parametric chirped-pulse amplification," *Optics Letters*, vol. 34, no. 16, pp. 2459–61, Aug. 2009.
[39] J. Rothhardt, S. Demmler, S. Hädrich, J. Limpert, and A. Tünnermann, "Octave-spanning OPCPA system delivering CEP-stable few-cycle pulses and 22 W of average power at 1 MHz repetition rate," *Optics Express*, vol. 20, no. 10, pp. 10870–8, May 2012.
[40] F. Tavella, A. Marcinkevicius, and F. Krausz, "90 mJ parametric chirped pulse amplification of 10 fs pulses," *Optics Express*, vol. 14, no. 26, pp. 12822–12827, 2006.
[41] O. Chalus, P. K. Bates, M. Smolarski, and J. Biegert, "Mid-IR short-pulse OPCPA with micro-Joule energy at 100 kHz," *Optics Express*, vol. 17, no. 5, pp. 3587–94, Mar. 2009.
[42] K.-H. Hong, S.-W. Huang, J. Moses, X. Fu, C.-J. Lai, G. Cirmi, A. Sell, E. Granados, P. Keathley, and F. X. Kärtner, "High-energy, phase-stable, ultrabroadband kHz OPCPA at 2.1 μm pumped by a picosecond cryogenic Yb:YAG laser," *Optics Express*, vol. 19, no. 16, pp. 15538–15548, 2011.
[43] Y. Deng, A. Schwarz, H. Fattahi, M. Ueffing, X. Gu, M. Ssiander, T. Metzger, V. Pervak, H. Ishizuki, T. Taira, T. Kobayashi, G. Marcus, F. Krausz, R. Kienberger, and N. Karpowicz, "Carrier-envelope-phase-stable, 1.2 mJ, 1.5 cycle laser pulses at 2.1 μm," *Optics Letters*, vol. 37, no. 23, pp. 4973–4975, 2012.
[44] S. Hädrich, S. Demmler, J. Rothhardt, C. Jocher, J. Limpert, and A. Tünnermann, "High-repetition-rate sub-5-fs pulses with 12 GW peak power from fiber-amplifier-pumped optical parametric chirped-pulse amplification," *Optics Letters*, vol. 36, no. 3, pp. 313–5, Feb. 2011.
[45] A. Vaupel, N. Bodnar, B. Webb, L. Shah, E. Cormier, and M. Richardson, "Energy-scaling of DPSS Picosecond Amplifiers for OPCPA Pumping," in *Conference on Lasers and Electro-Optics (CLEO)*, 2013, vol. 2, p. CM1N.2.

[46] A. Vaupel, N. Bodnar, B. Webb, M. Hemmer, and M. Richardson, "Design and preliminary results for a sub-5-fs, 100 mJ-level, CEP-stabilized laser facility-PhaSTHEUS," in *OSA High Intensity Lasers and High Field Phenomena (HILAS)*, 2011, p. HThE5.
[47] M. Hemmer, A. Vaupel, and M. Richardson, "High power, quasi-single cycle, phase-correlated laser systems for EUV and Attoscience studies," in *International Symposium on Ultra-fast Phenomena and Terahertz Waves (ISUPTW)*, 2010.
[48] F. Krausz and M. Ivanov, "Attosecond physics," *Reviews of Modern Physics*, vol. 81, no. 1, pp. 163–234, Feb. 2009.
[49] S. A. Trushin, K. Kosma, W. Fuss, and W. E. Schmid, "Sub-10-fs supercontinuum radiation generated by filamentation of few-cycle 800 nm pulses in argon," *Optics Letters*, vol. 32, no. 16, pp. 2432–4, Aug. 2007.
[50] N. Sanner, O. Utéza, B. Chimier, M. Sentis, P. Lassonde, F. Légaré, and J. C. Kieffer, "Toward determinism in surface damaging of dielectrics using few-cycle laser pulses," *Applied Physics Letters*, vol. 96, no. 7, p. 071111, 2010.
[51] M. Hemmer, A. Vaupel, B. Webb, and M. Richardson, "Multi-kHz, Multi-mJ, Phase Stabilized, OPCPA Amplifier System," in *Proceedings of SPIE 7578, Solid State Lasers XIX: Technology and Devices*, 2010, vol. 7578, pp. 757818–757818–8.
[52] M. Hemmer, A. Vaupel, and M. Richardson, "Current Status of the HERACLES, a Millijoule Level, Multi kHz, Few-Cycle, and CEP Stabilized OPCPA System," *Conference on Lasers and Electro-Optics (CLEO)*, p. CTuFF5, 2010.
[53] D. Herrmann, C. Homann, R. Tautz, M. Scharrer, P. S. J. Russel, F. Krausz, L. Veisz, and E. Riedle, "Approaching the full octave: Noncollinear optical parametric chirped pulse amplification with two-color pumping," *Optics Express*, vol. 18, no. 18, pp. 18752–62, Aug. 2010.
[54] J. Boullet, Y. Zaouter, R. Desmarchelier, M. Cazaux, F. Salin, J. Saby, R. Bello-Doua, and E. Cormier, "High power ytterbium-doped rod-type three-level photonic crystal fiber laser," *Optics Express*, vol. 16, no. 22, pp. 17891–17902, 2008.
[55] S. Backus, C. G. Durfee, M. M. Murnane, and H. C. Kapteyn, "High power ultrafast lasers," *Review of Scientific Instruments*, vol. 69, no. 3, pp. 1207–1223, 1998.
[56] G. Cerullo and S. De Silvestri, "Ultrafast optical parametric amplifiers," *Review of Scientific Instruments*, vol. 74, no. 1, p. 1, 2003.
[57] O. E. Martinez, J. P. Gordon, and R. L. Fork, "Negative group-velocity dispersion using refraction," *Journal of the Optical Society of America A*, vol. 1, no. 10, pp. 1003–1006, 1984.
[58] M. P. Kalachnikov, V. Karpov, H. Schönnagel, and W. Sandner, "100-Terawatt Titanium-Sapphire Laser System," *Laser Physics - Strong Field Phenomena*, vol. 12, no. 2, pp. 368–374, 2002.
[59] I. Matsushima, H. Yashiro, and T. Tomie, "10 kHz 54 W Ti:sapphire regenerative amplifier as a pumping laser of a laser-plasma X-ray source," in *Proceedings of SPIE*, 2008, vol. 7022, p. 70220M–70220M–9.
[60] E. B. Treacy, "Optical Pulse Compression With Diffraction Gratings," *IEEE Journal of Quantum Electronics*, no. 9, pp. 454–458, 1969.
[61] R. L. Fork, O. E. Martinez, and J. P. Gordon, "Negative dispersion using pairs of prisms," *Optics Letters*, vol. 9, no. 5, pp. 150–2, May 1984.
[62] T. Tanabe, M. Yamanaka, T. Okamoto, and F. Kannari, "Compensation for a Transfer Function of a Regenerative Amplifier to Generate Accurately Shaped Ultrashort Pulses in

Both the Amplitude and Phase," *Selected Topics in Quantum Electronics*, vol. 10, no. 1, pp. 221–228, 2004.
[63] K. Yamane, Z. Zhang, K. Oka, R. Morita, M. Yamashita, and A. Suguro, "Optical pulse compression to 3.4 fs in the monocycle region by feedback phase compensation," *Optics Letters*, vol. 28, no. 22, pp. 2258–60, Nov. 2003.
[64] A. Anderson, F. Lücking, T. Prikoszovits, M. Hofer, Z. Cheng, C. C. Neacsu, M. Scharrer, S. Rammler, P. S. J. Russell, G. Tempea, and A. Assion, "Multi-mJ carrier envelope phase stabilized few-cycle pulses generated by a tabletop laser system," *Applied Physics B*, vol. 103, no. 3, pp. 531–536, May 2011.
[65] T. Nagy, V. Pervak, and P. Simon, "Optimal pulse compression in long hollow fibers," *Optics Letters*, vol. 36, no. 22, pp. 4422–4, Nov. 2011.
[66] C. Jocher, T. Eidam, S. Hädrich, J. Limpert, and A. Tünnermann, "Sub 25 fs pulses from solid-core nonlinear compression stage at 250 W of average power," *Optics Letters*, vol. 37, no. 21, p. 4407, Oct. 2012.
[67] L. Shah, A. Vaupel, B. Webb, N. Bodnar, M. Hemmer, and M. Richardson, "The OPCPA approach to high-repetition-rate ultra-fast lasers," in *Advanced High Power Lasers and Beam Control Conference, DEPS 10th Annual Ultrashort Pulse Laser Workshop*, 2012.
[68] A. Dubietis, G. Jonušauskas, and A. Piskarskas, "Powerful femtosecond pulse generation by chirped and stretched pulse parametric amplification in BBO crystal," *Optics Communications*, vol. 88, pp. 437–440, 1992.
[69] S. Witte, R. T. Zinkstok, A. L. Wolf, W. Hogervorst, W. Ubachs, and K. S. E. Eikema, "A source of 2 terawatt, 2.7 cycle laser pulses based on noncollinear optical parametric chirped pulse amplification," *Optics Express*, vol. 14, no. 18, pp. 8168–77, Sep. 2006.
[70] M. Schultze, T. Binhammer, A. Steinmann, G. Palmer, M. Emons, and U. Morgner, "Few-cycle OPCPA system at 143 kHz with more than 1 microJ of pulse energy," *Optics Express*, vol. 18, no. 3, pp. 2836–41, Feb. 2010.
[71] S. Adachi, H. Ishii, T. Kanai, N. Ishii, A. Kosuge, and S. Watanabe, "1.5 mJ, 6.4 fs parametric chirped-pulse amplification system at 1 kHz," *Optics Letters*, vol. 32, no. 17, pp. 2487–2489, 2007.
[72] F. Tavella, Y. Nomura, L. Veisz, V. Pervak, A. Marcinkevicius, and F. Krausz, "Dispersion management for a sub-10-fs, 10 TW optical parametric chirped-pulse amplifier," *Optics Letters*, vol. 32, no. 15, pp. 2227–9, Aug. 2007.
[73] G. Andriukaitis, T. Balčiūnas, S. Ališauskas, A. Pugžlys, A. Baltuška, T. Popmintchev, M.-C. Chen, M. M. Murnane, and H. C. Kapteyn, "90 GW peak power few-cycle mid-infrared pulses from an optical parametric amplifier," *Optics Letters*, vol. 36, no. 15, pp. 2755–7, Aug. 2011.
[74] S. Klingebiel, I. Ahmad, C. Wandt, C. Skrobol, S. A. Trushin, Z. Major, F. Krausz, and S. Karsch, "Experimental and theoretical investigation of timing jitter inside a stretcher-compressor setup," *Optics Express*, vol. 20, no. 4, pp. 3443–3455, 2012.
[75] S. Fourmaux, S. Payeur, S. Buffechoux, P. Lassonde, C. St-Pierre, F. Martin, and J. C. Kieffer, "Pedestal cleaning for high laser pulse contrast ratio with a 100 TW class laser system," *Optics Express*, vol. 19, no. 9, pp. 8486–97, Apr. 2011.
[76] J. M. Mikhailova, A. Buck, A. Borot, K. Schmid, C. Sears, G. D. Tsakiris, F. Krausz, and L. Veisz, "Ultra-high-contrast few-cycle pulses for multipetawatt-class laser technology," *Optics Letters*, vol. 36, no. 16, pp. 3145–7, Aug. 2011.

[77] X. Gu, G. Marcus, Y. Deng, T. Metzger, C. Teisset, N. Ishii, T. Fuji, A. Baltuska, R. Butkus, V. Pervak, H. Ishizuki, T. Taira, T. Kobayashi, R. Kienberger, and F. Krausz, "Generation of carrier-envelope-phase-stable 2-cycle 740-μJ pulses at 2.1-μm carrier wavelength," *Optics Express*, vol. 17, no. 1, 2009.

[78] J. Rothhardt, S. Hädrich, E. Seise, M. Krebs, F. Tavella, A. Willner, S. Düsterer, H. Schlarb, J. Feldhaus, J. Limpert, J. Rossbach, and A. Tünnermann, "High average and peak power few-cycle laser pulses delivered by fiber pumped OPCPA system," *Optics Express*, vol. 18, no. 12, pp. 12719–26, Jun. 2010.

[79] C. Vozzi, G. Cirmi, C. Manzoni, E. Benedetti, F. Calegari, G. Sansone, S. Stagira, O. Svelto, S. De Silvestri, M. Nisoli, and G. Cerullo, "High-energy, few-optical-cycle pulses at 1.5 μm with passive carrier-envelope phase stabilization," *Optics Express*, vol. 14, no. 21, pp. 1150–1152, 2006.

[80] S. Adachi, N. Ishii, T. Kanai, A. Kosuge, J. Itatani, D. Yoshitomi, K. Torizuka, and S. Watanabe, "5-fs, multi-mJ, CEP-locked parametric chirped-pulse amplifier pumped by a 450-nm source at 1 kHz," *Optics Express*, vol. 16, no. 19, pp. 8168–8177, 2008.

[81] J. Moses, S.-W. Huang, K.-H. Hong, O. D. Mücke, E. L. Falcão-Filho, A. Benedick, F. O. Ilday, A. Dergachev, J. A. Bolger, B. J. Eggleton, and F. X. Kärtner, "Highly stable ultrabroadband mid-IR optical parametric chirped-pulse amplifier optimized for superfluorescence suppression," *Optics Letters*, vol. 34, no. 11, pp. 1639–41, Jun. 2009.

[82] O. Chalus, A. Thai, P. K. Bates, and J. Biegert, "Six-cycle mid-infrared source with 3.8 μJ at 100 kHz," *Optics Letters*, vol. 35, no. 19, pp. 3204–06, 2010.

[83] M. Emons, A. Steinmann, T. Binhammer, G. Palmer, M. Schultze, and U. Morgner, "Sub-10-fs pulses from a MHz-NOPA with pulse energies of 0.4 μJ," *Optics Express*, vol. 18, no. 2, pp. 1191–6, Jan. 2010.

[84] M. Schultze, T. Binhammer, G. Palmer, M. Emons, T. Lang, and U. Morgner, "Multi-μJ, CEP-stabilized, two-cycle pulses from an OPCPA system with up to 500 kHz repetition rate," *Optics Express*, vol. 18, no. 26, pp. 27291–7, Dec. 2010.

[85] T. Metzger, A. Schwarz, C. Y. Teisset, D. Sutter, A. Killi, R. Kienberger, and F. Krausz, "High-repetition-rate picosecond pump laser based on a Yb:YAG disk amplifier for optical parametric amplification," *Optics Letters*, vol. 34, no. 14, pp. 2123–5, Jul. 2009.

[86] K.-H. Hong, J. T. Gopinath, D. Rand, A. M. Siddiqui, S.-W. Huang, E. Li, B. J. Eggleton, J. D. Hybl, T. Y. Fan, and F. X. Kärtner, "High-energy, kHz-repetition-rate, ps cryogenic Yb:YAG chirped-pulse amplifier," *Optics Letters*, vol. 35, no. 11, pp. 1752–1754, 2010.

[87] D. C. Brown and V. A. Vitali, "Yb:YAG kinetics model including saturation and power conservation," *Quantum Electronics, IEEE Journal of*, vol. 47, no. 1, pp. 3–12, Jan. 2011.

[88] H. Furuse, J. Kawanaka, N. Miyanaga, T. Saiki, K. Imasaki, M. Fujita, K. Takeshita, S. Ishii, and Y. Izawa, "Zig-zag active-mirror laser with cryogenic Yb3+:YAG/YAG composite ceramics," *Optics Express*, vol. 19, no. 3, pp. 2448–55, Jan. 2011.

[89] B. A. Reagan, K. A. Wernsing, A. H. Curtis, F. J. Furch, B. M. Luther, D. Patel, C. S. Menoni, and J. J. Rocca, "Demonstration of a 100 Hz repetition rate gain-saturated diode-pumped table-top soft x-ray laser," *Optics Letters*, vol. 37, no. 17, pp. 3624–6, Sep. 2012.

[90] M. Schulz, R. Riedel, A. Willner, S. Düsterer, M. J. Prandolini, J. Feldhaus, B. Faatz, J. Rossbach, M. Drescher, and F. Tavella, "Pulsed operation of a high average power Yb:YAG thin-disk multipass amplifier," *Optics Express*, vol. 20, no. 5, pp. 5038–43, Feb. 2012.

[91] W. Koechner, *Solid-State Laser Engineering*. Springer Science+Business Media, Inc., 2006.

[92] H. Furuse, J. Kawanaka, K. Takeshita, N. Miyanaga, T. Saiki, K. Imasaki, M. Fujita, and S. Ishii, "Total-reflection active-mirror laser with cryogenic Yb:YAG ceramics," *Optics Letters*, vol. 34, no. 21, pp. 3439–41, Nov. 2009.
[93] Y. Wang, K. Inoue, H. Kan, T. Ogawa, and S. Wada, "Study on thermally induced depolarization of a probe beam by considering the thermal lens effect," *Journal of Physics D: Applied Physics*, vol. 42, no. 23, p. 235108, Dec. 2009.
[94] J. W. Kim, M. J. Yarrow, and W. A. Clarkson, "High power single-frequency continuous-wave Nd:YVO4 master-oscillator power amplifier," *Applied Physics B*, vol. 85, no. 4, pp. 539–543, Jul. 2006.
[95] G. Wagner, M. Shiler, and V. Wulfmeyer, "Simulations of thermal lensing of a Ti:Sapphire crystal end-pumped with high average power," *Optics Express*, vol. 13, no. 20, pp. 8045–55, Oct. 2005.
[96] D. C. Brown, J. M. Singley, K. Kowalewski, J. Guelzow, and V. Vitali, "High sustained average power cw and ultrafast Yb:YAG near-diffraction-limited cryogenic solid-state laser," *Optics Express*, vol. 18, no. 24, pp. 24770–92, Nov. 2010.
[97] K. Nicklaus, M. Hoefer, D. Hoffmann, J. Luttmann, R. Wester, and R. Poprawe, "MOPA with kW average power and multi MW peak power: experimental results, theoretical modeling, and scaling limits," *Proceedings of SPIE*, vol. 6100, pp. 610016–610016–11, 2006.
[98] R. Fluck, M. R. Hermann, and L. A. Hackel, "Energetic and thermal performance of high-gain diode-side-pumped Nd:YAG rods," *Applied Physics B*, vol. 70, no. 4, pp. 491–498, Apr. 2000.
[99] Y. Wang, K. Inoue, H. Kan, T. Ogawa, and S. Wada, "Birefringence compensation of two tandem-set Nd:YAG rods with different thermally induced features," *Journal of Optics A: Pure and Applied Optics*, vol. 11, no. 12, p. 125501, Dec. 2009.
[100] R. Fluck, M. R. Hermann, and L. A. Hackel, "Birefringence compensation in single solid-state rods," *Applied Physics Letters*, vol. 76, no. 12, p. 1513, 2000.
[101] F. Träger, *Springer Handbook of Lasers and Optics*. Springer Science+Business Media, Inc., 2007.
[102] J. C. Diels and W. Rudolph, *Ultrashort Laser Pulse Phenomena*. Elsevier, Inc., 2006.
[103] M. Hemmer, A. Vaupel, and M. C. Richardson, "Numerical Investigation of Ultra-broad Band Pulse Stretching and Compressing for OPCPA Applications," in *UltraFast Optics (UFO VII) and High Field Short Wavelength (HFSW XIII)*, 2009, p. -.
[104] J. Jiang, Z. Zhang, and T. Hasama, "Evaluation of chirped-pulse-amplification systems with Offner triplet telescope stretchers," *Journal of the Optical Society of America B*, vol. 19, no. 4, p. 678, Apr. 2002.
[105] R. L. Fork, C. H. Cruz, P. C. Becker, and C. V Shank, "Compression of optical pulses to six femtoseconds by using cubic phase compensation," *Optics Letters*, vol. 12, no. 7, pp. 483–5, Jul. 1987.
[106] A. Monmayrant, A. Arbouet, B. Girard, B. Chatel, A. Barman, B. J. Whitaker, and D. Kaplan, "AOPDF-shaped optical parametric amplifier output in the visible," *Applied Physics B*, vol. 81, no. 2–3, pp. 177–180, Jul. 2005.
[107] J. Zheng and H. Zacharias, "Design considerations for a compact grism stretcher for non-collinear optical parametric chirped-pulse amplification," *Applied Physics B*, vol. 96, no. 2–3, pp. 445–452, Mar. 2009.

[108] T. H. Dou, R. Tautz, X. Gu, G. Marcus, T. Feurer, F. Krausz, and L. Veisz, “Dispersion control with reflection grisms of an ultra-broadband spectrum approaching a full octave,” *Optics Express*, vol. 18, no. 26, pp. 27900–9, Dec. 2010.
[109] F. W. Helbing, G. Steinmeyer, and U. Keller, “Carrier-Envelope Offset Phase-Locking With Attosecond Timing Jitter,” *IEEE Journal of Quantum Electronics*, vol. 9, no. 4, pp. 1030–1040, 2003.
[110] D. J. Jones, S. A. Diddams, J. K. Ranka, A. Stentz, R. S. Windeler, J. L. Hall, and S. T. Cundiff, “Carrier-Envelope Phase Control of Femtosecond Mode-Locked Lasers and Direct Optical Frequency Synthesis,” *Science*, vol. 288, no. 5466, pp. 635–639, Apr. 2000.
[111] A. Apolonski, A. Poppe, G. Tempea, C. Spielmann, T. Udem, R. Holzwarth, T. W. Hänsch, and F. Krausz, “Controlling the Phase Evolution of Few-Cycle Light Pulses,” *Physical Review Letters*, vol. 85, no. 4, pp. 740–3, Jul. 2000.
[112] F. W. Helbing, G. Steinmeyer, J. Stenger, H. R. Telle, and U. Keller, “Carrier-envelope-offset dynamics and stabilization of femtosecond pulses,” *Applied Physics B: Lasers and Optics*, vol. 74, no. 9, pp. s35–s42, Jun. 2002.
[113] R. Ell, J. R. Birge, M. Araghchini, and F. X. Kärtner, “Carrier-envelope phase control by a composite plate,” *Optics Express*, vol. 14, no. 12, pp. 5829–37, Jun. 2006.
[114] T. Fordell, M. Miranda, A. Persson, and A. L’Huillier, “Carrier-envelope phase stabilization of a multi-millijoule, regenerative-amplifier-based chirped-pulse smplifier system,” *Optics Express*, vol. 17, no. 23, pp. 2070–2074, 2009.
[115] R. W. Boyd, *Nonlinear Optics*. Elsevier, Inc., 2008.
[116] R. A. Ganeev, I. A. Kulagin, A. I. Ryasnyansky, R. I. Tugushev, and T. Usmanov, “Characterization of nonlinear optical parameters of KDP, LiNbO3 and BBO crystals,” *Optics Communications*, vol. 229, no. 1–6, pp. 403–412, Jan. 2004.
[117] S. Demmler, J. Rothhardt, S. Hädrich, J. Bromage, J. Limpert, and A. Tünnermann, “Control of nonlinear spectral phase induced by ultra-broadband optical parametric amplification,” *Optics Letters*, vol. 37, no. 19, pp. 3933–5, Oct. 2012.
[118] G. D. Boyd and D. A. Kleinman, “Parametric Interaction of Focused Gaussian Light Beams,” *Journal of Applied Physics*, vol. 39, no. 8, p. 3597, 1968.
[119] A. Harth, M. Schultze, T. Lang, T. Binhammer, S. Rausch, and U. Morgner, “Two-color pumped OPCPA system emitting spectra spanning 1.5 octaves from VIS to NIR,” *Optics Express*, vol. 20, no. 3, pp. 3076–81, Jan. 2012.
[120] M. Lührmann, F. Harth, C. Theobald, T. Ulm, R. Knappe, A. Nebel, A. Klehr, G. Erbert, and J. A. L’huillier, “High average power Nd:YVO4 regenerative amplifier seeded by a gain switched diode laser,” *Proceedings of SPIE*, vol. 7912, pp. 791210–791210–8, 2011.
[121] M. Hemmer, A. Vaupel, M. Ramme, C. Willis, J. Bradford, V. Smirnov, L. Shah, L. Glebov, and M. Richardson, “A VBG-Stabilized Narrow Linewidth, Spectrally Tunable, Yb:YAG Thin-Disk Laser,” in *Conference on Lasers and Electro-Optics (CLEO)*, 2011, no. Figure 1, p. CWP3.
[122] A. V Okishev, C. Dorrer, V. I. Smirnov, L. B. Glebov, and J. D. Zuegel, “Spectral filtering in a diode-pumped Nd:YLF regenerative amplifier using a volume Bragg grating,” *Optics Express*, vol. 15, no. 13, pp. 8197–202, Jun. 2007.
[123] M. Hemmer, A. Vaupel, M. Wohlmuth, and M. Richardson, “OPCPA pump laser based on a regenerative amplifier with volume Bragg grating spectral filtering,” *Applied Physics B*, vol. 106, no. 3, pp. 599–603, Jan. 2012.

[124] M. Lührmann, C. Theobald, R. Wallenstein, and J. A. L'huillier, "High energy cw-diode pumped Nd:YVO4 regenerative amplifier with efficient second harmonic generation," *Optics Express*, vol. 17, no. 25, pp. 22761–6, Dec. 2009.
[125] T. Kanai, A. Suda, S. Bohman, M. Kaku, S. Yamaguchi, and K. Midorikawa, "Pointing stabilization of a high-repetition-rate high-power femtosecond laser for intense few-cycle pulse generation," *Applied Physics Letters*, vol. 92, no. 6, p. 061106, 2008.
[126] G. Genoud, F. Wojda, M. Burza, A. Persson, and C.-G. Wahlström, "Active control of the pointing of a multi-terawatt laser," *Review of Scientific Instruments*, vol. 82, no. 3, p. 033102, Mar. 2011.
[127] M. Siebold, M. Hornung, J. Hein, G. Paunescu, R. Sauerbrey, T. Bergmann, and G. Hollemann, "A high-average-power diode-pumped Nd:YVO4 regenerative laser amplifier for picosecond-pulses," *Applied Physics B: Lasers and Optics*, vol. 78, no. 3–4, pp. 287–290, Feb. 2004.
[128] M. Grishin, V. Gulbinas, and A. Michailovas, "Bifurcation suppression for stability improvement in Nd:YVO4 regenerative amplifier," *Optics Express*, vol. 17, no. 18, pp. 15700–8, Aug. 2009.
[129] K. Okamura and T. Kobayashi, "Output Energy Stabilization of Non-collinear Optical Parametric Amplifier," *Japanese Journal of Applied Physics*, vol. 48, no. 7, p. 070214, Jul. 2009.
[130] D. R. Walker, C. J. Flood, H. M. van Driel, U. J. Greiner, and H. H. Klingenberg, "High power diode-pumped Nd:YAG regenerative amplifier for picosecond pulses," *Applied Physics Letters*, vol. 65, no. 16, p. 1992, 1994.
[131] H. Lin, J. Li, J. He, and X. Liang, "High-power picosecond regenerative amplifier based on CW diode side-pumped Nd:YAG with high beam quality," *Chinese Optics Letters*, vol. 9, no. 8, pp. 9–11, 2011.
[132] B. C. Stuart, M. D. Feit, S. Herman, A. M. Rubenchik, B. W. Shore, and M. D. Perry, "Nanosecond-to-femtosecond laser-induced breakdown in dielectrics," *Physical Review B*, vol. 53, no. 4, pp. 1749–1761, Jan. 1996.
[133] K. Michailovas, V. Smilgevicius, and A. Michailovas, "Kilohertz rate picosecond pulses amplifier for pumping of OPCPA system," *OSA Advanced Solid-State Photonics (ASSP)*, vol. AW4A3, pp. 1–2, 2012.
[134] K. X. Liu, C. J. Flood, D. R. Walker, and H. M. van Driel, "Kerr lens mode locking of a diode-pumped Nd:YAG laser," *Optics Letters*, vol. 17, no. 19, p. 1361, Oct. 1992.
[135] R. Adair, L. Chase, and S. Payne, "Nonlinear refractive index of optical crystals," *Physical Review B, Condensed Matter*, vol. 39, no. 5, pp. 3337–3350, Feb. 1989.
[136] L. Luo, L. Chen, Z. R. Qiu, X. Y. Yu, D. C. Dai, J. Y. Zhou, and J. Kuhl, "Measurement of femtosecond resonant nonlinear refraction in Nd:YVO4 by degenerate pump-probe spectroscopy," *Journal of Applied Physics*, vol. 89, no. 12, p. 8342, 2001.
[137] R. Bhushan, K. Tsubakimoto, H. Yoshida, H. Fujita, and M. Nakatsuka, "Thermally Induced Birefringence Compensation in High Average Power Nd:YAG Laser," *Japanese Journal of Applied Physics*, vol. 46, no. 3A, pp. 1051–1053, Mar. 2007.
[138] A. Vaupel, N. Bodnar, M. Hemmer, and M. Richardson, "A joule-class, TEM00 spatial profile, narrow-linewidth laser system," in *Proceedings of SPIE*, 2011, vol. 7912, p. 79120U–1 to 79120U–7.

[139] A. K. Potemkin, T. V Barmashova, A. V Kirsanov, M. A. Martyanov, E. A. Khazanov, and A. A. Shaykin, "Spatial filters for high-peak-power multistage laser amplifiers," *Applied Optics*, vol. 46, no. 20, pp. 4423–30, Jul. 2007.
[140] M. Hemmer, A. Vaupel, and M. Richardson, "Toward a Multi-kHz, Multi-mJ, Few Cycle, Phase Stabilized Laser System," in *International Conference on Attosecond Physics (Atto-09, Post Deadline)*, 2009, vol. 684, p. 32826.
[141] R. Trebino, K. W. DeLong, D. N. Fittinghoff, J. N. Sweetser, M. A. Krumbügel, B. A. Richman, and D. J. Kane, "Measuring ultrashort laser pulses in the time-frequency domain using frequency-resolved optical gating," *Review of Scientific Instruments*, vol. 68, no. 9, pp. 3277–3295, 1997.
[142] C. Iaconis and I. A. Walmsley, "Self-referencing spectral interferometry for measuring ultrashort optical pulses," *IEEE Journal of Quantum Electronics*, vol. 35, no. 4, pp. 501–509, Apr. 1999.
[143] P. Baum, S. Lochbrunner, and E. Riedle, "Zero-additional-phase SPIDER: full characterization of visible and sub-20-fs ultraviolet pulses," *Optics Letters*, vol. 29, no. 2, pp. 210–2, Jan. 2004.
[144] J. R. Birge, R. Ell, and F. X. Kärtner, "Two-dimensional spectral shearing interferometry for few-cycle pulse characterization," *Optics Letters*, vol. 31, no. 13, pp. 2063–5, Jul. 2006.
[145] E. M. Kosik, A. S. Radunsky, I. A. Walmsley, and C. Dorrer, "Interferometric technique for measuring broadband ultrashort pulses at the sampling limit," *Optics Letters*, vol. 30, no. 3, pp. 326–8, Feb. 2005.
[146] A. S. Wyatt, I. A. Walmsley, G. Stibenz, and G. Steinmeyer, "Sub-10 fs pulse characterization using spatially encoded arrangement for spectral phase interferometry for direct electric field reconstruction," *Optics Letters*, vol. 31, no. 12, pp. 1914–6, Jun. 2006.
[147] C. Dorrer and I. A. Walmsley, "Accuracy criterion for ultrashort pulse characterization techniques: application to spectral phase interferometry for direct electric field reconstruction," *Journal of the Optical Society of America B*, vol. 19, no. 5, p. 1019, May 2002.
[148] R. Szipocs and A. Kohazi-Kis, "Theory and design of chirped dielectric laser mirrors," *Applied Physics B: Lasers and Optics*, vol. 135, pp. 115–135, 1997.
[149] F. X. Kärtner, U. Morgner, R. Ell, T. Schibli, J. G. Fujimoto, E. P. Ippen, V. Scheuer, G. Angelow, and T. Tschudi, "Ultrabroadband double-chirped mirror pairs for generation of octave spectra," *Journal of the Optical Society of America B*, vol. 18, no. 6, pp. 882–885, 2001.
[150] J. Moses, C. Manzoni, S.-W. Huang, G. Cerullo, and F. X. Kärtner, "Temporal optimization of ultrabroadband high-energy OPCPA," *Optics Express*, vol. 17, no. 7, pp. 5540–55, Mar. 2009.
[151] S. Witte, R. T. Zinkstok, W. Hogervorst, and K. S. E. Eikema, "Numerical simulations for performance optimization of a few-cycle terawatt NOPCPA system," *Applied Physics B*, vol. 87, no. 4, pp. 677–684, May 2007.
[152] J. Moses and S.-W. Huang, "Conformal profile theory for performance scaling of ultrabroadband optical parametric chirped pulse amplification," *Journal of the Optical Society of America B*, vol. 28, no. 4, p. 812, Mar. 2011.
[153] F. Tavella, a Marcinkevičius, and F. Krausz, "Investigation of the superfluorescence and signal amplification in an ultrabroadband multiterawatt optical parametric chirped pulse amplifier system," *New Journal of Physics*, vol. 8, no. 10, pp. 219–219, Oct. 2006.

[154] C. Manzoni, J. Moses, F. X. Kärtner, and G. Cerullo, “Excess quantum noise in optical parametric chirped-pulse amplification,” *Optics Express*, vol. 19, no. 9, pp. 8357–66, May 2011.
[155] S. Friberg and P. Smith, “Nonlinear optical glasses for ultrafast optical switches,” *IEEE Journal of Quantum Electronics*, vol. 23, no. 12, pp. 2089–2094, Dec. 1987.
[156] H. Nakatani, W. R. Bosenberg, L. K. Cheng, and C. L. Tang, “Laser-induced damage in beta-barium metaborate,” *Applied Physics Letters*, vol. 53, no. 26, p. 2587, 1988.
[157] J. Limpert, F. Röser, D. N. Schimpf, E. Seise, T. Eidam, S. Hädrich, J. Rothhardt, C. J. Misas, and A. Tünnermann, “High Repetition Rate Gigawatt Peak Power Fiber Laser Systems: Challenges, Design, and Experiment,” *Selected Topics in Quantum Electronics*, vol. 15, no. 1, pp. 159–169, 2009.
[158] A. V Smith and J. J. Smith, “Mode instability in high power fiber amplifiers,” *Optics Express*, vol. 19, no. 11, pp. 10180–92, May 2011.
[159] H.-J. Otto, F. Stutzki, F. Jansen, T. Eidam, C. Jauregui, J. Limpert, and A. Tünnermann, “Temporal dynamics of mode instabilities in high-power fiber lasers and amplifiers,” *Optics Express*, vol. 20, no. 14, pp. 15710–22, Jul. 2012.
[160] T. Eidam, J. Rothhardt, F. Stutzki, F. Jansen, S. Hädrich, H. Carstens, C. Jauregui, J. Limpert, and A. Tünnermann, “Fiber chirped-pulse amplification system emitting 3.8 GW peak power,” *Optics Express*, vol. 19, no. 1, pp. 255–60, Jan. 2011.
[161] T. Eidam, S. Hanf, E. Seise, T. V Andersen, T. Gabler, C. Wirth, T. Schreiber, J. Limpert, and A. Tünnermann, “Femtosecond fiber CPA system emitting 830 W average output power,” *Optics Letters*, vol. 35, no. 2, pp. 94–6, Jan. 2010.
[162] A. Klenke, E. Seise, S. Demmler, J. Rothhardt, S. Breitkopf, J. Limpert, and A. Tünnermann, “Coherently-combined two channel femtosecond fiber CPA system producing 3 mJ pulse energy,” *Optics Express*, vol. 19, no. 24, pp. 24280–5, Nov. 2011.
[163] E. Zeromskis, A. Dubietis, G. Tamosauskas, and A. Piskarskas, “Gain bandwidth broadening of the continuum-seeded optical parametric amplifier by use of two pump beams,” *Optics Communications*, vol. 203, no. March, pp. 435–440, 2002.
[164] S. Ališauskas, R. Butkus, V. Pyragaitė, V. Smilgevičius, A. Stabinis, and A. Piskarskas, “Prospects for increasing average power of optical parametric chirped pulse amplifiers via multi-beam pumping,” *Optics Communications*, vol. 283, no. 3, pp. 469–473, Feb. 2010.
[165] J. Limpert, C. Aguergaray, S. Montant, I. Manek-Hönninger, S. Petit, D. Descamps, E. Cormier, and F. Salin, “Ultra-broad bandwidth parametric amplification at degeneracy,” *Optics Express*, vol. 13, no. 19, pp. 7386–92, Sep. 2005.
[166] J. M. Dudley, G. Genty, and S. Coen, “Supercontinuum generation in photonic crystal fiber,” *Reviews of Modern Physics*, vol. 78, no. 4, pp. 1135–1184, Oct. 2006.
[167] J. Limpert, N. Deguil-Robin, I. Manek-Hönninger, F. Salin, F. Röser, A. Liem, T. Schreiber, S. Nolte, H. Zellmer, A. Tünnermann, J. Broeng, A. Petersson, and C. Jakobsen, “High-power rod-type photonic crystal fiber laser,” *Optics Express*, vol. 13, no. 4, pp. 1055–8, Feb. 2005.
[168] J. Boullet, Y. Zaouter, E. Cormier, and J. Limpert, “31µJ , 220fs , 1MHz Fiber Chirped Pulse Amplification System,” in *Conference on Lasers and Electro-Optics (CLEO)*, 2008, p. CThB1.
[169] Y. Zaouter, J. Boullet, L. Huang, C. Aguergaray, D. N. Papadopoulos, M. Hanna, F. Druon, E. Mottay, P. Georges, and E. Cormier, “High energy direct amplification of femtosecond

pulse in a highly non-linear fiber amplifier," in *OSA Advanced Solid-State Photonics (ASSP)*, 2008, p. 128_1.
[170] I. Martial, D. Papadopulos, M. Hanna, F. Druon, and P. Georges, "Nonlinear compression in a rod-type fiber for high energy ultrashort pulse generation," *Optics Express*, vol. 17, no. 13, pp. 11155–60, Jun. 2009.
[171] Y. Zaouter, J. Boullet, E. Mottay, and E. Cormier, "Transform-limited 100 µJ , 340 MW pulses from a nonlinear-fiber chirped-pulse amplifier using a mismatched grating stretcher - compressor," *Optics Letters*, vol. 33, no. 13, pp. 1527–9, Jul. 2008.
[172] J. Rothhardt, S. Demmler, S. Hädrich, T. Peschel, J. Limpert, and A. Tünnermann, "Thermal effects in high average power optical parametric amplifiers," *Optics Letters*, vol. 38, no. 5, pp. 763–5, Mar. 2013.
[173] D. N. Nikogosyan, *Nonlinear Optical Crystals: A Complete Survey*. 2005, p. 427.
[174] J. Kleinbauer, R. Knappe, and R. Wallenstein, "13-W picosecond Nd:GdVO4 regenerative amplifier with 200-kHz repetition rate," *Applied Physics B*, vol. 81, no. 2–3, pp. 163–166, Jun. 2005.
[175] K.-H. Hong, A. Siddiqui, J. Moses, J. Gopinath, J. Hybl, F. O. Ilday, T. Y. Fan, and F. X. Kärtner, "Generation of 287 W, 5.5 ps pulses at 78 MHz repetition rate from a cryogenically cooled Yb:YAG amplifier seeded by a fiber chirped-pulse amplification system," *Optics Letters*, vol. 33, no. 21, pp. 2473–5, Nov. 2008.
[176] A. Pugžlys, G. Andriukaitis, A. Baltuška, L. Su, J. Xu, H. Li, R. Li, W. J. Lai, P. B. Phua, A. Marcinkevicius, M. E. Fermann, L. Giniunas, R. Danielius, and S. Ališauskas, "Multi-mJ, 200-fs, cw-pumped, cryogenically cooled, Yb,Na:CaF2 amplifier," *Optics Letters*, vol. 34, no. 13, pp. 2075–2077, 2009.
[177] J. Tümmler, R. Jung, H. Stiel, P. V. Nickles, and W. Sandner, "High-repetition-rate chirped-pulse-amplification thin-disk laser system with joule-level pulse energy," *Optics Letters*, vol. 34, no. 9, pp. 1378–1380, 2009.
[178] J. Fu, Q. S. Pang, L. Chang, Z. A. Bai, Q. K. Ai, L. Y. Chen, M. Chen, G. Li, Y. F. Ma, Z. W. Fan, G. Niu, J. Yu, Y. Liu, X. Zhang, W. Y. Kang, and K. He, "Picosecond laser system with 30-W average power via cavity dumping and amplifying," *Laser Physics*, vol. 21, no. 6, pp. 1042–1046, May 2011.
[179] P. Russbueldt, T. Mans, J. Weitenberg, H. D. Hoffmann, and R. Poprawe, "Compact diode-pumped 1.1 kW Yb:YAG Innoslab femtosecond amplifier," *Optics Letters*, vol. 35, no. 24, pp. 4169–71, Dec. 2010.
[180] H. Kalaycioglu, B. Oktem, C. Senel, P. P. Paltani, and F. O. Ilday, "Microjoule-energy, 1 MHz repetition rate pulses from all-fiber-integrated nonlinear chirped-pulse amplifier," *Optics Letters*, vol. 35, no. 7, pp. 959–61, Apr. 2010.
[181] A. H. Curtis, B. A. Reagan, K. A. Wernsing, F. J. Furch, B. M. Luther, and J. J. Rocca, "Demonstration of a compact 100 Hz, 0.1 J, diode-pumped picosecond laser," *Optics Letters*, vol. 36, no. 11, pp. 2164–6, Jun. 2011.
[182] D. A. Rand, S. E. J. Shaw, J. R. Ochoa, D. J. Ripin, A. Taylor, T. Y. Fan, H. Martin, S. Hawes, J. Zhang, S. Sarkisyan, E. Wilson, and P. Lundquist, "Picosecond pulses from a cryogenically cooled, composite amplifier using Yb:YAG and Yb:GSAG," *Optics Letters*, vol. 36, no. 3, pp. 340–2, Feb. 2011.
[183] D. N. Papadopoulos, A. Pellegrina, L. P. Ramirez, P. Georges, and F. Druon, "Broadband high-energy diode-pumped Yb:KYW multipass amplifier," *Optics Letters*, vol. 36, no. 19, pp. 3816–8, Oct. 2011.

[184] M. Suzuki, H. Kiriyama, I. Daito, Y. Ochi, H. Okada, M. Sato, Y. Tamaoki, T. Yoshii, J. Maeda, S. Matsuoka, H. Kan, P. R. Bolton, A. Sugiyama, K. Kondo, and S. Kawanishi, "Hundred mJ, sub-picoseconds, high temporal contrast OPCPA/Yb:YAG ceramic thin disk hybrid laser system," *Applied Physics B*, vol. 105, no. 2, pp. 181–184, Sep. 2011.

[185] S. Klingebiel, C. Wandt, C. Skrobol, I. Ahmad, S. A. Trushin, Z. Major, F. Krausz, and S. Karsch, "High energy picosecond Yb:YAG CPA system at 10 Hz repetition rate for pumping optical parametric amplifiers," *Optics Express*, vol. 19, no. 6, pp. 5357–63, Mar. 2011.

[186] M. Schulz, R. Riedel, A. Willner, T. Mans, C. Schnitzler, P. Russbueldt, J. Dolkemeyer, E. Seise, T. Gottschall, S. Hädrich, S. Duesterer, H. Schlarb, J. Feldhaus, J. Limpert, B. Faatz, A. Tünnermann, J. Rossbach, M. Drescher, and F. Tavella, "Yb:YAG Innoslab amplifier: efficient high repetition rate subpicosecond pumping system for optical parametric chirped pulse amplification," *Optics Letters*, vol. 36, no. 13, pp. 2456–8, Jul. 2011.

[187] C. Heese, A. E. Oehler, L. Gallmann, and U. Keller, "High-energy picosecond Nd:YVO4 slab amplifier for OPCPA pumping," *Applied Physics B*, vol. 103, no. 1, pp. 5–8, Apr. 2011.

[188] D. E. Miller, L. E. Zapata, D. J. Ripin, and T. Y. Fan, "Sub-picosecond pulses at 100 W average power from a Yb:YLF chirped-pulse amplification system," *Optics Letters*, vol. 37, no. 13, pp. 2700–2, Jul. 2012.

[189] G. H. Kim, J. Yang, S. a Chizhov, E. G. Sall, A. V Kulik, V. E. Yashin, D. S. Lee, and U. Kang, "High average-power ultrafast CPA Yb:KYW laser system with dual-slab amplifier," *Optics Express*, vol. 20, no. 4, pp. 3434–42, Feb. 2012.

[190] L. Daniault, M. Hanna, D. N. Papadopoulos, Y. Zaouter, E. Mottay, F. Druon, and P. Georges, "High peak-power stretcher-free femtosecond fiber amplifier using passive spatio-temporal coherent combining," *Optics Express*, vol. 20, no. 19, pp. 21627–21634, 2012.

[191] J. Adamonis, R. Antipenkov, J. Kolenda, A. Michailovas, A. P. Piskarskas, and A. Varanavicius, "High-energy Nd:YAG-amplification system for OPCPA pumping," *Quantum Electronics*, vol. 42, no. 7, pp. 567–574, Jul. 2012.